

Tissue-like Hydrogels by Design

By

Shaoting Lin

B.S., Tsinghua University, China, 2010

M.S., Tsinghua University, China, 2013

Submitted to the Department of Mechanical Engineering
in partial fulfillment of the requirements for the degree of

Doctor of Philosophy

at the

MASSACHUSETTS INSTITUTE OF TECHNOLOGY

Sep 2019

© Massachusetts Institute of Technology 2019. All rights reserved.

Signature redacted

Author.....

.....

Department of Mechanical Engineering

Signature redacted

July 31, 2019

Certificated by.....

.....

Xuanhe Zhao

~~Associate~~ Professor of Mechanical Engineering

Signature redacted

Thesis Supervisor

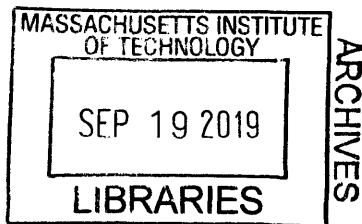
Accepted by.....

.....

Nicolas Hadjiconstantinou

Professor of Mechanical Engineering

Chairman, Department Committee on Graduate Theses



Tissue-like Hydrogels by Design

By

Shaoting Lin

Submitted to the Department of Mechanical Engineering

on July 31, 2019, in partial fulfillment of the

requirements for the degree of

Doctor of Philosophy

Abstract

Human bodies are mostly made of soft, wet yet robust biological hydrogels such as cartilages, ligaments, and muscles. The biological hydrogels commonly possess mechanical properties such as high toughness, resilience and fatigue resistance to guarantee the bodies' reliable functions and activities. While hydrogels with tissue-like mechanical properties are highly desirable in applications as diverse as tissue engineering, drug delivery and soft machines, these properties are rarely achieved in synthetic hydrogels. The first part of this dissertation is aimed to design synthetic hydrogels that possess tissue-like mechanical properties, including high toughness, resilience and fatigue threshold, through combined theory, modeling and experiments. First, we develop a coupled cohesive-zone and Mullins effect model to predict the fracture energies of tough hydrogels. Based on the model, we further provide a toughening diagram that can guide the design of new tough hydrogels. Second, we propose that delaying mechanical dissipations in tough hydrogels can make the hydrogels resilient under moderate deformation while still

high toughness and high resilience for hydrogels. Third, we study fatigue fracture in hydrogels and show that the introduction of nanocrystalline domains and aligned nanofibrils can substantially increase hydrogels' fatigue-resistant properties.

In the second part of this dissertation, we study mechanical instabilities in hydrogels. Under tension, a layer of confined elastic material such as hydrogel can exhibit various modes of mechanical instabilities, including cavitation, fingering and fringe instabilities. While the cavitation has been extensively studied, the fingering and fringe instabilities have not been well understood, and the relations and interactions of these instabilities have not been explored yet. We systematically study the formation, transition, interaction and co-existence of mechanical instabilities in confined elastic layers under tension. Through combined experimental, numerical and theoretical analysis, we find that the mode of instability is determined by both geometry and mechanical properties of the elastic layer through two non-dimensional parameters: layer's lateral dimension over its thickness and elastocapillary length over the defect size. A phase diagram is calculated to quantitatively predict the occurrence of any mode of instability, which can help the design of robust adhesives by rationally harnessing the desired mode of instabilities while suppressing the other modes.

Thesis Supervisor and Committee Chair:

Professor Xuanhe Zhao, Department of Mechanical Engineering

Thesis Committee Members:

Professor Lallit Anand, Department of Mechanical Engineering

Professor Rohan Abeyaratne, Department of Mechanical Engineering

Professor Gareth H. McKinley, Department of Mechanical Engineering

Acknowledgements

First and foremost, I would like to express my deepest appreciation to Professor Xuanhe Zhao for his unconditional support, patient training, and vigorous encouragement. Working with Professor Zhao has been a tremendous experience. During the past six years, Professor Zhao has patiently trained me to become a researcher. He actively encouraged me to explore new fields, propose bold ideas, and tackle challenging but impactful problems. His research taste, his writing style and his knowledge of mechanics in soft materials will accompany me towards the endeavor of carrying out researches in future.

I would also express my sincere thanks to my doctoral thesis committee members Professor Lallit Anand, Professor Rohan Abeyaratne, and Professor Gareth H. McKinley for their thoughtful guidance and supportive feedback on my research. I am grateful for Professor Lallit Anand, who taught me fundamentals in solid mechanics and gave me numerous research suggestions on fracture and instabilities in soft materials. I am also grateful for Professor Rohan Abeyaratne, with whom I enjoyed studying the phenomenon of elastic instabilities in confined hydrogel layers. At the same time, I have benefited much from the discussion and collaboration with Professor Gareth H. McKinley on the problems related to rheology properties in hydrogels, viscoelastic fracture in hydrogels, and fatigue fracture in hydrogels.

I would like to deliver my sincere thanks to Professor Yong Xia and Professor Qing Zhou at Tsinghua University in China as well. Without their selfless guidance, supports and recommendations, I could not come to United States to pursue my Ph.D. degree.

This adventure would not have been possible without the help of my colleagues and friends. My appreciation first goes to Dr. Teng Zhang, currently professor at Syracuse University, who mentored me on the study of fracture and instabilities in soft materials. My thanks also go to Dr. Tal Cohen, currently professor at Massachusetts Institute of Technology, with whom we worked together on discovering fringe instability in hydrogels. I highly enjoyed the experience I have

shared with Hyunwoo Yuk, Xinyue Liu, Ji Liu and Yunwei Mao, who provided me numerous help in experiments, simulation, and theory. Particularly Yunwei Mao derived the theory for predicting the onset of fringe and fingering instabilities in Chapter 7. Both rich scientific insights from them and fruitful conversations with them benefited me a lot and helped me to be a mature researcher. Special thanks go to the member of Zhao group members as well, especially German Alberto Parada, Kai Zhang, and Baoyang Lu from Zhao group at MIT and Yihao Zhou, Sungmin Hong, Changyong Cao, Qiming Wang, and Jianfeng Zang from Zhao group at Duke. I also appreciate the collaboration with Hyun-Chae Loh from Professor Admir Masic's group, Jake Song from Professor Gareth H. McKinley's and Niels Holten-Andersen's groups, Jiawei Zhou from Professor Gang Chen's group, Bianca Giovanardi and Adam Andrzej Sliwiak from Professor Raul Radovitzky's group, Zachary Kean from Professor Stephen L Craig's group, Christoph Steiger from Professor Giovanni Traverso's group, Evgenia P Gilshteyn from Professor Albert G Nasibulin's group, and Jiliang Hu from Professor Ming Guo's group. Many thanks go to all my friends during my study at MIT, Duke, and Tsinghua University, especially Juner Zhu, Tao Gao, Hongchuan Wei. It was wonderful experience to know them and work with them.

A lot of the work in this thesis was done using the facilities of Institute for Soldier Nanotechnologies (ISN) at MIT and Center for Materials Science and Engineering (CMSE). I would like to thank the research staff there, especially Charles Settens at CMSE.

Finally, I must express my profound gratitude to my father Lian-Sheng Lin, my mother Wan-Zhen Xu and other family members for their understanding and support. This accomplishment would not have been possible without them. The gratitude particularly goes to my girlfriend Xinyue Liu, who is also my long lasting coworker in life and research. Her wisdom, love, optimism and grit empowered me to finish the PhD work.

Cambridge, MA

Shaoting Lin

July 23, 2019

Contents

Abstract	2
Acknowledgements	4
1. Introduction	32
1.1 Biological tissues	32
1.2 Hydrogels	34
1.2.1 Mechanical properties of hydrogels	34
1.2.2 Fracture of hydrogels	36
1.2.3 Fatigue of hydrogels	38
1.2.4 Elastic instabilities in hydrogels	39
1.3 Motivation	40
1.3.1 Design mechanical properties of hydrogels	40
1.3.2 Understanding mechanical instabilities in confined hydrogel layers	40
1.4 Research methodology	40
1.5 Plan of this dissertation	41
1.6 List of publications for each chapter	42
Part I: Design tissue-like properties of hydrogels	
2. Design of tough hydrogels	44
2.1 Introduction	45

2.2	Scaling analysis.....	46
2.3	Coupled cohesive-zone and Mullins effect model.....	48
2.4	Theoretical and numerical results	54
2.5	Experimental validation	58
2.5.1	Material preparation.....	58
2.5.2	Calibration of material parameters.....	58
2.5.3	Validation.....	60
2.6	Concluding remarks	61
3.	Design of resilient yet tough hydrogels	63
3.1	Introduction.....	64
3.2	Definition and experimental characterization	65
3.3	Delayed dissipation to reconcile resilience and toughness	66
3.4	Implementation of delayed dissipation	67
3.5	Experimental validation	68
3.5.1	Material.....	68
3.5.2	Experimental validation	69
3.6	Conclusion	72
4.	Design of fatigue-resistant hydrogels	74
4.1	Introduction.....	75
4.2	Definition and experimental characterization	77

4.3 Materials and methods	79
4.3.1 Synthesis of PVA hydrogels	79
4.3.2 Measurement of residual water and crystallinity in dry samples	80
4.3.3 Measurement of water content and crystallinity in swollen samples.....	82
4.3.4 AFM phase imaging.....	83
4.3.5 X-ray scattering.....	83
4.3.6 Raman spectroscopy	83
4.3.7 Measurement of the fatigue threshold.....	84
4.4 Results.....	85
4.4.1 Characterization of the crystalline morphology in PVA Hydrogels	85
4.4.2 Characterization of fatigue properties of PVA hydrogels.....	90
4.5 Concluding remarks	94
5. Design of muscle-like hydrogels	96
5.1 Introduction.....	97
5.2 Design of muscle-like hydrogels	99
5.3 Materials and methods	100
5.3.1 Materials	100
5.3.2 Confocal imaging of PVA hydrogels in wet state.....	101
5.3.3 X-ray scattering.....	101
5.3.4 SEM imaging	102
5.3.5 AFM phase imaging.....	102

5.3.6 Mechanical characterization	103
5.3.7 Measurement of water content.....	104
5.3.8 Measurement of crystallinities.....	104
5.4 Random and aligned nanofibrillar structures.....	106
5.5 Combinational muscle-like properties	111
5.6 Mechanisms for superior compliances.....	115
5.7 Mechanisms for high fatigue thresholds.....	118
5.8 Conclusions.....	119

Part II: Mechanical instabilities in confined hydrogel layers

6. Fringe instability in constrained soft elastic layers	122
6.1 Introduction.....	123
6.2 Experimental methods	126
6.3 Numerical methods	128
6.4 Results and discussion	129
6.4.1 Meniscus shape prior to instabilities.....	130
6.4.2 Theoretical model	133
6.4.3 Transition between fingering and fringe instabilities	136
6.4.4 Critical stress, stretch and wavelength for fringe instability.....	139
6.5 Conclusion	142
7. Instabilities in confined elastic layers under Tension	143

7.1 Introduction.....	144
7.2 Physical and dimensionless parameters	147
7.3 Experimental and simulation methods.....	148
7.3.1 Sample preparation	148
7.3.2 Mechanical testing	149
7.3.3 Finite-element simulation	150
7.4 Modes of instabilities.....	150
7.5 Theoretical analysis	152
7.5.1 Large deformation and stress fields in constrained elastic layers under tension	153
7.5.2 Onset of fringe and fingering instabilities.....	160
7.6 Onset of cavitation instability	166
7.7 Evolution of instabilities	170
7.7.1 Monotonic vs. non-monotonic stress-stretch relations	171
7.7.2 Type I fingering vs. Type II fingering	172
7.8 A phase diagram for instabilities	175
7.9 Coexistence and interactions of instabilities.....	177
7.10 Concluding remarks	180
8. Conclusions and future outlook.....	182
8.1 Summary of contributions.....	182
8.2 Outlook for future work.....	183

Appendix A1: Detailed Derivation of the Theory in Chapter 6	185
Appendix A2: Detailed Derivation of the Theory in Chapter 7	190
A2.1 Large Deformation Field in Cylindrical Layer under Tension	190
A2.2 Detailed derivation of the onset of instabilities via linear perturbation analysis	197
Bibliography	210

List of Figures

Figure 1-1: Hierarchical and heterogeneous structures in animal tissues including (a) skeletal muscle, (b) cartilage, (c) aorta, and (d) heart valve. 34

Figure 1-2: Representative work on the design of tough hydrogels. (a) Double network hydrogel made of poly(2-acrylamido-2-methylpropanesulfonic acid) (PAMPS) and poly(acrylamide) (PAAm). (b) Interpenetrating network hydrogel made of PAAm and alginate. (c) Fiber reinforced hydrogel composites made of PAAm, alginate, and polycaprolactone (PCL). (d) Summarized mechanisms for the design of tough hydrogels across multi-length scales including chain scission of covalent bonds, fracture of reversible bonds, melting of crystallinities, domain transformation, pull out of fibrils, fibers, and formation of elastic instabilities..... 36

Figure 1-3: Illustration of research methodology. (a) Bio-inspiration from nature’s routes to design mechanical properties. (b) Design principle. (c) Implementation of the principle via various mechanisms. (d) Material protocols for design matrix. (e) Demand-driven engineering applications. 41

Figure 2-1: Schematic illustration of extrinsic mechanical dissipation enhancing fracture energies in tough hydrogels..... 47

Figure 2-2: Schematics of the model for fracture in soft tough materials. (a) The intrinsic fracture energy of the soft material is characterized as a cohesive-zone model with triangle traction–separation law. (b) The mechanical dissipation in the process zone is characterized by the Mullins effect. A typical stress–stretch curve of the soft material under cyclic pure-shear tensile deformation. The hysteresis loop in the curve indicates mechanical dissipation. 49

Figure 2-3: The modified Ogden-Roxburgh for Mullins effect. (a) The relation between maximum hysteresis ratio h_{\max} and damage constant r for a neo-Hookean material with Mullins effect under pure-shear tensile deformation. (b) The calculated hysteresis ratio h as a function of normalized stored strain energy U/U_{\max} for different values of damage constant m/U_{\max} for a neo-Hookean material with Mullins effect under pure-shear tensile deformation. (c) The calculated stress-stretch hysteresis for a neo-Hookean material with Mullins effect under pure-shear tensile deformation. 52

Figure 2-4: Schematic of pure-shear test for measuring fracture energy of hydrogels. (a) Notched samples are stretched to critical distance of L_c until the crack propagates. (b) Un-notched samples are stretched to L_c with the force F recorded and the fracture energy of the hydrogel can be calculated as $\Gamma = (\int_{L_0}^{L_c} F dl) / (W_0 T_0)$, where W_0 , T_0 and L_0 represents width, thickness and initial gage length of the sample, respectively. 53

Figure 2-5: Calculated fracture energies of soft materials from the model. (a) Calculated Γ as a function of Γ_0 with different S_{\max} / μ and h_{\max} . The value of m/U_{\max} is set to 0.01. (b) Calculated Γ as a function of h_{\max} with different S_{\max} / μ and m/U_{\max} . (c) Calculated dimensionless parameter α^* as a function of m/U_{\max} 56

Figure 2-6: A quantitative diagram for toughening mechanisms of soft materials. The toughness enhancement ratio Γ / Γ_0 as a function of the maximum hysteresis ratio h_{\max} and the normalized critical energy scale for significant dissipation m/U_{\max} 57

Figure 2-7: (a) Comparison of the experimentally measured stress–stretch curve and fitted curve using one term Ogden model. (b) Experimentally measured cyclic stress-stretch curves at different

stretches. (c) The measured hysteresis ratios of the material deformed to different stretches and the calculated hysteresis ratio by the modified Ogden–Roxburgh model with $r=1.516$ and $m = 4.274 \text{ kJ/m}^3$ 59

Figure 2-8: (a) Schematic illustration of the method for measuring intrinsic fracture energy via pre-deformation. (b) Fracture energy as a function of pre-deformation λ_p 60

Figure 2-9: Force–displacement curves of the notched sample under pure-shear test measured from the experiment and predicted by the model. 61

Figure 2-10: The strain field in the notched sample under pure-shear test to different stretches: (a) measured by digital image correlation method (DIC) in the experiment and (b) predicted by the model..... 61

Figure 3-1: (a) Resilient material requires low mechanical dissipation under deformation, indicated by small hysteresis in the stress-strain curve. (b) Tough material requires high dissipation during crack propagation in it, indicated by large hysteresis in the stress-strain curve..... 65

Figure 3-2: Resilient and tough hydrogel can be designed with delayed dissipation. The hydrogel is resilient when deformed within a resilient domain λ_R , but significantly dissipative when deformed beyond λ_R . Hydrogel around a crack tip will be deformed beyond λ_R and therefore significantly dissipates mechanical energy to toughen the hydrogel..... 66

Figure 3-3: Schematics of a practical method to implement the design principle by controlling damage of interpenetrating-network hydrogels. The pre-stretch will damage the short-chain network in the hydrogels to controlled degrees. If the pre-stretched hydrogel is further deformed within the value of λ_R , it will be resilient. If the sequent deformation is beyond the value of λ_R , more chains in the short-chain network can be fractured to further dissipate mechanical energy. 68

Figure 3-4: Experimental validation of the design principle and method with PAAm-alginate hydrogel. (a) Schematics of the pre-stretch and further deformation of the hydrogel sample. (b) Stress vs. stretch curves of the sample pre-stretched to $\lambda_R = 5$ and further stretched to $\lambda_{max} = 5$ and 8, respectively. (c) Stress vs. stretch curves of the sample with $\lambda_R = 5$ stretched to $\lambda_{max} = 2, 3,$ and 4 at different rates. 70

Figure 3-5: Tunable resilience and fracture toughness of tough and resilient PAAm-alginate hydrogels. (a) Resilience R as a function of maximum stretch λ_{max} for samples with $\lambda_R = 4, 5$ and 6, respectively. (b) Fracture energy Γ vs. resilient domain λ_R of the hydrogels, error bar denote STD, n=3; (c) Distribution of the maximum principal stretch around the crack tip of a hydrogel with $\lambda_R = 5$ under pure-shear test before crack propagation. (d) Maximum principal stretch along the central line of the sample. 71

Figure 3-6: Resilience measured at maximum stretch $\lambda_{max} = 2, 3$ and 4 for samples with $\lambda_R = 2, 3$ and 4 after 10 min, 20 hours and 70 hours, respectively. 72

Figure 3-7: Comparison of fracture toughness and resilience of various synthetic and biological hydrogels..... 73

Figure 4-1: Illustration of mechanisms by controlled introduction of crystalline domains. (a) Fatigue crack propagation in an amorphous hydrogel under cyclic loads. (b) Fatigue crack propagation in hydrogels with low crystallinities under cyclic loads. (c) Fatigue crack propagation in hydrogels with high crystallinities under cyclic loads. The yellow areas represent crystalline domains, and the blue areas denote amorphous domains. 77

Figure 4-2: Schematic illustration of experimentally measuring fatigue threshold of hydrogels. (a) Illustration of measuring nominal stress S vs. stretch λ curves over N cycles of the applied stretch

λ^A . The stress-stretch curve reaches steady state as N reaches a critical value N^* . (b) Illustration of measuring crack extension per cycle dc / dN vs. energy release rate G curves. 79

Figure 4-3: (a) Measured mass normalized by the initial mass (at swollen state) of freeze-thawed PVA sample versus air-drying time. (b) The amount of residual water can be calculated from the endothermic transition ranging from 60 °C to 180 °C on the DSC curves..... 82

Figure 4-4: Experiment method for measuring fatigue threshold. (a) Schematic illustration of test setup. (b) Digital correlation method for calibration of the correlation between stretch λ in gauge length and applied distance d . Scale bars in b are 5 mm..... 85

Figure 4-5: (a) Representative DSC thermographs of chemically-crosslinked (Ch), freeze-thawed (FT) and dry-annealed PVA with annealing time of 0, 3, 10, 90 min. (b) Water contents of chemically-crosslinked (Ch), freeze-thawed (FT) and dry-annealed PVA with annealing time of 0, 1, 3, 5, 10, 90 min. (c) Measured crystallinity in the dry and swollen states of Ch, FT and dry-annealed PVA with annealing time of 0, 1, 3, 5, 10, 90 min..... 87

Figure 4-6: (a) Representative SAXS profiles of FT hydrogel and dry-annealed PVA with annealing time of 0, 10, and 90 min. (b) Representative WAXS profiles of annealed PVA with annealing time of 0, 3, 10, and 90 min. (c) SAXS profiles of 90-min dry-annealed PVA in the dry state and the swollen state. The insets illustrate the increase of the distance between adjacent crystalline domains due to swelling of amorphous polymer chains. (d) The estimated average distance between adjacent crystalline domains L and average crystalline domain size D of dry-annealed PVA with annealing time of 0, 1, 3, 5, 10, 90 min. Data in (d) are means \pm SD, $n = 3.89$

Figure 4-7: (a) AFM phase images of dry-annealed hydrogel with annealing time of 0 min. (b) AFM phase images of dry-annealed hydrogel with annealing time of 90 min..... 90

Figure 4-8: Shakedown softening and stress versus stretch curves of three types of PVA hydrogels. Nominal stress S vs. stretch λ curves over cyclic loads for (a) chemically-crosslinked hydrogel at an applied stretch of $\lambda^A = 1.6$, (b) freeze-thawed hydrogel at an applied stretch of $\lambda^A = 2.2$, and (c) 90-min dry-annealed hydrogel at an applied stretch of $\lambda^A = 2.0$. (d) Maximum stress at the stretch of 1.6 versus cycle number of chemically-crosslinked hydrogel, (e) Maximum stress at the stretch of 2.2 versus cycle number of freeze-thawed PVA. (f) Maximum stress at the stretch of 2.0 versus cycle number of 90-min dry-annealed PVA..... 91

Figure 4-9: Measurement of fatigue thresholds of PVA hydrogels. Crack extension per cycle dc/dN vs. applied energy release rate G for (a) chemically-crosslinked hydrogel, (b) freeze-thawed hydrogel, and (c) dry-annealed hydrogel with annealing time of 90 min. (d) The fatigue threshold increases with the crystallinity of the hydrogel in the swollen state. (e) Validation of fatigue threshold as high as 1000 J/m^2 in 90-min dry-annealed hydrogel using the single-notch test. Data in d are means \pm SD, $n = 3$. Scale bars are 5 mm and 1 mm for left and right images in (e). 92

Figure 4-10: Validation of high fatigue threshold with pure shear test. Images of the notched sample for 90-min dry-annealed PVA at the 1st cycle and 10,000th cycle under the applied energy release rates of (a) 519 J/m^2 , (b) 918 J/m^2 and (c) 980 J/m^2 . (d) Crack extension Δc versus cycle number N under the applied energy release rates of 519, 918, 980, 1013 and 1100 J/m^2 . (e) Crack extension per cycle dc/dN the applied energy release rate G in linear scale. The inset plot shows the same dc/dN for the applied energy release rates of 980, 1013 and 1100 J/m^2 in log scale. Under the energy release rate of 519 and 918 J/m^2 , no crack extension can be observed over 10,000 cycles under a microscope with pixel resolution of $20 \mu\text{m}$. Under the energy release rate of 980, 1013 and 1100 J/m^2 , the crack extension per cycle is 0.01, 0.36 and $32 \mu\text{m}$ per cycle, respectively. Scale bars in (a), (b), and (c) are 1 mm..... 93

Figure 4-11: Mechanical characterization of PVA hydrogels with various crystallinities. (a) Nominal stress vs. stretch curves of dry-annealed PVA with annealing time of 3, 5, 10 and 90 min. (b) Nominal stress vs. stretch curves of chemically crosslinked PVA, freeze-thawed PVA and dry-annealed PVA with annealing time of 0 and 1 min. (c) Fracture energy versus crystallinity in the swollen state. (d) Young's modulus versus crystallinity in the swollen state. (e) Tensile strength versus crystallinity in the swollen state. Data in (c), (d) and (e) are means \pm SD, n = 3..... 94

Figure 5-1: Design of muscle-like hydrogels. (a) Schematic illustration of the microstructure of a PVA hydrogel with randomly-oriented nanofibrils before mechanical training and a PVA hydrogel with aligned nanofibrils after mechanical training (i.e., cyclic pre-stretches). (b) Similar aligned nanofibrillar architectures of human skeletal muscles and mechanically trained hydrogels. (c) Comparison of combinational properties of human skeletal muscle and mechanically trained hydrogel. 99

Figure 5-2: (a) The chemical reaction for conjugation of fluoro-chrome on PVA. (b) Confocal image of chemically cross-linked PVA hydrogel. Confocal images and corresponding histograms of (c) a hydrogel with randomly-oriented nanofibrils before training (i.e., freeze-thawed PVA) and (d) a hydrogel with aligned nanofibrils after training (i.e., pre-stretched PVA). P in the histograms represents the probability of nanofibrils at each aligned direction θ . Scale bars in (b), (c) and (d) are 50 μ m. 106

Figure 5-3: Microstructures of PVA hydrogels before and after mechanical training. (a) Confocal images and corresponding histograms of a hydrogel with randomly-oriented nanofibrils before training (i.e., freeze-thawed PVA) and a hydrogel with aligned nanofibrils after training (i.e., pre-stretched PVA). P in the histograms represents the probability of nanofibrils at each aligned direction θ . (b) SAXS patterns and corresponding scattering intensity I vs. Azimuthal angle θ curve

of a hydrogel with randomly-oriented nanofibrils before training (i.e., freeze-thawed PVA), and hydrogel with aligned nanofibrils after training (i.e., pre-stretched PVA). a.u., arbitrary units. (c) SEM images of a hydrogel with randomly-oriented nanofibrils before training (i.e., freeze-thawed PVA) and a hydrogel with aligned nanofibrils after training (i.e., pre-stretched PVA). (d) AFM phase images of a hydrogel with randomly-oriented nanofibrils before training (i.e., freeze-thawed PVA) and a hydrogel with aligned nanofibrils after training (i.e., pre-stretched PVA). Scale bars are 50 μm in (a), 20 μm for left image in (c), 10 μm for right image in (c), and 100 nm in (d). 107

Figure 5-4: Confocal images, SAXS, and WAXS patterns of the freeze-thawed PVA hydrogel under a single cycle of load. (a) Representative stress vs. stretch curve of the freeze-thawed PVA hydrogel. (b) Confocal images, (c) SAXS patterns, and (d) WAXS patterns of the freeze-thawed PVA hydrogel at the applied stretch of i: $\lambda = 1$, ii: $\lambda = 1.6$, iii: $\lambda = 2.2$ under loading and at the applied stretch of iv: $\lambda = 1.3$ under unloading. Scale bars in (b) are 250 μm . 108

Figure 5-5: Residual stretch of prestretched PVA hydrogels. (a) The residual stretch is defined as the ratio of the length at undeformed state after training L_R over the length at undeformed state before training L_0 . (b) Residual stretch after N_p cycles of applied prestretches of 4.6. (c) Residual plastic stretch after 1000 cycles of prestretches of λ_p . 109

Figure 5-6: Measurement of nanofibril diameters in the pre-stretched PVA hydrogel. (a) Confocal image. (b) SEM image. The sample for SEM imaging was first mechanically stretched to induce delamination of nanofibrils, and immediately crosslinked by glutaraldehyde to avoid further collapse during supercritical drying, followed by SEM observation. The measured diameters of aligned nanofibrils in the hydrogel range from ~ 200 nm to ~ 1 μm . Scar bar is 20 μm in (a) and 5 μm in (b). 110

Figure 5-7: (a) Representative thermal gravimetric analysis (TGA) curve of the freeze-thawed PVA hydrogel. m , m_{swollen} , and m_{dry} denote the mass of the sample during TGA measurement, in the swollen state, and in fully dry state, respectively. (b) Differential scanning calorimetry (DSC) thermographs of chemically cross-linked (i.e., Ch), freeze-thawed (i.e., FT), and prestretched PVA hydrogels (i.e., PFT). (c) Summarized water contents and crystallinities in the swollen state of chemically cross-linked PVA (Ch), freeze-thawed PVA (FT), and pre-stretched PVA (PFT).. 111

Figure 5-8: Mechanical properties of PVA hydrogels before and after mechanical training. (a) Nominal stress versus stretch curves of chemically cross-linked (Ch), freeze-thawed (FT), and pre-stretched PVA hydrogels parallel to (PFT //) and perpendicular to (PFT \perp) nanofibrils. The X mark indicates the point of fracture. (b) Crack extension per cycle dc/dN versus applied energy release rate G of pre-stretched PVA hydrogels parallel to (PFT //) and perpendicular to (PFT \perp) nanofibrils. (c) Summarized Young's moduli E , ultimate nominal tensile strengths S , and fatigue thresholds of chemically cross-linked (Ch), freeze-thawed (FT) and pre-stretched PVA hydrogels parallel to (PFT //) and perpendicular to (PFT \perp) nanofibrils..... 112

Figure 5-9: Comparison of hysteresis in PVA hydrogels before and after mechanical training. (a) Loading-unloading nominal stress versus stretch curves of PVA hydrogels before and after training. (b) Nominal stress over loading cycles of PVA hydrogels before and after training with maximum applied stretch of 4.5 and 2.2, respectively..... 113

Figure 5-10: Validation of high fatigue threshold of the prestretched PVA hydrogel. (a) Nominal stress versus stretch of the prestretched PVA hydrogel after prolonged cycles of 1000. The enclosed area indicated by red line denotes the strain energy at the applied stretch of 2.2, i.e., $W(\lambda = 2.2) = \int_1^{2.2} Sd\lambda$. (b) The effective (nominal stress $F/((W-c)t)$ versus cycle number N of the prestretched PVA hydrogel with a pre-crack c of 0.7 mm, where F is the measured force, W is the

sample width, and t is the sample thickness. (c) Images of prestretched PVA hydrogel with a pre-crack at the applied energy release rate of 1250 J/m^2 at the cycle number of 10,000, 20,000, and 30,000..... 113

Figure 5-11: Fatigue thresholds of PVA hydrogels. (a) Chemically cross-linked PVA hydrogel. (b) Freeze-thawed PVA hydrogel. 114

Figure 5-12: (a) Comparison chart in the plot of nominal tensile strength and Young's modulus among tough hydrogels (e.g., PAAm-alginate (44), polyampholyte (62), freeze-thawed PVA (184), dry-annealed PVA (184), PVA-PAAm (110), and hydrogel composites (50)), biological tissues (e.g., skeletal muscle (166, 167)) and trained hydrogel (i.e., pre-stretched PVA). The dashed lines denote the linear relation between strength and modulus with strength-modulus ratio S/E of 0.1, 1, and 10. (b) Comparison chart in the plot of fatigue thresholds and water contents among tough hydrogels (199) (e.g., PAAm-alginate, PAAm-PAMPS, freeze-thawed PVA) and nanocrystalline hydrogels (e.g., dry-annealed PVA) (184), biological tissues (e.g., skeletal muscle), and trained hydrogel (i.e., pre-stretched PVA). Data in (a) and (b) are means \pm SD, $n = 3$ 115

Figure 5-13: Mechanisms for high compliances of pre-stretched PVA hydrogels with aligned nanofibrils. (a) Nominal stress versus stretch curve of pre-stretched PVA hydrogel with aligned nanofibrils and corresponding SAXS pattern at the stretch of 1, 1.4, 1.8, and 2.2. (b) The corrected scattering intensity Iq^2 versus vector q parallel to nanofibrils (i.e., $\theta = 0^\circ$) of pre-stretched PVA hydrogel at the stretch of 1, 1.4, 1.8, and 2.2. (c) The corrected scattering intensity Iq^2 versus vector q perpendicular to nanofibrils (i.e., $\theta = 90^\circ$) of pre-stretched PVA hydrogel at the stretch of 1, 1.4, 1.8, and 2.2. (d) Calculated average distance between adjacent nanocrystalline domains of pre-stretched PVA hydrogel parallel to nanofibrils $L_{//}$ (i.e., $\theta = 0^\circ$) and perpendicular to nanofibrils L_{\perp} (i.e., $\theta = 90^\circ$) at the stretch of 1, 1.4, 1.8, and 2.2. (e) The measured scattering intensity I vs.

Azimuthal angle θ curves of pre-stretched PVA hydrogel at the stretch of 1, 1.4, 1.8, and 2.2. a.u., arbitrary units. Data in (d) are means \pm SD, $n = 3$. The dashed red lines in the inset scattering pattern in (b) and (c) indicate the direction parallel to nanofibrils and perpendicular to nanofibrils, respectively. 117

Figure 5-14: Mechanisms for high fatigue thresholds of pre-stretched PVA hydrogels with aligned nanofibrils. Schematic illustration of nanofibril morphology in (a) notched pre-stretched PVA hydrogel where crack is perpendicular to the longitudinal direction of nanofibrils, (c) notched pre-stretched PVA hydrogel where crack is parallel to the longitudinal direction of nanofibrils, and (e) freeze-thawed PVA hydrogel. Corresponding confocal images of notched samples under different stretches for (b) pre-stretched PVA hydrogel where crack is perpendicular to the longitudinal direction of nanofibrils, (d) pre-stretched PVA hydrogel where crack is parallel to the longitudinal direction of nanofibrils, and (f) freeze-thawed PVA hydrogel. The yellow arrows in confocal images indicate the direction of aligned nanofibrils around crack tip. Scale bars are 250 μm in (b), 100 μm in (d), and 250 μm in (f). 119

Figure 6-1: Schematics of constrained soft elastic layers that undergo the fingering and fringe instabilities. (a) The fingering instability occurs in relatively thin layers (i.e., $W/H > 6$); (b) The fringe instability occurs in relatively thick layers (i.e., $W/H < 3$); (c) Deformation of the exposed meniscus of a relatively thin layer prior to the fingering instability (i.e., $W/H > 6$); (d) Deformation of the exposed meniscus of a relatively thick layer prior to the fringe instability (i.e., $W/H < 3$). Note that the length of the layer is much larger than its thickness in both cases, (i.e., $L/H \gg 1$). 124

Figure 6-2: Stress-stretch curves at the loading curve of 2, 20, 200 mm/min. Loading-unloading stress-stretch curve at the rate of $1/30 \text{ s}^{-1}$ 126

Figure 6-3: Test setup for the experimental measurement. 128

Figure 6-4: The nominal stress-stretch curve for the sample with $W / H = 3.2$ of various bulk modulus. (b) The nominal stress-stretch curve for the sample with $W / H = 4.0$ of various mesh size. 129

Figure 6-5: Experimental, simulation and theoretical results on the deformation in relatively thick layers. (a) Comparison of experimental and simulation results on deformation of a layer with $W/H = 2$ under various applied stretches prior to the fringe instability. (b) Comparison of experimental, simulation and theoretical results on the meniscus shape of a layer with $W/H = 2$ at applied stretch $\lambda = 2$ 131

Figure 6-6: Non-diffusible colored dye is covered on the surface of transparent hydrogel sample to distinguish with the meniscus profile at the constrained boundary. 131

Figure 6-7: Experimental, simulation and theoretical results on the fringe instability in relatively thick layers. (a) Experimental observation of the formation of fringe instability for a layer with $W/H = 2$ as the applied stretch increases. (b) Numerical simulation of the formation of fringe instability for a layer with $W/H = 2$ as the applied stretch increases. $\bar{\sigma}$ represents the von Mises stress..... 132

Figure 6-8: (a) Experimental observation of the formation of fingering instability for sample with the width-thickness ratio of 2 as strain increases. (b) Numerical simulation of the formation of fingering instability for a sample with the identical dimension..... 133

Figure 6-9: Specimen cross-section in deformed and undeformed configurations. 134

Figure 6-10: Experimental, simulation and theoretical results for the applied nominal stress S vs. the applied stretch λ for layers with various width-thickness ratios. (a) Experimentally measured curves of S vs. λ for layers with $W/H = 8, 6, 5.1, 4.4, 2.5, 2, 1.5, 1$ and 0.5 . The critical points for

the onset of instabilities are marked on the corresponding curves. (b) Simulation curves of S vs. λ for layers with $W/H = 8, 6, 5.1, 4.2, 4, 3.8, 2.5, 2, 1.5, 1$ and 0.5 . The critical points for the onset of instabilities are marked on the corresponding curves. (c) Theoretical curves of S vs. λ for layers with $W/H = 8, 7, 6, 5.1, 4, 2$ and 1 . The dashed curve represent the stability limit..... 137

Figure 6-11: Normalized strain energy versus applied stretch in the sample with necking mode (i.e., 2D simulation) and the sample with undulated fingering mode (i.e., 3D simulation). 138

Figure 6-12: The amplitude versus applied stretch curves under loading and unloading for a fringe instability..... 139

Figure 6-13: Experimental, simulation and theoretical results on the characteristics of fingering and fringe instabilities. (a) Numerical simulation results on stress contours in layers with $W/H = 0.5, 1, 2$ and 4 right before the fringe instability. The stress represents the normalized nominal stress component along the loading direction S_{xx} / μ . (b) The critical nominal stress for the onset of instabilities in layers with various width-thickness ratios. (c) The critical applied stretch for the onset of instabilities in layers with various width-thickness ratios. (d) The wavelength of instabilities in layers with various width-thickness ratios. 140

Figure 7-1: Schematics on deformation and instabilities in confined elastics layers under tension. (a) Experimental setup. (b) The cross-section of the constrained elastic layer in un-deformed and deformed state. (c) Illustration of fringe instability, fingering instability and cavitation instability, corresponding to small, moderate and large aspect ratio $\alpha = D / H$, respectively. 146

Figure 7-2: Materials for the constrained elastic layers. (a) Measured nominal stress-stretch curves for the samples with various constituents. Solid line represents the experimental data; dashed line represents the fitted neo-Hookean model. (b) Weight ratio of polyacrylamide (AAm) and N,N'-

methylenabisacrylamide (Bis), shear modulus μ and elastocapillary length γ / μ for each material.

..... 149

Figure 7-3: Morphology difference between fringe instability and fingering instability. (a) Undulation contours at the different planes right after the onset of fringe instability for the sample with $\alpha = 2$. Maximum amplitude occurs at $\bar{Z} = \pm 0.81$. (b) Undulation contours at the different planes right after the onset of fingering instability for the sample with $\alpha = 12$. Maximum amplitude occurs at $\bar{Z} = 0$. (c) The normalized amplitude of undulation contours versus \bar{Z} right after the onset of instabilities for the sample with $\alpha = 2$ and $\alpha = 12$. (d) The \bar{Z}_0 for the maximum amplitude of the undulation contours versus aspect ratios. 152

Figure 7-4: Theoretical and simulation results on the deformation and stress fields in constrained neo-Hookean layers under tension. (a) Comparison between theory and simulation of the meniscus profiles for the sample with aspect ratio of $\alpha = 4$ at the stretch of $\lambda = 1.5$, $\lambda = 2.0$ and $\lambda = 2.5$. Solid line represents the theoretical results; dashed line represents the simulation results. (b) Comparison between theory and simulation of the meniscus profiles for the sample with aspect ratio of $\alpha = 8$ at the stretch of $\lambda = 1.3$, $\lambda = 1.6$ and $\lambda = 1.9$. Solid line represents the theoretical results; dashed line represents the simulation results. (c) Theoretically calculated applied nominal stress versus stretch for the samples with various aspect ratios. (d) Theoretically calculated hydrostatic pressure at the center of the samples versus stretch for the sample with various aspect ratios..... 158

Figure 7-5: Theoretical and simulation results on the critical points of fingering instability and fringe instability for the sample with aspect ratios $\alpha > 4$. a) Comparison of the critical stretch λ_c for the onset of instabilities between theory and simulation. b) Comparison of the critical mode

number ω_c between theory and simulation. a) Comparison of the critical applied stress S_c between theory and simulation. 164

Figure 7-6: Theoretical results on the transition between fringe and fingering instability. (a) Critical stretch for the sample with the locations for the initiation of undulations at $\bar{Z}_0 = 0$ and $\bar{Z}_0 = 0.2$. (b) The location of the initiation of the instabilities \bar{Z}_0 for the sample with different aspect ratios..... 166

Figure 7-7: Theoretical results on the critical points for cavitation instability. (a) Schematic of the growth of pre-existing cavity within a cylindrical sample. (b) Applied hydrostatic traction T / μ on the spherical shell versus the expansion ratio λ_A of pre-existing cavity for the material with various β . (c) Critical hydrostatic traction T_c / μ for the material with various β . (d) Theoretically calculated applied nominal stress S / μ versus hydrostatic pressure p_0 / μ at the center of the sample. Dash line denotes the solution from theory with small strain assumption when $\alpha \rightarrow \infty$. (e) Theoretically calculated stretch λ versus hydrostatic pressure p_0 / μ at the center of the sample. (f) Critical applied nominal stress S_c / μ for cavitation instability in samples with various α and β . (g) Critical applied nominal stretch λ_c / μ for cavitation instability in samples with various α and β 168

Figure 7-8: Theoretical results on the transition between fingering instability and cavitation instability. a) Critical applied nominal stress for fingering stability and cavitation instability with various dimensionless capillary number β . b) Theoretical calculation of the critical transition aspect ratio $\alpha_{fingering-cavitation}$. Dashed line represents the linear fitting curve from the theoretical calculation. 169

Figure 7-9: Experimental and simulation results on fringe instability. a) Experimental observation and b) corresponding simulations for the formation of fringe instability for the sample with $\alpha = 2$. c) Applied nominal stress versus stretch curves from experiments (solid lines) and simulations (dashed line) for the sample with $\alpha = 2, 3, 4,$ and 5 171

Figure 7-10: Experimental and simulation results on fingering instability. (a) Experimental observation and corresponding simulations for the formation of Type I fingering instability for the sample with $\alpha = 12$. (b) Applied nominal stress versus stretch curves from experiments and simulations for the sample with $\alpha = 12$. (c) Experimental observation and corresponding simulations for the formation of Type II fingering instability for the sample with $\alpha = 32$. (d) Applied nominal stress versus stretch curves from experiments and simulations for the sample with $\alpha = 32$. Here, the bulk modulus in simulation is set as $K = 200\mu$ to match well with the experimental results, which means the sample we used is not ideally incompressible. 174

Figure 7-11: (a) Schematic illustration of the stress versus stretch curve for type I fingering instability occurring in the layer with small α . (b) Schematic illustration of the stress versus curve for type II fingering instability occurring in the layer with large α . (c) Experimental and simulation results on the critical stress S_c and the peak stress S_p to identify the transition between Type I fingering instability and Type II fingering instability. When $\alpha > 20$, the critical stress for the onset of fingering instability deviates from the maximum peak stress, where Type II fingering instability sets in. 175

Figure 7-12: Phase diagram for the initial occurrence mode of mechanical instabilities. The lines are from theory and simulation, and the dots are from experiments. Red circular dots denote the occurrence of fringe instability, blue square dots denote the occurrence of Type I fingering

instability, green triangular dots denote the occurrence of Type II fingering instability and purple pentagon dots denote the occurrence of cavitation instability. 176

Figure 7-13: Coexistence of cavitation instability and fingering instability. a), b) and c) A cavity forms suddenly within the sample, and then the applied nominal stress keeps increasing up to the maximum point which corresponds to the initiation of fingering instability at the exposed surface. The sample has an aspect ratio $\alpha = 20$ (i.e. $D = 40\text{mm}$ and $H = 2\text{mm}$) and dimensionless number of $\beta \approx 7$ ($\gamma \approx 0.07 \text{ N/m}^2$, $\mu \approx 10 \text{ kPa}$ and $A \approx 1 \mu\text{m}$). d), e) and f) Type II fingering forms first at the exposed surface and a cavity forms suddenly within the sample with the further increase of the applied nominal stress, which exhibits the coexistence of Type II fingering instability and cavitation instability. The sample has an aspect ratio $\alpha = 28$ (i.e. $D = 56\text{mm}$ and $H = 2\text{mm}$) and dimensionless number of $\beta \approx 35$ ($\gamma \approx 0.07 \text{ N/m}^2$, $\mu \approx 2 \text{ kPa}$ and $A \approx 1 \mu\text{m}$). The stretch rate of both experiments are 0.016 s^{-1} 179

List of Tables

Table 1.1: Mechanical properties of various biological tissues including cartilages (1, 7-13), tendons (14-16), ligaments (17, 18), heart valves (19, 20), aortae (21-23), and skeletal muscles (22, 24). * Data is not available.	33
Table 4.1: Crystallinities and water contents in chemically-crosslinked (Ch), freeze-thawed (FT) and dry-annealed PVA with annealing time of 0, 1, 3, 5, 10, 90 min.....	87
Table 5.1: Comparison of combinational properties in various soft materials. Comparison of Young's moduli, water contents, nominal strengths, and fatigue thresholds of strain-stiffening hydrogels (181, 182), bottlebrush elastomers (166, 183), tough hydrogels (43, 44), hydrogel composites (50, 185), nanocrystalline hydrogels (184), and muscle-like hydrogels in this work (49).	98

List of Symbols

Γ	Total fracture energy
Γ_0	Intrinsic fracture energy
Γ_D	The fracture energy from mechanical dissipation
\bar{U}_D	Mechanical energy dissipated per unit volume of the process zone
l_D	Height of the process zone
U_D	Mechanical energy dissipated per unit volume of the material under pure-shear tensile deformation
S	Nominal stress
λ	Stretch
S_{\max}	Maximum nominal stress under pure-shear tensile deformation
μ	Shear modulus
x	Distance from the point to the crack tip
U_{\max}	Maximum mechanical work done on the material under pure-shear tension
α^*	A dimensionless number in the governing equation for total fracture energy of soft tough materials
t_n	Nominal surface tractions on the crack surface along normal direction
t_s	Nominal surface tractions on the crack surface along tangential direction
δ_{\max}	Maximum separation in a cohesive-zone model with triangle-separation law
h	Hysteresis ratio of the material under pure-shear deformation
W	The free energy function of an incompressible material with Mullins effect
\mathbf{F}	Deformation gradient tensor
η	The damage variable in Ogden-Roxburgh model
ϕ	The damage function in Ogden-Roxburgh model
\tilde{W}	The free energy function of a pure elastic material without Mullins effect
β^*	A parameter in Ogden-Roxburgh model for numerical stabilization
r, m	Damage constants in Ogden-Roxburgh model
G^{ss}	The steady-state critical energy release rate
R	Resilience
λ^A	Applied stretch
N	Cycle number
c	Current crack length at undeformed configuration
G	Applied energy release rate

G_c	Critical energy release rate below which the fatigue crack will not propagate under infinite cycles of loads
N^*	Critical cycle number when the stress-stretch curve reaches steady state
$H_{residual}$	The energy for evaporation of the residual water per unit mass of the dry sample
H_{water}^0	Latent heat of water evaporation
$H_{crystalline}$	The crystalline domains per unit mass of the dry sample
$H_{crystalline}^0$	The enthalpy of fusion of 100 wt.% crystalline PVA
X_{dry}	The crystallinity in the ideally dry sample
$X_{swollen}$	The crystallinity in the swollen sample
L	The average distance between adjacent crystalline domains
D	The average size of crystalline domains
I	The scattering intensity
q	The scattering vector
k^*	A dimensionless shape factor in Scherrer's equation
$\bar{\beta}$	The half-width of the maximum diffraction peak
θ^*	Bragg angle
λ_p	Residual plastic stretch in trained PVA hydrogel
N_p	Number of cycles of prestretching
l_{finger}	The wavelength of the fingering instability
l_{fringe}	The wavelength of the fringe instability
α	Aspect ratio of a cylindrical layer
β	Elastocapillary length
γ	Surface tension
κ	An internal loading parameter in a confined cylindrical layer
p_0	Hydrostatic pressure at the center of the samples
λ_c	The critical stretch for the onset of fringe or fingering instability
ω_c	The critical mode number of fringe or fingering instability
\bar{Z}_0	The location of the initiation of the instabilities
ω_c	The critical mode number of fringe or fingering instability
\bar{Z}_0	The location of the initiation of the instabilities

Chapter 1

Introduction

1.1 Biological tissues

Human bodies are mostly made of soft, wet yet robust biological hydrogels such as cartilages, ligaments, and muscles. The biological hydrogels commonly possess mechanical properties such as high toughness, resilience and fatigue resistance to guarantee the bodies' reliable functions and activities. For example, cartilage is known for the ability to absorb the shock and reduce the friction between bones. Data show that the human knee joint cartilage can sustain compressive stresses of 4-9 MPa for 1 million cycles per year, maintaining a fracture energy as high as 1000 J/m² (1). Skeletal muscles can sustain a high tensile stress of 1 MPa over 1 million cycles per year with fracture energy of 1000 J/m², which provides effective and robust contraction forces to move bones (2). Heart valve is the source of robust and efficient blood circulation, which enables continuous nutrition supply and stable metabolism. To achieve these functions, heart valve generally shows both high resilience of 80% and high toughness of 1200 J/m² (3, 4), which are seemingly contradictory properties of synthetic hydrogels. In short, Table 1.1 summarizes a set of mechanical properties (i.e., Young's modulus, tensile strength, failure strain, fracture energy, and resilience) of various load-bearing tissues. Here, resilience is defined by the ratio of the integrated area of loading stress versus strain curve and the integrated area of unloading stress versus strain curve (5, 6).

Table 1.1: Mechanical properties of various biological tissues including cartilages (1, 7-13), tendons (14-16), ligaments (17, 18), heart valves (19, 20), aortae (21-23), and skeletal muscles (22, 24). * Data is not available.

Material	Young's modulus [MPa]	Tensile strength [MPa]	Failure strain [%]	Fracture energy [J/m²]	Resilience [%]
Cartilage	0.5-0.7	0.5-2.5	40-120	800-1,800	55-98
Tendon	300-400	40-90	6-15	*	77-90
Ligament	100-300	26-36	18-30	25,000-36,000	95
Heart valve	0.1-15	0.4-2.6	22-30	160-200	*
Aorta	0.2-1.5	0.2-3.7	20-130	20-120	70-90
Skeletal muscle	0.1-0.3	0.3-0.5	30-60	2,500	*

The mechanical properties of biological tissues are mainly attributed to their hierarchical and heterogeneous structures across multiple length scales from molecular-scale assemblies to nanoscale and microscale fibrous alignment as shown in Fig. 1-1 (25). Taking cartilage as an example, it consists of three layers, i.e., superficial tangential zone, middle transitional zone, and deep zone (26). The superficial tangential zone provides an efficient lubrication mechanism with an extremely low coefficient of friction, therefore giving load-bearing functions of cartilages (27). The middle zone and deep zone of cartilages form transitional interface from the uncalcified collagen nanofibrils to calcified collagen nanofibrils to bones. At the interface, nanostructured composites of aligned collagen nanofibrils and ordered hydroxyapatite nanocrystals are anchored on bones, leading to fatigue-resistant adhesions of cartilages to bones (28-33).

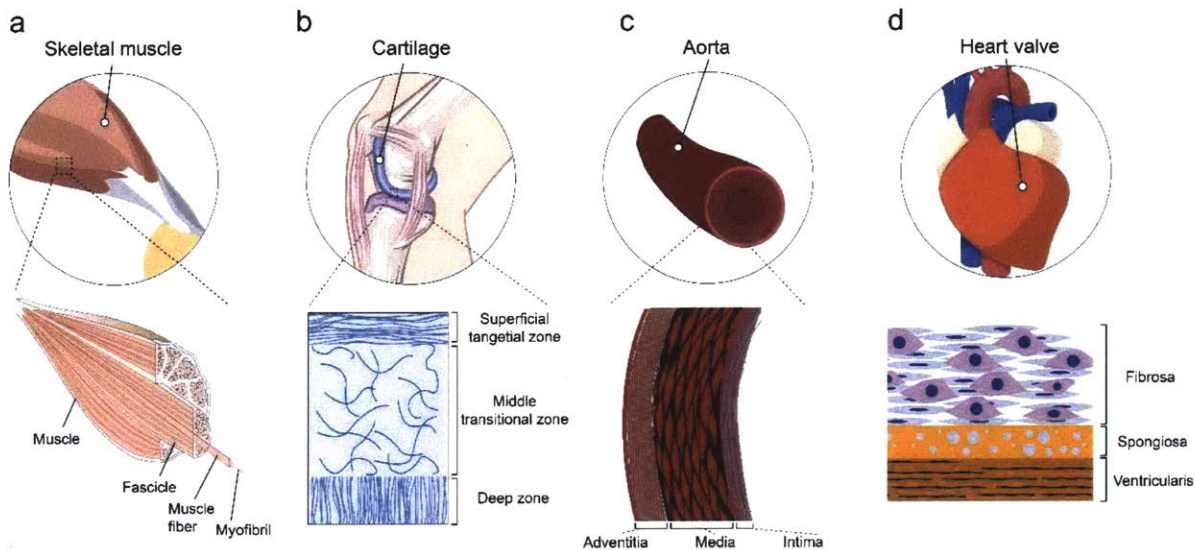


Figure 1-1: Hierarchical and heterogeneous structures in animal tissues including (a) skeletal muscle, (b) cartilage, (c) aorta, and (d) heart valve.

1.2 Hydrogels

As polymer networks infiltrated with water, hydrogels are as soft and wet as biological tissues. The porosity of polymer networks in hydrogels provides their permeability to small molecules, allowing transportations in various forms (e.g., diffusion, reaction, and convection). While the cross-linked polymer networks impart hydrogels' elasticity, maintaining their physical integrity. Owing to their unique integration of solid and liquid properties, hydrogels are mechanically and biologically compatible with natural tissues and regarded as an ideal material candidate for interfacing human body. Emerging applications have been explored for hydrogels as diverse as scaffolds for tissue engineering (34), vehicles for drug delivery (35), contact lenses (36), breast implants (37), and pH/chemical/temperature sensors (38-40).

1.2.1 Mechanical properties of hydrogels

Common hydrogels, typically composed of a single network, are mechanically brittle with fracture energy as low as 0.1 to 10 J/m² (41), far below that of biological tissues (e.g., ~ 1000 J/m² for

cartilages) and majority of engineering materials (e.g., $\sim 1000 \text{ J/m}^2$ for metals, plastics, and elastomers). One reason for the low fracture energy of conventional hydrogels is their liquid-like nature (i.e., low fraction of polymer chains and negligible interactions between chains). Another reason is the nature of single-network architecture, which is sensitive to defects and heterogeneity of the network structure (41). When a force is applied to a conventional hydrogel, stress is concentrated either at the chain around defects or at the shortest chain in a heterogeneous network structure, which leads to a failure at a low applied force. Due to the low resistance against crack propagation, conventional hydrogels have been limited to the applications where mechanical properties are not of great concern, such as drug delivery (42) and cell culture (41).

Intensive researches have been focused on enhancing hydrogels' toughness over the last two decades. The pioneer work dates back to Gong et al.'s double network hydrogel (43), in which one long-chain network is stretchy giving the elasticity while the other short-chain network ruptures and dissipates energy when the hydrogel is deformed. In addition to the double network hydrogel, the other milestones in designing tough hydrogels include interpenetrating network hydrogels (44) which implement dissipation mechanisms via fracture of reversible bonds (Fig. 1-2b) and hydrogel composites (45) involving nanoscale hybrid crosslinking and macroscale fiber reinforcements (Fig. 1-2c). As summarized in Fig. 1-2d, the mechanisms for toughness enhancement in hydrogels (46) span from chain-level dissipations via breaking chains (44, 45), melting of crystallinities (47), and phase transformation of domains (48) to meso-scale dissipations via pulling out fibrils (49) and/or fibers (50). The mechanical dissipations could even occur at macro scale (i.e., mm) via the formation of various instabilities (e.g., fringe, fingering, and cavitation instability in confined elastic layers) (51, 52).

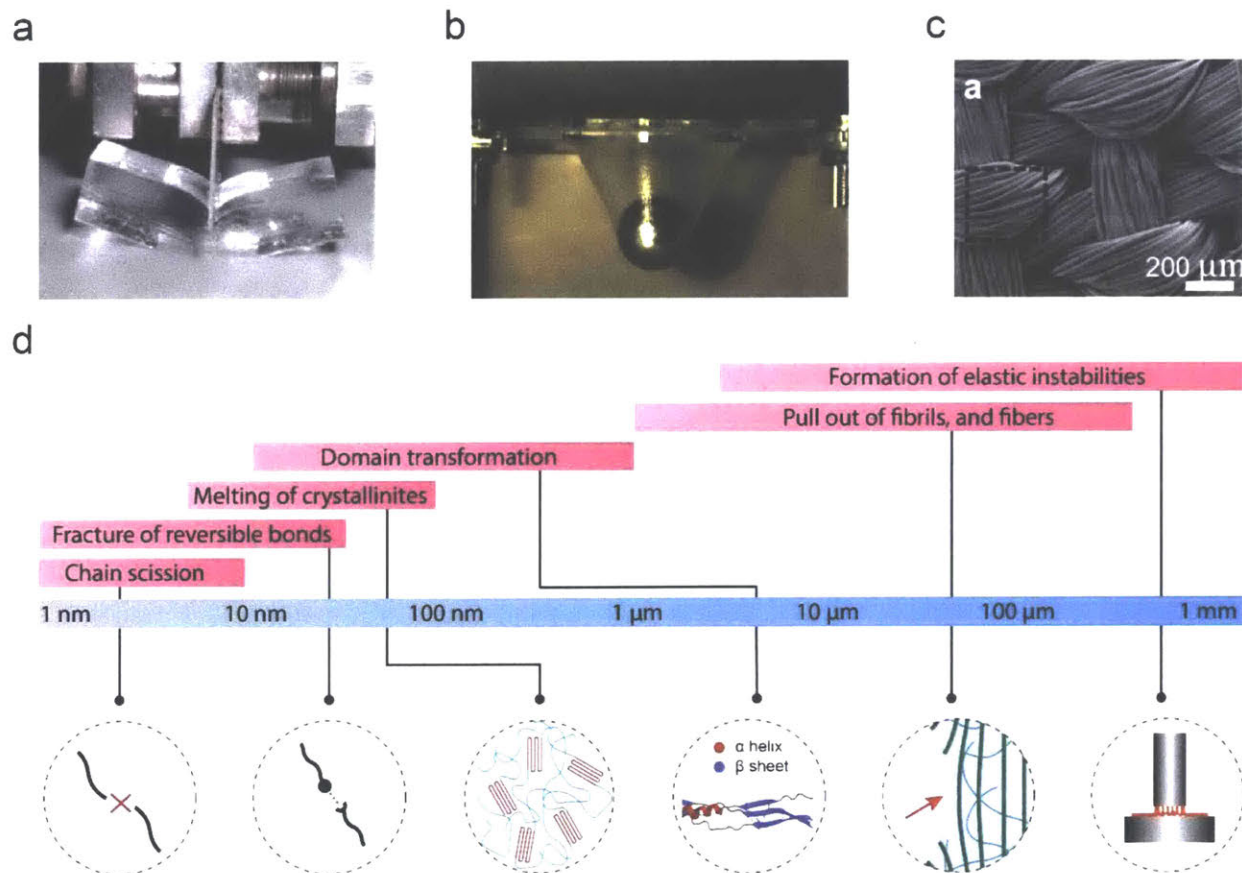


Figure 1-2: Representative work on the design of tough hydrogels. (a) Double network hydrogel made of poly(2-acrylamido-2-methylpropanesulfonic acid) (PAMPS) and poly(acrylamide) (PAAm). (b) Interpenetrating network hydrogel made of PAAm and alginate. (c) Fiber reinforced hydrogel composites made of PAAm, alginate, and polycaprolactone (PCL). (d) Summarized mechanisms for the design of tough hydrogels across multi-length scales including chain scission of covalent bonds, fracture of reversible bonds, melting of crystallinities, domain transformation, pull out of fibrils, fibers, and formation of elastic instabilities.

1.2.2 Fracture of hydrogels

The intrinsic fracture energies of common hydrogels are low. According to the Lake-Thomas theory, the intrinsic fracture energy of a polymer network can be estimated by $\Gamma_0 = bU_{bond}L$, where b is the number of C-C bonds per unit volume in an elastomer, U_{bond} is the dissociation energy of one C-C bond, and L is the characteristic length of a polymer chain (53). The number of C-C bonds per unit volume of an elastomer b can be estimated by $A\rho/M$ on the order of 10^{28}

m^{-3} , where A is the Avogadro constant $6.02 \times 10^{23} \text{ mol}^{-1}$, ρ is the density of the elastomer typically in the range of 1 to 1.4 g/cm^3 , M is the molecular weight of one monomer typically on the order of 100 g/mol . The dissociation energy of one C-C bond U_{bond} is in the range of 2 to 4 eV (54). The characteristic length L can be estimated by $L = l\sqrt{n}$, where l is the size of one monomer on the order of 0.1 to 0.4 nm and n is the number of monomers in one polymer chain typically in the range of 100 to 1000 (55). Therefore, the intrinsic fracture energy of an elastomer is on the order of 1-50 J/m^2 . Swelling of hydrogels leads to lower fraction of polymer chains compared with elastomers. Specifically, the number of C-C bonds per unit volume in a hydrogel is diluted by $b_{hydrogel} = \phi b$ with ϕ as the volume fraction of the polymer in the hydrogel. The size of a layer of polymer chain $L_{hydrogel}$ increases by $L_{hydrogel} = \phi^{-1/3}L$ accordingly. Consequently, the intrinsic fracture energy of a swollen hydrogel is reduced to $\Gamma_0 = \phi^{2/3}bUL$. Although the Lake-Thomas theory works very well for elastomers and hydrogels qualitatively, the quantitative validation of the theory has been controversial (53, 56-58). For example, Sakai et al. (56) measured the fracture energy of the hydrogel with controlled ideal network, showing the measured intrinsic fracture energy is higher than that from theoretical prediction by an enhancement factor of three. Anand et al. recently proposed a theoretical model for the progressive damage and rupture of elastomeric materials (53, 58, 59). By using the model, they conclude that the scaling of Lake-Thomas theory does not hold for the elastomers with weak and stretchable crosslinks due to the energetic failure of crosslinks (53). Suo et al. studied the effects of network imperfection (57). Their experimental observation supports that imperfect network amplifies the toughness by two orders of magnitude. The development of generalized Lake-Thomas theory for quantitatively predicting the intrinsic fracture energies of elastomers or hydrogels is an emerging research topic.

In tough hydrogels, propagation of a crack not only relies on the scission of polymer chains across crack surface but also is retarded by the mechanical dissipation in a process zone surrounding a crack tip. In general, three types of dissipation mechanisms (e.g. Mullins effect (60, 61), viscoelastic effect (62), and poroelastic effect (63, 64)) can be implemented for the design of tough hydrogels. Mullins effect refers to the phenomenon as an irreversible softening of the stress-strain curve (i.e. irreversible damage) that occurs whenever the load increases beyond its maximum value during previous loading history (65). It is a particular aspect of mechanical response observed in filled rubbers (e.g. filled with carbon black (66)), but prevails in most tough hydrogels (44). The mechanical dissipation from Mullins effect is rate-independent (67-69). Viscoelasticity is the other mechanism for inducing energy dissipation in hydrogels. Unlike Mullins effect, viscoelastic effect is a rate-dependent mechanism. Viscoelasticity has been achieved in tough gels through various types of reversible crosslinking including ionic interaction (44, 70), electrostatic interaction (62), metal-ligand coordination (71-73) and host-guest interaction (74). In addition to Mullins effect and viscoelastic toughening, poroelasticity of hydrogels gives the third toughening mechanism from solvent pressure (63, 64, 75, 76), which is also rate-dependent.

1.2.3 Fatigue of hydrogels

Existing tough hydrogels suffer from fatigue fracture under multiple cycles of mechanical loads (77-79), because the resistance to fatigue-crack propagation after prolonged cycles of loads is the energy required to fracture a single layer of polymer chains (i.e., the intrinsic fracture energy of the hydrogel), which is unaffected by the additional dissipation mechanisms introduced in tough hydrogels (78, 79). The reported fatigue thresholds of various tough hydrogels are 8.4 J/m² for polyacrylamide (PAAm)-polyvinyl alcohol (PVA) (79) and 53.2 J/m² for PAAm-alginate (78), on the same order of magnitude as their intrinsic fracture energies. The highest fatigue threshold for

hydrogels reported so far is 418 J/m^2 for a double network hydrogel, poly(2-acrylamido-2-methyl-1-propanesulfonic acid) (PAMPS)-PAAm, which possibly can be attributed to the PAAm network with very long polymer chains and thus high intrinsic fracture energy (43, 80).

1.2.4 Elastic instabilities in hydrogels

Mechanical instabilities are ubiquitous in nature (81) and daily life (82). Instabilities can form due to various loadings, such as compression (83), tension (84), constrained swelling (85), differential growth (86). When the loading reaches a critical value, an instability pattern emerges by minimizing the total energy of the system. Intensive researches have been focused on various modes of surface instabilities including creases (87), wrinkles (88), folds (89), and ridges (90).

Hydrogels typically have superior compliance, high stretchability, and relatively high surface tension, which makes it possible to form new modes of instabilities (91). For example, various modes of mechanical instabilities in confined elastic layers under tension have been discovered (51, 92-95). If the elastic layer partially debonds from the rigid body, the delaminated interface can undulate periodically to give the interfacial undulation (92, 96-99). If perfect bonding between the elastic layer and the rigid bodies is maintained, a cavity can nucleate and grow within the elastic layer when the hydrostatic tensile stress in any region of the elastic layer reaches a critical value, giving the cavitation instability (e.g., **Fig. 1c**) (95, 100-103). Even if perfect bonding between the elastic layer and the rigid substrates is maintained and cavitation instability is suppressed by tuning the material properties and geometry of the elastic layer, the exposed meniscus can become unstable, forming fingering instability (93, 94, 104).

1.3 Motivation

1.3.1 Design tissue-like mechanical properties of hydrogels

The first aim of the thesis is to design hydrogels with tissue-like mechanical properties (i.e., high toughness, resilience, and fatigue-resistance). Despite the challenge, the design of tissue-like hydrogels is of both fundamental and practical importance. On the fundamental side, understanding nature's routes to achieve these properties can serve as the guideline for the design of tissue-like man-made hydrogels. On the practical importance, the emerging applications of hydrogels in soft machines require the hydrogels to achieve long-lasting, reliable, functional, and predictable performances (105).

1.3.2 Understanding mechanical instabilities in confined hydrogel layers

The second aim of the thesis is to study and explore a few modes of mechanical instabilities forming in confined elastic layers. The formation and interaction of these mechanical instabilities highly affect the mechanical robustness of engineering structures. For example, the load capacity of the adhesives depends on the initial occurrence mode of mechanical instabilities (106). The occurrences of mechanical instabilities also initiate different failure mechanisms ranging from interfacial fracture to cohesive failure in relevant structures (107). Systematic understanding of mechanical instabilities in confined elastic layers can guide the design of mechanically robust hydrogel adhesives.

1.4 Research methodology

Nature is a rich source of knowledge for innovative designs. Over billions of years of evolution, biological systems find solutions for different classes of problems through optimization of nature's designs. The methodology of bio-inspiration and biomimicry has been adopted since five hundred

years ago when Leonardo da Vinci designed a number of bioinspired inventions (e.g., flying machine) far ahead of his time (108). Specifically, nature designs soft tough tissues with robust mechanical properties via hierarchical and heterogeneous structures, which are unmatched by the synthetic hydrogels yet. Understanding the routes adopted by nature can serve as the inspiration source for the design of synthetic hydrogels.

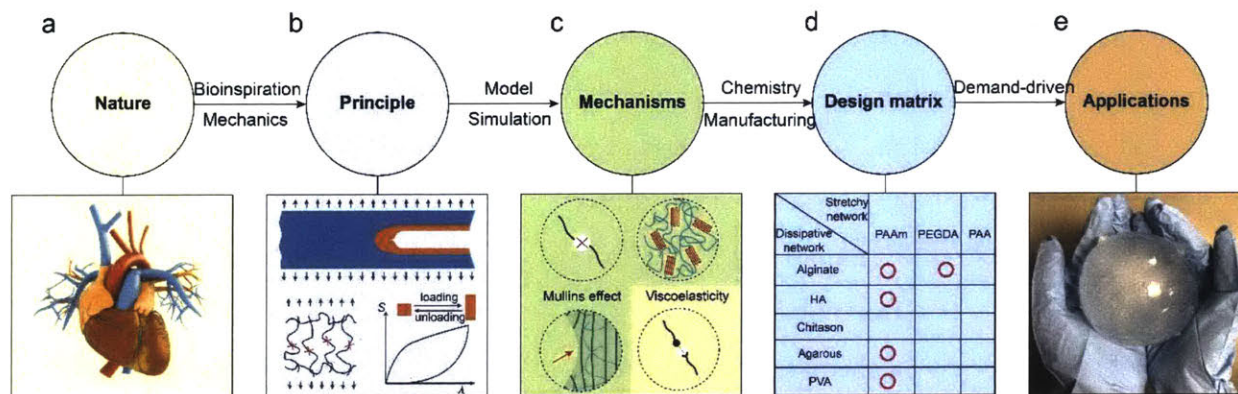


Figure 1-3: Illustration of research methodology. (a) Bio-inspiration from nature’s routes to design mechanical properties. (b) Design principle. (c) Implementation of the principle via various mechanisms. (d) Material protocols for design matrix. (e) Demand-driven engineering applications.

1.5 Plan of this dissertation

The first section of the dissertation focuses on the design of mechanical properties of hydrogels. In Chapter 2, we perform scaling analysis and develop a continuum model for predicting fracture energies in soft tough hydrogels. In Chapter 3, we propose a method to design hydrogels that can achieve both high toughness and high resilience. In Chapter 4, we propose to enhance anti-fatigue properties in synthetic hydrogels by the introduction of nanocrystalline domains. In Chapter 5, we propose a facile approach to achieve muscle-like combinational mechanical properties in hydrogels by mechanical training. The second section of the dissertation studies fringe, fingering, and cavitation instabilities in hydrogels. In Chapter 6, we discover a new mode of instability (i.e., fringe instability) in confined elastic layers. In Chapter 7, we study the formation and interaction

of various modes of mechanical instabilities in confined hydrogel layers. Lastly, we provide the conclusions and summarize the contributions of the thesis in Chapter 8.

1.6 List of publications for each chapter

Thesis chapter	Journal publications
Chapter 2	T. Zhang, S. Lin , H. Yuk, X. Zhao, Predicting fracture energies and crack-tip fields of soft tough materials. <i>Extreme Mech Lett</i> 4 , 1-8 (2015).
Chapter 3	S. Lin , Y. Zhou, X. Zhao, Designing extremely resilient and tough hydrogels via delayed dissipation. <i>Extreme Mech Lett</i> 1 , 70-75 (2014).
Chapter 4	S. Lin , X. Liu, J. Liu, H. Yuk, H.-C. Loh, G. A. Parada, C. Settens, J. Song, A. Masic, G. H. McKinley, Anti-fatigue-fracture hydrogels. <i>Sci Adv</i> 5 , eaau8528 (2019).
Chapter 5	S. Lin , J. Liu, X. Liu, X. Zhao, Muscle-like fatigue-resistant hydrogels by mechanical training. <i>Proc. Natl. Acad. Sci. U. S. A.</i> 116 , 10244-10249 (2019).
Chapter 6	S. Lin , T. Cohen, T. Zhang, H. Yuk, R. Abeyaratne, X. Zhao, Fringe instability in constrained soft elastic layers. <i>Soft Matter</i> 12 , 8899-8906 (2016).
Chapter 7	S. Lin , Y. Mao, R. Radovitzky, X. Zhao, Instabilities in confined elastic layers under tension: Fringe, fingering and cavitation. <i>J Mech Phys Solids</i> 106 , 229-256 (2017).
Other related publications	
	S. Lin , C. Cao, Q. Wang, M. Gonzalez, J. E. Dolbow, X. Zhao, Design of stiff, tough and stretchy hydrogel composites via nanoscale hybrid crosslinking and macroscale fiber reinforcement. <i>Soft Matter</i> 10 , 7519-7527 (2014).
	S. Lin , H. Yuk, T. Zhang, G. A. Parada, H. Koo, C. Yu, X. Zhao, Stretchable Hydrogel Electronics and Devices. <i>Adv Mater</i> , (2015).
	X. Liu, C. Steiger, S. Lin , G. A. Parada, J. Liu, H. F. Chan, H. Yuk, N. V. Phan, J. Collins, S. Tamang, Ingestible hydrogel device. <i>Nat Commun</i> 10 , (2019).

Part I

Design tissue-like properties of hydrogels

Chapter 2

Design of tough hydrogels

2.1 Introduction

Most parts of animal bodies consist of soft tissues such as muscles, cartilages, tendons, ligaments, heart valves, and skins have relatively low stiffness (i.e., around 100 kPa) but high fracture energy around 1000 J/m². These soft yet tough tissues are crucial for the survival of animals under various internal and external mechanical loads. Similarly, many applications of hydrogels require them to maintain physical integrity over time and even carry and/or sustain mechanical loads.

Owing to their scientific and technological importance, various soft tough materials have been developed in recent decades (43-45, 50, 109-114). The intrinsic fracture energy of soft materials – i.e., the energy required to fracture a layer of polymer chains in front of the crack (115) – is relatively low; and it is qualitatively known that the toughening of soft materials generally relies on mechanical dissipation in process zones around cracks (41, 46, 116, 117). However, it is still not well understood how the intrinsic fracture energy and mechanical dissipation cooperate synergistically to give rise to high fracture toughness of soft materials (70). Furthermore, physical models that can predict the fracture energy and crack-tip strain fields of soft materials are of imminent importance to the design of new soft tough materials, but such predictive models still do not exist.

In this chapter, we report a scaling law and a continuum model that quantitatively accounts for the synergistic contributions of intrinsic fracture energies and dissipations to the total fracture energies of soft materials. We characterize the essential physical features of intrinsic fracture energy and dissipation using the cohesive-zone model and Mullins-effect model, respectively, implemented in finite element software, ABAQUS. Our calculation shows that the total fracture energy of soft material scales linearly with its intrinsic fracture energy, while the effect of dissipation manifests as a scaling pre-factor that can be much higher than one. To validate the

theory and model, we measure the stress–strain hysteresis and intrinsic fracture energies of polyacrylamide-alginate (PAAm-alginate) hydrogels of different compositions, which represent soft tough materials with different properties (44, 118). Using the material parameters measured independently, our model can quantitatively predict the fracture energies of different soft materials as well as strain fields and crack propagations in them. Based on the model, we further calculate a toughening diagram that can guide the design of new soft tough materials.

2.2 Scaling analysis

Let us consider a notched soft material undergoing the pure-shear test to measure its fracture energy in mode I loading, as illustrated in Fig. 2-1 (119). Crack propagation in the soft material requires the scission of at least a layer of polymer chains. The required mechanical energy for chain scission divided by the area of crack surface at undeformed state gives the intrinsic fracture energy Γ_0 . In addition, material elements in a process zone around the crack will also be deformed and undeformed as the crack propagates. If mechanical energy is dissipated during this process, the dissipated energy divided by the area of crack surface at undeformed state further contributes to the total fracture energy by Γ_D . Therefore, the total fracture energy of a soft material can be expressed as

$$\Gamma = \Gamma_0 + \Gamma_D \quad (2.1)$$

where $\Gamma_D = \bar{U}_D l_D$ and \bar{U}_D is the mechanical energy dissipated per the volume of the process zone, and l_D is the height of the process zone in the soft material at undeformed state. Since material elements in the process zone approximately undergo the pure-shear deformation (120) (i.e., tensile deformation of a thin sheet with one lateral dimension fixed as illustrated in Fig. 2-4), we further have $\bar{U}_D \propto U_D (S = S_{\max})$, where U_D is the mechanical energy dissipated per unit volume of the

soft material under pure-shear tensile deformation, and S_{\max} is the maximum nominal stress that can be achieved in the material under pure-shear tensile deformation.

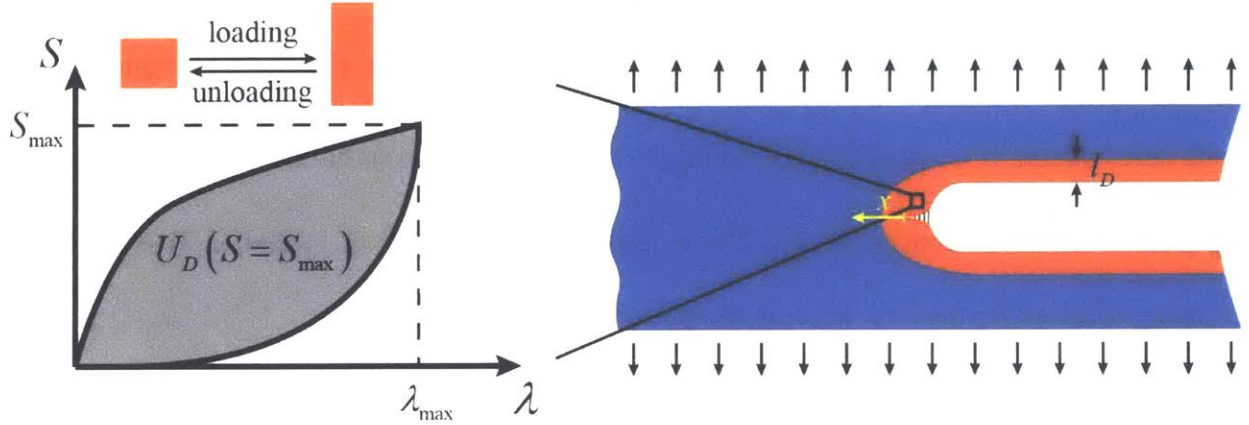


Figure 2-1: Schematic illustration of extrinsic mechanical dissipation enhancing fracture energies in tough hydrogels.

Deformation and stress fields around the tip of a crack in soft materials are highly affected by various degrees of strain stiffening effects such as neo-Hookean model, exponentially hardening model and Gent model (121). Here, we focus on a soft material represented by the neo-Hookean solid in pure-shear test, the leading order of the nominal stress at a point near crack tip scales as $S \propto \sqrt{2\Gamma\mu / \pi x}$ (61, 121), where μ is the shear modulus of the materials, Γ is the total fracture energy, and x is the distance from the point to the crack tip. Since only a region of the material around crack tip is under sufficiently high deformation (i.e., material inside the process zone) to significantly contribute to energy dissipation, we can choose a critical stress level to determine the boundary of the process zone. It can be argued that the critical stress level is on the same order as the maximum stress (S_{\max}) in the sample, and therefore the size of the process zone according to the crack tip stress field scales as

$$l_D \sim \frac{\mu\Gamma}{S_{\max}^2} \quad (2.2)$$

or equivalently,

$$l_D \sim \frac{\Gamma}{U_{\max}} \quad (2.3)$$

where $U_{\max} \sim S_{\max}^2 / \mu$ is the maximum mechanical work done on the material under pure-shear tensile deformation. It is noted that the scaling of $U_{\max} \sim S_{\max}^2 / \mu$ is valid for the material with a long plateau of stress-stretch curve (122). A combination of Eqs. (2.1) and (2.2) leads to a governing equation for the total fracture energy of soft tough materials,

$$\Gamma \sim \frac{\Gamma_0}{1 - \alpha^* h_{\max}} \quad (2.4)$$

where $h_{\max} = U_D (S = S_{\max}) / U_{\max}$ is the ratio between the maximum dissipation and maximum mechanical work done on the material, and $0 \leq \alpha^* \leq 1$ is a dimensionless number depending on the stress-strain hysteresis of the material deformed to different levels of stresses.

2.3 Coupled cohesive-zone and Mullins effect model

Next, we develop a continuum model that can predict the fracture energy of soft tough materials, using material parameters measured independently. The continuum model needs to quantitatively capture the synergistic contributions of intrinsic fracture energy and mechanical dissipation in process zone to the total fracture energy. In order to model the intrinsic fracture energy of soft materials, we adopt a triangle cohesive-zone model governed by the maximum nominal stress S_{\max} and maximum nominal separation δ_{\max} on the expected crack path (123). The damage initiation of the cohesive layer follows the quadratic nominal stress criterion

$$\left(\frac{t_n}{S_{\max}} \right)^2 + \left(\frac{t_s}{S_{\max}} \right)^2 = 1 \quad (2.5)$$

where t_n and t_s represent the nominal surface tractions on the crack surface along normal and tangential directions, respectively. When Eq. (2.5) is satisfied, the cohesive layer enters into the softening regime, which is described by the linear damage evolution function illustrated in Fig. 2-2. The cohesive-zone model prescribes the intrinsic fracture energy of the soft materials to be

$$\Gamma_0 = \frac{1}{2} S_{\max} \delta_{\max} \quad (2.6)$$

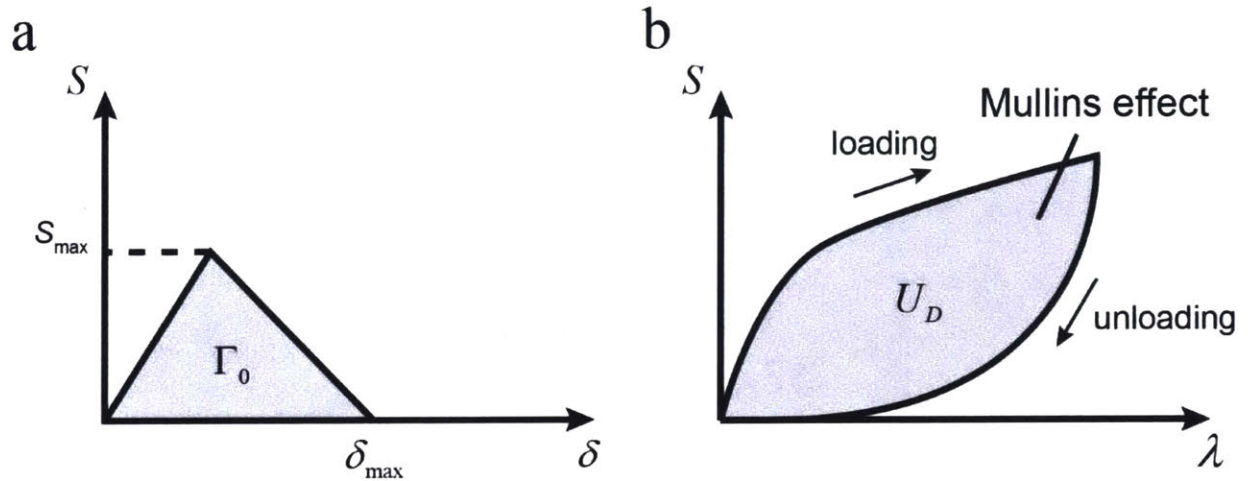


Figure 2-2: Schematics of the model for fracture in soft tough materials. (a) The intrinsic fracture energy of the soft material is characterized as a cohesive-zone model with triangle traction–separation law. (b) The mechanical dissipation in the process zone is characterized by the Mullins effect. A typical stress–stretch curve of the soft material under cyclic pure-shear tensile deformation. The hysteresis loop in the curve indicates mechanical dissipation.

To physically implement the cohesive-zone model, the maximum stress S_{\max} of the cohesive zone is taken as the measured failure stress of the material under pure-shear tension, and the maximum separation δ_{\max} is calculated based on the experimentally measured intrinsic fracture energy of the material Γ_0 and Eq. (2.6), i.e., $\delta_{\max} = 2\Gamma_0 / S_{\max}$.

Mechanical dissipation in the process zone may arise from viscoelasticity (124, 125), plasticity (110), and/or partial damage of the soft materials; and such dissipations manifest as

hysteresis loops on stress-strain curves of the material. To capture the essential effect of dissipation in process zone on toughening, we model the dissipation as the Mullins effect in soft materials. The Mullins effect gives hysteresis loops in the stress-stretch curves of the materials under loading-unloading cycles. We redefine the hysteresis ratio of the material under pure-shear tensile deformation as

$$h = U_D / U \quad (2.7)$$

where U and U_D are the mechanical work done on and the energy dissipation in a unit volume of the soft material under pure-shear tensile deformation, respectively. The hysteresis ratio of the soft material generally increases with the deformation of (or the work done on) the material due to the accumulation of material damage and eventually reaches a maximum value, i.e., $h(S = S_{\max}) = h_{\max}$ (Fig. 2-3c), which is used in Eq. (2.4). To describe the Mullins effect in soft materials, we adopt the modified Ogden-Roxburgh model (126) used in Abaqus. In brief, the free energy function of an incompressible material with Mullins effect can be expressed as

$$W(\mathbf{F}, \eta) = \eta \tilde{W}(\mathbf{F}) + \phi(\eta) \quad (2.8)$$

where \mathbf{F} is the deformation gradient tensor, η is a damage variable ($0 < \eta \leq 1$), \tilde{W} is the free energy function of a pure elastic material without Mullins effect, and $\phi(\eta)$ is referred to as the damage function. The damage variable η characterizes the stress softening due to material damage. The material is in its virgin state if $\eta = 1$ and fully damaged state if $\eta = 0$. The damage function and damage variable in Eq. (2.8) can be expressed as

$$\phi(\eta) = \left[\int_1^\eta (m + \beta W^m) \operatorname{erf}^{-1}(r(1-\eta)) - W^m \right] d\eta \quad (2.9a)$$

$$\eta = 1 - \frac{1}{r} \operatorname{erf} \left[(W^m - \tilde{W}) / (m + \beta W^m) \right] \quad (2.9b)$$

where $W^m = -\phi'(\eta = 1)$ denotes the maximum strain energy density of the material before unloading, erf is the error function, β^* is a positive number to avoid overly stiff response at the initiation of unloading from relatively large stretch levels, and r and m are constants that characterize the damage properties of the material. Throughout the calculations, we set $\beta^* = 0.1$ for numerical stabilization. The parameter r in Eq. (2.9) indicates the maximum extent of the material damage related to the virgin state, which therefore determines the maximum hysteresis ratio of the material under pure-shear tensile deformation h_{\max} . Fig. 2-3a gives the relation between h_{\max} and r for a neo-Hookean material with Mullins effect under pure-shear tensile deformation. It is evident that h_{\max} is a monotonic decreasing function of r . The parameter m in Eq. (2.9) represents a critical energy scale that acts as a threshold for activating significant dissipation in the material. Fig. 2-3b shows the calculated hysteresis ratio h as a function of U/U_{\max} for different values of m/U_{\max} for a neo-Hookean material with Mullins effect under pure-shear tensile deformation. If $U/U_{\max} < m/U_{\max}$ for a material under pure-shear tensile deformation, the hysteresis ratio h is generally much smaller than h_{\max} , which means that the deformation of (or the work done on) the material is not sufficient to induce significant dissipation. If $U/U_{\max} \gg m/U_{\max}$, the hysteresis ratio h can reach a value close to h_{\max} , which means that significant dissipation has been activated. Therefore, the parameter m/U_{\max} indicates the speed of h increasing from 0 to h_{\max} as a function of U/U_{\max} ; a smaller value of m/U_{\max} gives a faster transition to h_{\max} .

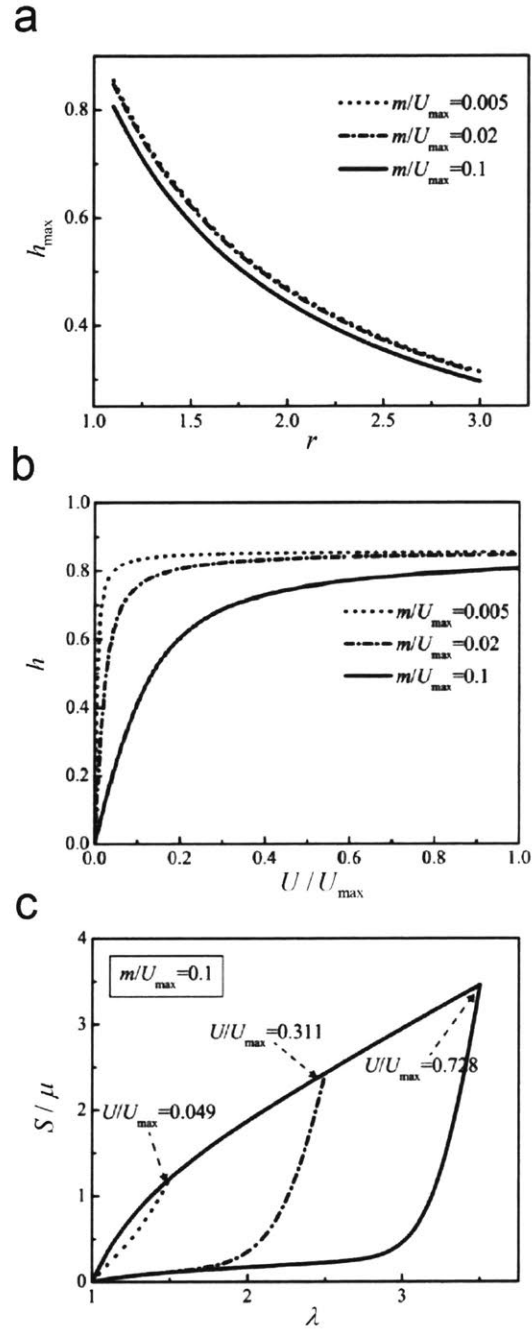


Figure 2-3: The modified Ogden-Roxburgh for Mullins effect. (a) The relation between maximum hysteresis ratio h_{\max} and damage constant r for a neo-Hookean material with Mullins effect under pure-shear tensile deformation. (b) The calculated hysteresis ratio h as a function of normalized stored strain energy U/U_{\max} for different values of damage constant m/U_{\max} for a neo-Hookean material with Mullins effect under pure-shear tensile deformation. (c) The calculated stress-stretch hysteresis for a neo-Hookean material with Mullins effect under pure-shear tensile deformation.

To physically implement the Mullins-effect model, the free energy function $\tilde{W}(\mathbf{F})$ in Eq. (2.9) can be obtained by fitting a hyperelastic material to the stress-stretch curve of soft material under monotonic loading. The parameters r and m in Eq. (2.9) can be obtained from multiple stress-stretch hysteresis of the soft material deformed to different stretches.

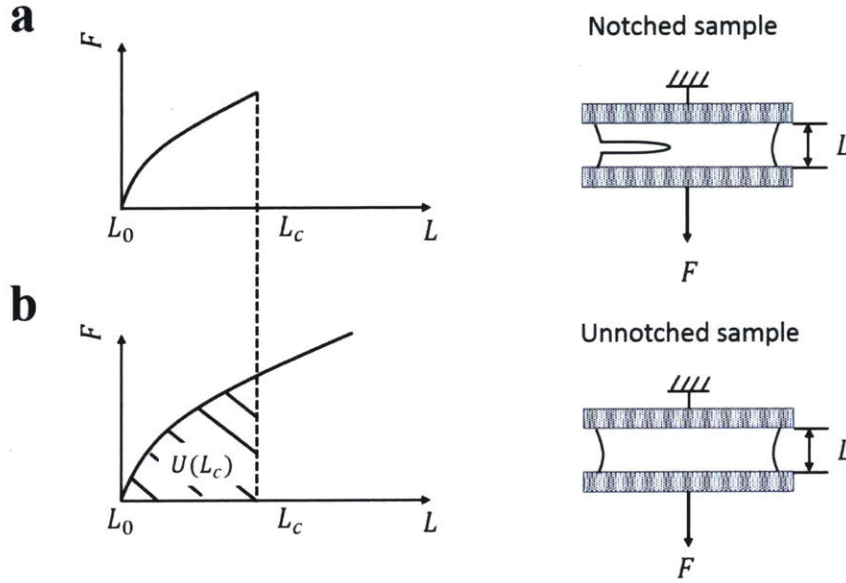


Figure 2-4: Schematic of pure-shear test for measuring fracture energy of hydrogels. (a) Notched samples are stretched to critical distance of L_c until the crack propagates. (b) Un-notched samples are stretched to L_c with the force F recorded and the fracture energy of the hydrogel can be calculated as $\Gamma = (\int_{L_0}^{L_c} F dl) / (W_0 T_0)$, where W_0 , T_0 and L_0 represents width, thickness and initial gage length of the sample, respectively.

In order to calculate the total fracture energy and crack-tip strain field of soft material, the pure-shear test is simulated in the coupled cohesive-zone and Mullins-effect model. In brief, two identical pieces of a soft material are clamped along their long edges with rigid plates. A notch is introduced into the first sample, which is then gradually pulled to a stretch of λ_c times of its undeformed length until a crack steadily propagates from the notch. Thereafter, the second sample without notch is uniformly stretched to the same critical stretch λ_c with the applied stress S

recorded. The total fracture energy of the soft material can be calculated as $\Gamma = L_0 \int_1^{\lambda_c} S d\lambda$, where L_0 is the height of the sample shown in Fig. 2-4.

We next discuss the difference in critical stretches for crack initiation and steady-state propagation and therefore the difference in corresponding fracture energies. The crack initiation happens at the same critical stretch for a material with and without energy dissipation (i.e., with and without Mullins effect), because the unloading process and thus dissipative properties of the materials do not affect crack initiation. The measured fracture energy corresponding to crack initiation reflects the intrinsic fracture energy of a material. On the other hand, the critical stretches for steady-state propagation of crack in a material with and without energy dissipation can be very different. For pure elastic samples (i.e., without Mullins effect), the steady-state propagation of crack follows right after the crack initiation. For samples with dissipation (i.e., with Mullins effect), the steady-state propagation of crack, however, can occur at a much larger stretch than crack initiation, because the unloaded material around the crack has been softened-reflecting the toughening effect of mechanical dissipation. In the current study, we use the fracture energy measured at steady-state propagation of crack (i.e., the steady-state critical energy release rate G^{ss}) to give the total fracture energy Γ of materials with and without dissipation.

2.4 Theoretical and numerical results

Next, we will use the coupled cohesive-zone and Mullins-effect model to validate the scaling for total fracture energies of soft materials. The soft material under loading is taken as a neo-Hookean material with initial shear modulus μ . Based on the coupled cohesive-zone and Mullins effect model, the total fracture energy of the soft material, Γ , is mainly determined by a set of four parameters including μ , Γ_0 , h_{\max} , S_{\max} , and m/U_{\max} . (Note that U_{\max} is approximately equal to

$S_{\max}^2 / 2\mu$ for neo-Hookean materials) We will vary these parameters independently in the model, and calculate the fracture energy of the materials following the pure-shear method described above. Without loss of generality, we use the initial shear modulus μ to normalize S_{\max} , Γ_0 and Γ . In Fig. 2-5a, the calculated values of Γ are plotted as functions of Γ_0 in all the calculated cases. With this knowledge in mind, we next explore the enhanced ratio of the fracture energy Γ/Γ_0 due to mechanical dissipation in the process zone. We calculate Γ/Γ_0 as functions of h_{\max} for various combinations of S_{\max}/μ and m/U_{\max} . Fig. 2-4b shows that the relation $\Gamma/\Gamma_0 = 1/(1-\alpha^* \cdot h_{\max})$ is valid for wide ranges of S_{\max}/μ (i.e., from 2 to 6) and m/U_{\max} (i.e., 0.005-0.1). In addition, it can be seen that the calculated values of Γ/Γ_0 from models with different S_{\max}/μ but the same m/U_{\max} are approximately the same. This means the parameter α^* in Eq. (2.4) mainly depends on the normalized critical energy scale, m/U_{\max} . In Fig. 2-4c, we summarize the calculated parameter α^* as a function of m/U_{\max} for different values of S_{\max}/μ . It is evident that α^* does not depend on S_{\max}/μ , which is consistent with the result in Fig. 2-5b. In addition, α^* is a monotonic decreasing function of m/U_{\max} . This trend can be qualitatively understood as follows. When the normalized work done on a material element in the process zone exceeds a critical value m/U_{\max} , the element begins to dissipate mechanical energy significantly. Therefore, for materials with otherwise the same properties, a lower value of m/U_{\max} gives more dissipation in the process zone and thus a higher enhancement of the fracture energy, i.e., higher value of Γ/Γ_0 . Based on the models' results in Fig. 2-5c, we further fit α as a function of m/U_{\max} for

$$\alpha^* \approx 0.33 + \frac{0.034}{m/U_{\max} + 0.045} \quad (2.10)$$

This fitting equation was recently theoretically derived and validated by Long et al. as well (61).

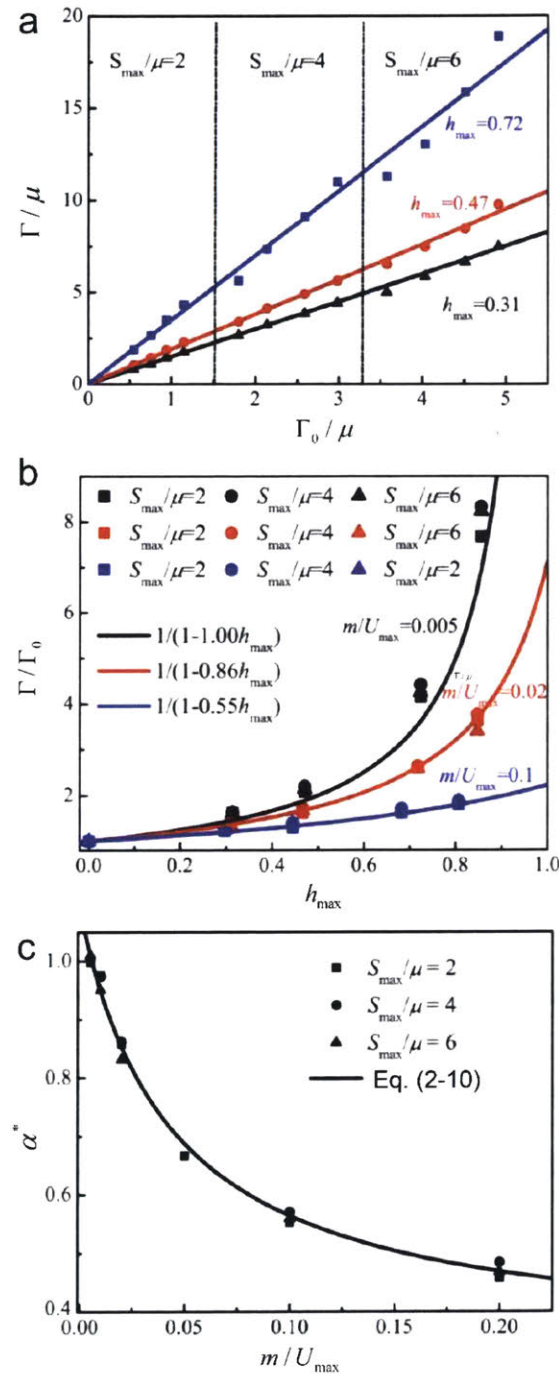


Figure 2-5: Calculated fracture energies of soft materials from the model. (a) Calculated Γ as a function of Γ_0 with different S_{\max}/μ and h_{\max} . The value of m/U_{\max} is set to 0.01. (b) Calculated Γ as a function of h_{\max} with different S_{\max}/μ and m/U_{\max} . (c) Calculated dimensionless parameter α^* as a function of m/U_{\max} .

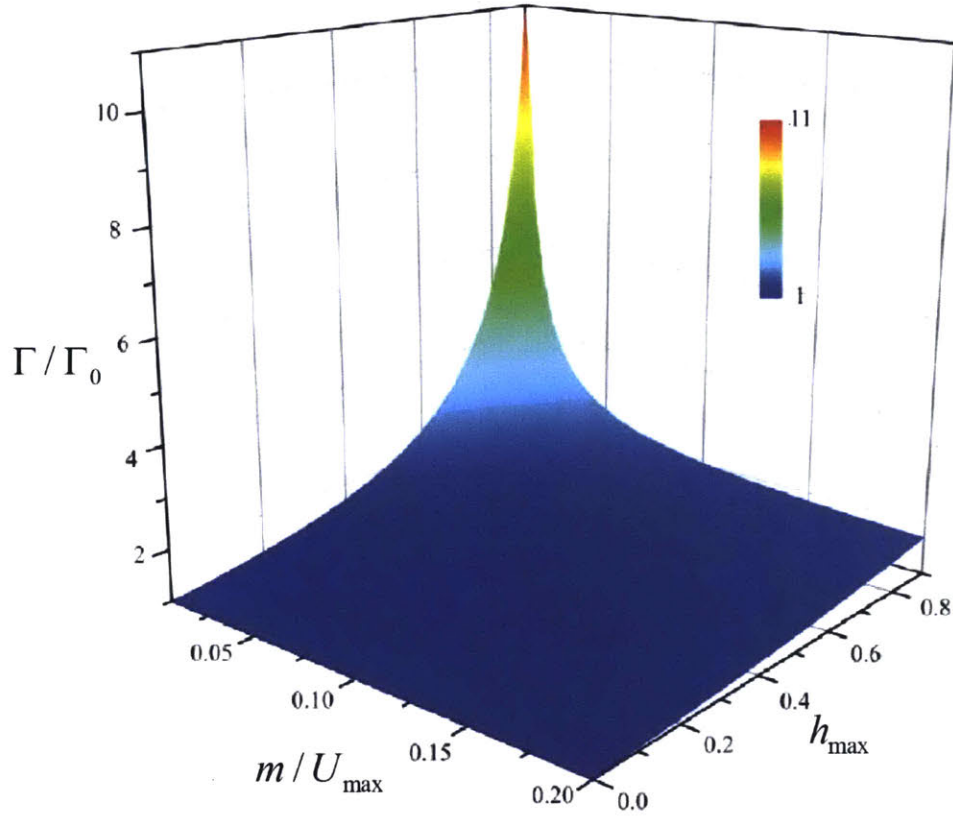


Figure 2-6: A quantitative diagram for toughening mechanisms of soft materials. The toughness enhancement ratio Γ/Γ_0 as a function of the maximum hysteresis ratio h_{\max} and the normalized critical energy scale for significant dissipation m/U_{\max} .

Based on Eqs. (2.4) and (2.10), we summarize the toughness enhancement of soft materials, Γ/Γ_0 , as a function of the maximum hysteresis ratio h_{\max} and the normalized critical energy scale for significant dissipation m/U_{\max} in Fig. 2-6. The results reveal three critical factors in toughening of soft materials: (1) high intrinsic fracture energy (i.e., high Γ_0), (2) high value of maximum hysteresis ratio (i.e., high h_{\max}), and (3) quick transition to the maximum hysteresis (i.e., low m/U_{\max}). These findings are consistent with the underlying physical mechanisms for the design of soft tough materials, such as large amounts of long stretchy polymer chains for high intrinsic fracture energy, sacrificial bonds for high energy dissipation, and high stretchability for a

quick transition from zero to maximum hysteresis ratio. Our theoretical models can quantify the contributions from each factor, and therefore provide quantitative guidelines for the design of future soft tough materials.

2.5 Experimental validation

2.5.1 Material preparation

To validate the model, we take the interpenetrating-network hydrogel of PAAm-Alginate as a model material system to investigate the toughness enhancement by introducing energy dissipation in a realistic soft material. A pre-gel solution is prepared by mixing 4.1 mL 4.8 wt% alginate (Sigma, A2033) and 5.5 mL 18.7 wt% acrylamide (Sigma, A8887). We add 900 μL 0.2g/100ml N,N-methylenebisacrylamide (Sigma, 146072) as the crosslinker for polyacrylamide and 102 μL 0.2 M ammonium persulphate (Sigma, 248614) as a photo initiator for polyacrylamide. After degassing the pre-gel solution in a vacuum chamber, we add respectively 200 μL or 300 μL (sample 1: 200 μL ; sample 2: 300 μL) 1 M calcium sulphate (Sigma, C3771) as the crosslinker for alginate and 8.2 μL N,N,N',N'-tetramethylethylenediamine (Sigma, T7024-50M) as the initiation accelerator for polyacrylamide to form hydrogels with different energy dissipation. Thereafter, the pre-gel solution is infused into a glass mold and is subjected to ultraviolet light irradiation for 60 minutes with 8 W power and 254 nm wavelength to cure the hydrogel.

2.5.2 Calibration of material parameters

We measure stress–stretch curves and various hysteresis ratios of the hydrogel under pure-shear tensile deformation up to the maximum stress S_{\max} , and then implement the measured data into the modified Ogden-Roxburgh model in ABAQUS. As shown in Fig. 2-7a, the pure elastic deformation of the hydrogel can be well described by the Ogden hyperelastic model (127). In Fig. 2-7c, we compare the measured hysteresis ratio of the hydrogel under different deformation (i.e.,

different U/U_{\max}) with the model's prediction, validating that the Ogden-Roxburgh model can accurately characterize the dissipative property of the hydrogel. In order to measure the intrinsic fracture energy of the hydrogel, we pre-deform the hydrogel samples to a level of stress approximately S_{\max} for multiple cycles to deplete the dissipative capacity of the samples (44, 118). This measured value overestimates the tough hydrogels' intrinsic fracture energy since a few cycles of pre-stretching is not sufficient for completely depleting the fracture energy (78). (Note that the alternative approach to identify the intrinsic fracture energy is to measure its fatigue threshold.) Thereafter, the pure-shear test is used to measure the stress-stretch hysteresis and fracture energy of the pre-deformed sample. There is almost no stress-stretch hysteresis of the sample pre-deformed to S_{\max} (118), indicating negligible mechanical dissipation of the sample. In addition, the measured fracture energy as a function of pre-deformation indeed reaches an asymptote (Fig. 2-8b), which gives the intrinsic fracture energy of the hydrogel without the effect of dissipation in the process zone. The measured intrinsic energy is then implemented through the cohesive-zone model in ABAQUS.

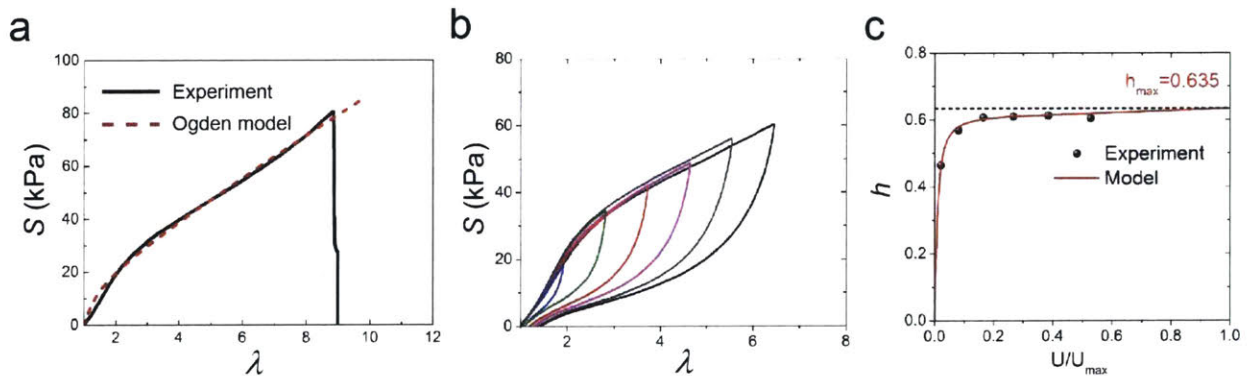


Figure 2-7: (a) Comparison of the experimentally measured stress–stretch curve and fitted curve using one term Ogden model. (b) Experimentally measured cyclic stress–stretch curves at different stretches. (c) The measured hysteresis ratios of the material deformed to different stretches and the calculated hysteresis ratio by the modified Ogden–Roxburgh model with $r = 1.516$ and $m = 4.274 \text{ kJ/m}^3$.

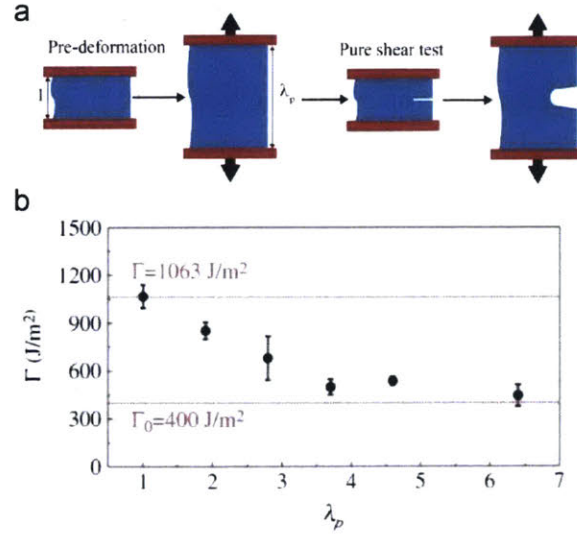


Figure 2-8: (a) Schematic illustration of the method for measuring intrinsic fracture energy via pre-deformation. (b) Fracture energy as a function of pre-deformation λ_p .

2.5.3 Validation

Now that the material parameters of the hydrogel have been independently measured and implemented in the continuum model, we will perform the pure-shear tests on samples both in experiments and in the model to obtain the fracture energies of the hydrogel. The hydrogel strip for experimentally measuring the fracture energy has a dimension of $L_0=20$ mm, $W_0=180$ mm and cut length $a=90$ mm (Fig. 2-4), which also applies to the numerical simulations presented in Fig. 2-10. As demonstrated by previous study (42), the current size is large enough to obtain fracture energies that are independent of the specimen size. It should be noted that, in other studies, the process zone can be as large as the tested sample, making the fracture toughness as an extrinsic quantity depending on the specimen size. In Fig. 2-9, we compare the force-displacement curves of the notched sample from experiment and calculation, and find that the theoretically predicted curve and critical point for steady-state crack propagation are in good agreement with experimental results. We further use digital image correlation (DIC) method to measure the strain field around

the notch in the sample under pure-shear test. As shown in Fig. 2-10, the strain fields around the notch predicted by the model are consistent with the measured results by DIC.

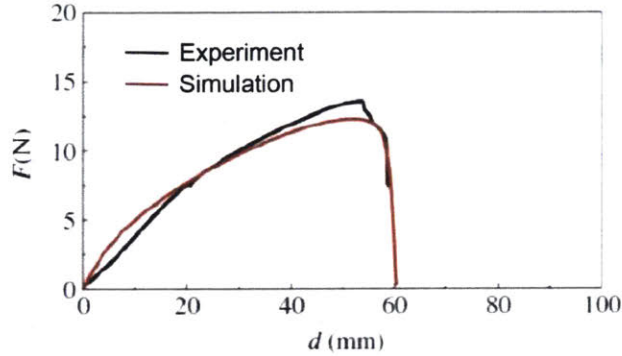


Figure 2-9: Force–displacement curves of the notched sample under pure-shear test measured from the experiment and predicted by the model.

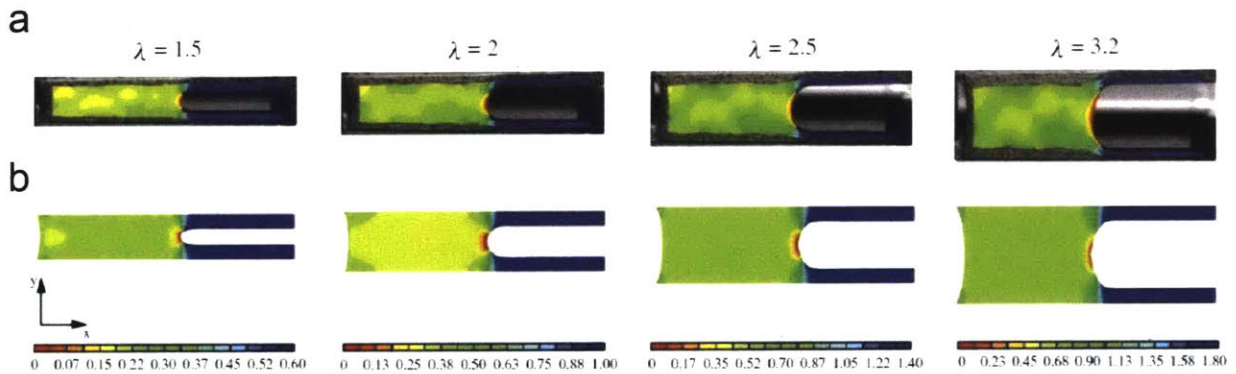


Figure 2-10: The strain field in the notched sample under pure-shear test to different stretches: (a) measured by digital image correlation method (DIC) in the experiment and (b) predicted by the model.

2.6 Concluding remarks

In this chapter, we propose a scaling law that accounts for synergistic effects of intrinsic fracture energies and mechanical dissipations on the toughening of soft materials. We then develop a coupled cohesive-zone and Mullins effect model to quantitatively predict the fracture energies and crack-tip strain fields in soft tough materials, using material parameters measured independently. The theory and the model show that the toughening of a soft material relies on high intrinsic fracture energy of the material, high value of maximum hysteresis ratio of the material, and quick

transition to the maximum hysteresis in the material under deformation. We further perform pure-shear experiments coupled with DIC method on tough hydrogels to measure their fracture energies and strain fields around crack tips, and show that the experimental results match well with the model's predictions. The theory and model can provide quantitative guidance for the design of future soft tough materials.

Chapter 3

Design of resilient yet tough hydrogels

3.1 Introduction

High resilience of a materials requires low mechanical dissipation of the material under deformation, which is indicated by small hysteresis loops in the stress-strain curves of the material being deformed and undeformed (e.g., Fig. 3-1a). On the other hand, high toughness requires significant mechanical dissipation during crack propagation in a material, and thus large hysteresis loops in the corresponding stress-strain curves of the material (e.g., Fig. 3-1b). While resilience and toughness seem to be a pair of intrinsically contradictory properties for a material, many biological tissues or hydrogels are indeed both resilient and tough. For example, heart valves (3, 4, 128, 129), which need to deform more than 3×10^9 cycles over their lifetime (129), generally can achieve both high resilience ($>80\%$) (4) and high toughness ($>1200 \text{ J/m}^2$) (128) in order to be both energy-efficient and robust. Designing synthetic hydrogels that are both tough and resilient will not only help the replacement and regeneration of relevant tissues such as heart valves, but also advance fundamental knowledge in mechanics and materials science. Despite the successes in developing hydrogels with high toughness (43-46, 50, 62, 130) or high resilience (6, 131), recent efforts on designing both tough and resilient hydrogels mostly focus on one property (e.g. reporting resilience without toughness) (132-134). In addition, existing works in the field mostly rely on specific materials (132-134). However, a general principle together with practical methods that can guide the design of resilient and tough hydrogels using different materials will be particularly valuable.

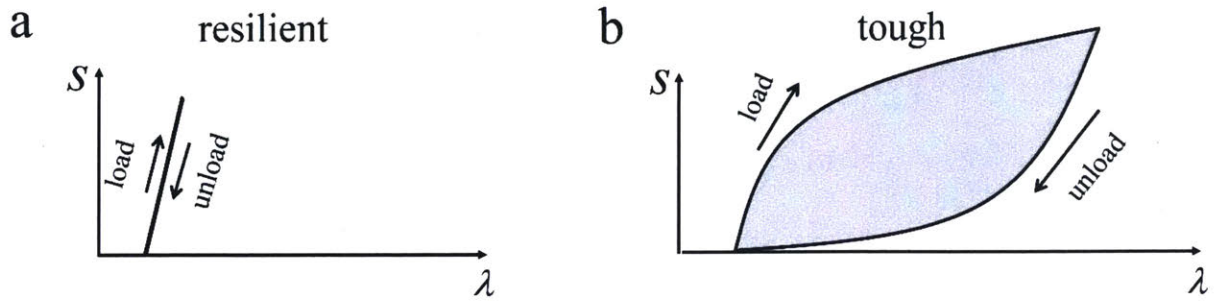


Figure 3-1: (a) Resilient material requires low mechanical dissipation under deformation, indicated by small hysteresis in the stress-strain curve. (b) Tough material requires high dissipation during crack propagation in it, indicated by large hysteresis in the stress-strain curve.

3.2 Definition and experimental characterization

Resilience refers to the ability of a material to deform and spring back to its original shape elastically with no loss of mechanical energy. Quantitatively, resilience of a soft material is defined as the ratio of energy released in deformation recovery to the energy that causes the deformation. To experimentally measure this quantity, it can be obtained by dropping a weighted ball from a specific height onto a given material and measuring the rebound height of the ball (ASTM D2632). Here, we take an alternative approach to measure the resilience of one soft material by performing cyclic tensile loading. The resilience of a material can be calculated by

$$R = 1 - \frac{\oint S d\lambda}{\int_1^{\lambda_{\max}} S d\lambda} \quad (3.1)$$

where $\oint S d\lambda$ is the area of hysteresis loop in the loading-unloading cycle, $\int_1^{\lambda_{\max}} S d\lambda$ is the area under the loading curve, S is the nominal stress in the sample, and λ_{\max} is the maximum nominal stretch in the cycle.

3.3 Delayed dissipation to reconcile resilience and toughness

Heart valve generally shows both high resilience of 80% and high toughness of 1200 J/m² (3, 4). The properties of high resilience and high toughness of heart valve are mainly attributed to the elastin and collagen in its layered structure via the mechanism of delayed dissipation. Heart valve is composed of two layers, i.e., the fibrosa and ventricularis, separated by a loose spongiosa (135) (Fig. 1-1d). Although the elastin is mechanically weak (~10 kPa), the elastin in ventricularis provides dominant restorative force for pulling back the fibrosa into its folded shape at small deformation (<60%), giving high resilience. When the heart valve is highly deformed with full extension, the collagen fibrils in fibrosa take over the load, resulting in high toughness.

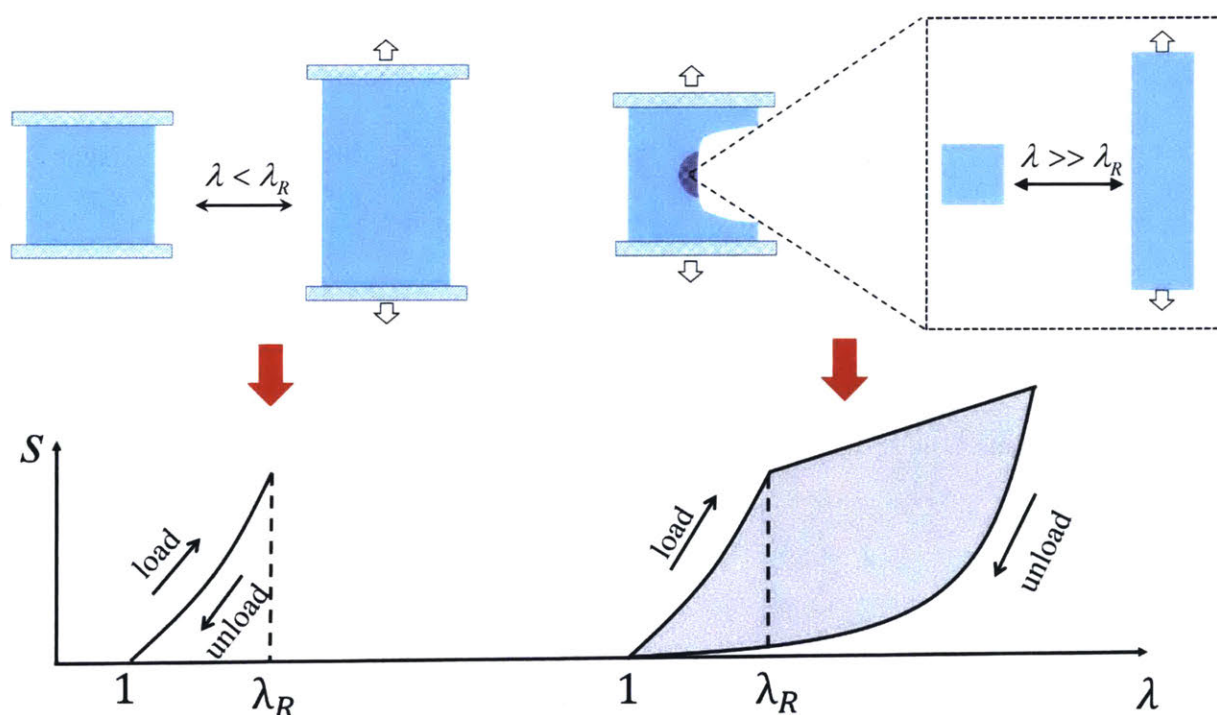


Figure 3-2: Resilient and tough hydrogel can be designed with delayed dissipation. The hydrogel is resilient when deformed within a resilient domain λ_R , but significantly dissipative when deformed beyond λ_R . Hydrogel around a crack tip will be deformed beyond λ_R and therefore significantly dissipates mechanical energy to toughen the hydrogel.

Here, inspired from nature, we further propose to design a *resilient domain*, Λ_R , in tough hydrogels via pre-deformation, so that (1) when $\Lambda_{\max} \leq \Lambda_R$, the hydrogel is resilient; (2) when $\Lambda_{\max} > \Lambda_R$, deformation of the hydrogel significantly dissipates mechanical energy, where Λ_R is a measurement of pre-deformation, such as principal stretch, the first invariant of Green deformation tensor (136), and effective stretch of polymer chains (137), and Λ_{\max} is the same measurement of the maximum deformation of the hydrogel in one loading-unloading cycle.

Since the hydrogel samples in the current study will all undergo pure-shear tension, different measurements of deformation will lead to equivalent results. To focus on the essential idea, we will choose the principal stretch along the applied force direction, λ , as the measurement of deformation. Therefore, the hydrogel is resilient when the maximum principal stretch of the hydrogel along the applied force direction $\lambda_{\max} \leq \lambda_R$, and highly dissipative when $\lambda_{\max} > \lambda_R$ (Fig. 3-2). In particular, the hydrogel around crack tips can be highly stretched over λ_R , and therefore significantly dissipate mechanical energy to toughen the hydrogel (Fig. 3-2).

3.4 Implementation of delayed dissipation

To implement the design principle, we pre-stretch interpenetrating-network hydrogels with distinctly different chain lengths to λ_R (Fig. 3-3) (43, 44). The pre-stretch will damage the short-chain network in the hydrogels to controlled degrees, which tend to increase with the pre-stretch. As a result, if the pre-stretched hydrogel is further deformed within the value of λ_R , it will be highly resilient; since the available sacrificial chains or bonds within the value of λ_R have been mostly consumed. On the other hand, if the subsequent deformation is beyond the value of λ_R ,

hydrogel, leading to the high toughness of the resultant hydrogel (44). The preparation of PAAM-alginate hydrogel is as follows.

- A pre-gel solution is prepared by mixing 4.1 mL 4.8 wt% alginate (Sigma, A2033) and 5.5 mL 18.7 wt% acrylamide (Sigma, A8887). We add 377 μL 0.2g/100ml N,N-methylenebisacrylamide (Sigma, 146072) as the crosslinker for polyacrylamide and 102 μL 0.2 M ammonium persulphate (Sigma, 248614) as a photo initiator for polyacrylamide.
- After degassing the pre-gel solution in a vacuum chamber, we add 200 μL 1 M calcium sulphate (Sigma, C3771) as the crosslinker for alginate and 8.2 μL N,N,N',N'-tetramethylethylenediamine (Sigma, T7024-50M) as the initiation accelerator for polyacrylamide.
- Thereafter, the pre-gel solution is infused into a glass mold measuring $80 \times 60 \times 2 \text{mm}^3$ and is subjected to ultraviolet light irradiation for 60 minutes with 8 W power and 254 nm wavelength to cure the hydrogel.
- The resultant hydrogel is soaked in Dulbecco's Modified Eagle Medium (DMEM) for 15 hours to swell to equilibrium, approximating the physiological conditions *in vivo* (138).

3.5.2 Experimental validation

To validate the efficacy of pre-stretch method to achieve both high resilience and high toughness, we first load the sample to $\lambda_R = 5$ and then unloaded for 5 cycles to deplete the sacrificial bonds and chains (see Fig. 3-4a). Thereafter, the pre-stretched hydrogel sample is further stretched to maximum principal stretches of $\lambda_{\max} = 2, 3, 4, 5$ and 8 with a rate of 0.02 s^{-1} and then unloaded (Figs. 3-4, b and c). It can be seen that when $\lambda_{\max} < \lambda_R$, the hysteresis loop in the loading-unloading curves are almost negligible, indicating negligible mechanical dissipation and high resilience. Furthermore, we increase the loading rate on the pre-stretched sample to 0.1 s^{-1} , and

find that the small hysteresis loops are unaffected. On the other hand, when the pre-stretched sample is deformed to $\lambda_{\max} = 8$ (i.e., beyond resilient domain), an apparent hysteresis loop appears, indicating significant mechanical dissipation.

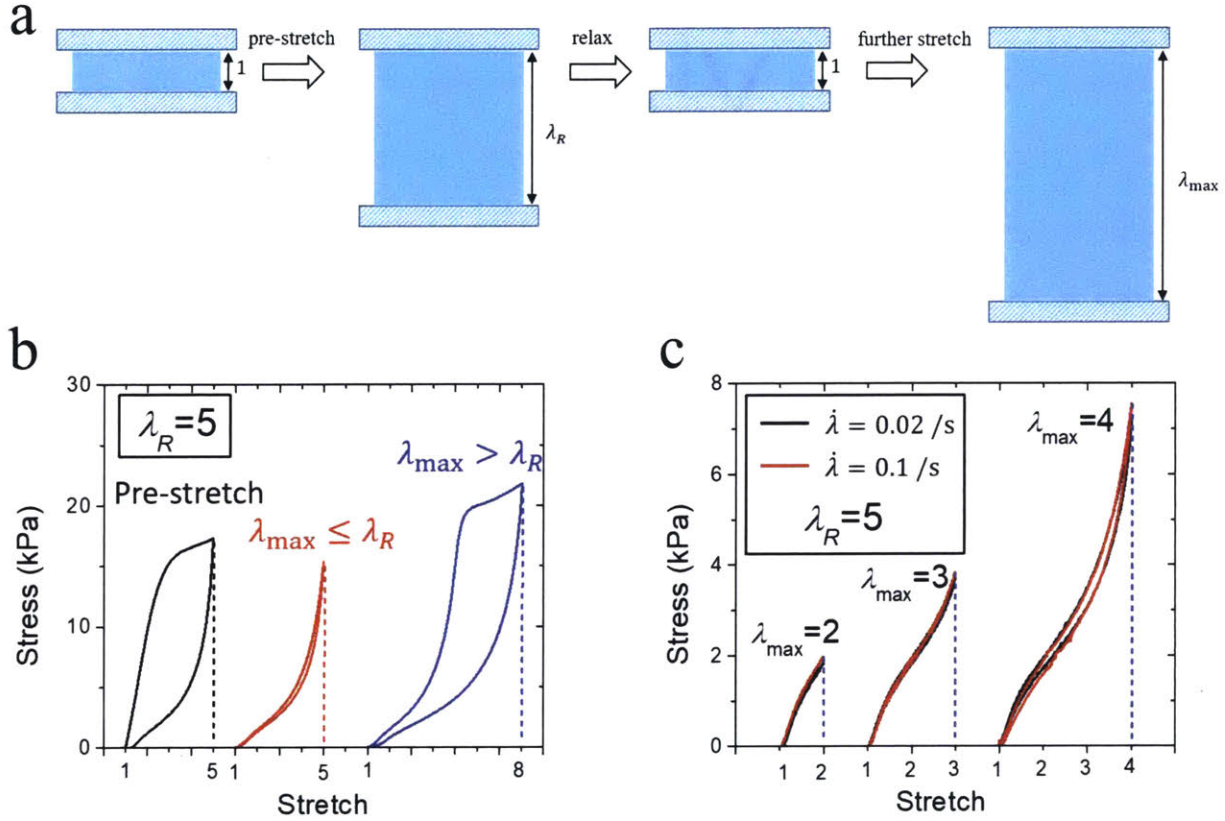


Figure 3-4: Experimental validation of the design principle and method with PAAM-alginate hydrogel. (a) Schematics of the pre-stretch and further deformation of the hydrogel sample. (b) Stress vs. stretch curves of the sample pre-stretched to $\lambda_R = 5$ and further stretched to $\lambda_{\max} = 5$ and 8 , respectively. (c) Stress vs. stretch curves of the sample with $\lambda_R = 5$ stretched to $\lambda_{\max} = 2, 3$, and 4 at different rates.

Moreover, the resilient domain of the hydrogel can also be tuned by changing the value of the pre-stretch λ_R . We next pre-stretch hydrogel samples to $\lambda_R = 4, 5$ and 6 , respectively and then measure the resilience of the samples under various deformations (Fig. 3-5). As shown in Fig. 3-5a, for various values of λ_R , when $\lambda_{\max} \leq \lambda_R$, the resilience of the hydrogels is consistently high, over 90%; when $\lambda_{\max} > \lambda_R$, the resilience decreases drastically in some cases (e.g., $R = 35\%$,

when $\lambda_R = 4$ and $\lambda_{\max} = 8$), indicating significant mechanical dissipation. We further use pure-shear tests to measure the fracture toughness of hydrogels pre-stretched to various resilient domains (i.e., $\lambda_R = 1-5$). From Fig. 3-5b, it can be seen that the fracture toughness can indeed maintain a relatively high level, over 1800 J/m^2 . To validate that the high toughness is due to the deformation of hydrogels around crack tip above λ_R , we use digital image correlation technique (139, 140) to obtain the distribution of maximum principal stretches around the notch of a tough and resilient hydrogel with $\lambda_R = 5$. From Fig. 3-5, c and d, it can be seen that the maximum principal stretch in the region around the notch tip can indeed reach values much higher than λ_R before crack propagation to dissipate mechanical energy and therefore toughen the hydrogel.

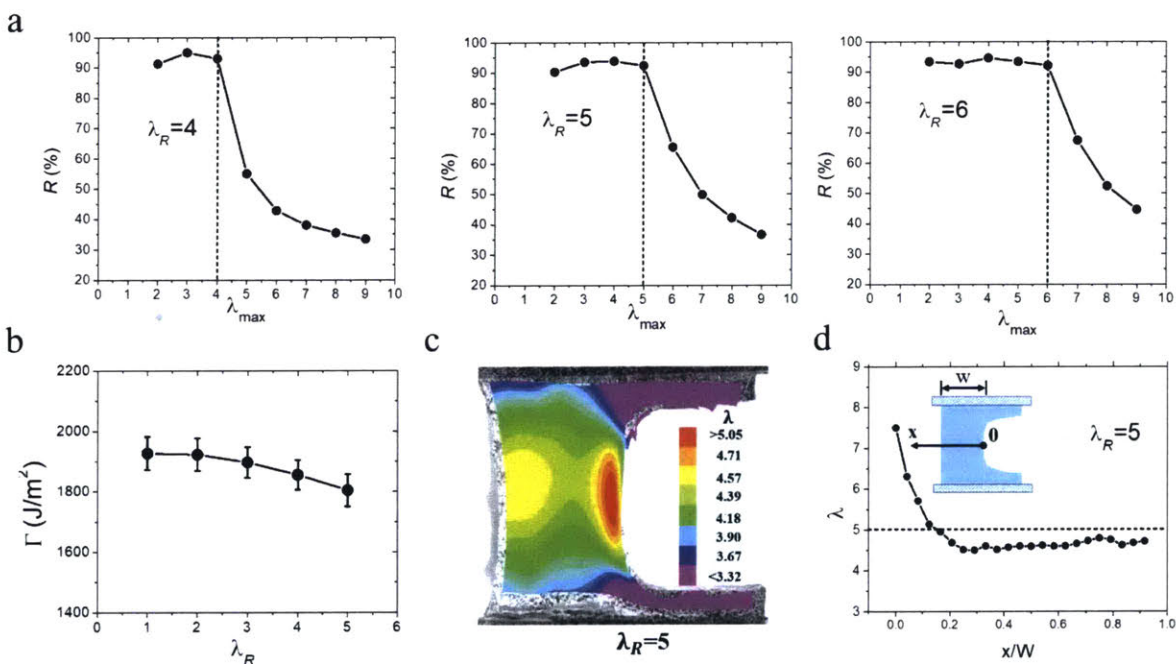


Figure 3-5: Tunable resilience and fracture toughness of tough and resilient PAAm-alginate hydrogels. (a) Resilience R as a function of maximum stretch λ_{\max} for samples with $\lambda_R = 4$, 5 and 6 , respectively. (b) Fracture energy Γ vs. resilient domain λ_R of the hydrogels, error bar denote STD, $n=3$; (c) Distribution of the maximum principal stretch around the crack tip of a hydrogel with $\lambda_R = 5$ under pure-shear test before crack propagation. (d) Maximum principal stretch along the central line of the sample.

While the dissociated ionic crosslinkings in alginate network can reform after pre-stretching the PAAm-alginate hydrogels to decrease the resilience of the hydrogel (44), it seems swelling the hydrogels in media can significantly reduce this effect (Fig. 3-6). For example, a hydrogel pre-stretched to $\lambda_R = 3$ can maintain high resilience of 77% over 67 hours.

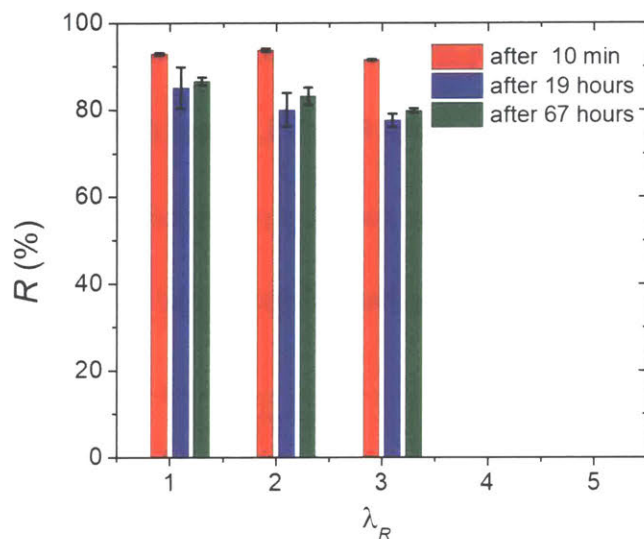


Figure 3-6: Resilience measured at maximum stretch $\lambda_{max} = 2, 3$ and 4 for samples with $\lambda_R = 2, 3$ and 4 after 10 min, 20 hours and 70 hours, respectively.

3.6 Conclusion

In conclusion, we report a general principle for the design of resilient and tough hydrogels via delayed dissipation. Based on the principle, a resilient domain is defined for the deformation of tough hydrogels. We further implement the delayed dissipation and resilient domain by pre-stretching interpenetrating-network hydrogels to damage the short-chain network within controlled ranges, achieving extremely high resilience ($\sim 95\%$) and high toughness ($\sim 1900 \text{ J/m}^2$) (see Fig. 3-8 for comparison with counterpart biological and synthetic hydrogels (3, 4, 6, 128)). Since the design principle and method reported here are material-independent, we expect they can be used to make existing tough hydrogels resilient and to design future tough and resilient

hydrogels. In addition, it is noted that natural rubbers indeed achieve high resilience and high toughness via delayed dissipation at large deformations, when polymer chains begin to detach from reinforcing particles, giving the Mullins effect (141). It is expected the design principle and method proposed here can be used to design new tough and resilient elastomers such as triple-network tough elastomers recently developed (142).

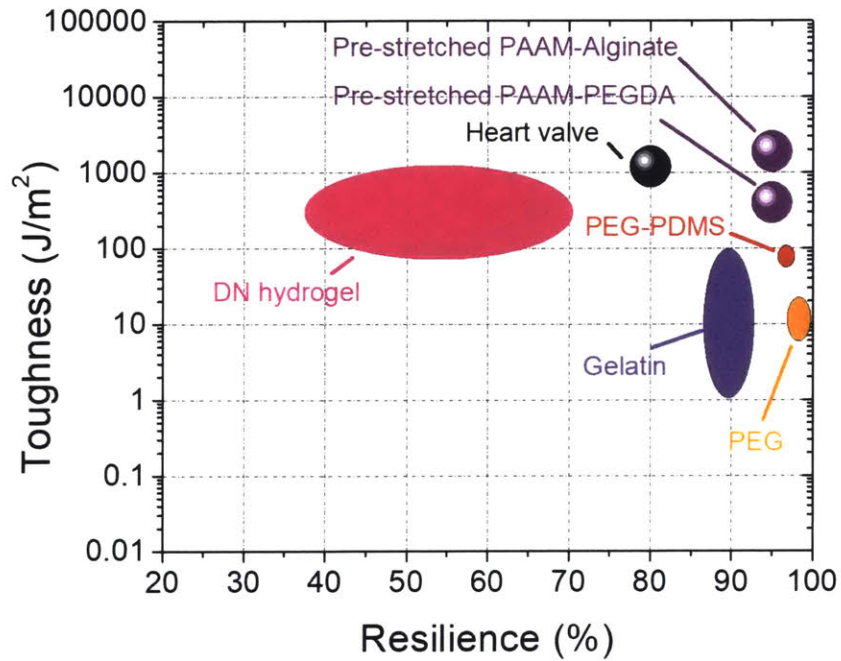


Figure 3-7: Comparison of fracture toughness and resilience of various synthetic and biological hydrogels.

Chapter 4

Design of fatigue-resistant hydrogels

4.1 Introduction

As polymer networks infiltrated with water, hydrogels have been widely used as scaffolds for tissue engineering (34), vehicles for drug delivery (143) and model platforms for biological studies (144). More recently, hydrogels have been explored for applications in devices and machines, including wearable electronics (145, 146), soft robotics (147), adhesives (42, 148, 149), and hydrogel-based soft machines (77, 150). The use of hydrogels in devices and machines requires them to maintain robustness under cyclic mechanical loads. Following the pioneering work by Gong et al. (43), hydrogels have been made tough to resist crack propagation under a single cycle of mechanical load (44, 62, 151). The toughening of hydrogels is achieved by integrating mechanisms for dissipating mechanical energies such as fracture of short polymer chains and reversible crosslinks into stretchy polymer networks (41, 46). However, existing tough hydrogels still suffer from fatigue fracture under multiple cycles of mechanical loads (77-79), because the resistance to fatigue-crack propagation after prolonged cycles of loads is the energy required to fracture a single layer of polymer chains (i.e., the intrinsic fracture energy of the hydrogel), which is unaffected by the additional dissipation mechanisms introduced in tough hydrogels (78, 79). The reported fatigue thresholds of various tough hydrogels are 8.4 J/m² for polyacrylamide (PAAm)-polyvinyl alcohol (PVA) (79) and 53.2 J/m² for PAAm-alginate (78), the same order as their intrinsic fracture energies. The highest fatigue threshold for hydrogels reported so far is 418 J/m² for a double network hydrogel, poly(2-acrylamido-2-methyl-1-propanesulfonic acid) (PAMPS)-PAAm, which possibly can be attributed to the PAAm network with very long polymer chains and thus high intrinsic fracture energy (43, 80). A general strategy towards the design of anti-fatigue-fracture hydrogels has remained as a critical need and a central challenge for long-term applications of hydrogels in devices and machines.

In contrast to synthetic hydrogels, biological tissues such as cartilages, tendons, muscles and heart valves show extraordinary anti-fatigue property. For example, the knee joint of an average person needs to sustain peak stresses of 4–9 MPa for 1 million cycles per year, and its fracture energy after prolonged cycles of loads is above 1,000 J/m² (22, 152). The anti-fatigue property of biological tissues possibly arises from the inherent highly ordered and partially crystalline structures of collagen fibers in the tissues (153).

Inspired by anti-fatigue biological tissues, we hypothesize that the increase of crystallinity in synthetic hydrogels can significantly enhance their fatigue thresholds, due to the need to fracture crystalline domains for fatigue-crack propagation (Fig. 4-1). The energy per unit area required to fracture crystalline domains of a polymer per unit area is much higher than that required to fracture a single layer of amorphous chains of the same polymer (154). To test the hypothesis, we select PVA as a model hydrogel with tunable crystallinity. We increase the annealing time (after freeze-thawing and air-drying) of the PVA hydrogel to give higher crystallinity, larger crystalline domain size, and smaller average distance between adjacent domains in the hydrogel (Fig. 4-1a). We then measure the fatigue thresholds of PVA hydrogels with various crystallinities (Fig. 4-1, b and c). We find that the increase of crystallinity can significantly enhance the fatigue thresholds of PVA hydrogels. In particular, the fatigue threshold can exceed 1,000 J/m² when the crystallinity of PVA in the swollen state reaches 18.9 wt.%. By annealing selected regions in hydrogels, we further propose a strategy to pattern highly-crystalline regions in the PVA hydrogels to render them resistant to fatigue-fracture but still maintain their high water contents and low moduli. With this strategy, we create *kirigami hydrogel sheets* that are highly stretchable and resistant to fatigue-fracture by introducing patterned cuts into hydrogel sheets and then reinforcing the cut tips. The

current work not only reveals a new anti-fatigue-fracture mechanism in hydrogels but also provides a practical method to design anti-fatigue-fracture hydrogels for diverse applications.

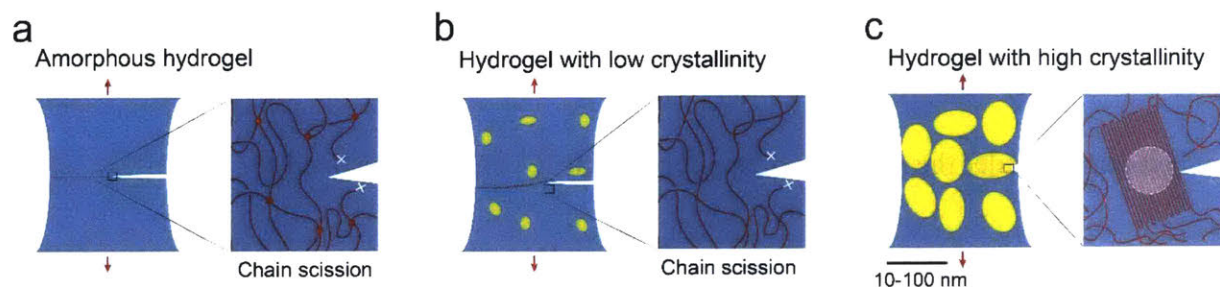


Figure 4-1: Illustration of mechanisms by controlled introduction of crystalline domains. (a) Fatigue crack propagation in an amorphous hydrogel under cyclic loads. (b) Fatigue crack propagation in hydrogels with low crystallinities under cyclic loads. (c) Fatigue crack propagation in hydrogels with high crystallinities under cyclic loads. The yellow areas represent crystalline domains, and the blue areas denote amorphous domains.

4.2 Definition and experimental characterization

We adopt one physical parameter, i.e., fatigue threshold (or alternatively termed as fatigue limit), to quantify hydrogel's ability to resist fatigue-crack propagation under repeated mechanical loads. Fatigue threshold is defined as the minimum fracture energy at which crack does not initiate in hydrogels over cycles. This physical quantity was first adopted to quantify elastomers' fatigue properties (155, 156). By physical definition, fatigue threshold is corresponding to the intrinsic fracture energy (i.e, the energy required to rupture a layer of polymer chains for elastomers and hydrogels).

Fatigue threshold can be commonly measured using single-notch tension method and pure shear method. Here, we adopt the single-notch tension method to measure the fatigue threshold of hydrogels, which has been widely used in fatigue tests of rubbers (155, 156). To validate the measured fatigue threshold, we use both single-notch tension method and pure shear method. Notably, all fatigue tests in this study are performed on fully-swollen hydrogels immersed in a

water bath, to prevent the dehydration-induced crack propagation (Fig. 4-1). We use dogbone-shaped samples and perform cyclic tensile tests on both notched and unnotched samples, which are otherwise the same. The nominal stress versus stretch curves (i.e., S vs. λ) of unnotched samples are obtained over N cycles of applied stretch λ^A . The strain energy density W of the unnotched sample under the N_{th} cycle of applied stretch λ^A can be calculated as

$$W(\lambda^A, N) = \int_1^{\lambda^A} S d\lambda \quad (4.1)$$

where S and λ are the measured nominal stress and stretch, respectively. Thereafter, the same cyclic stretch λ^A is applied on the notched sample, measuring the evolution of the cut length in undeformed state c with the cycle number N . The applied energy release rate G in the notched sample under the N_{th} cycle of applied stretch λ^A can be calculated as (155, 156)

$$G(\lambda^A, N) = 2k(\lambda^A) \cdot c(N) \cdot W(\lambda^A, N) \quad (4.2)$$

where k is a slowly varying function of the applied stretch expressed as $k = 3/\sqrt{\lambda^A}$, c the current crack length at undeformed configuration, and W the strain energy density measured in the unnotched sample (Eq. 4.1). By systematically varying the applied stretch λ^A , we can obtain a plot of crack extension per cycle versus the applied energy release rate (i.e., dc/dN vs. G). By linearly extrapolating the curve of dc/dN vs. G to the intercept with the abscissa, we can approximately obtain the critical energy release rate G_c , below which the fatigue crack will not propagate under infinite cycles of loads. By definition, the fatigue threshold Γ_0 is equal to the critical energy release rate G_c . To validate that this extrapolated value G_c is indeed the fatigue threshold Γ_0 , we further apply G_c to the notched sample using both single-notch method and pure

shear method (78) over 30,000 cycles (to approximate infinite cycles of loads) and observe crack extension over cycles.

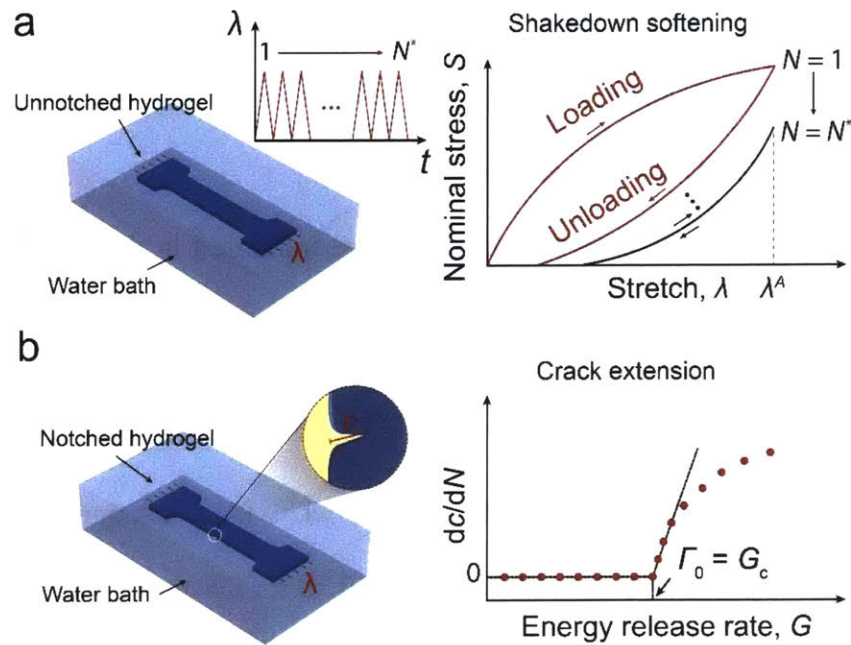


Figure 4-2: Schematic illustration of experimentally measuring fatigue threshold of hydrogels. (a) Illustration of measuring nominal stress S vs. stretch λ curves over N cycles of the applied stretch λ^A . The stress-stretch curve reaches steady state as N reaches a critical value N^* . (b) Illustration of measuring crack extension per cycle dc/dN vs. energy release rate G curves.

4.3 Materials and methods

4.3.1 Synthesis of PVA hydrogels

All types of PVA hydrogels are synthesized from 10 wt.% poly(vinyl alcohol) (PVA; Mw 146,000-186,000, 99+% hydrolyzed; Sigma-Aldrich, 363065) solution. The solution was heated in a water bath at 100 °C with stirring for 5 h.

Chemically-crosslinked PVA hydrogels

- To synthesize chemically-crosslinked PVA hydrogels, we added 10 μ l glutaraldehyde (25%, Sigma-Aldrich, G6257) as a crosslinker to 1 ml 10 wt.% PVA solution, and added

10 μ l hydrochloric acid (36.5%-38%, J.T. Baker, 9535-02) as an accelerator into the other 1 ml 10 wt.% PVA solution.

- We then mixed and defoamed each of them by using centrifugal mixer (AR-100; Thinky).
- The final mixtures, obtained by mixing and defoaming the two solutions together, were then casted into a mold and allowed to cure for 2 h.
- The chemically-crosslinked PVA hydrogels were immersed in deionized water for two days to remove unreacted chemicals.

Freeze-thawed PVA hydrogels

- To fabricate freeze-thawed PVA hydrogels, 10 wt.% PVA solutions after mixing and defoaming were poured into a mold, frozen at -20 °C for 8 h and thawed at 25 °C for 3 h.
- The freeze-thawed hydrogels were further dried in an incubator (New Brunswick Scientific, C25) at 37 °C for 2 h, and then annealed at 100 °C for a controlled time (i.e., 0, 1, 3, 5, 10, or 90 min).
- All as-prepared PVA hydrogels were immersed in water to achieve their equilibrium-swollen state.

4.3.2 Measurement of residual water and crystallinity in dry samples

We measured the crystallinities of the resultant PVA hydrogels in their dry state by differential scanning calorimetry (DSC/cell: RCS1-3277 Cooling System: DSC1-0107). For as-prepared chemically-crosslinked PVA and freeze-thawed PVA, we used excessive chemical crosslinks to fix the amorphous polymer chains before air-drying, minimizing the formation of further crystalline domains during the air-drying process. We first soaked the samples (thickness of 1mm) in the aqueous solution consisting of 10 ml glutaraldehyde (25 %, Sigma-Aldrich, G6257), 500 μ l

hydrochloric acid (36.5%-38%, J.T. Baker, 9535-02) and 50 ml DI water for 2 h. Thereafter, we soaked the samples in a DI water bath for 2 h to remove the residual hydrochloric acid. The samples were further dried in an incubator (New Brunswick Scientific, C25) at 37 °C for 2 h.

Thereafter, we measured the mass of residual water $m_{residual}$, the mass of crystalline domains $m_{crystalline}$ and the total mass of the dry samples (with residual water) m using DSC. In a typical DSC measurement, we first weighed the total mass of the dry sample (with residual water) m . The sample were thereafter placed in a Tzero-pan and heated up from 50 °C to 250 °C at the rate of 20 °C/min under nitrogen atmosphere with flow rate of 30 mL/min. As shown in Fig. 4-3b, the curve of heat flow shows a broad peak from 60 °C to 180 °C, indicating that the sample contains a small amount of residual water. The integration of the endothermic transition ranging from 60 °C to 180 °C gives the energy for evaporation of the residual water per unit mass of the dry sample (with residual water) $H_{residual}$. Therefore, the mass of the residual water $m_{residual}$ can be calculated as

$$m_{residual} = m \cdot \frac{H_{residual}}{H_{water}^0} \quad (4.3)$$

where $H_{water}^0 = 2260$ J/g is the latent heat of water evaporation. The curve of heat flow shows another narrow peak ranging from 200 °C to 250 °C corresponds to melting of crystalline domains.

The integration of the endothermic transition ranging from 200 °C to 250 °C gives the energy for fusing the crystalline domains per unit mass of the dry sample (with residual water) $H_{crystalline}$.

Therefore, the mass of the crystalline domains $m_{crystalline}$ can be calculated as

$$m_{crystalline} = m \cdot \frac{H_{crystalline}}{H_{crystalline}^0} \quad (4.4)$$

where $H_{crystalline}^0 = 138.6 \text{ J/g}$ is the enthalpy of fusion of 100 wt.% crystalline PVA measured at the equilibrium melting point T_m^0 (157). Therefore, the crystallinity in the ideally dry sample X_{dry} (without residual water) can be calculated as

$$X_{dry} = \frac{m_{crystalline}}{m - m_{residual}} \quad (4.5)$$

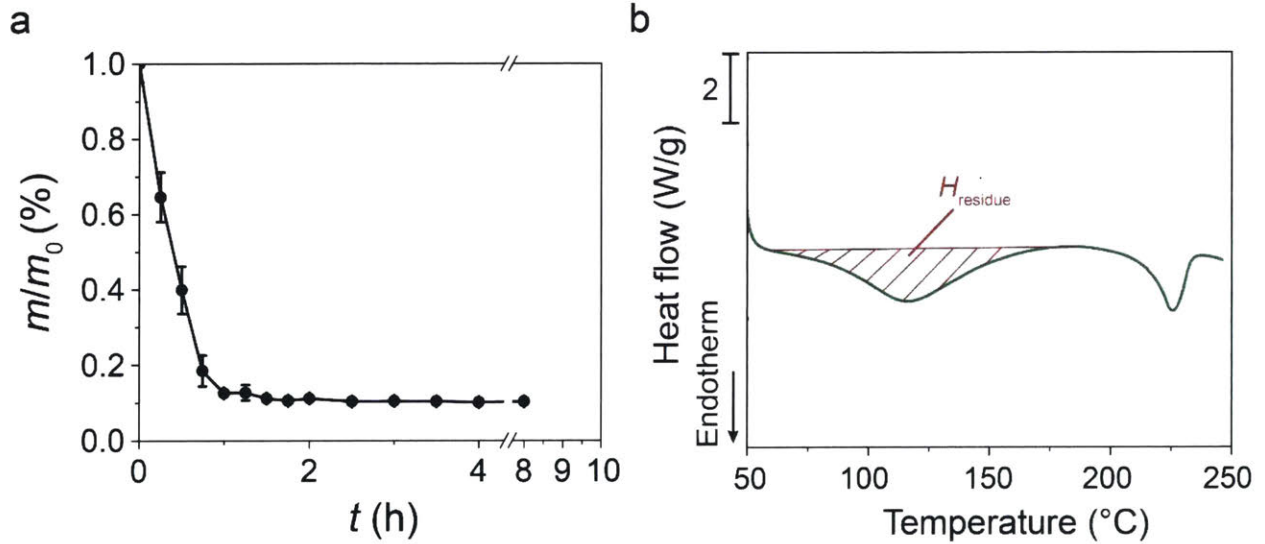


Figure 4-3: (a) Measured mass normalized by the initial mass (at swollen state) of freeze-thawed PVA sample versus air-drying time. (b) The amount of residual water can be calculated from the endothermic transition ranging from 60 °C to 180 °C on the DSC curves.

4.3.3 Measurement of water content and crystallinity in swollen samples

The swollen hydrogels weighing $m_{swollen}$ were placed in an incubator (New Brunswick Scientific, C25) at 37 °C for 2 h, and weighed m after air-drying (Fig. 4-3a). The mass of the residual water in the as-prepared dry samples $m_{residual}$ were measured in the previous section. Therefore, the water content in the swollen state can be calculated as $(m_{swollen} - m + m_{residual}) / m_{swollen}$ and the polymer

content in the swollen state can be calculated as $(m - m_{residual}) / m_{swollen}$. In addition, the crystallinity in the swollen sample $X_{swollen}$ can be calculated as

$$X_{swollen} = \frac{m_{crystalline}}{m_{swollen}} = X_{dry} \cdot \frac{m - m_{residual}}{m_{swollen}} \quad (4.4)$$

where $m_{crystalline}$ and X_{dry} were measured in the previous section.

4.3.4 AFM phase imaging

AFM phase images were acquired by atomic force microscope (MFP-3D, Asylum Research) in tapping mode. Dry free-standing PVA films were directly attached onto sample stage by double-sided carbon tape. The probe lightly taps on the sample surface with recorded phase shift angle of the probe motion relative to a driving oscillator. The bright regions with high phase angle correspond to regions with relative high modulus; and the dark regions with low phase angle correspond to regions with relative low modulus.

4.3.5 X-ray scattering

The X-ray scattering measurement was performed with Pilatus3R 300K detector Bruker Nanostar SAXS in X-ray Diffraction Shared Experimental Facility at MIT. We used small angle 2 mm beamstop with sample-detector distance of 1059.1 mm for SAXS measurements and wide angle 2mm beamstop with sample-detector distance of 109.1 mm for WAXS measurements. The exposure time was set as 300 s. Raw SAXS and WAXS patterns were processed with various corrections with MATLAB-based GIXSGUI software before analysis.

4.3.6 Raman spectroscopy

Each sample was hydrated for more than 2 h and then pressed between a glass slide and a cover slip in order to ensure a flat surface. The cover slip was then sealed at the edges with nail polish to

prevent the hydrogel from drying. A confocal Raman microscope (Alpha300RA; WiTec, Germany) with 20× objective (Zeiss, Germany) was used. Nd:YAG laser (532 nm) was used as the excitation source with the maximum power of 75mW. Data was collected with a CCD detector (DU401A-BV; Andor, UK) behind a 600 g/mm grating spectrometer (UHTS 300; WiTec, Germany). 20 μm resolution Raman map of 4×3 mm scan area was acquired with the accumulation time of 1 second per point. Each point was pre-bleached for 400 ms to decrease the effect of fluorescence. Cosmic ray removal and background subtraction were performed to clean the spectra. The intensity of O-H bond within the PVA and water were calculated by integrating the spectra in the range of 2,800-3,000 cm⁻¹ and 3,075-3,625 cm⁻¹, respectively. The ratio of PVA and water was then calculated and plotted as a heatmap.

4.3.7 Measurement of the fatigue threshold

All the mechanical tests were performed in a water bath at 25°C with U-stretch (CellScale, Canada). For mechanically weak samples (e.g., the Ch and FT hydrogels), a load cell with maximum force of 4.4 N was used; for mechanically strong samples (e.g., Anneal-90), a load cell with maximum force of 44 N was used. The dumbbell-shape sample had the dimensions at as-prepared state with the width of 5mm, thickness of 0.8mm and gauge length of 10mm. The nominal stress S was measured from the recorded force F divided by width W and thickness t in the swollen state. To measure the applied stretch λ in gauge length, we adopted digital image correlation method and calibrated the correlation between λ and loading distance d at gripping points (Fig. 4-5). A digital microscope (AM4815ZT; Dino-Lite, resolution 20 μm/pixel) was used to record the crack extension. Since dry annealed PVA is transparent when immersing in water, we spread a small amount of graphite powder on the surface of sample for visualization.

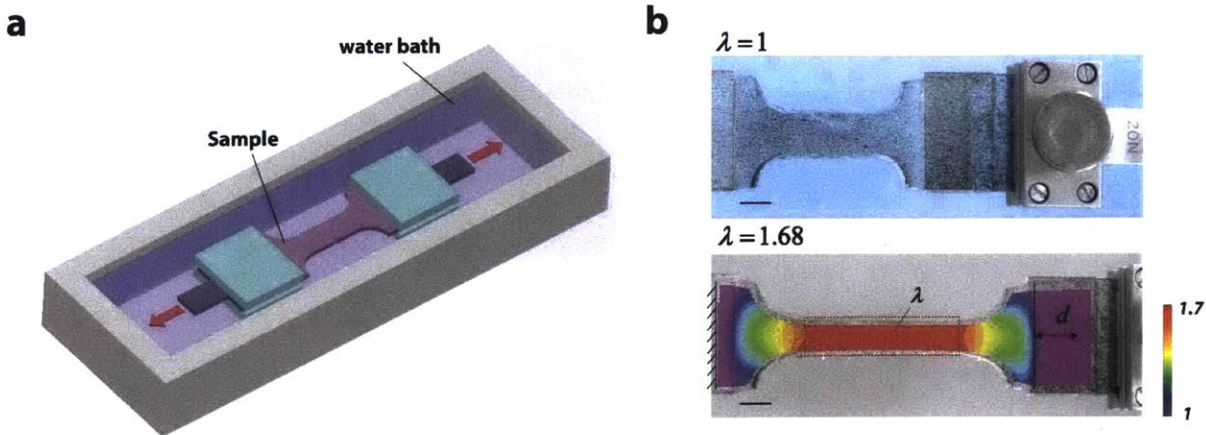


Figure 4-4: Experiment method for measuring fatigue threshold. (a) Schematic illustration of test setup. (b) Digital correlation method for calibration of the correlation between stretch λ in gauge length and applied distance d . Scale bars in b are 5 mm.

4.4 Results

To validate the hypothesis that the increase of crystallinity in hydrogels can significantly enhance their fatigue thresholds, we use PVA hydrogels as a model material system with tunable crystallinity. We first freeze a solution of uncrosslinked PVA at $-20\text{ }^{\circ}\text{C}$ for 8 h and thaw it at $25\text{ }^{\circ}\text{C}$ for 3 h, to form a hydrogel crosslinked by crystalline domains (158). The freeze-thawed PVA hydrogel is further dried in an incubator at $37\text{ }^{\circ}\text{C}$ and then annealed at $100\text{ }^{\circ}\text{C}$ for various times ranging from 0 min to 90 min (159). (The hydrogel dry-annealed for 0 min means no annealing process.) The crystallinity of the hydrogel can be tuned by drying and annealing it with different times. As a control sample, we also fabricate a chemically-crosslinked PVA as a reference hydrogel containing an amorphous polymer network (See Materials and Methods in section 4.2).

4.4.1 Characterization of the crystalline morphology in PVA Hydrogels

We first measure the crystallinities of the resultant PVA hydrogels in their dry state by differential scanning calorimetry (DSC). For the chemically-crosslinked and free-thawed PVA hydrogels, we use excessive chemical crosslinks to fix the amorphous polymer chains before air-drying them in

an incubator at 37 °C (see Materials and Methods for details). The excessive chemical crosslinks minimize the formation of further crystalline domains during air-drying process (157, 160). As shown in Fig. 4-5a, both the chemically-crosslinked and freeze-thawed PVA hydrogels show negligible endotherm peaks with the measured crystallinities in the dry state of 0.2 wt.% and 2.1 wt.%, respectively. However, when the freeze-thawed PVA (without excessive chemical crosslinks) is dried in air, the crystallinity in the dry state increases to 37.7 wt.% (see Fig. 4-5a). The increase of the crystallinity implies that substantially more crystalline domains nucleate during the air-drying process (159). The crystallinity further increases gradually by increasing the annealing time. When the sample is annealed for 90 min at 100 °C, the crystallinity in the dry state reaches 47.3 wt.%. In addition to the crystallinities in the dry state measured from DSC, we further measure the water contents in the fully swollen samples shown in Fig. 4-5b and calculate the corresponding crystallinities in the swollen state shown in Fig. 4-5c. It is well-known that the as-prepared dry PVA samples may contain residual water bonded with polymer chains (157). The amount of residual water can be calculated from the endothermic transition ranging from 60 °C to 180 °C on the DSC curves (158). The above reported crystallinities in the dry state (without residual water), water contents and crystallinities in the swollen state have been corrected to account for the weights of residual water in the as-prepared dry samples (see Materials and methods in section 4.2, Table 4.1 and Fig. 4-3 for details).

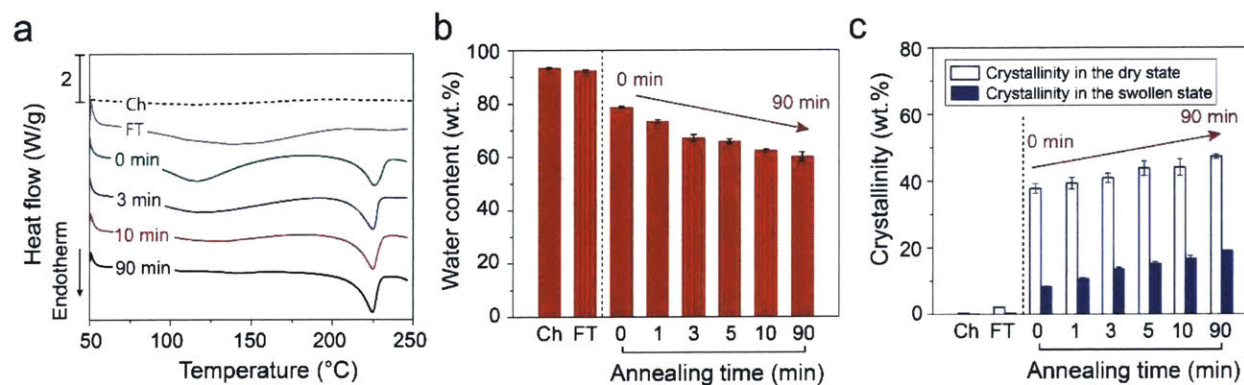


Figure 4-5: (a) Representative DSC thermographs of chemically-crosslinked (Ch), freeze-thawed (FT) and dry-annealed PVA with annealing time of 0, 3, 10, 90 min. (b) Water contents of chemically-crosslinked (Ch), freeze-thawed (FT) and dry-annealed PVA with annealing time of 0, 1, 3, 5, 10, 90 min. (c) Measured crystallinity in the dry and swollen states of Ch, FT and dry-annealed PVA with annealing time of 0, 1, 3, 5, 10, 90 min.

Table 4.1: Crystallinities and water contents in chemically-crosslinked (Ch), freeze-thawed (FT) and dry-annealed PVA with annealing time of 0, 1, 3, 5, 10, 90 min.

Sample name	Crystallinity in the dry state without residual water (wt. %)	Water content in the swollen state (wt. %)	Crystallinity in the swollen state (wt. %)
Ch	0.23±0.16	93.4±0.2	0.02±0.01
FT	2.1±0.2	92.2±0.5	0.16±0.02
0 min	37.7±1.4	78.6±0.4	8.1±0.3
1 min	39.3±1.7	73.3±3.5	10.5±0.5
3 min	40.9±1.4	66.9±1.3	13.5±0.5
5 min	43.8±2.2	65.8±0.9	15.0±0.8
10 min	44.1±2.4	62.2±2.6	16.6±0.9
90 min	47.3±0.6	59.9±1.7	18.9±0.2

To quantify the evolution of crystalline morphology, we measure the average distance between adjacent crystalline domains L through small-angle X-ray scattering (SAXS) and the average size of crystalline domains D through wide-angle X-ray scattering (WAXS). We first perform SAXS measurements on the samples in the swollen state after subtracting the water background, measuring the scattering intensity $I(q)$ versus the scattering vector q . To identify the location of the peak intensity, we correct the intensity by multiplying the scattering intensity with

the scattering vector q (161). As shown in Fig. 4-6a, there is no peak in the plot of the corrected intensity Iq versus the scattering vector q for the freeze-thawed hydrogel, which implies negligible interference between adjacent crystalline domains. For the hydrogel dry-annealed for 0 min, there is a slight shoulder shown in the corrected intensity curve, which indicates stronger interference between adjacent domains. The average distance between adjacent crystalline domains L can be estimated from the critical vector corresponding to the peak intensity q_{max} , following the Bragg expression $L = 2\pi / q_{max}$ (161). The average distance for the hydrogel dry-annealed for 0 min is estimated to be 21 nm in the swollen state. As the annealing time increases to 90 min, the average distance L decreases to 13 nm in the swollen state (Fig. 4-6d). As a control case, we also measure SAXS profiles of the hydrogel dry-annealed 90 min in the dry state. As shown in Fig. 4-6c, the average distance between adjacent crystalline domains in the dry state is around 9 nm, smaller than the distance in the same hydrogel in the swollen state (i.e., 13 nm). This is because swelling of the interstitial amorphous polymer chains increases the distance between adjacent crystalline domains.

We further perform WAXS measurements on the hydrogels in their dry state using Ni-filtered $\text{CuK}\alpha 1$ radiation with X-ray wavelength $\lambda^* = 1.54 \text{ \AA}$. As shown in Fig. 4-6b, all dry-annealed PVA hydrogels show a strong diffraction peak at $2\theta = 19.7^\circ$, which corresponds to the typical reflection plane of $(10\bar{1})$ in semi-crystalline PVA (162). In addition, small peaks at $2\theta = 11.5^\circ$ and 23.1° are also observed in the hydrogel dry-annealed for 90 min, suggesting a high crystallinity in the hydrogel, which is consistent with the DSC measurement. By identifying the half-width of the maximum diffraction peak $\bar{\beta}$, the average size of crystalline domains D can be approximately calculated using Scherrer's equation $D = k^* \lambda^* / (\bar{\beta} \cos \theta^*)$ (163), where k^* is a dimensionless shape factor varying with the actual shape of the crystalline domain; λ^* is the

wavelength of X-ray diffraction; and θ^* is the Bragg angle. Here, $\bar{\beta}$ is identified after subtracting the instrumental line broadening; and the dimensionless shape factor k^* is set as 1, approximating the spherical shape of the crystalline domains (164). As shown in Fig. 4-6d, by increasing the annealing time from 0 min to 90 min, the average size of the crystalline domains increases from 3.8 nm to 6.5 nm. This trend is consistent with the decrease of the average distance between adjacent crystalline domains with annealing time, since the growth of the crystalline domains consumes the interstitial amorphous polymer chains.

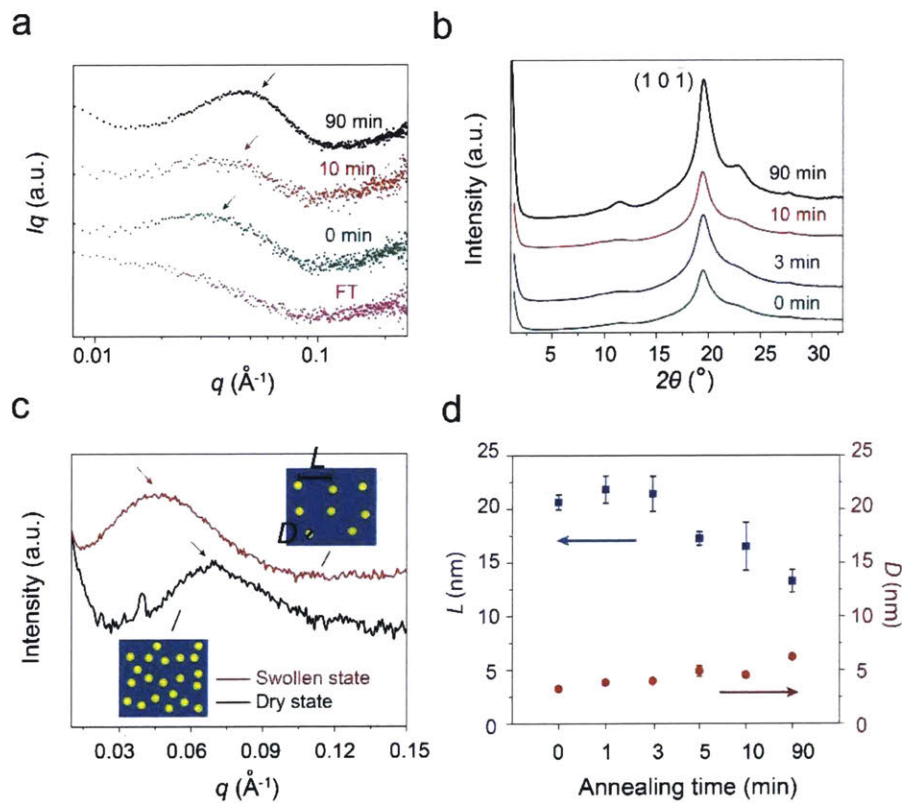


Figure 4-6: (a) Representative SAXS profiles of FT hydrogel and dry-annealed PVA with annealing time of 0, 10, and 90 min. (b) Representative WAXS profiles of annealed PVA with annealing time of 0, 3, 10, and 90 min. (c) SAXS profiles of 90-min dry-annealed PVA in the dry state and the swollen state. The insets illustrate the increase of the distance between adjacent crystalline domains due to swelling of amorphous polymer chains. (d) The estimated average distance between adjacent crystalline domains L and average crystalline domain size D of dry-annealed PVA with annealing time of 0, 1, 3, 5, 10, 90 min. Data in (d) are means \pm SD, $n = 3$.

To further validate the tuning of crystalline domains in the PVA hydrogel with annealing time, we use tapping-mode atomic force microscopy (AFM) to obtain phase images of the hydrogels dry-annealed for 0 min and 90 min, respectively. The bright areas in Fig. 4-7 correspond to the regions with relatively high modulus (mainly crystalline domains), whereas the dark areas represent the regions with relatively low modulus (mainly amorphous domains). As shown in Fig. 4-7, the morphology of isolated crystalline domains is observed in the hydrogel dry-annealed for 0 min, while the hydrogel dry-annealed for 90 min shows larger aggregated crystalline domains.

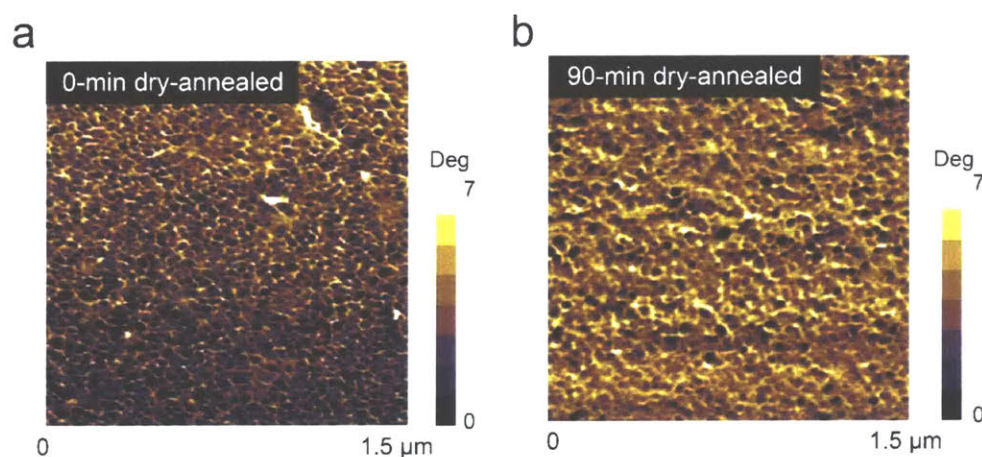


Figure 4-7: (a) AFM phase images of dry-annealed hydrogel with annealing time of 0 min. (b) AFM phase images of dry-annealed hydrogel with annealing time of 90 min.

4.4.2 Characterization of fatigue properties of PVA hydrogels

We adopt the single-notch method to measure the fatigue threshold of PVA hydrogels (155, 156) (Fig. 4-2). For cyclic tensile tests on unnotched samples (Fig. 4-8), both chemically-crosslinked PVA and freeze-thawed PVA show negligible Mullins effect, and their S vs. λ curves reach steady states after only a few cycles (i.e., 10 for chemically-crosslinked PVA at an applied stretch of 1.6, and 200 for freeze-thawed PVA at an applied stretch of 2.2). On the other hand, the dry-annealed PVA hydrogels exhibit a more significant Mullins effect, due to mechanical dissipation

caused by melting and reorientation of crystalline domains (161). As the stretch further increases, the crystalline domains may transform into aligned fibrils along the loading direction (161). The energy required to damage the crystalline domains and fibrils is much higher than that to fracture a single layer of the same polymer in amorphous state. The hydrogel dry-annealed 90 min reaches steady state after 1,000 cycles of applied stretches of $\lambda^A = 2$ (Fig. 4-8, c and f). Despite the Mullins effect, the steady-state maximum nominal stress of the hydrogel dry-annealed for 90 min is much higher than that of both the chemically-crosslinked PVA and the freeze-thawed PVA at the same applied stretch of $\lambda^A = 2$ (e.g., 2.3 MPa for hydrogel dry-annealed 90 min, 15 kPa for chemically-crosslinked PVA, and 3 kPa for freeze-thawed PVA in Fig. 4-8, d-f).

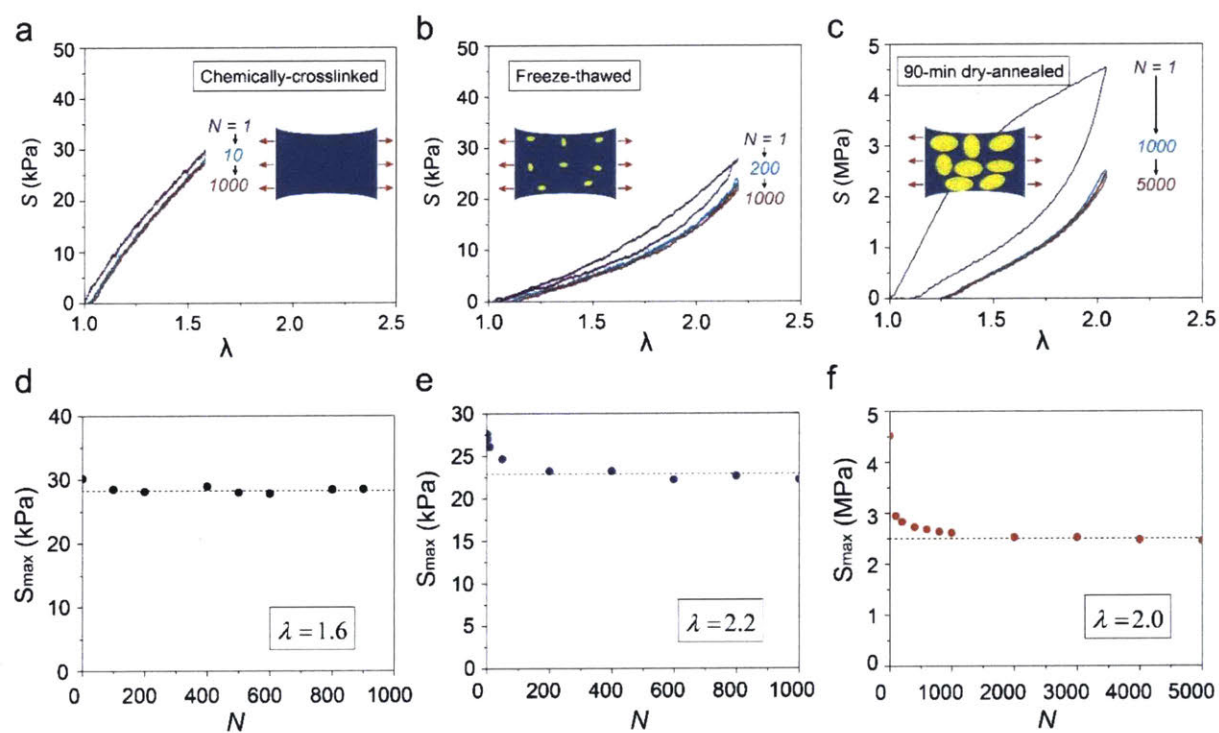


Figure 4-8: Shakedown softening and stress versus stretch curves of three types of PVA hydrogels. Nominal stress S vs. stretch λ curves over cyclic loads for (a) chemically-crosslinked hydrogel at an applied stretch of $\lambda^A = 1.6$, (b) freeze-thawed hydrogel at an applied stretch of $\lambda^A = 2.2$, and (c) 90-min dry-annealed hydrogel at an applied stretch of $\lambda^A = 2.0$. (d) Maximum stress at the stretch of 1.6 versus cycle number of chemically-crosslinked hydrogel, (e) Maximum stress at the stretch of 2.2 versus cycle number of chemically-crosslinked hydrogel, and (f) Maximum stress at the stretch of 2.0 versus cycle number of 90-min dry-annealed hydrogel.

of freeze-thawed PVA. (f) Maximum stress at the stretch of 2.0 versus cycle number of 90-min dry-annealed PVA.

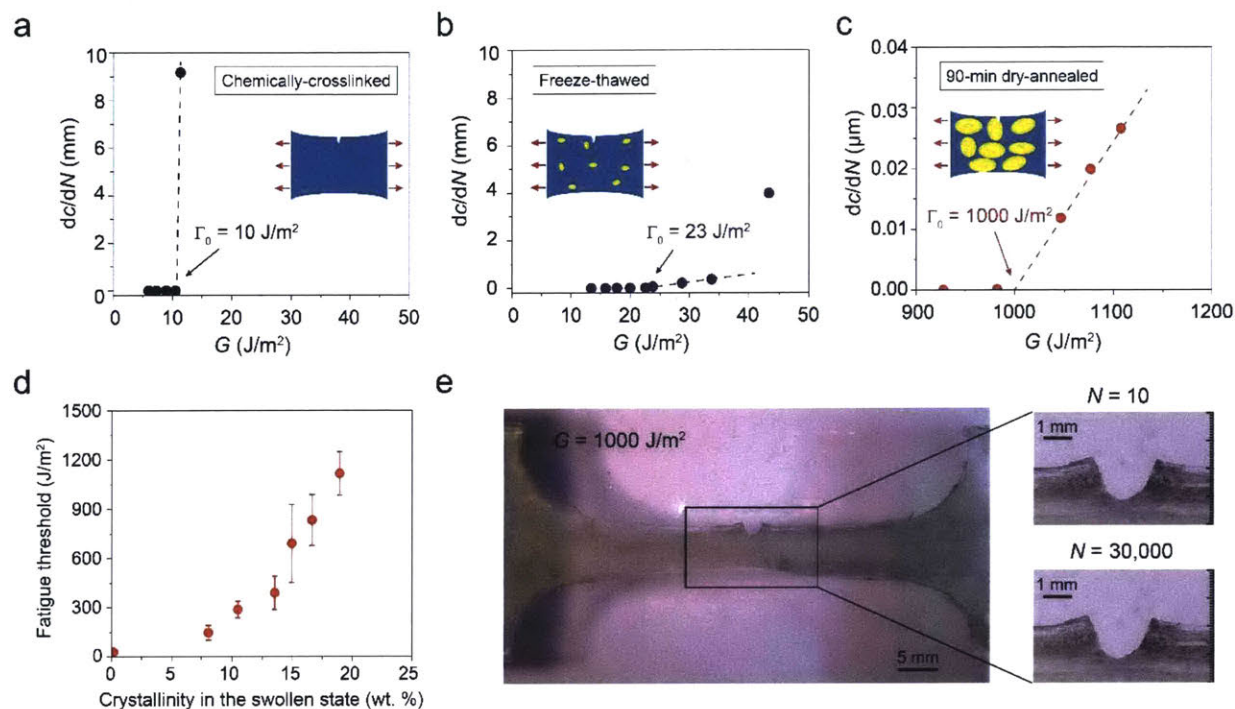


Figure 4-9: Measurement of fatigue thresholds of PVA hydrogels. Crack extension per cycle dc/dN vs. applied energy release rate G for (a) chemically-crosslinked hydrogel, (b) freeze-thawed hydrogel, and (c) dry-annealed hydrogel with annealing time of 90 min. (d) The fatigue threshold increases with the crystallinity of the hydrogel in the swollen state. (e) Validation of fatigue threshold as high as 1000 J/m^2 in 90-min dry-annealed hydrogel using the single-notch test. Data in d are means \pm SD, $n = 3$. Scale bars are 5 mm and 1 mm for left and right images in (e).

For cyclic tensile tests on notched samples, a pre-crack is cut using a razor blade with tip radius of around $200 \mu\text{m}$ and initial crack length around 1 mm, smaller than one-fifth of the width of the sample (155). A digital microscope (AM4815ZT, Dino-Lite, resolution $20 \mu\text{m}/\text{pixel}$) is used to record the cut length under cyclic loads. We first apply cyclic loads with a small applied stretch (i.e., $\lambda^A = 1.3$) on a notched sample. If the crack remains quasi-stationary with crack extension per cycle (dc/dN) smaller than $20 \text{ nm}/\text{cycle}$ (i.e., no detectable crack extension in 1,000 cycles), the applied cyclic stretch is increased by the increment of $\Delta\lambda^A = 0.1$ for other notched samples until crack propagation greater than $20 \text{ nm}/\text{cycle}$ is captured. As shown in Fig. 4-9, a and b, the fatigue thresholds of chemically-crosslinked PVA and freeze-thawed PVA are measured to be 10 J/m^2 and 23 J/m^2 , respectively. The fatigue threshold for the hydrogel dry-annealed 0 min increases

to 110 J/m^2 . As the annealing time increases, the fatigue threshold further increases. In particular, for the hydrogel dry-annealed 90 min, the fatigue threshold can achieve 1000 J/m^2 (Fig. 4-9c). The measured fatigue threshold of the hydrogel dry-annealed 90 min from the pure-shear test is 918 J/m^2 , consistent with the single-notch test (Fig. 4-10). The dependence of fatigue threshold on the crystallinity is summarized in Fig. 4-9d. The fatigue threshold increases with the crystallinity and demonstrates a sharp jump when the crystallinity in the swollen state reaches approximate 15 wt.%.

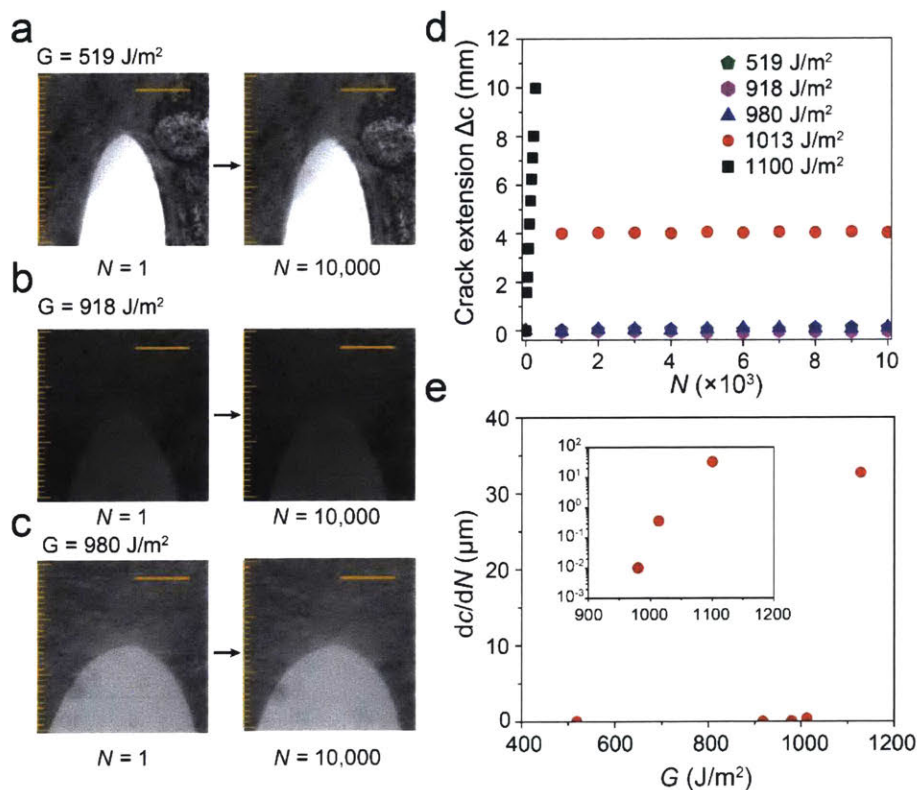


Figure 4-10: Validation of high fatigue threshold with pure shear test. Images of the notched sample for 90-min dry-annealed PVA at the 1st cycle and 10,000th cycle under the applied energy release rates of (a) 519 J/m^2 , (b) 918 J/m^2 and (c) 980 J/m^2 . (d) Crack extension Δc versus cycle number N under the applied energy release rates of 519, 918, 980, 1013 and 1100 J/m^2 . (e) Crack extension per cycle dc/dN the applied energy release rate G in linear scale. The inset plot shows the same dc/dN for the applied energy release rates of 980, 1013 and 1100 J/m^2 in log scale. Under the energy release rate of 519 and 918 J/m^2 , no crack extension can be observed over 10,000 cycles under a microscope with pixel resolution of $20 \mu\text{m}$. Under the energy release rate of 980, 1013 and 1100 J/m^2 , the crack extension per cycle is 0.01, 0.36 and $32 \mu\text{m}$ per cycle, respectively. Scale bars in (a), (b), and (c) are 1 mm.

In addition to fatigue tests, we also measure the nominal stress versus stretch curves of all hydrogels to obtain their Young's moduli and tensile strengths (Fig. 4-11, a and b). As shown in

Fig. 4-11, d and e, both the Young's modulus and tensile strength increase with the hydrogels' crystallinity and show dramatic enhancements when the crystallinity in the swollen state reaches approximate 15 wt.% (165). This sharp jump in Young's modulus and tensile strength is consistent with the dramatic increase of fatigue threshold of the hydrogel at approximate 15 wt.% crystallinity in the swollen state (Fig. 4-9e).

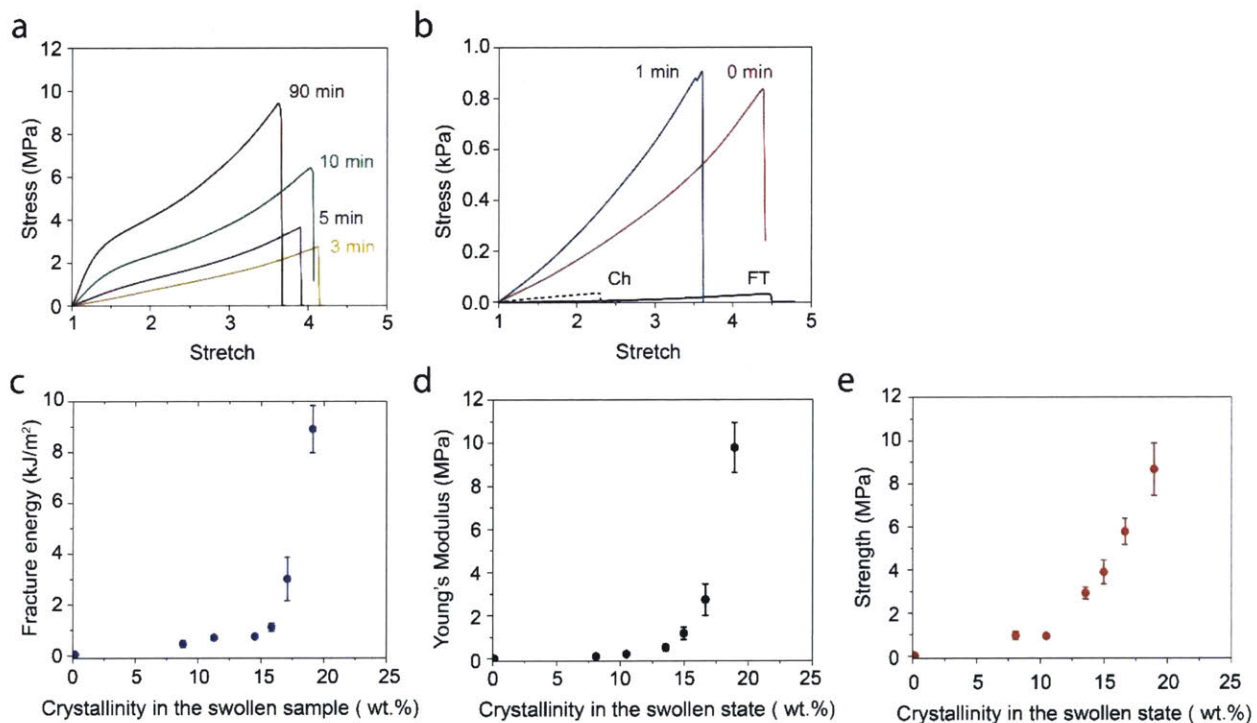


Figure 4-11: Mechanical characterization of PVA hydrogels with various crystallinities. (a) Nominal stress vs. stretch curves of dry-annealed PVA with annealing time of 3, 5, 10 and 90 min. (b) Nominal stress vs. stretch curves of chemically crosslinked PVA, freeze-thawed PVA and dry-annealed PVA with annealing time of 0 and 1 min. (c) Fracture energy versus crystallinity in the swollen state. (d) Young's modulus versus crystallinity in the swollen state. (e) Tensile strength versus crystallinity in the swollen state. Data in (c), (d) and (e) are means \pm SD, $n = 3$.

4.5 Concluding remarks

We have discovered that the fatigue threshold of hydrogels can be greatly enhanced by designing crystalline domains in the hydrogels. We have used PVA hydrogels as a model material to validate

this new mechanism for designing anti-fatigue-fracture hydrogels. The fatigue threshold of a PVA hydrogel with the crystallinity of 18.9 wt.% in the swollen state can achieve over 1000 J/m². The capability to enhance anti-fatigue performances of synthetic hydrogels can potentially make a number of future research directions and applications possible such as hydrogel-based gastric-retentive devices, implantable tissue replacements of meniscus, and intervertebral disk and cartilage, demanding long-term mechanical robustness when interacting with human body.

Chapter 5

Design of muscle-like hydrogels

5.1 Introduction

Biological load-bearing tissues such as skeletal muscles commonly show J-shaped stress-strain behaviors with low Young's moduli and high strengths on the order of 100 kPa and 1 MPa, respectively (166, 167). Moreover, despite their high water contents over 75 wt% (2), skeletal muscles can sustain a high stress of 1 MPa over 1 million cycles per year, with a fatigue resistance over 1000 J/m² (22). The combinational properties of skeletal muscles (i.e., high fatigue resistances, high strengths, superior compliances, and high water contents) are highly desirable for hydrogels' nascent applications in soft biological devices, such as load bearing artificial tissues (168), hydrogel bioelectronics (169-172), hydrogel optical fibers (173, 174), ingestible hydrogel devices (175), robust hydrogel coatings on medical devices (42, 148, 176-178), and hydrogel soft robots (147, 179, 180).

Although various molecular and macromolecular engineering approaches have replicated parts of biological muscles' characteristics, none of them can synergistically replicate all these attributes in one single material system (See Table 5.1). For example, both strain-stiffening hydrogels (181, 182) and bottle brush polymer networks (166, 183) can mimic the J-shaped stress-strain behaviors, but their fracture toughnesses are still much lower than biological tissues, since no significant mechanical dissipation has been introduced in these materials for toughness enhancement. Although various tough hydrogels (43, 44) have been developed by incorporating various dissipation mechanisms, they are susceptible to fatigue fracture under repeated mechanical loads, since the resistance to fatigue crack propagation after prolonged repeated mechanical loads is the energy required to fracture a single layer of polymer chains, unaffected by the additional dissipation (115). Recently, introduction of well-controlled nanocrystalline domains (184) has shown to substantially increase a hydrogel's fatigue threshold (i.e., the minimal fracture energy at

which crack propagation occurs under cyclic loads), but the growth of nanocrystalline domains consumes interstitial amorphous polymer chains and therefore increases the Young's modulus and reduces the water content of the hydrogel.

	Strain-stiffening hydrogels	Bottlebrush elastomers	Tough hydrogels	Hydrogel composites	Nanocrystalline hydrogels	Muscle-like hydrogels
E (kPa) Young's modulus	0.01-0.5	1-100	10-100	1000-10,000	1000-10,000	200
W (wt %) Water content	> 99	0	90	60-80	60-70	84
S (kPa) Nominal strength	~ 0.2	10-100	100-1000	1000-10,000	4000-10,000	5200
Γ_c (J/m ²) Fatigue threshold	~ 1	~ 10	50-400	~ 1000	400-1000	1250

Table 5.1: Comparison of combinational properties in various soft materials. Comparison of Young's moduli, water contents, nominal strengths, and fatigue thresholds of strain-stiffening hydrogels (181, 182), bottlebrush elastomers (166, 183), tough hydrogels (43, 44), hydrogel composites (50, 185), nanocrystalline hydrogels (184), and muscle-like hydrogels in this work (49).

In this chapter, we propose a strategy to achieve the combinational muscle-like properties in synthetic hydrogels via mechanical training for the first time (Fig. 5-1a). Using freeze-thawed polyvinyl alcohol (PVA) hydrogel as a model material, we successfully mimic the aligned nanofibrillar architectures in skeletal muscles (Fig. 5-1b). The developed hydrogels by mechanical training can achieve an extremely high fatigue threshold (1250 J/m²) and tensile strength (5.2 MPa), while maintaining a high water content (84 wt%) and low Young's modulus (200 kPa), reaching combinational muscle-level properties for the first time (154) (Fig. 5-1c). *In situ* confocal microscopy of the hydrogels' fracturing processes reveals that the fatigue resistance mechanism for the hydrogels is the crack pinning by the aligned nanofibrils, which require much higher energy to fracture than the corresponding amorphous polymer chains. *In situ* X-ray scattering of the hydrogels under elongation further reveals that the low Young's moduli of the hydrogels are attributed to the stretching of polymer chains, orientation of nanocrystalline domains and sliding of aligned nanofibrils under moderate stretches.

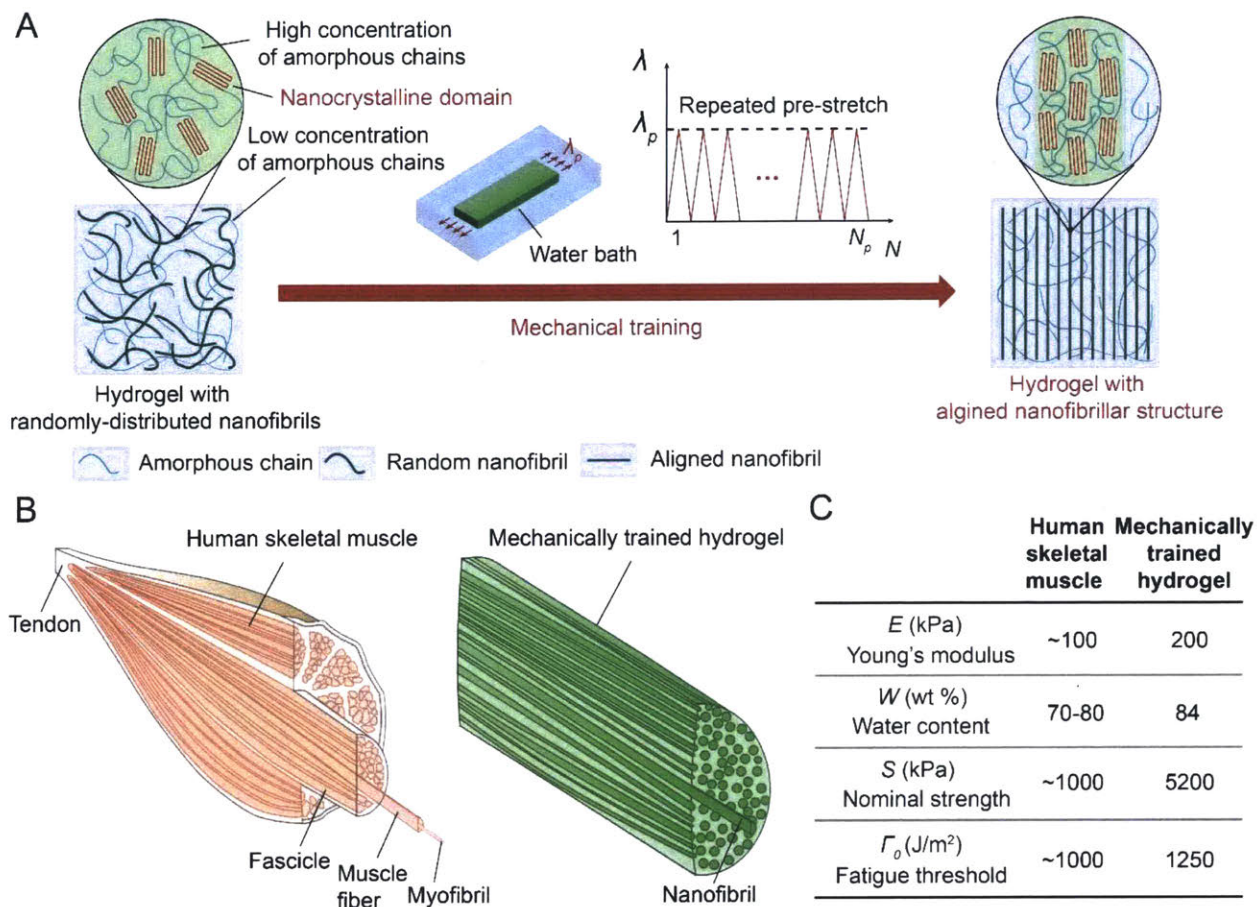


Figure 5-1: Design of muscle-like hydrogels. (a) Schematic illustration of the microstructure of a PVA hydrogel with randomly-oriented nanofibrils before mechanical training and a PVA hydrogel with aligned nanofibrils after mechanical training (i.e., cyclic pre-stretches). (b) Similar aligned nanofibrillar architectures of human skeletal muscles and mechanically trained hydrogels. (c) Comparison of combinational properties of human skeletal muscle and mechanically trained hydrogel.

5.2 Design of muscle-like hydrogels

Figure 5-1a schematically illustrates our strategy to design synthetic hydrogels with combinational properties comparable to skeletal muscles. The strategy first involves growing compliant nanofibrils in PVA hydrogels by forming two separated phases (186): i). high concentration of polymer chains in the form of nanofibrils cross-linked by nanocrystalline domains, and ii). low concentration of amorphous polymer chains. PVA polymer chains possess abundant hydroxyl side groups, which can readily form intra-/inter-chain hydrogen bonding. Upon exposure to a low

temperature below freezing temperature (i.e., $-20\text{ }^{\circ}\text{C}$), the water freezes and forms ice crystals that can expel PVA chains to form regions of high polymer concentrations. As the PVA chains come into close contact with each other, nanocrystalline domains nucleate with the formation of hydrogen bonds (*158, 187, 188*). These interactions (i.e., hydrogen bonding) remain intact in the subsequent thawing process, leading to a physically cross-linked network of nanofibrils. The dendritic growth of ice crystals further leads to a random distribution of these nanofibrils (*189*).

To form the aligned nanofibrillar structures, the pristine freeze-thawed hydrogels with randomly-distributed nanofibrils are exposed to repeated pre-stretches in a water bath as mechanical training, similar to the exercise of skeletal muscles. Under repeated exercise, skeletal muscles get strengthened by self-growing, accompanied by the disruption of the nanofibrillar structures in skeletal muscle and growth of new muscle nanofibrils (*190*). Similarly, repeated pre-stretches applied on the hydrogels with randomly-distributed nanofibrils are accompanied by the disruption of randomly-oriented nanocrystalline domains, followed by gradual alignment of nanofibrils with newly-formed aligned nanocrystalline domains (*191*). One merit of our training strategy is that it does not require any extra supply of building blocks (i.e., monomers) during the mechanical training (*192*).

5.3 Materials and methods

5.3.1 Materials

All PVA hydrogels (i.e., chemically cross-linked, freeze-thawed, and pre-stretched PVA hydrogels) were synthesized from 10 wt% poly(vinyl alcohol) (PVA; Mw 146,000-186,000, 99+% hydrolyzed; Sigma-Aldrich, 363065) solution. The procedure for fabricating freeze-thawed PVA hydrogel is described in Section 4.3.1. The freeze-thawing process was repeated for five cycles. To fabricate the pre-stretched PVA hydrogel, we cyclically pre-stretched the freeze-thawed

hydrogel in a water bath using mechanical stretcher (Cellscale, Canada). The sufficiently aligned nanofibrils were achieved by applying the maximum applied stretch of 4.6 for 1000 cycles.

5.3.2 Confocal imaging of PVA hydrogels in wet state.

To visualize the microstructures of the PVA hydrogels, a fluorescent dye, 5-([4,6-dichlorotriazin-2-yl]amino)fluorescein hydrochloride (5-DTAF), was used to label the PVA side groups (Fig. 5-2a). Specifically, PVA hydrogel samples were first immersed in a large volume of sodium bicarbonate solution (0.1 M, pH 9.0) 12 hours to equilibrate the pH within the samples. 5 mg of 5-DTAF dissolved in 1.0 mL of anhydrous dimethyl sulfoxide (DMSO) was further added into 100 mL of sodium bicarbonate solution (0.1 M, pH 9.0) to form a reactive dye solution. The pH-equilibrated PVA samples were immersed in the dye solution for 12 hours at 4 °C in the dark to form conjugated fluorochromes. Finally, the hydrogel samples were rinsed several times with deionized water to wash away the non-conjugated dyes, prior to fluorescence imaging. The hydrogel microstructures were imaged using a confocal microscope (Leica TCS SP8). Laser intensity, filter sensitivity, and grayscale threshold were adjusted in each application to optimize the contrast of the images. *In situ* fluorescent imaging of the PVA hydrogel samples during uniaxial stretching was conducted using a linear stretcher (Micro Vice Holder, STJ-0116).

5.3.3 X-ray scattering

We investigated nanocrystalline morphologies in nanofibrils of freeze-thawed PVA hydrogels before and after the pre-stretches through small angle X-ray scattering (SAXS). The X-ray scattering measurements were performed with a Pilatus3R 300K detector (Bruker Nanostar SAXS in X-ray diffraction shared experimental facility). The measured scattering intensity I of PVA hydrogels in the swollen state was corrected by subtracting the water background. A customized

linear stretcher was designed to hold the samples at the various stretches for *in situ* X-ray scattering measurements.

5.3.4 SEM imaging

The SEM images were acquired with supercritical-dried samples by a scanning electron microscope (JEOL 5910). We followed the reported experimental protocol to probe the nanoscale structures of the pre-stretched PVA (193). A notched sample was gradually elongated to a stretch of 2 without obvious crack propagation in order to delaminate the fibrils near the notch. The PVA sample was immediately immersed in a 2.5 wt% glutaraldehyde solution for 3 hours to fix the structure, and dehydrated through a series of alcohol solutions in ascending concentration (30, 50, 70, 90, 95, and 100 vol% twice) in order to avoid the non-uniform shrinkage. The dehydrated PVA sample was fractured along the notch using forceps immediately after frozen in liquid nitrogen. The fractured samples were kept in ethanol and dried in a supercritical dryer (Automegasamdri Series C, Tousimis). The dried fracture surfaces were then sputter coated with gold and observed by SEM (JEOL 5910).

5.3.5 AFM phase imaging

AFM phase images were acquired with an atomic force microscope (MFP-3D, Asylum Research) in tapping mode. Dry freestanding PVA films were directly attached onto the sample stage with a double-sided carbon tape. The probe lightly tapped on the sample surface with a recorded phase shift angle of the probe motion relative to a driving oscillator. The bright regions with high phase angles correspond to regions with a relatively high modulus, and the dark regions with low phase angles correspond to regions with a relatively low modulus.

5.3.6 Mechanical characterization

All the mechanical tests were performed in a water bath at 25°C with a U-stretch testing device (CellScale, Canada). For mechanically weak samples (e.g., the chemically cross-linked hydrogel), a load cell with a maximum force of 4.4 N was used; for mechanically strong samples (e.g., the freeze-thawed and pre-stretched PVA hydrogels), a load cell with a maximum force of 44 N was used. The nominal stress S was measured from the recorded force F divided by width W and thickness t in the swollen state. The stretch was calculated by the applied displacement divided by gauge length of the sample at undeformed state. The Young's modulus was calculated from the initial slope of the nominal stress versus stretch curve. The ultimate tensile strength was identified at the maximum nominal stress when the sample ruptures.

To measure the fatigue threshold of PVA hydrogels, we adopted the single-notch method, which was widely used in fatigue tests of rubbers. All fatigue tests in this study were performed on fully swollen hydrogels immersed in a water bath to prevent the dehydration induced crack propagation. Cyclic tensile tests were conducted on notched and unnotched samples with identical dogbone shapes. The initial crack length in notched sample was smaller than one-fifth of the width of the sample. The curves of nominal stress S versus stretch λ of the unnotched samples were obtained over N th cycles with the maximum applied stretch of λ_{\max} . The strain energy density of the unnotched sample under the N th cycle with the maximum applied stretch of λ_{\max} can be calculated as $W(\lambda_{\max}, N) = \int_1^{\lambda_{\max}} S d\lambda$. Thereafter, the same maximum applied stretch λ_{\max} was applied on the notched sample, and we recorded the crack length at undeformed state c over cycles using a digital microscope (AM4815ZT, Dino-Lite; resolution, 20 mm/pixel). The applied energy release rate G in the notched sample under the N th cycle with the maximum applied stretch of λ_{\max} can be calculated as $G(\lambda_{\max}, N) = 2k(\lambda_{\max}) \cdot c(N) \cdot W(\lambda_{\max}, N)$, where k is a slowly varying

function of the applied stretch as $k = 3 / \sqrt{\lambda_{\max}}$. By varying the applied stretch of λ_{\max} , we acquired the curve of crack extension per cycle dc/dN versus the applied energy release rate G . The fatigue threshold can be obtained by linearly extrapolating the curve of dc/dN vs. G to the intercept with the abscissa.

5.3.7 Measurement of water content

We measured the water content in swollen PVA hydrogels using thermal gravimetric analysis (furnace: TGA1-0075, control unit: DCC1-00177). We first cut a disk shape of swollen PVA hydrogels of 3-7 mg. The swollen hydrogels weighing m_{swollen} in a titanium pan without any water droplet on the surface of the samples. The samples were thereafter heated up from 30 °C to 150 °C at the rate of 20 °C/min, and then 150 °C to 160 °C at the rate of 5 °C/min under a nitrogen atmosphere at a flow rate of 30 mL/min. The measured mass of the sample was recorded. In Fig. S7, a typical TGA curve of the pristine freeze-thawed PVA hydrogels is plotted. The mass of the sample decreases with the increase of the temperature and gradually reaches a plateau m_{dry} when the all residual water in the sample evaporates. The water contents of the swollen PVA hydrogels ϕ_{water} were identified by $1 - m_{\text{dry}} / m_{\text{swollen}}$.

5.3.8 Measurement of crystallinities

We measured the crystallinities of the resultant PVA hydrogels by differential scanning calorimetry (DSC/cell: RCS1-3277, cooling system: DSC1-0107), following the experimental protocols in the paper (184). Before air-drying the PVA hydrogels for DSC measurements, we first used excess chemical cross-links to fix the amorphous polymer chains to minimize the further formation of crystalline domains during the air-drying process. Specifically, we soaked the samples (thickness of 1 mm) in the aqueous solution consisting of 10 mL of glutaraldehyde (25

vol%); 500 μ L of hydrochloric acid (36.5 to 38 wt%), and 100 mL of DI water for 1 hour. Thereafter, we soaked the samples in a deionized water bath for 1 hour to remove the extra glutaraldehyde and hydrochloric acid. The samples were further dried in an incubator (New Brunswick Scientific, C25) at 37 °C for 1 hour.

In a typical DSC measurement, we first weighed the total mass of the air-dried sample m (still with residual water). The sample was thereafter placed in a Tzero pan and heated up from 50 °C to 250 °C at the rate of 20 °C/min under a nitrogen atmosphere with flow rate of 30 mL/min. The curve of heat flow shows a broad peak from 60 °C to 180 °C, indicating that the air-dried sample contained a small amount of residual water. The integration of the endothermic transition ranging from 60 °C to 180 °C gives the enthalpy for evaporation of the residual water per unit mass of the dry sample (with residual water) $H_{residual}$. Therefore, the mass of the residual water $m_{residual}$ can be calculated as $m_{residual} = m \cdot H_{residual} / H_{water}^0$, where $H_{water}^0 = 2260$ J/g is the latent heat of water evaporation. The curve of heat flow shows another narrow peak ranging from 200 °C to 250 °C corresponding to melting of the crystalline domains. The integration of the endothermic transition ranging from 200 °C to 250 °C gives the enthalpy for melting the crystalline domains per unit mass of the dry sample (with residual water) $H_{crystalline}$. Therefore, the mass of the crystalline domains $m_{crystalline}$ can be calculated as $m_{crystalline} = m \cdot H_{crystalline} / H_{crystalline}^0$, where $H_{crystalline}^0 = 138.6$ J/g is the enthalpy of fusion of 100 wt.% crystalline PVA measured at the equilibrium melting point T_m^0 (157). Therefore, the crystallinity in the ideally dry sample X_{dry} (without residual water) can be calculated as $X_{dry} = m_{crystalline} / (m - m_{residual})$. With measured water content from TGA, the crystallinity in the swollen state can be calculated as $X_{swollen} = X_{dry} \cdot (1 - \phi_{water})$.

5.4 Random and aligned nanofibrillar structures

We first use the confocal laser scanning microscopy to visualize the nanofibrils in the pristine freeze-thawed PVA hydrogel. Fluorochrome is conjugated to the PVA macromolecules by immersing the freeze-thawed hydrogels in a reactive dye solution (194) (Fig. 5-2a). With the conjugated fluorochromes, the PVA-rich phases are visible in green in the form of randomly-distributed nanofibrils (Fig. 5-3), while regions with relatively low concentrations of PVA polymers (i.e., water-rich phase between adjacent nanofibrils) are dark. As a control, the chemically cross-linked PVA hydrogel shows green luminance with uniform brightness, indicating the uniform distribution of PVA amorphous chains (Fig. 5-2b).

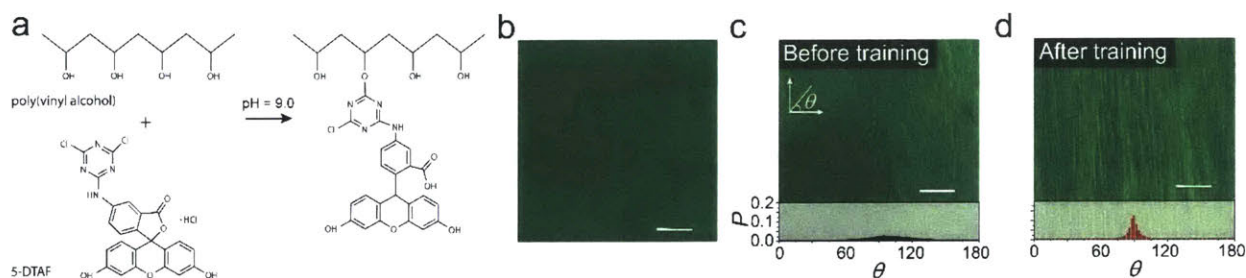


Figure 5-2: (a) The chemical reaction for conjugation of fluorochrome on PVA. (b) Confocal image of chemically cross-linked PVA hydrogel. Confocal images and corresponding histograms of (c) a hydrogel with randomly-oriented nanofibrils before training (i.e., freeze-thawed PVA) and (d) a hydrogel with aligned nanofibrils after training (i.e., pre-stretched PVA). P in the histograms represents the probability of nanofibrils at each aligned direction θ . Scale bars in (b), (c) and (d) are 50 μm .

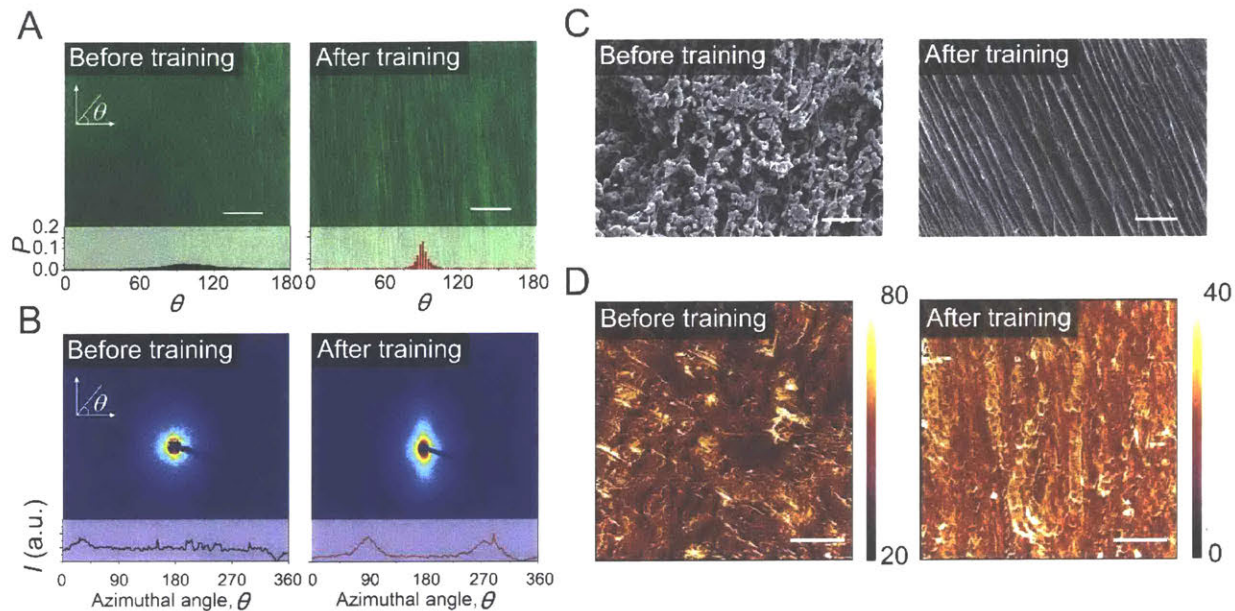


Figure 5-3: Microstructures of PVA hydrogels before and after mechanical training. (a) Confocal images and corresponding histograms of a hydrogel with randomly-oriented nanofibrils before training (i.e., freeze-thawed PVA) and a hydrogel with aligned nanofibrils after training (i.e., pre-stretched PVA). P in the histograms represents the probability of nanofibrils at each aligned direction θ . (b) SAXS patterns and corresponding scattering intensity I vs. Azimuthal angle θ curve of a hydrogel with randomly-oriented nanofibrils before training (i.e., freeze-thawed PVA), and hydrogel with aligned nanofibrils after training (i.e., pre-stretched PVA). a.u., arbitrary units. (c) SEM images of a hydrogel with randomly-oriented nanofibrils before training (i.e., freeze-thawed PVA) and a hydrogel with aligned nanofibrils after training (i.e., pre-stretched PVA). (d) AFM phase images of a hydrogel with randomly-oriented nanofibrils before training (i.e., freeze-thawed PVA) and a hydrogel with aligned nanofibrils after training (i.e., pre-stretched PVA). Scale bars are 50 μm in (a), 20 μm for left image in (c), 10 μm for right image in (c), and 100 nm in (d).

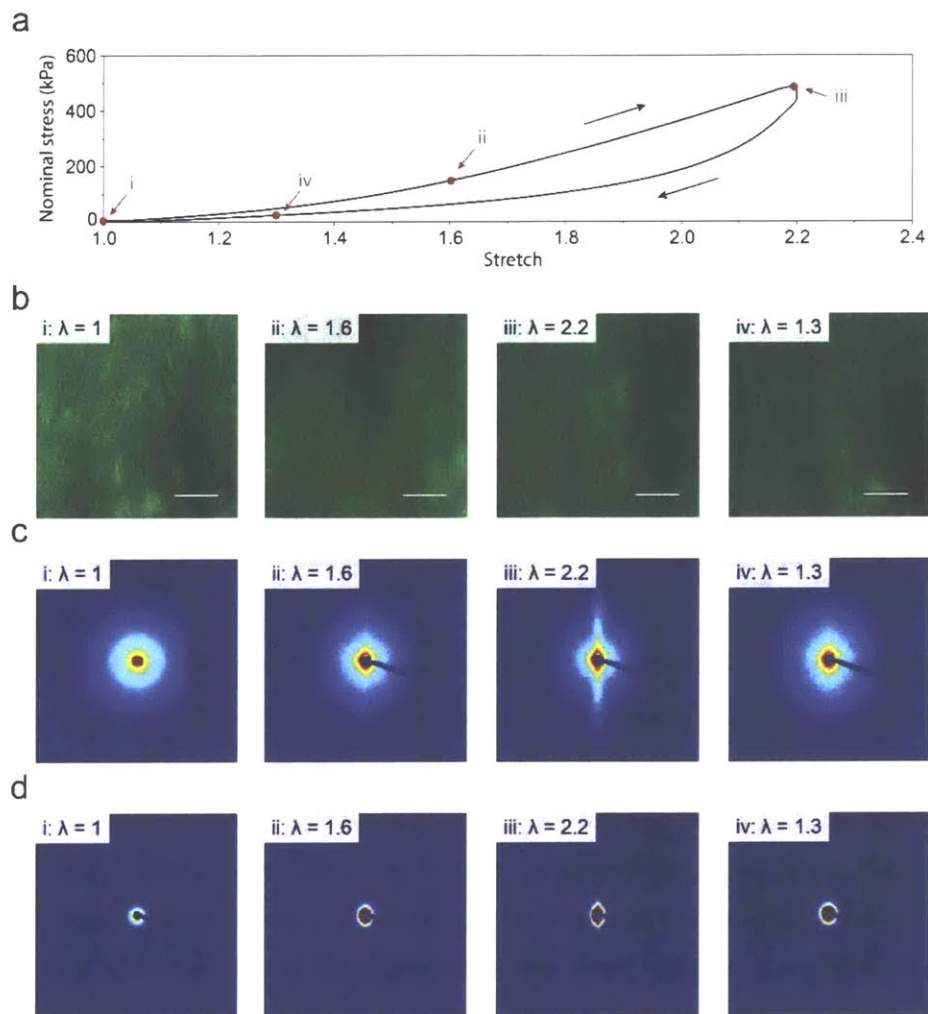


Figure 5-4: Confocal images, SAXS, and WAXS patterns of the freeze-thawed PVA hydrogel under a single cycle of load. (a) Representative stress vs. stretch curve of the freeze-thawed PVA hydrogel. (b) Confocal images, (c) SAXS patterns, and (d) WAXS patterns of the freeze-thawed PVA hydrogel at the applied stretch of i: $\lambda = 1$, ii: $\lambda = 1.6$, iii: $\lambda = 2.2$ under loading and at the applied stretch of iv: $\lambda = 1.3$ under unloading. Scale bars in (b) are 250 μm .

We next show that the freeze-thawed PVA hydrogel can form aligned nanofibrillar structures by repeated pre-stretches in a water bath (Fig. 5-3a and Fig. 5-4). The confocal images of the pre-stretched PVA hydrogel in Fig. 5-3a and Fig. 5-4 confirm that the randomly-distributed nanofibrils gradually reorient and align towards the direction of the applied pre-stretches. It is noted that once the first cycle of pre-stretch is relaxed, the aligned nanofibrils mostly recover their

previous random distribution elastically (See Fig. 5-4). As the cycle number increases, plastic deformation accumulates in the hydrogel, which gradually elongates along the pre-stretched direction, and finally preserves the alignment (See Fig. 5-5). The alignment of nanofibrils reaches a steady state after sufficient cycles of pre-stretches (i.e., 1000 cycles of pre-stretches of 4.6). The alignment of the nanofibrils in the pre-stretched PVA hydrogels is also validated through scanning electron microscopy (SEM) images (Fig. 5-3c) and atomic force microscopy (AFM) phase images (Fig. 4-3d). Small angle X-ray scattering (SAXS) patterns (Fig. 5-3b) further reveal that the nanocrystalline domains in nanofibrils have been reoriented during the pre-stretches. In addition, the measured diameters of the nanofibrils range from ~ 200 nm to ~ 1 μ m (See Fig. 5-6 and Fig. 5-3, a and c).

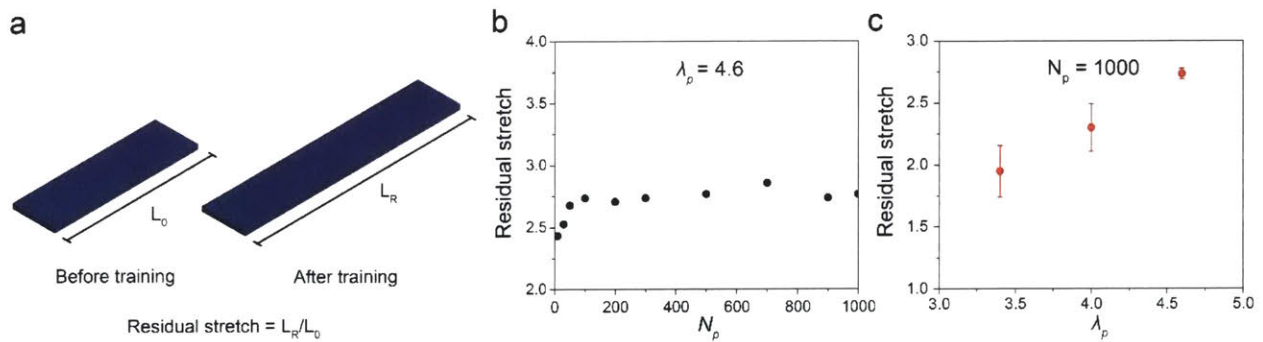


Figure 5-5: Residual stretch of prestretched PVA hydrogels. (a) The residual stretch is defined as the ratio of the length at undeformed state after training L_R over the length at undeformed state before training L_0 . (b) Residual stretch after N_p cycles of applied prestretches of 4.6. (c) Residual plastic stretch after 1000 cycles of prestretches of λ_p .

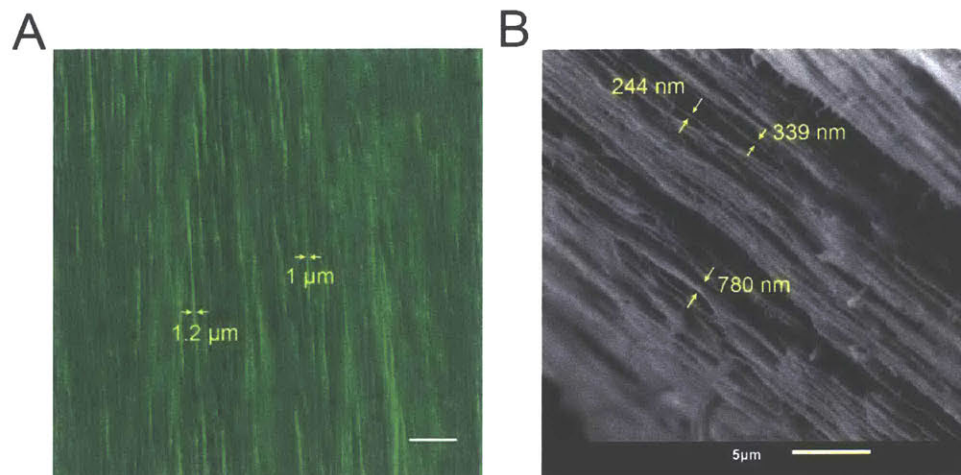


Figure 5-6: Measurement of nanofibril diameters in the pre-stretched PVA hydrogel. (a) Confocal image. (b) SEM image. The sample for SEM imaging was first mechanically stretched to induce delamination of nanofibrils, and immediately crosslinked by glutaraldehyde to avoid further collapse during supercritical drying, followed by SEM observation. The measured diameters of aligned nanofibrils in the hydrogel range from ~ 200 nm to ~ 1 μm . Scar bar is 20 μm in (a) and 5 μm in (b).

Existing approaches to introduce ordered nanocrystalline domains and aligned structures in hydrogels include cold-drawing (195), pre-stretching in air (196), and constrained air-drying (197), which fail to retain their original high water contents, due to the formation of additional excessive nanocrystalline domains. By contrast, the pre-stretched PVA hydrogel obtained from our strategy can still maintain a high water content of 84 wt% (Fig. 5-7c), close to the pristine freeze-thawed PVA samples (88 wt%). The differential scanning calorimetry (DSC) results further show that the crystallinity in the swollen state of the pre-stretched PVA hydrogel is only 2.8 wt% (Fig. 5-7b), slightly higher than the pristine freeze-thawed PVA hydrogel (1.8 wt%) (Fig. 5-7c). The slightly increased crystallinity could be attributed to the newly-formed nanocrystalline domains during the nanofibrillar alignments under cyclic pre-stretches (198). Both high water content and low crystallinity in our pre-stretched PVA hydrogel indicate that our strategy could

substantially suppress the undesirable excessive crystallization while maintaining water contents and compliances of the hydrogels.

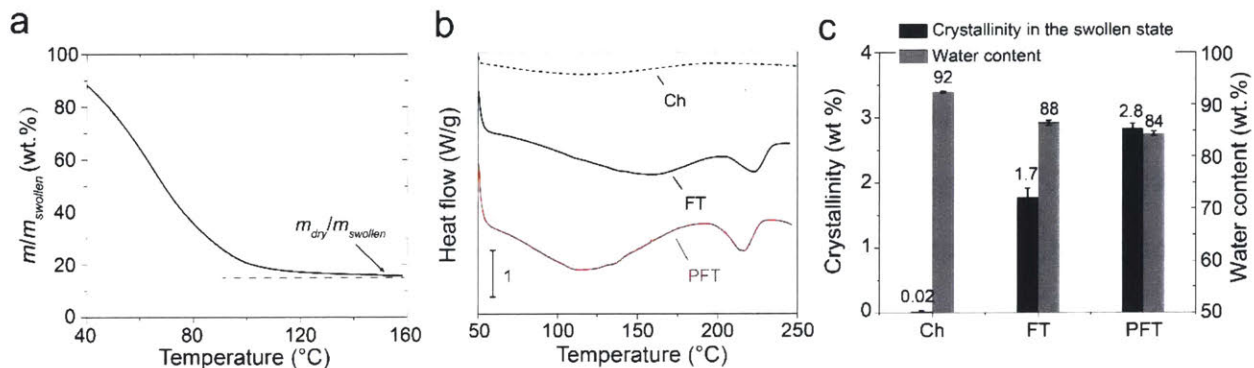


Figure 5-7: (a) Representative thermal gravimetric analysis (TGA) curve of the freeze-thawed PVA hydrogel. m , $m_{swollen}$, and m_{dry} denote the mass of the sample during TGA measurement, in the swollen state, and in fully dry state, respectively. (b) Differential scanning calorimetry (DSC) thermographs of chemically cross-linked (i.e., Ch), freeze-thawed (i.e., FT), and pre-stretched PVA hydrogels (i.e., PFT). (c) Summarized water contents and crystallinities in the swollen state of chemically cross-linked PVA (Ch), freeze-thawed PVA (FT), and pre-stretched PVA (PFT).

5.5 Combinational muscle-like properties

We further demonstrate the combinational muscle-like mechanical properties in the pre-stretched PVA hydrogel (Fig. 5-8). At small stretches, the pre-stretched PVA hydrogel demonstrates a low Young's modulus along directions both parallel (210 kPa) and perpendicular (140 kPa) to the aligned nanofibrils, similar to the pristine freeze-thawed PVA hydrogels (100 kPa) (Fig. 5-8, a and c). At high stretches, the pre-stretched PVA hydrogel stiffens drastically parallel to the aligned nanofibrils, exhibiting a J-shaped stress versus stretch curve, similar to that of skeletal muscles (166). In addition, the pre-stretched PVA hydrogel shows an extremely high ultimate nominal tensile strength of 5.2 MPa parallel to the aligned nanofibrils, which is 4.3 times of the pristine freeze-thawed hydrogel's strength (1.2 MPa) and 26 times of the chemically cross-linked hydrogel's strength (0.2 MPa) (Fig. 5-8, a and c). The ultimate nominal tensile strength of the pre-stretched PVA hydrogel perpendicular to nanofibrils is measured to be 1.1 MPa, close to the value

of the pristine freeze-thawed hydrogel (i.e., 1.2 MPa). The pre-stretched PVA hydrogel also shows high resilience with negligible hysteresis when stretched along the aligned nanofibrils (See Fig. 5-9). The fatigue threshold of the pre-stretched PVA hydrogel measured along the aligned nanofibrils reaches a record-high value of $1,250 \text{ J/m}^2$ (Fig. 5-8b), orders of magnitude higher than those of existing tough hydrogels ($10\sim 100 \text{ J/m}^2$) (78, 80, 199). To validate the high fatigue threshold of the pre-stretched PVA hydrogels parallel to the aligned nanofibrils, we also apply cyclic loads on a single-notch tensile specimen with the energy release rate of 1250 J/m^2 and observe no crack extension over 30,000 cycles (Fig. 5-10). By contrast, the fatigue threshold perpendicular to the aligned nanofibrils is 233 J/m^2 , which is on the same order as that of the pristine freeze-thawed PVA hydrogel (i.e., 310 J/m^2 , Fig. 5-11), but still much larger than that of the chemically cross-linked PVA hydrogel (i.e., 10 J/m^2 , Fig. 5-11). The large difference between the fatigue resistances parallel to and perpendicular to the aligned fibrils manifests the anisotropic fatigue properties in the pre-stretched PVA hydrogel.

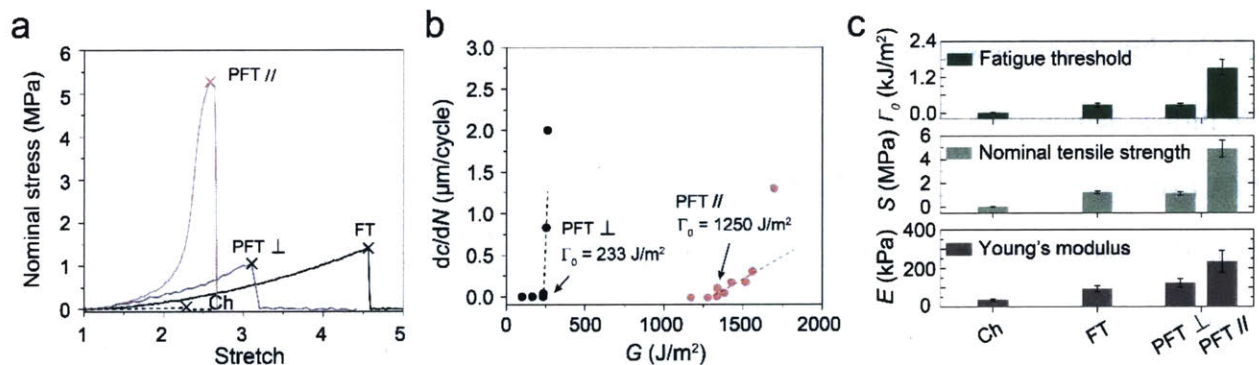


Figure 5-8: Mechanical properties of PVA hydrogels before and after mechanical training. (a) Nominal stress versus stretch curves of chemically cross-linked (Ch), freeze-thawed (FT), and pre-stretched PVA hydrogels parallel to (PFT //) and perpendicular to (PFT ⊥) nanofibrils. The X mark indicates the point of fracture. (b) Crack extension per cycle dc/dN versus applied energy release rate G of pre-stretched PVA hydrogels parallel to (PFT //) and perpendicular to (PFT ⊥) nanofibrils. (c) Summarized Young's moduli E , ultimate nominal tensile strengths S , and fatigue thresholds Γ_0 of chemically cross-linked (Ch), freeze-thawed (FT) and pre-stretched PVA hydrogels parallel to (PFT //) and perpendicular to (PFT ⊥) nanofibrils.

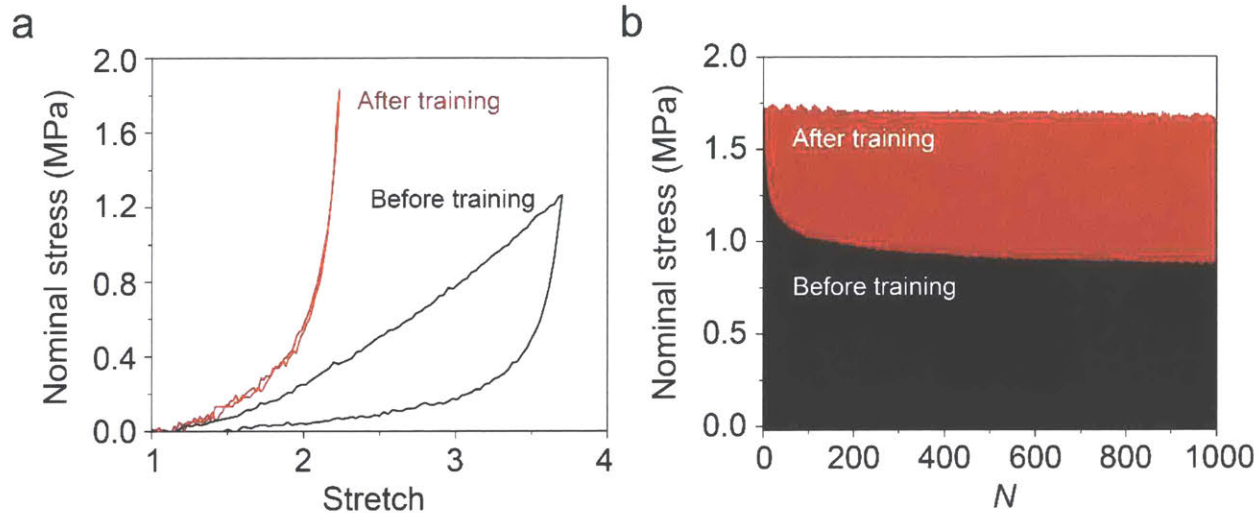


Figure 5-9: Comparison of hysteresis in PVA hydrogels before and after mechanical training. (a) Loading-unloading nominal stress versus stretch curves of PVA hydrogels before and after training. (b) Nominal stress over loading cycles of PVA hydrogels before and after training with maximum applied stretch of 4.5 and 2.2, respectively.

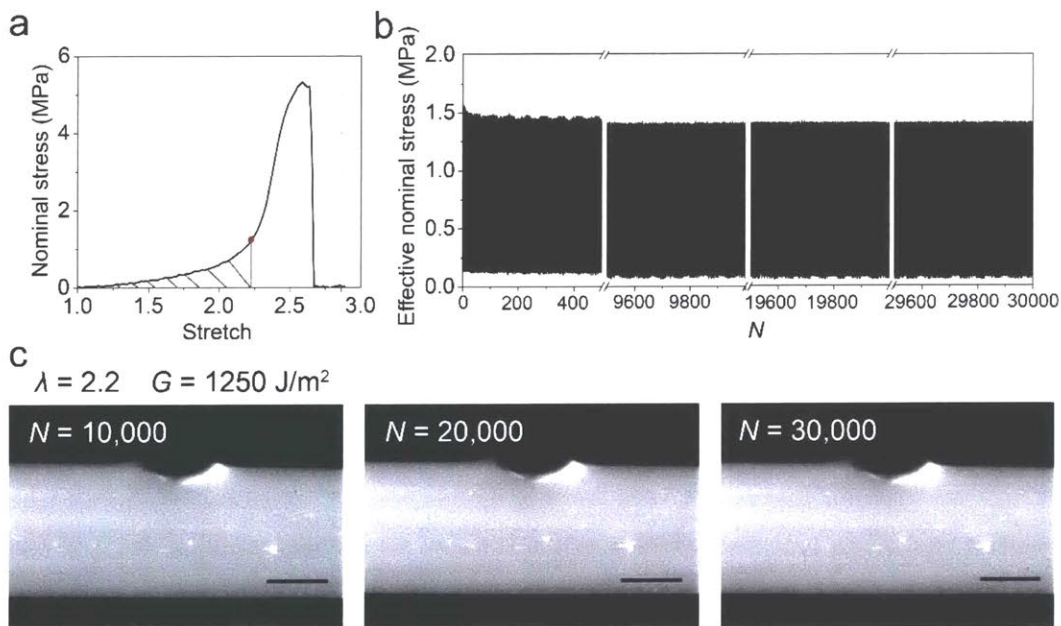


Figure 5-10: Validation of high fatigue threshold of the prestretched PVA hydrogel. (a) Nominal stress versus stretch of the prestretched PVA hydrogel after prolonged cycles of 1000. The enclosed area indicated by red line denotes the strain energy at the applied stretch of 2.2, i.e., $W(\lambda = 2.2) = \int_1^{2.2} Sd\lambda$. (b) The effective nominal stress $F/((W-c)t)$ versus cycle number N of the prestretched PVA hydrogel with a pre-

crack c of 0.7 mm, where F is the measured force, W is the sample width, and t is the sample thickness. (c) Images of prestretched PVA hydrogel with a pre-crack at the applied energy release rate of 1250 J/m^2 at the cycle number of 10,000, 20,000, and 30,000.

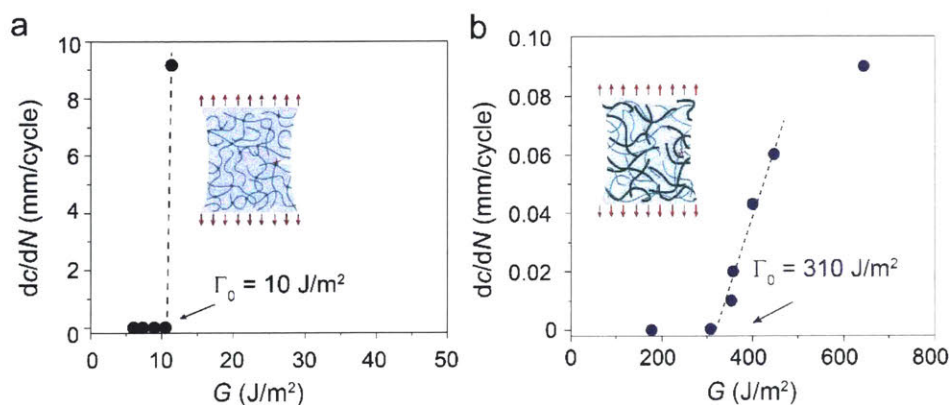


Figure 5-11: Fatigue thresholds of PVA hydrogels. (a) Chemically cross-linked PVA hydrogel. (b) Freeze-thawed PVA hydrogel.

To compare our results with existing hydrogels and biological tissues, we summarize the nominal tensile strengths, Young's moduli, fatigue thresholds, and water contents of various tough hydrogels (43, 44, 62, 110, 184, 200, 201) and biological tissues (166) in Fig. 5-12. The strength-modulus ratios S/E of existing tough hydrogels such as PAAm-alginate (44), PVA-PAAm (110), dry annealed PVA (184), freeze-thawed PVA (202), polyampholyte hydrogels, fiber reinforced hydrogel composites (50, 200), wood hydrogels (201), and constrained air-drying hydrogels (197) are in the range of 0.1 to 10 (Fig. 3E). Remarkably, the strength-modulus ratio S/E of the pre-stretched PVA hydrogel is as high as 50, since the high strength of the pre-stretched PVA hydrogel is accompanied by its low Young's modulus.

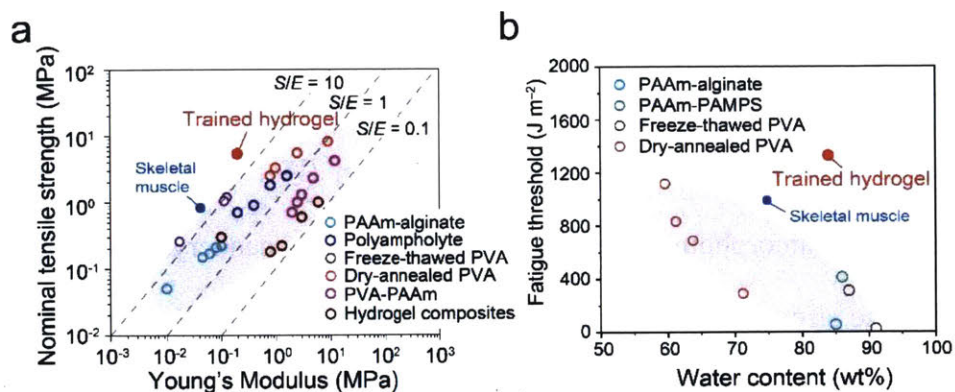


Figure 5-12: (a) Comparison chart in the plot of nominal tensile strength and Young's modulus among tough hydrogels (e.g., PAAm-alginate (44), polyampholyte (62), freeze-thawed PVA (184), dry-annealed PVA (184), PVA-PAAm (110), and hydrogel composites (50)), biological tissues (e.g., skeletal muscle (166, 167)) and trained hydrogel (i.e., pre-stretched PVA). The dashed lines denote the linear relation between strength and modulus with strength-modulus ratio S/E of 0.1, 1, and 10. (b) Comparison chart in the plot of fatigue thresholds and water contents among tough hydrogels (199) (e.g., PAAm-alginate, PAAm-PAMPS, freeze-thawed PVA) and nanocrystalline hydrogels (e.g., dry-annealed PVA) (184), biological tissues (e.g., skeletal muscle), and trained hydrogel (i.e., pre-stretched PVA). Data in (a) and (b) are means \pm SD, $n = 3$.

In addition to the challenge in designing synthetic hydrogels with superior compliances and high strengths, the combinational properties of high fatigue threshold and high water content have not been achieved in existing hydrogels (Fig. 5-12b). By following our strategy, the fatigue threshold of the pre-stretched PVA hydrogel can achieve a high value of $1,250 \text{ J/m}^2$ along with a high water content of 84 wt%, outperforming existing hydrogels and biological tissues.

5.6 Mechanisms for superior compliances.

In situ small angle X-ray scattering (SAXS) measurements offer insights into the mechanism for the superior compliance of the pre-stretched PVA hydrogel at small deformations (Fig. 5-13a). The nanocrystalline morphology in the pre-stretched PVA hydrogel (in the swollen state) is investigated by SAXS analysis at the applied stretch of 1, 1.4, 1.8, and 2.2. As shown in Fig. 5-13, b and d, the average distance between neighboring nanocrystalline domains parallel to aligned

nanofibrils $L//$ (i.e., $\theta = 0^\circ$) for the pre-stretched PVA hydrogel at undeformed state (i.e., $\lambda = 1$) is estimated to be 13.2 nm. As the applied stretch increases to 2.2, the average distance between neighboring nanocrystalline domains increases to 15.5 nm (Fig. 5-13d), which indicates the stretching of interstitial amorphous chains between the adjacent nanocrystalline domains in the nanofibrils. Since the stretch of interstitial amorphous chains (e.g., 15.5 nm/13.2 nm) is much lower than the corresponding applied stretch (e.g., 2.2), sliding between nanofibrils may also occur during stretching. In comparison, the scattering curves show negligible difference at different stretches perpendicular to the aligned nanofibrils $L\perp$ (i.e., $\theta = 90^\circ$) (Fig. 5-13c), which implies the average distance between neighboring nanocrystalline domains perpendicular to the aligned nanofibrils $L\perp$ (i.e., $\theta = 90^\circ$) remains constant with negligible lateral contraction as the stretch increases.

We further plot the scattering intensity I versus direction θ to quantify the degree of orientation of nanocrystalline domains during stretching (Fig. 5-13e). At the undeformed state (i.e., $\lambda = 1$), there are peaks along the pre-stretched direction (i.e., $\theta = 0^\circ$), implying that the orientation of nanocrystalline domains along the pre-stretched direction exists in the undeformed sample. As the applied stretch increases, the peaks along the pre-stretched direction (i.e., $\theta = 0^\circ$) become more pronounced, indicating that the applied stretch can drive additional orientation of nanocrystalline domains. Overall, the stretch of interstitial amorphous chains, orientation of nanocrystalline domains and sliding between nanofibrils account for the superior compliance of the pre-stretched PVA hydrogel at moderate deformations along the aligned nanofibrils.

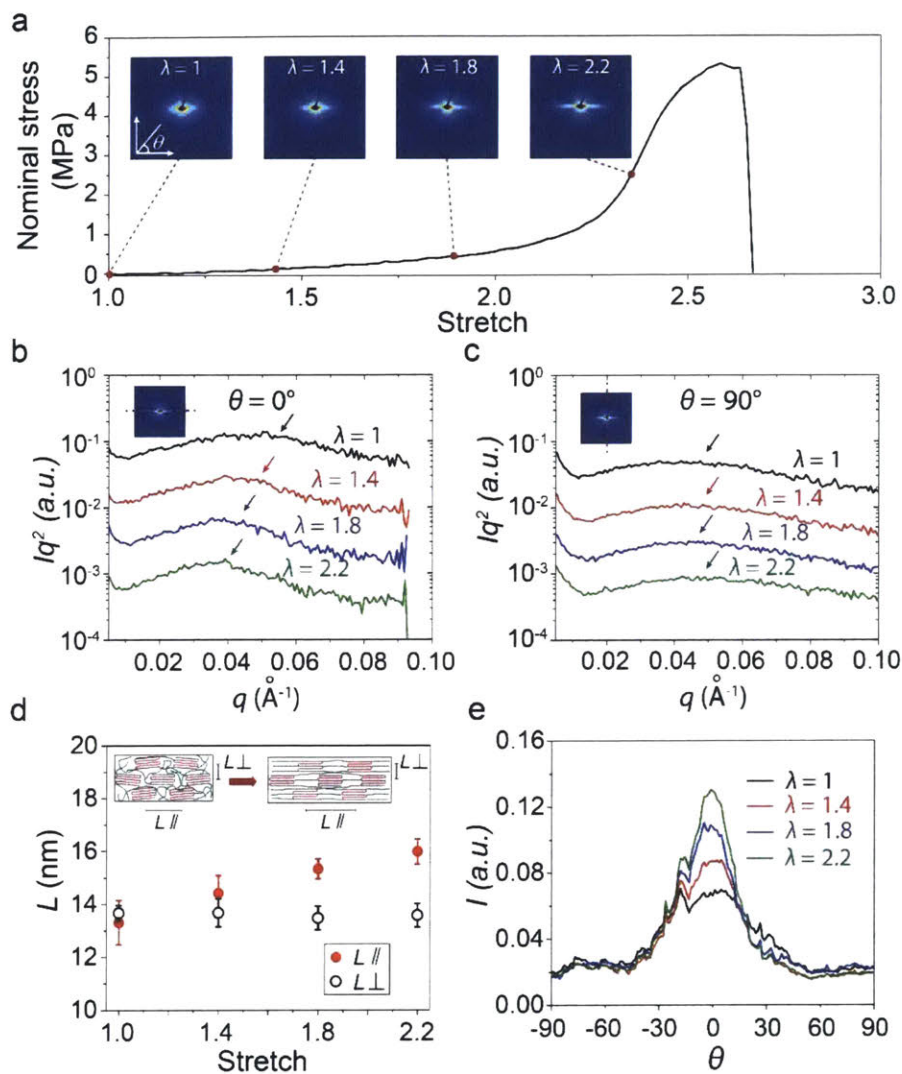


Figure 5-13: Mechanisms for high compliances of pre-stretched PVA hydrogels with aligned nanofibrils. (a) Nominal stress versus stretch curve of pre-stretched PVA hydrogel with aligned nanofibrils and corresponding SAXS pattern at the stretch of 1, 1.4, 1.8, and 2.2. (b) The corrected scattering intensity Iq^2 versus vector q parallel to nanofibrils (i.e., $\theta = 0^\circ$) of pre-stretched PVA hydrogel at the stretch of 1, 1.4, 1.8, and 2.2. (c) The corrected scattering intensity Iq^2 versus vector q perpendicular to nanofibrils (i.e., $\theta = 90^\circ$) of pre-stretched PVA hydrogel at the stretch of 1, 1.4, 1.8, and 2.2. (d) Calculated average distance between adjacent nanocrystalline domains of pre-stretched PVA hydrogel parallel to nanofibrils $L \parallel$ (i.e., $\theta = 0^\circ$) and perpendicular to nanofibrils $L \perp$ (i.e., $\theta = 90^\circ$) at the stretch of 1, 1.4, 1.8, and 2.2. (e) The measured scattering intensity I vs. Azimuthal angle θ curves of pre-stretched PVA hydrogel at the stretch of 1, 1.4, 1.8, and 2.2. a.u., arbitrary units. Data in (d) are means \pm SD, $n = 3$. The dashed red lines in the inset scattering pattern in (b) and (c) indicate the direction parallel to nanofibrils and perpendicular to nanofibrils, respectively.

Furthermore, the high compliances of the pristine freeze-thawed PVA hydrogel and the pre-stretched PVA hydrogel stretched perpendicularly to the aligned nanofibrils can be attributed to the orientation of randomly-distributed nanofibrils and the stretching of amorphous polymer chains between adjacent nanofibrils, respectively.

5.7 Mechanisms for high fatigue thresholds

In situ confocal laser scanning microscopy further explains the mechanism for the high fatigue threshold of the pre-stretched PVA hydrogel. As shown in Fig. 5-14, a and b, the aligned nanofibrils are perpendicular to the crack path and pin the crack due to the high strength of the nanofibrils. There is no observable crack propagation at the applied stretch of 2.4. As the applied stretch further increases to 2.6, the nanofibrils at the crack tip are pulled out from the hydrogel but still bridge the crack tip. As the crack propagates, the rupture of the nanofibrils requires a much higher energy per unit area than fracturing the corresponding amorphous polymer chains, giving rise to a much higher fatigue threshold (1250 J/m^2) than that of the amorphous polymer networks (10 J/m^2). Notably, the crack pinned by the aligned nanofibrils does not branch or tilt under high static and cyclic loads (e.g., Fig. 5-14b and Fig. 5-10), assuring the hydrogel's high fatigue threshold. By contrast, crack branching and tilting has been observed in hydrogels reinforced by microscale phase separation (203) and in elastomers reinforced by macroscale fibers (204). It will be interesting to study the effects of the reinforcements across different length scales in future.

When the crack is parallel to the aligned nanofibrils, the crack begins to propagate in between neighboring nanofibrils at the applied stretch of 1.5, fracturing interstitial amorphous chains between the adjacent nanofibrils (Fig. 5-14, c and d). Similarly, in freeze-thawed PVA hydrogel, the initially randomly-oriented nanofibrils gradually align parallel to the crack contour with the increase of the applied stretch, followed by fracturing interstitial amorphous chains (Fig.

5-14, e and f). In addition, due to the very long amorphous chains between the adjacent nanofibrils (115), the fatigue thresholds of the pristine freeze-thawed PVA hydrogel and the pre-stretched PVA hydrogel with a crack along the aligned nanofibrils are still moderately high (310 J/m² and 233 J/m², respectively).

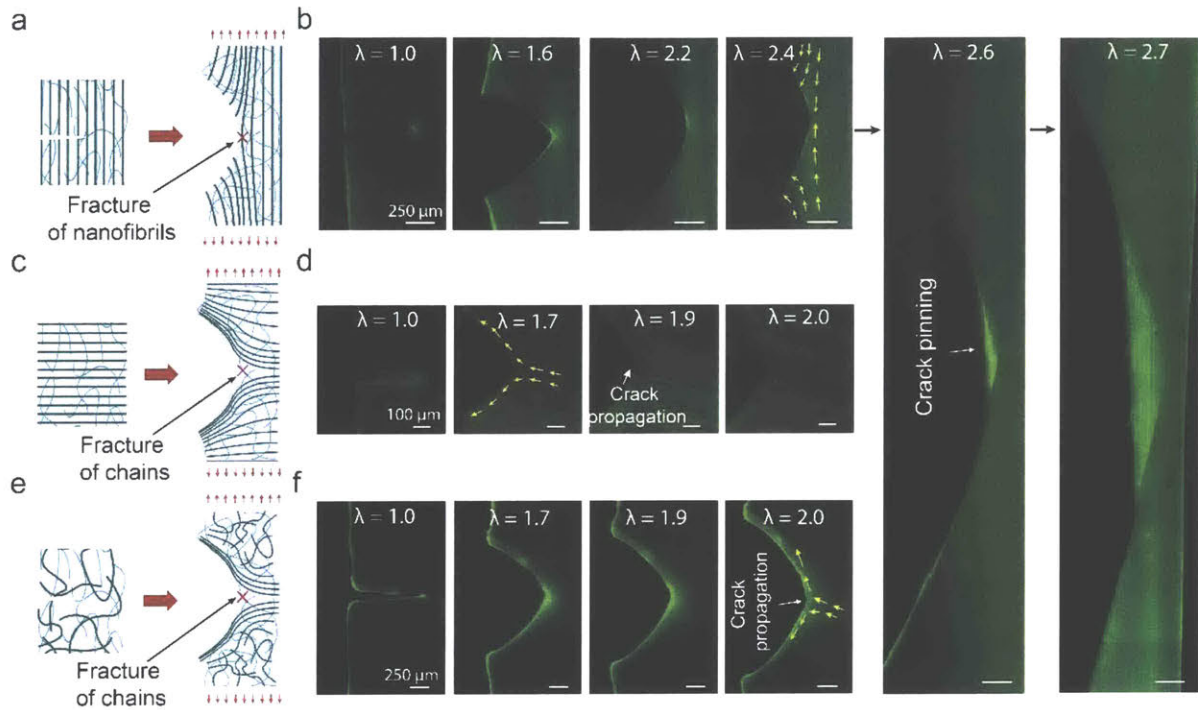


Figure 5-14: Mechanisms for high fatigue thresholds of pre-stretched PVA hydrogels with aligned nanofibrils. Schematic illustration of nanofibril morphology in (a) notched pre-stretched PVA hydrogel where crack is perpendicular to the longitudinal direction of nanofibrils, (c) notched pre-stretched PVA hydrogel where crack is parallel to the longitudinal direction of nanofibrils, and (e) freeze-thawed PVA hydrogel. Corresponding confocal images of notched samples under different stretches for (b) pre-stretched PVA hydrogel where crack is perpendicular to the longitudinal direction of nanofibrils, (d) pre-stretched PVA hydrogel where crack is parallel to the longitudinal direction of nanofibrils, and (f) freeze-thawed PVA hydrogel. The yellow arrows in confocal images indicate the direction of aligned nanofibrils around crack tip. Scale bars are 250 μm in (b), 100 μm in (d), and 250 μm in (f).

5.8 Conclusions

The classical Lake-Thomas model predicts that the fatigue threshold of a polymer network is the energy required to fracture a single layer of amorphous polymer chains, on the order of 1-100 J/m²

(115). We have proposed that the design principle for fatigue-resistant (or anti-fatigue-fracture) hydrogels is to make the fatigue crack encounter and fracture objects requiring energies per unit area much higher than that for fracturing a single layer of amorphous polymer chains (184). We have shown that high densities of nanocrystalline domains in hydrogels can act as the high-energy phase to effectively pin fatigue cracks and greatly enhance the fatigue thresholds of nanocrystalline hydrogels up to 1000 J/m^2 , exceeding the Lake-Thomas limit (184). However, the nanocrystalline domains also significantly increase the Young's moduli of the hydrogels, due to nanocrystalline domains' high rigidity over 1 GPa (184).

While a much higher energy is also required to fracture nanofibrils than the corresponding amorphous polymer chains, the rigidity of nanofibrils under moderate stretches can be designed to be relatively low (205). In this paper, we further establish that aligning these nanofibrils in hydrogels by mechanical training can empower the integration of muscle-like performances, i.e., high fatigue thresholds (1250 J/m^2), high strengths (5.2 MPa), low Young's moduli (200 kPa) and high water contents (84 wt%), into one single hydrogel material. The capability of making strong, fatigue-resistant yet soft hydrogels can enable various biomedical applications that interact with the human body for long-lasting performances. This work also opens a new avenue to mechanically engineer alignments of nanofibrils and orientations of nanocrystalline domains in hydrogels.

Part II

Mechanical instabilities in confined hydrogel layers

Chapter 6

Fringe instability in constrained soft elastic layers

6.1 Introduction

Soft elastic layers constrained between relatively rigid bodies appear in biological glues (206-209), joints (210) and engineering applications including sealants, insulators, bearings, and adhesives (42, 106). When the rigid bodies are pulled apart, the stressed layer can undergo various modes of mechanical instabilities due to a combination of the elastic layer's incompressibility, the mechanical constraints and the applied loads. For example, if the hydrostatic tensile stress in any region of the elastic layer reaches a critical value, a cavity can nucleate and grow in that region, leading to the cavitation instability (95, 100, 106, 211, 212). If the elastic layer partially debonds from the rigid body, the delaminated interface can undulate periodically to give the interfacial instability (92, 96-99). Even if perfect bonding between the elastic layer and the rigid bodies is maintained, the exposed meniscus can become unstable, forming spatially periodic fingers of air that invade the elastic layer (Fig. 6-1a) (93, 94, 104). Morphologically the elastic fingering instability resembles the viscous fingering instability in thin fluid layers (213-216); however, the elastic and viscous fingering follows different governing laws. Whereas the abovementioned instabilities have been intensively studied in cases where the layer's thickness is much smaller than its lateral dimensions (*i.e.*, length and width), will any mechanical instability occur if the constrained layer's thickness is comparable to or larger than one lateral dimension (e.g., width)?

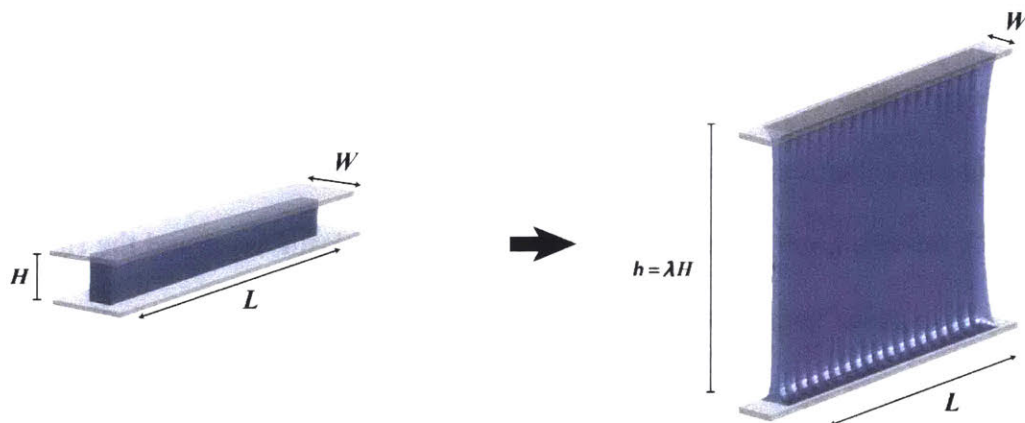
Here we show that a constrained soft elastic layer with comparable thickness and width can indeed undergo mechanical instability, which forms on its exposed surfaces but is localized at the constrained fringes of the layer (Fig. 6-1b). When subjected to tension, the middle portion of the layer elongates nearly uniformly but the constrained fringe portions of the layer deform nonuniformly. As the applied stretch reaches a critical value, the exposed surfaces of the fringe

portions begin to undulate periodically without debonding from the rigid bodies, giving the fringe instability (Fig. 6-1b).

a



b



c



d

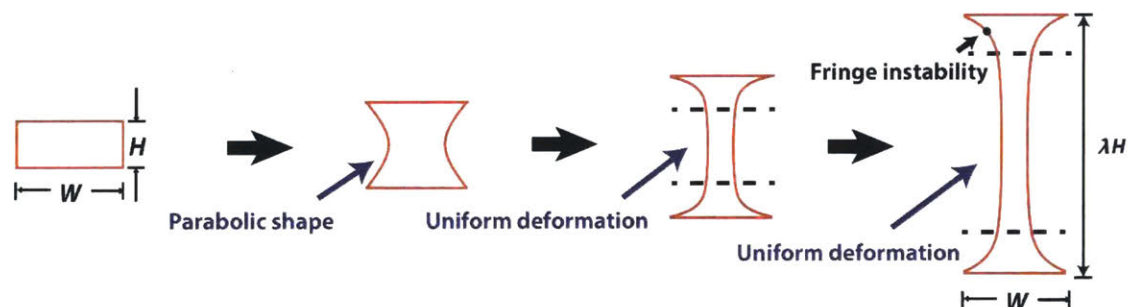


Figure 6-1: Schematics of constrained soft elastic layers that undergo the fingering and fringe instabilities. (a) The fingering instability occurs in relatively thin layers (i.e., $W/H > 6$); (b) The fringe instability occurs in relatively thick layers (i.e., $W/H < 3$); (c) Deformation of the exposed meniscus of a relatively

thin layer prior to the fingering instability (i.e., $W/H > 6$); (d) Deformation of the exposed meniscus of a relatively thick layer prior to the fringe instability (i.e., $W/H < 3$). Note that the length of the layer is much larger than its thickness in both cases, (i.e., $L/H \gg 1$).

While both the fingering (93, 94) and fringe instabilities occur on the elastic layers' exposed surfaces, the two modes of instabilities are dramatically different. To quantitatively understand the fringe instability and its differences from fingering instability, we combine experiments, theory and numerical simulations to show that: (i) The deformed layer's meniscus, prior to fringe instability, is not parabolic as is the meniscus before fingering instability (Fig. 6-1, c and d). (ii) In load-controlled elongations, the reported fingering instability is associated with a snap-through buckling, which manifests as peaks on the stress-strain curves for relatively thin samples¹. Such snap-through does not exist in relatively thick specimens, in which the fringe instability dominates. (iii) The critical applied stretch for the onset of fringe instability increases with the decrease of the layer's width-thickness ratio to a finite value of 3.9, which is associated with a constant nominal stress level of 3.8 times of the layer's shear modulus. (iv) The wavelength of the fringe instability scales with the elastic layer's width, but the wavelength of the fingering instability scales with the layer's thickness. The discovery of the fringe instability and quantitative comparisons between fringe and fingering instabilities will advance the current understanding of mechanical instabilities in soft materials and biological adhesives capable of large deformation. Moreover, the fundamental differences in the mechanical response of constrained elastic layers that differ only by their dimensions are expected to be useful in the design and engineering of advanced adhesives and joints (42, 217), as well as various sealants, insulators and bearings.

¹ For brevity, throughout the text we refer to layers of thickness that is much smaller than the in-plane dimensions as 'thin layers', while 'thick layers' are considered to have a thickness of the order of the in-plane dimensions or larger.

6.2 Experimental methods

To make a soft yet stretchable hydrogel sample, a precursor solution was prepared by mixing 5.5 mL 12 wt.% acrylamide (Sigma, A8887), 4.1 mL 2.5 wt.% alginate (Sigma, A2033), 500 μL 0.2 wt.% N,Nmethylenebisacrylamide (Sigma, 146072) as the crosslinker for polyacrylamide and 102 μL 0.2 M ammonium persulphate (Sigma, 248614) as an initiator for polyacrylamide. After degassing the precursor solution in a vacuum chamber, we added 8.2 μL N,N,N',N'-tetramethylethylenediamine (Sigma, T7024-50M) as the crosslinking accelerator for acrylamide. The shear modulus of the hydrogel was measured to be 2 kPa, and negligible rate dependence with slight hysteresis was observed in the stress-strain response of the hydrogel under loading-unloading cycles (Fig. 6-2).

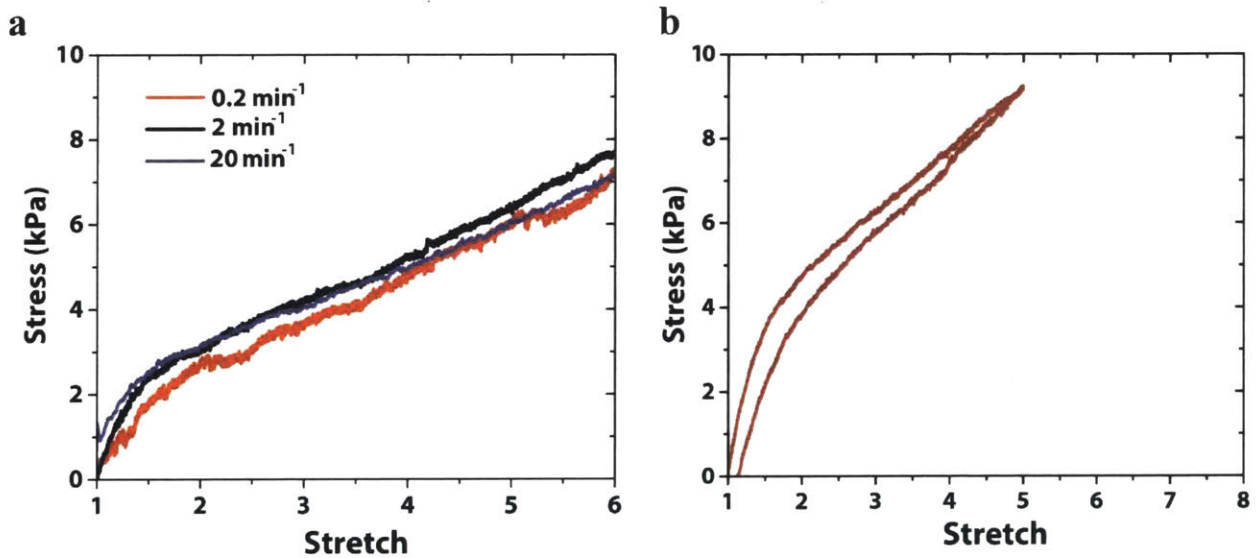


Figure 6-2: Stress-stretch curves at the loading curve of 2, 20, 200 mm/min. Loading-unloading stress-stretch curve at the rate of $1/30 \text{ s}^{-1}$.

The experimental setup used in the current study is illustrated schematically in Fig. 6-3. A layer of a soft yet stretchable hydrogel was robustly bonded onto two thick and transparent glass substrates (42). The width of the hydrogel layer W was varied from 3 mm to 37.8 mm and the thickness H from 1.5 mm to 6 mm, so that the width-thickness ratio of the elastic layer (W/H)

was selected in a wide range from 0.5 to 25, in contrast to previous studies focusing on relatively thin sheets (e.g., $W/H \geq 5$ (93, 94)). The length of the layer L was fixed to 75 mm, so that $L \gg H$ in all experiments. During a typical test, the bottom glass substrate of the sample was fixed, and the top glass substrate was pulled upward at a speed of 30 mm/min without causing any lateral displacement, using a universal material test machine (2 kN load cell; Zwick / Roell Z2.5). The applied force was measured by the load cell, and the deformation of the layer's free surfaces were recorded by cameras viewing from two directions (e.g., top view, side view). Owing to the low modulus, high stretchability and negligible defects of the hydrogel (44, 60, 118, 145) and the robust hydrogel-glass interfaces (42), the cavitation and interfacial instabilities were suppressed in the current experiments. Depending on the width-thickness ratio of the elastic layer, the exposed free surfaces will deform into different meniscus shapes and then destabilize to exhibit the fingering or fringe undulation patterns (Fig. 6-1).

Due to the constrained boundary, the meniscus profile at the visible edge is slightly larger than that in the center part of the sample. To clearly measure the meniscus profile in the center of the sample, we covered the transparent gel with in-diffusible dye on the lateral free surface of the sample. The reason why we chose in-diffusible dye is to prevent the formation of a fuzzy boundary which may be induced by the diffusible dye.

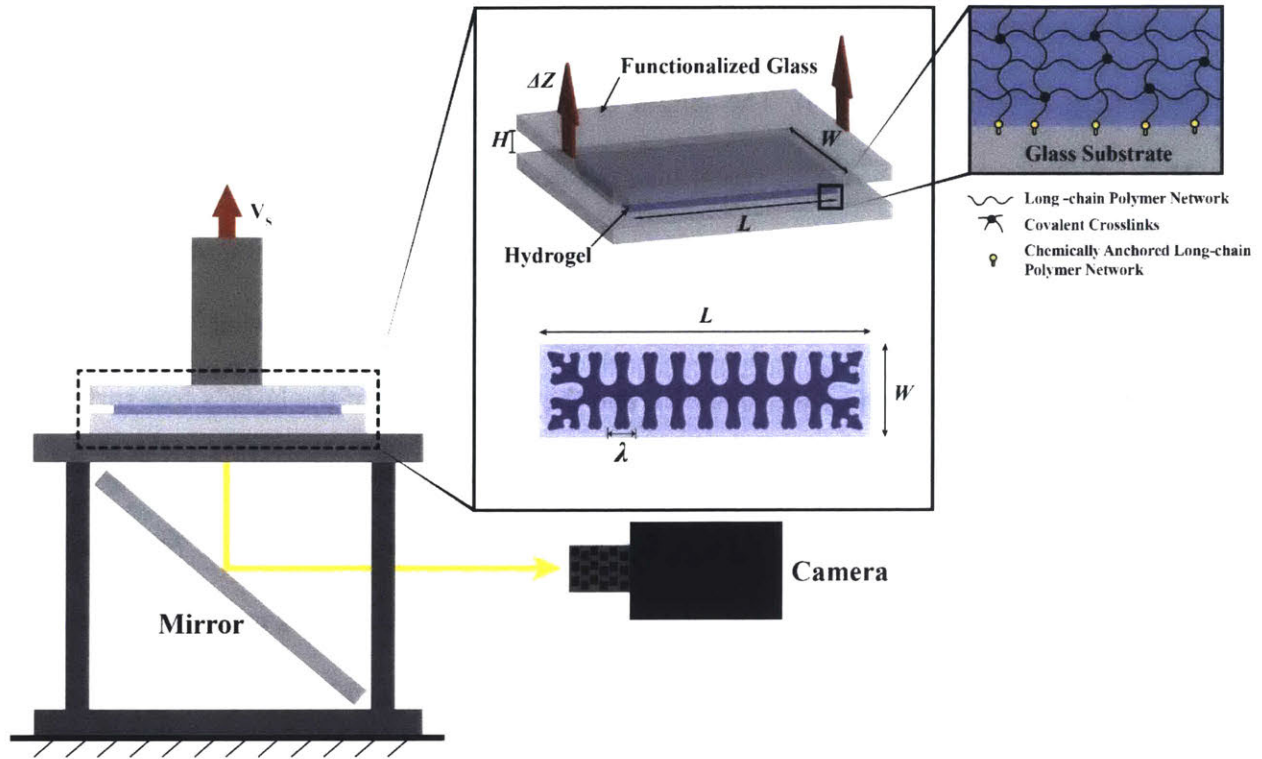


Figure 6-3: Test setup for the experimental measurement.

6.3 Numerical methods

Numerical simulations to capture the deformation and instability of the elastic layer were carried out with the finite element method using ABAQUS/Explicit. Since the effect of water diffusion in the hydrogel is negligible during the time of deformation in the current study (98), the hydrogel was modeled as a nearly incompressible neo-Hookean material with shear modulus μ and bulk modulus K of 1 kPa and 200 kPa, respectively. This gives an effective Poisson's ratio of 0.497, which is shown to be sufficiently accurate in Fig. 6-4a. All simulation models have the same dimensions as the experimental specimens. Symmetry conditions were applied in the mid-plane along the thickness direction and all side surfaces were set to be stress free. A constant velocity along the upward direction was prescribed on the top surface of the elastic layer, and the bottom surface was fixed. A mass scaling technique was used to maintain a quasi-static loading process.

The model was discretized with an 8-node linear brick, C3D8R element. The mesh size was taken as small as $\sim 1/10$ of the smallest feature dimension for all samples (e.g., 0.05 mm for $W/H < 2$; 0.1 mm for $2 \leq W/H \leq 4$ and 0.2 mm for $W/H > 4$) to ensure the accuracy of the simulation (Fig. 6-4b).

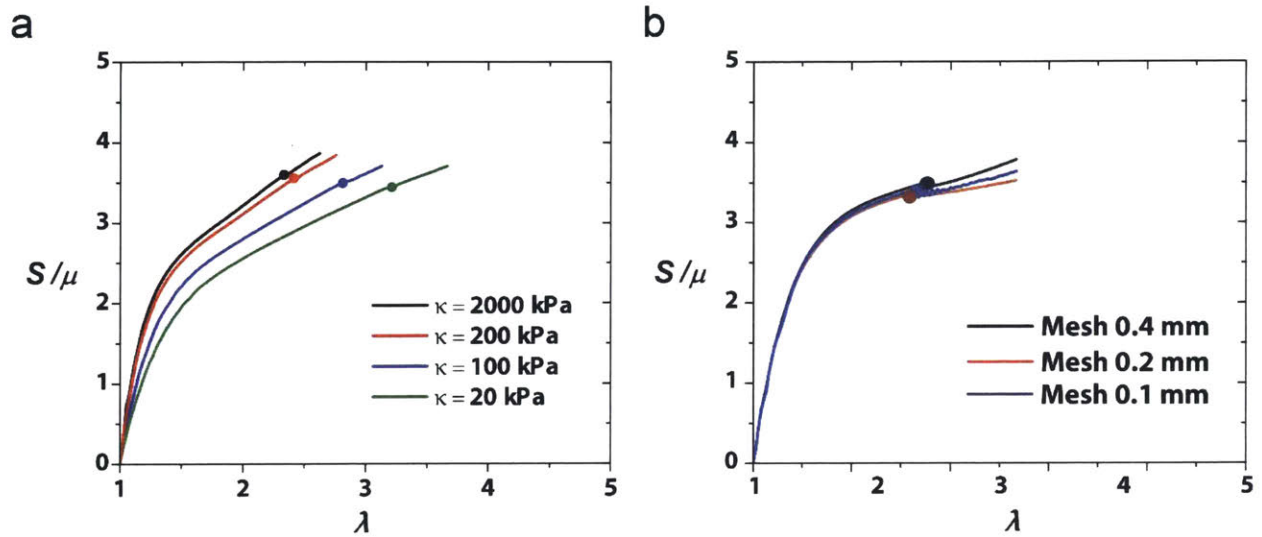


Figure 6-4: The nominal stress-stretch curve for the sample with $W/H = 3.2$ of various bulk modulus. (b) The nominal stress-stretch curve for the sample with $W/H = 4.0$ of various mesh size.

6.4 Results and discussion

In both experiments and simulations, the elastic layer with initial thickness of H is deformed to the current thickness h , and the applied stretch is defined as $\lambda = h/H$. Fig. 5-1 schematically illustrates the qualitative differences between fingering and fringe instabilities, both of which occur on the exposed meniscus of elastic layers. If the layer is relatively thin or its width-thickness ratio is relatively high (e.g., $W/H > 6$), the deformed meniscus maintains a parabolic shape (Fig. 6-1c), until a spatially periodic pattern of fingers of air invade the meniscus at a critical applied stretch λ_c (Fig. 6-1a) (93, 94). On the other hand, if the layer's width is comparable with or lower than its thickness (e.g., $W/H < 3$), the middle portion of the layer elongates nearly uniformly but the constrained fringe portions deform non-uniformly under relatively high applied stretches (Fig.

6-1d). As the applied stretch reaches a critical value λ_c , the free surfaces of the fringe portions gradually begin to undulate into a periodic pattern while the middle portion of the layer maintains uniform elongation (Fig. 6-1b). An exact width-thickness ratio at which the transition between fingering and fringe instabilities occurs cannot be visually detected due to the geometrical similarity in the transition regime $3 < W / H < 6$. Nevertheless, a clear transition point is observed in the stress-stretch response of the samples as will be explained in light of experimental, numerical and theoretical results.

6.4.1 Meniscus shape prior to instabilities

Fig. 6-5a and Fig. 6-5b show both experimental and simulation results for the meniscus shape of an elastic layer with comparable width and thickness (e.g., $W / H = 2$) under various levels of applied stretches, before the onset of any instability. (Due to the effects of front edges in experimental samples, the shape of the experimentally observed meniscus is highlighted by dash lines. See Fig. 6-6 for details on determining the meniscus.) Under relatively low applied stretch (e.g., $\lambda \leq 1.25$), the meniscus of the elastic layer follows the parabolic shape (218). However, as the applied stretch further increases (e.g. to $\lambda = 1.5, 2$), the middle portion of the meniscus elongates uniformly and the constrained fringe portions deform nonuniformly into a V shape. The shape of the highly-deformed meniscus significantly deviates from the parabolic shape assumed in previous studies on fingering instabilities (93, 218). From Fig. 6-5, a and b, it can be seen that the numerical model can accurately predict the evolution of the meniscus shape with the increasing stretch (i.e., from parabolic to non-parabolic). In addition, since the middle portion of the layer is uniformly elongated under high applied stretches (e.g., $\lambda = 1.5, 2$), there is no driving force for the formation of fingering instability in the middle portion of the layer in the sample.

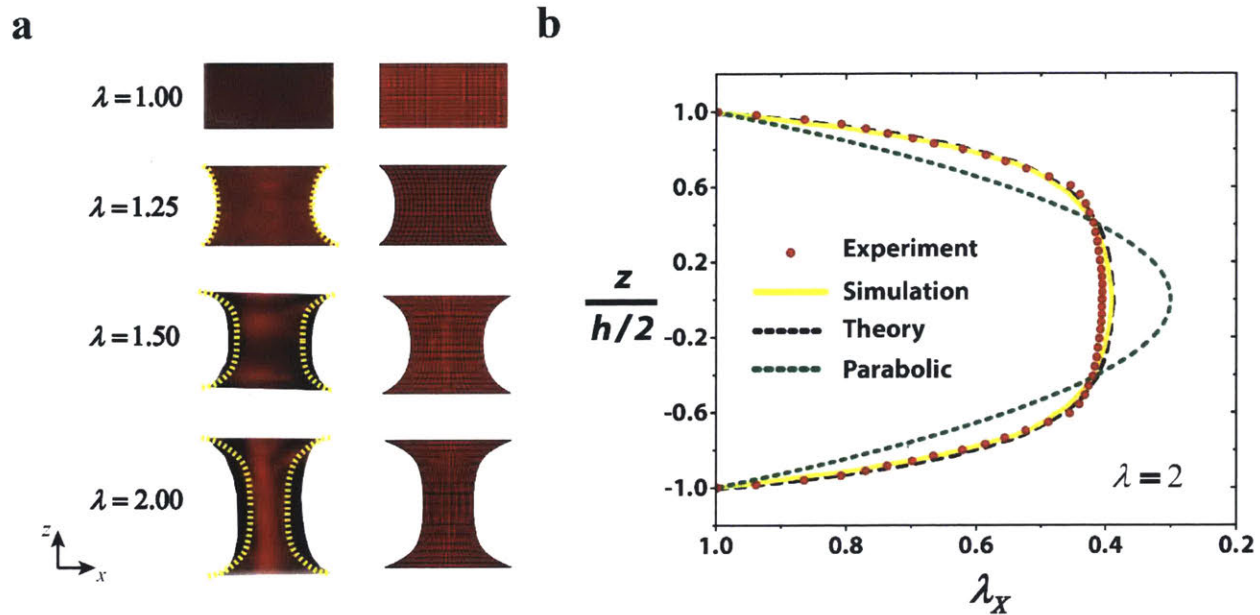


Figure 6-5: Experimental, simulation and theoretical results on the deformation in relatively thick layers. (a) Comparison of experimental and simulation results on deformation of a layer with $W/H = 2$ under various applied stretches prior to the fringe instability. (b) Comparison of experimental, simulation and theoretical results on the meniscus shape of a layer with $W/H = 2$ at applied stretch $\lambda = 2$.

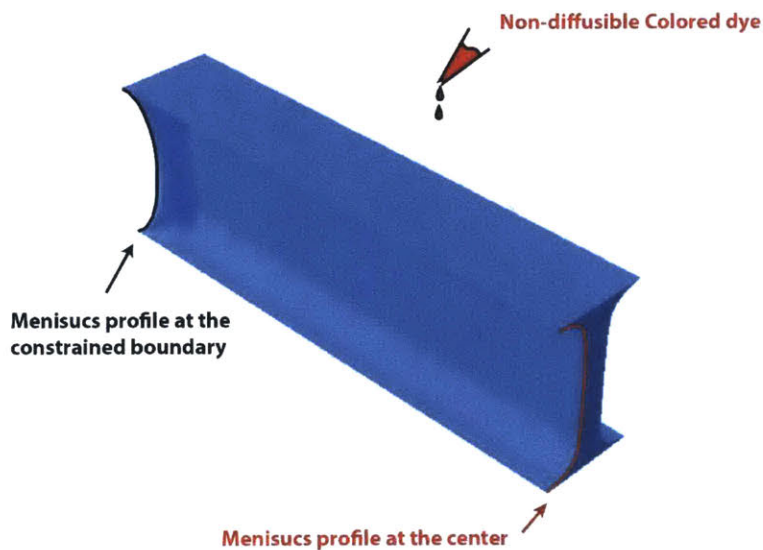


Figure 6-6: Non-diffusible colored dye is covered on the surface of transparent hydrogel sample to distinguish with the meniscus profile at the constrained boundary.

Instead, as the soft elastic layer ($W/H = 2$) is stretched to a critical point $\lambda_c \approx 3.2$, the exposed surface of the fringe portions becomes unstable - beginning to undulate periodically while the middle portion of the layer maintains uniform elongation (Fig. 6-7a). If the applied stretch further increases, the undulation in the fringe portions increases in magnitude while maintaining a constant wavelength. The layer maintains adhering on the rigid bodies throughout the process of deformation and fringe instability. Once the applied stretch is relaxed, the elastic layer restores its undeformed state. Evidently, the fringe instability is qualitatively different from the fingering instability that occurs in relatively thin elastic layers (*e.g.*, $W/H = 8$ in Fig. 5-8). Fig. 6-7b further shows that the numerical simulation can quantitatively predict the experimental observations of fringe instability. The simulation also confirms that the middle portion of the layer deforms almost uniformly while the fringe portions undergo the instability.

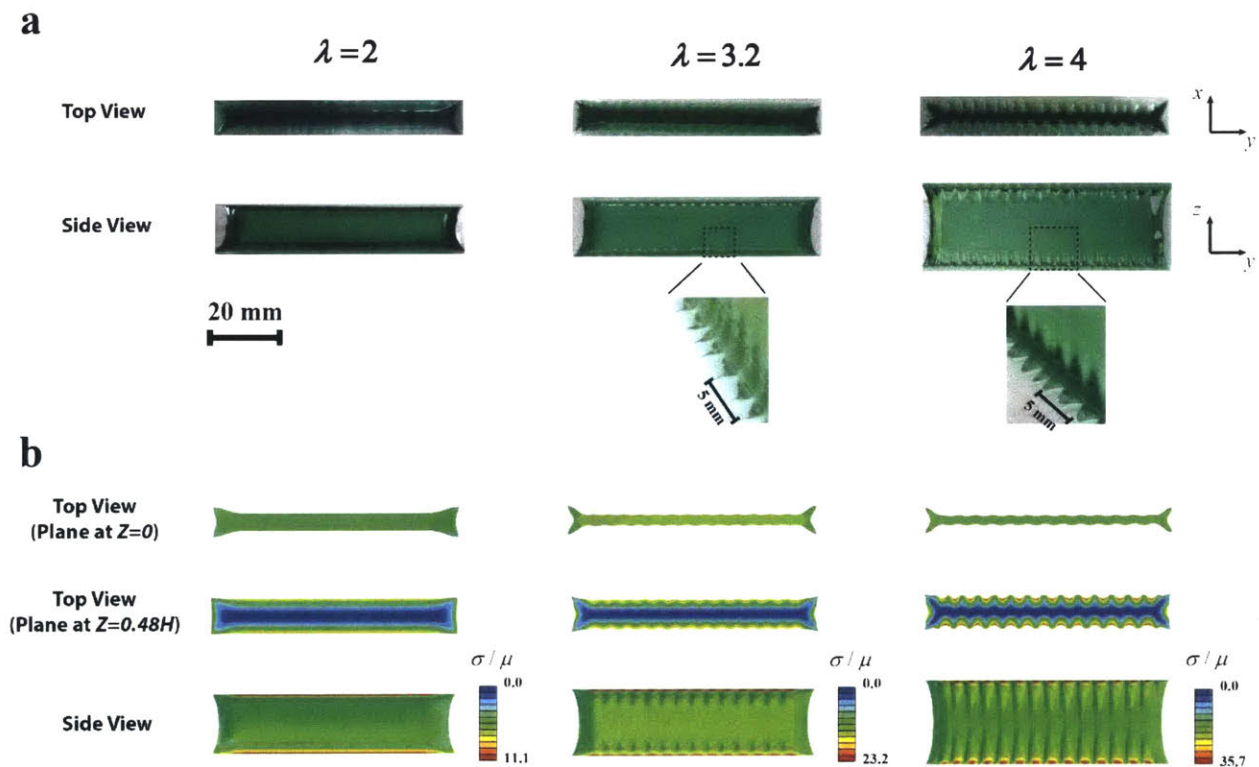


Figure 6-7: Experimental, simulation and theoretical results on the fringe instability in relatively thick layers. (a) Experimental observation of the formation of fringe instability for a layer with $W/H = 2$ as the

applied stretch increases. (b) Numerical simulation of the formation of fringe instability for a layer with $W/H = 2$ as the applied stretch increases. $\bar{\sigma}$ represents the von Mises stress.

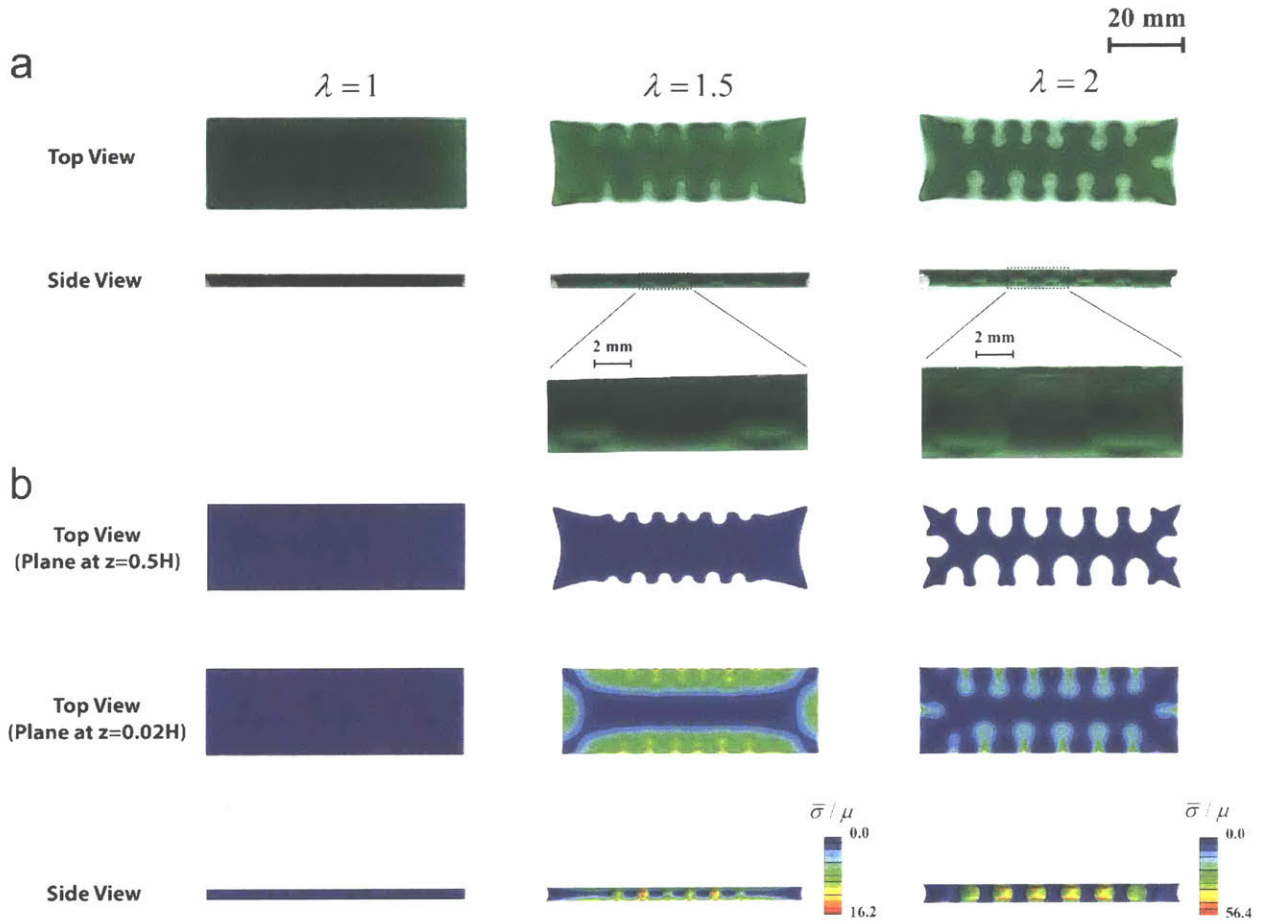


Figure 6-8: (a) Experimental observation of the formation of fingering instability for sample with the width-thickness ratio of 2 as strain increases. (b) Numerical simulation of the formation of fingering instability for a sample with the identical dimension.

6.4.2 Theoretical model

Next, we will resort to theory and scaling laws to better understand the experimental and simulation results on the deformation and instabilities in constrained elastic layers with various aspect ratios. While existing studies on fingering instabilities are generally limited to relatively thin layers (*e.g.*, $W/H > 6$) in which the meniscus shape is assumed to be parabolic (93, 219) (Fig. 6-1c), herein we develop a theory that accounts for the deformation of constrained elastic layers with a wide range of width-thickness ratios and is valid for exceedingly large deformations. Geometrically, the

layer in the undeformed state occupies a region $-W/2 < X < W/2$, $-\infty < Y < \infty$ and $-H/2 < Z < H/2$, and a material particle in the layer is labeled by its coordinate (X, Y, Z) in the undeformed state (see Fig. 6-9). In the deformed state, the material particle moves to a place of coordinates (x, y, z) , which are functions of (X, Y, Z) . We restrict the analysis to plane-strain deformation in the $X - Z$ plane and, without loss of generality, the layer is taken to deform symmetrically with respect to the $Z = 0$ and $X = 0$ planes.

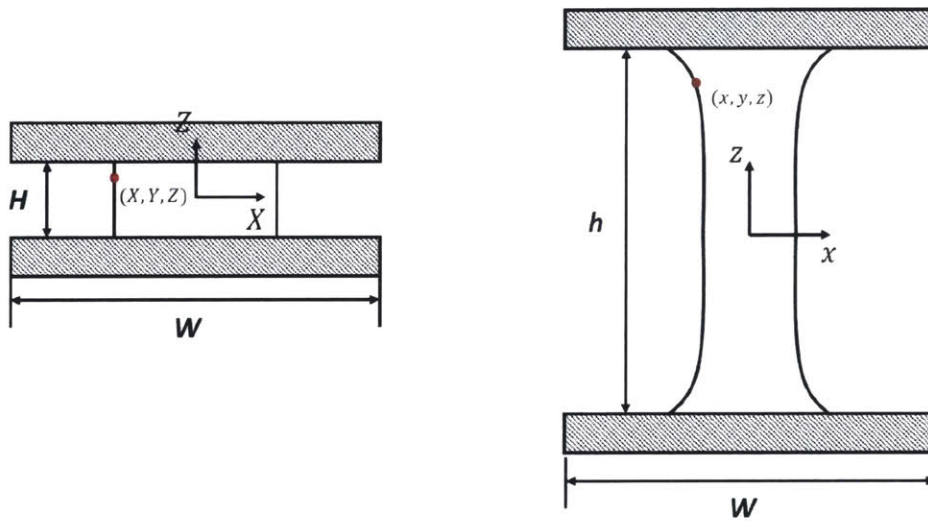


Figure 6-9: Specimen cross-section in deformed and undeformed configurations.

We make a single assumption on the deformation of the layer, that is, any horizontal plane in the layer at the undeformed state remains planar upon deformation (219) (see the simulation results in Fig. 6-5a for validation of the assumption). Based on the above assumption and the incompressibility of the elastic layer, we can express the deformation gradient of the layer as (see detailed derivation in supporting information)

$$\mathbf{F} = \begin{bmatrix} \lambda_x & 0 & X\lambda'_x \\ 0 & 1 & 0 \\ 0 & 0 & 1/\lambda_x \end{bmatrix} \quad (6.1)$$

where the in-plane stretch component $\lambda_x = \lambda_x(Z)$ is independent of the horizontal location, and the superposed prime denotes differentiation along Z . Since the width of the elastic layer at a vertical location Z deforms from W to $\lambda_x W$, we further define λ_x as the meniscus shape function of the elastic layer.

The elastic layer is taken as a neo-Hookean material with strain energy density function $\Psi = \frac{\mu}{2} [\text{tr}(\mathbf{F}\mathbf{F}^T) - 3]$. By minimizing the elastic energy of the layer, the meniscus shape function is found to obey a first-order differential equation

$$\frac{W}{2} \frac{d\lambda_x}{dZ} = \sqrt{3(\lambda_x^2 - \lambda_{x0}^2) + 3(\lambda_x^{-2} - \lambda_{x0}^{-2}) + C(\lambda_x^{-1} - \lambda_{x0}^{-1})} \quad (6.2)$$

Where $\lambda_{x0} = \lambda_x(Z = 0)$ is the meniscus shape function at the vertical mid-point of the layer, and C is a dimensionless integration constant that can be obtained by applying the boundary conditions

$$\lambda_x(Z = \pm H/2) = 1, \quad \lambda = \int_0^{H/2} \frac{2dZ}{\lambda_x H} \quad (6.3)$$

Solving Eqs. (6.2) and (6.3) yields the meniscus shape function λ_x , deformation gradient \mathbf{F} and elastic energy density Ψ of the layer as functions of the applied stretch λ . The total elastic energy of the layer per unit length in Y direction, E , can then be calculated by integrating Ψ over the volume of the layer. We further define the averaged nominal stress applied on the layer as the applied force divided by the undeformed horizontal cross-section area, which can be calculated as

$$S = \frac{1}{WH} \frac{dE}{d\lambda} \quad (6.4)$$

Accordingly we can derive relations between the applied stretch λ , the applied nominal stress S and the meniscus shape λ_x for layers with a wide range of width-thickness ratios (see detailed derivation in Appendix A1). In comparison with both experiments and simulations, it is

found that the present analytical solution provides accurate predictions of the meniscus shape even for exceedingly high applied stretches and across the entire regime of specimen dimensions considered in this study. For example, we show in Fig. 6-5b, the meniscus shape of a layer with $W/H = 2$ at applied stretch of $\lambda = 2$ given by the theory, experiment and numerical simulation. It can be seen that the theory can accurately predict the non-parabolic shape of a relatively thick layer (*i.e.*, $W/H = 2$) under high stretches.

6.4.3 Transition between fingering and fringe instabilities

Fig. 6-10 gives the curves of applied nominal stress S vs. applied stretch λ for elastic layers with various width-thickness ratios (*i.e.*, $0.5 \leq W/H \leq 8$); obtained from experiments (Fig. 6-10a), numerical simulations (Fig. 6-10b) and Eq. (6.4) of the analytical investigation (Fig. 6-10c). Depending on the width-thickness ratio of the layer, the S vs. λ curves can be monotonic or non-monotonic. For relatively thin layers (*e.g.*, $W/H = 6$ and 8), where the fingering instability occurs, the S vs. λ curves are not monotonic. The peak values correspond to the critical points S_c and λ_c for the onset of the fingering instability. The non-monotonic S vs. λ relation is consistent with the subcritical nature of the fingering instability (93). Notably, although the theoretical analysis does not account for the undulated pattern in fingering instability, it can still predict the non-monotonic relations of S vs. λ for relatively thin layers (*i.e.*, $W/H > 5.1$ in Fig. 6-10c). The area of the middle portion becomes smaller under stretch (Fig. 6-10a), and the geometrical effect causes the decrease of the nominal stress (Fig. 6-10c). Analogous to the Considère's criterion for necking, the peaks on the theoretical S vs. λ curves (Fig. 6-10c) indicate a tight upper bound of the critical points for onset of fingering instability. Since the undulated fingering has lower potential energy than the non-undulated necking predicted by the theory (Fig. 6-11), the fingering instability appears in our experiments and simulations of the samples with relatively thin layers (*i.e.*,

$W/H > 5.1$). In addition, the experiments, simulations and theory all show that S_c increases and λ_c decreases with the rise of W/H , which is consistent with previous reports for fingering instability (93). Notably, the upper-bound critical stretch for the onset of fingering instability obtained from the analytical solution will approach a plateau of 1.4 as the width-thickness ratio increases (Fig. 6c).

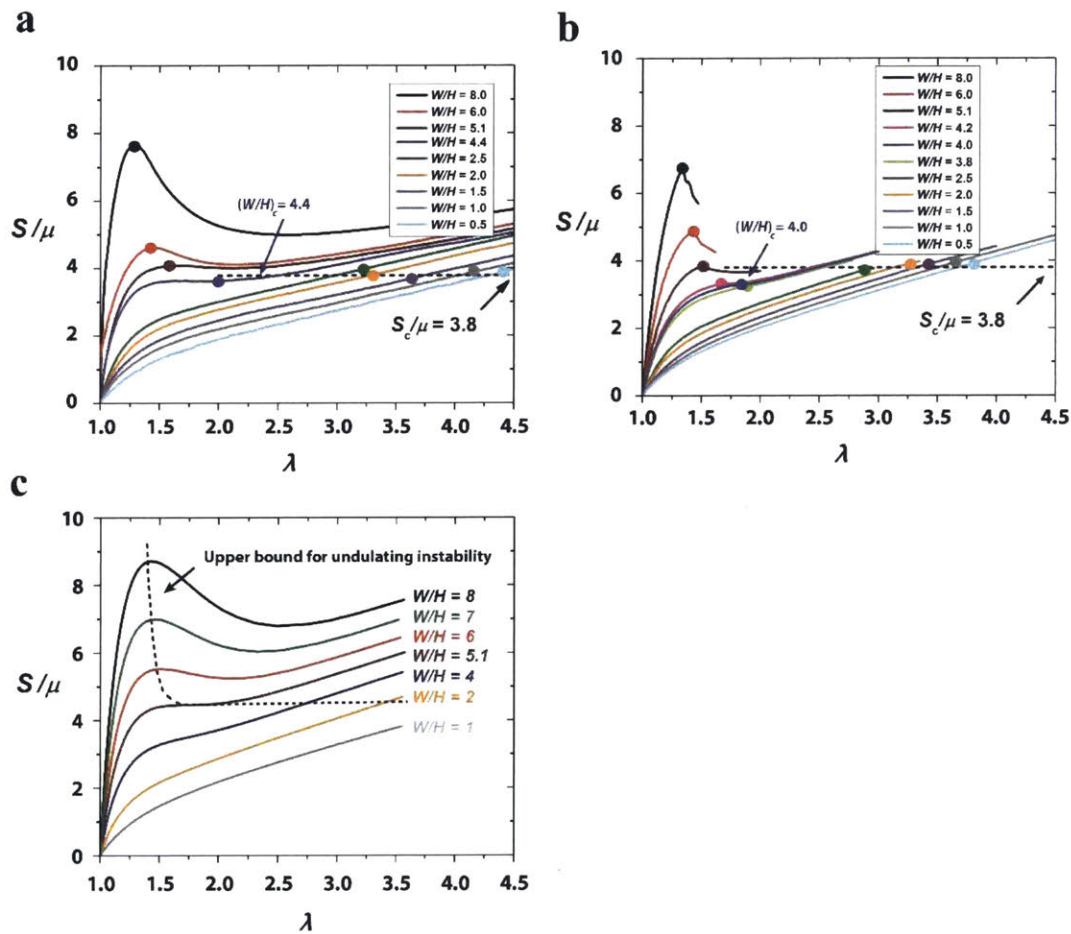


Figure 6-10: Experimental, simulation and theoretical results for the applied nominal stress S vs. the applied stretch λ for layers with various width-thickness ratios. (a) Experimentally measured curves of S vs. λ for layers with $W/H = 8, 6, 5.1, 4.4, 2.5, 2, 1.5, 1$ and 0.5 . The critical points for the onset of instabilities are marked on the corresponding curves. (b) Simulation curves of S vs. λ for layers with $W/H = 8, 6, 5.1, 4.2, 4, 3.8, 2.5, 2, 1.5, 1$ and 0.5 . The critical points for the onset of instabilities are marked on the corresponding curves. (c) Theoretical curves of S vs. λ for layers with $W/H = 8, 7, 6, 5.1, 4, 2$ and 1 . The dashed curve represent the stability limit.

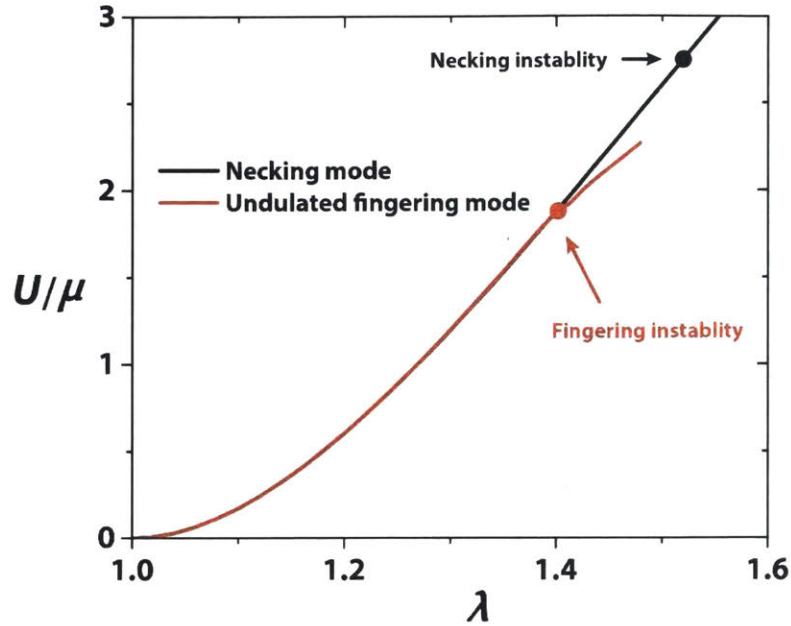


Figure 6-11: Normalized strain energy versus applied stretch in the sample with necking mode (i.e., 2D simulation) and the sample with undulated fingering mode (i.e., 3D simulation).

On the other hand, for relatively thick layers (e.g., $W/H = 2.5, 2, 1.5, 1$ and 0.5 in Fig. 6-10c), the curves of S vs. λ obtained from experiments, simulations and theory are all monotonic; and the fringe instability is observed in these samples. Strikingly, from both experimental and simulation results, we find that the critical nominal stress for fringe instability in layers with decreasing W/H ratios approaches an approximately constant value of $S_c \approx 3.8\mu$ (Fig. 6-10b and Fig. 6-13b). Returning to the analytical results in Fig. 6-10c, and according to the above argument, we may thus obtain an approximate theoretical stability limit by assuming that the fringe instability sets in at the same constant, level of stress from the transition point (where the fingering instability peak vanishes) and to lower width-thickness ratios, as shown by the continuation of the dashed line therein. In addition, different from the subcritical fingering instability (93), the fringe instability forms gradually with negligible hysteresis on the pattern amplitude vs. applied stretch curves obtained from loading and unloading of the sample (Fig. 6-12).

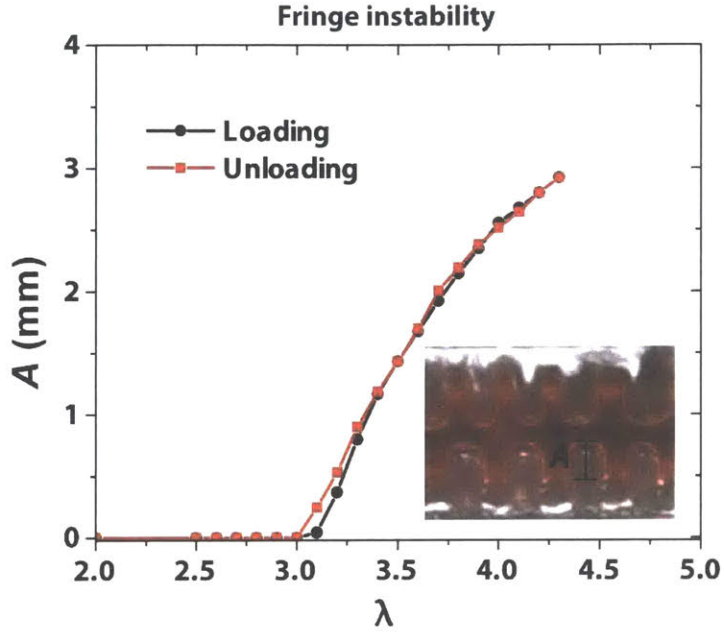


Figure 6-12: The amplitude versus applied stretch curves under loading and unloading for a fringe instability.

To identify the critical width-thickness ratio $(W/H)_c$ for the transition between the fingering and the fringe instabilities, we performed a series of experiments and simulations in an intermediate range of width-thickness ratios (e.g., $W/H = 3.8, 4.0, 4.2, 4.3, 4.4, 4.5, 5.1$). As shown in Fig. 6-10a, the non-monotonic behavior of the nominal stress-stretch curves disappears as W/H decreases to 4.4 in the experiments. In simulation, the critical width-thickness ratio is identified as $(W/H)_c = 4$. This slight difference between the experiment and simulation is possibly due to the deviation of the layer's mechanical properties from the neo-Hookean model. In this study, we take the simulation result $(W/H)_c = 4$ as the critical width-thickness ratio for the transition between the fingering and fringe instabilities.

6.4.4 Critical stress, stretch and wavelength for fringe instability

To better understand the characteristics of fringe instability, we plot the nominal stress S_{zz} contours in relatively thick layers (e.g., $W/H = 0.5, 1, 2, \text{ and } 4$) right before the onset of the

fringe instability (Fig. 6-12a). At this critical point, the middle portion of the specimens is in a state of nearly uniform uniaxial plane-strain tension, which therefore does not cause the fingering instability (Fig. 6-13a). On the other hand, the fringe portions exhibit a self-similar state of deformation, which is subjected to tensile stress yet constrained by the rigid surfaces. A combination of the tensile stress, mechanical constraint, and materials incompressibility cause the surfaces of fringe portions to undulate, giving the fringe instability.

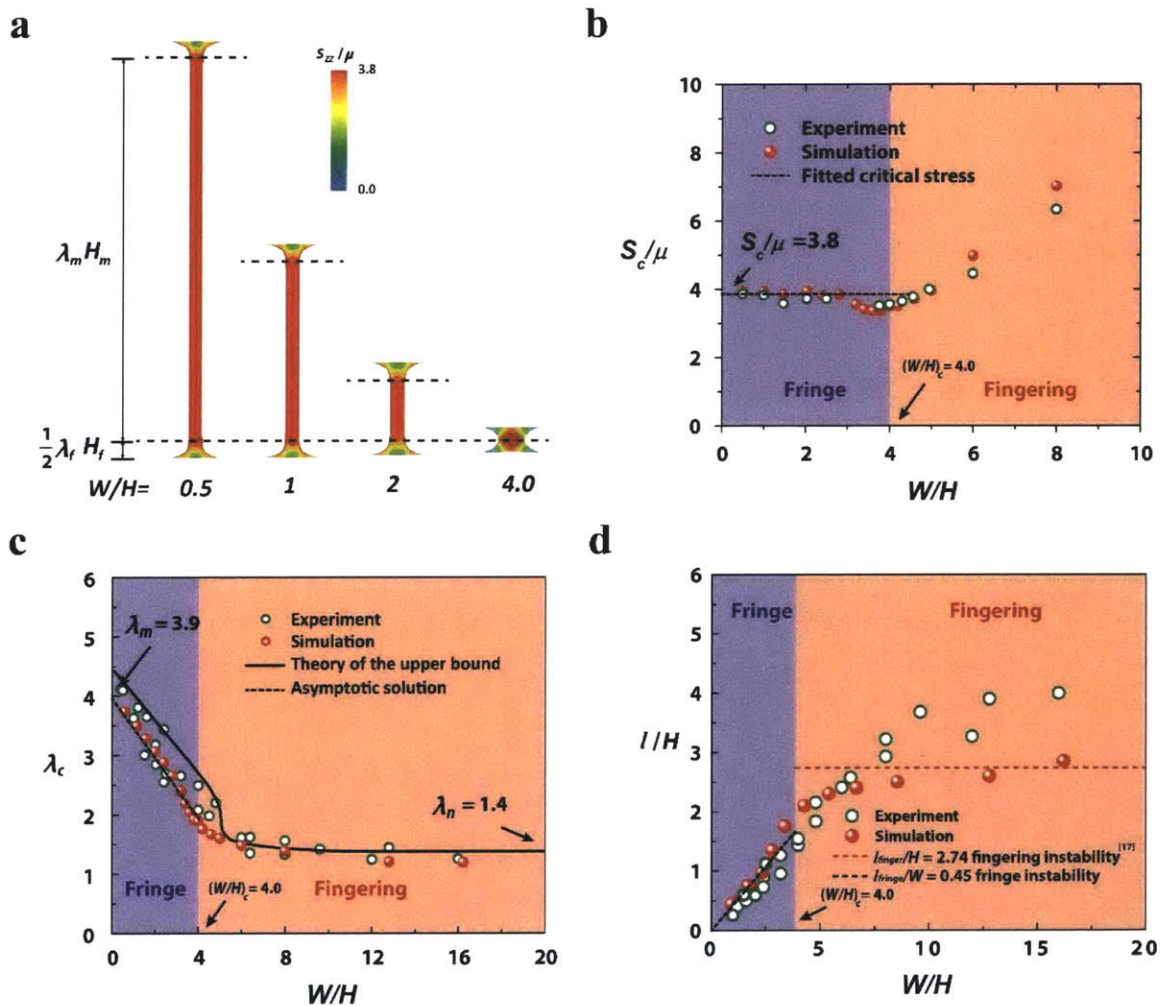


Figure 6-13: Experimental, simulation and theoretical results on the characteristics of fingering and fringe instabilities. (a) Numerical simulation results on stress contours in layers with $W/H = 0.5, 1, 2$ and 4 right before the fringe instability. The stress represents the normalized nominal stress component along the loading direction S_{zz} / μ . (b) The critical nominal stress for the onset of instabilities in layers with various

width-thickness ratios. (c) The critical applied stretch for the onset of instabilities in layers with various width-thickness ratios. (d) The wavelength of instabilities in layers with various width-thickness ratios.

We denote the thickness of the middle and fringe portions at the undeformed state as H_m and H_f , respectively. Based on the minimum layer thickness for the fringe instability, i.e., $(W/H)_c = 4$, we can further obtain $H_f = W/4$ and $H_m = H - H_f$. At the critical point for fringe instability, the stretch in the fringe portion λ_f is independent of W/H and can be obtained from the simulation result for $W/H = 4$ as $\lambda_f = 1.8$. The critical stretch in the middle portion λ_m is dictated by the nominal stress-stretch relation in plane-strain tension, i.e. $S_c / \mu = \lambda_m - \lambda_m^{-3} = 3.8$, which gives $\lambda_m = 3.9$. Therefore, the asymptotic solution of the critical stretch for the onset of the fringe instability can be expressed as

$$\lambda_c = \frac{\lambda_f H_f + \lambda_m (H - H_f)}{H} \approx 3.9 - 0.52 \frac{W}{H} \quad (5)$$

In Fig. 6-13c, we summarize the critical stretch levels for both the fringe and fingering instabilities obtained from experiments, simulation and theory. It can be seen that the above linear relation and the simulations can consistently predict the critical stretches for both types of instabilities. The analytical solution further provides a tight upper bound for the critical stretches in the entire range.

While it is known that the wavelength of the fingering instability l_{finger} scales with the elastic layer's thickness H (Fig. 6-13d), the wavelength of the fringe instability l_{fringe} does not follow such scaling since the thickness of the middle portions does not affect the fringe instability wavelength. Instead, the relevant length scale for the fringe instability wavelength is the fringe portion's thickness, which scales with the layer's width. Therefore, the wavelength for fringe

instability scales with the elastic layer's width, instead of its thickness. This dependence has been validated by both experimental and simulation results in Fig. 6-13d. In addition, by fitting to the experimental and simulation results, we can further obtain the pre-factors for the scales, i.e.,

$$l_{fringe} \approx 0.45W .$$

6.5 Conclusion

Pulling apart two rigid constraints that are connected by a thick layer of tough elastic material, to induce stretches deep into the nonlinear regime of the material response, exposes a geometrical instability that has not been previously reported. This instability, which we refer to as - fringe instability, emerges when the distance between the constraints reaches a critical point. Then localized undulating patterns begin to form near the fringes of the elastic layer. We find that this instability is dominant as long as the thickness of the layer is of the order of its in-plane dimensions or larger. For thin layers, a different mode of instability is dominant – the elastic fingering instability. By combining experiments, numerical simulations and analytical investigation, we explain the distinct properties of the two geometrical instabilities and obtain quantitative measures for the critical stress, stretch, and wavelength of the fringe instability. We find that while a snap-through instability appears in thin elastic layers, once the applied stress levels exceed a critical value, thick specimens do not exhibit such a global instability and a localized bifurcation mode emerges. This fundamental difference in the mechanical response of elastic slabs, that may have only slight differences in their dimensions, together with the quantitative measures for the geometrical features and stress levels associated with the instabilities, are essential in guiding the design and engineering of modern adhesive joints as well as in advancing the current understanding of those that exist in nature.

Chapter 7

Instabilities in confined elastic layers under Tension

7.1 Introduction

Elastic layers with top and bottom surfaces adhered to rigid bodies are abundant in biological organisms such as mussel plaques on rocks (220), barnacle glues on ship hulks (209) and tendons on bones (206, 221). In addition to the examples in nature, the stressed elastic layers have been widely adopted in engineering applications such as sealants, insulators, bearings, and adhesives (93, 106, 222). More recently, tough and soft hydrogel adhesives (42, 144, 223, 224) have also been used in biocompatible soft robotics (147, 225, 226), electronics (145, 227) and living devices (146, 228).

When the rigid bodies are pulled apart, the stressed elastic layers can undergo various modes of mechanical instabilities due to mechanical loads and constraints. The formation and interaction of these mechanical instabilities highly affect the mechanical robustness of engineering structures. For example, the load capacity of the adhesives highly depends on the occurrence of mechanical instabilities (106). The emergence of mechanical instabilities can also initiate different failure mechanisms ranging from interfacial fracture to cohesive failure in relevant structures (107).

In recent decades, various modes of mechanical instabilities in confined elastic layers under tension have been discovered (51, 92-95). If the elastic layer partially debonds from the rigid body, the delaminated interface can undulate periodically to give the interfacial undulation (92, 96-99). If perfect bonding between the elastic layer and the rigid bodies is maintained, a cavity can nucleate and grow within the elastic layer when the hydrostatic tensile stress in any region of the elastic layer reaches a critical value, giving the cavitation instability (e.g., Fig. 7-1c) (95, 100-103). Even if perfect bonding between the elastic layer and the rigid substrates is maintained and cavitation instability is suppressed by tuning the material properties and geometry of the elastic layer, the exposed meniscus can become unstable, forming fingering instability (93, 94, 104) or fringe

instability (51). While fingering instability initiates at the middle section of the exposed meniscus, fringe instability forms at the fringe portion of the exposed meniscus (e.g., Fig. 7-1).

This paper is aimed to provide a systematic understanding on the relations and interactions of the three modes of instabilities in perfectly-bonded elastic layers under tension: cavitation instability, Type I and Type II fingering instability, and fringe instability. While the cavitation instability has been intensively studied (95, 102, 229, 230), the recently-discovered fingering and fringe instabilities have not been well understood (93, 94). It is known that the instability is determined by the geometries and mechanical properties of the elastic layers, but there exists no model or theory to predict which mode (i.e., cavitation, fingering or fringe) will emerge in perfectly-bonded elastic layers under tension.

In this paper, we perform the systematic study on the formation, transition, interaction and co-existence of mechanical instabilities in confined elastic layers under tension, through combined experimental, numerical and theoretical analysis. We first discuss the characteristic features of individual mode of instability. Then we develop a theory for large deformation in a confined elastic layer with cylindrical shape under tension. The theory can correlate the applied stress, the applied stretch and the hydrostatic pressure in the elastic layer. Thereafter, we perform the linear perturbation analysis on the deformation of the elastic layer to theoretically predict the onset of fringe and fingering instabilities; and theoretically calculate the critical stress and critical stretch of cavitation instability. We find that the initial occurrence of instability can be tuned by both geometrical and mechanical properties of the elastic layer through two non-dimensional parameters: layer's lateral dimension over its thickness and elastocapillary length over the defect size. We further show that cavitation instability and fingering instability can coexist in one elastic layer under tension. Systematically understanding of the formation and interactions of various

mechanical instabilities in elastic layers under tension can provide a guideline for the design of robust adhesives by rationally harnessing the desired mode of instabilities while suppressing the other modes.

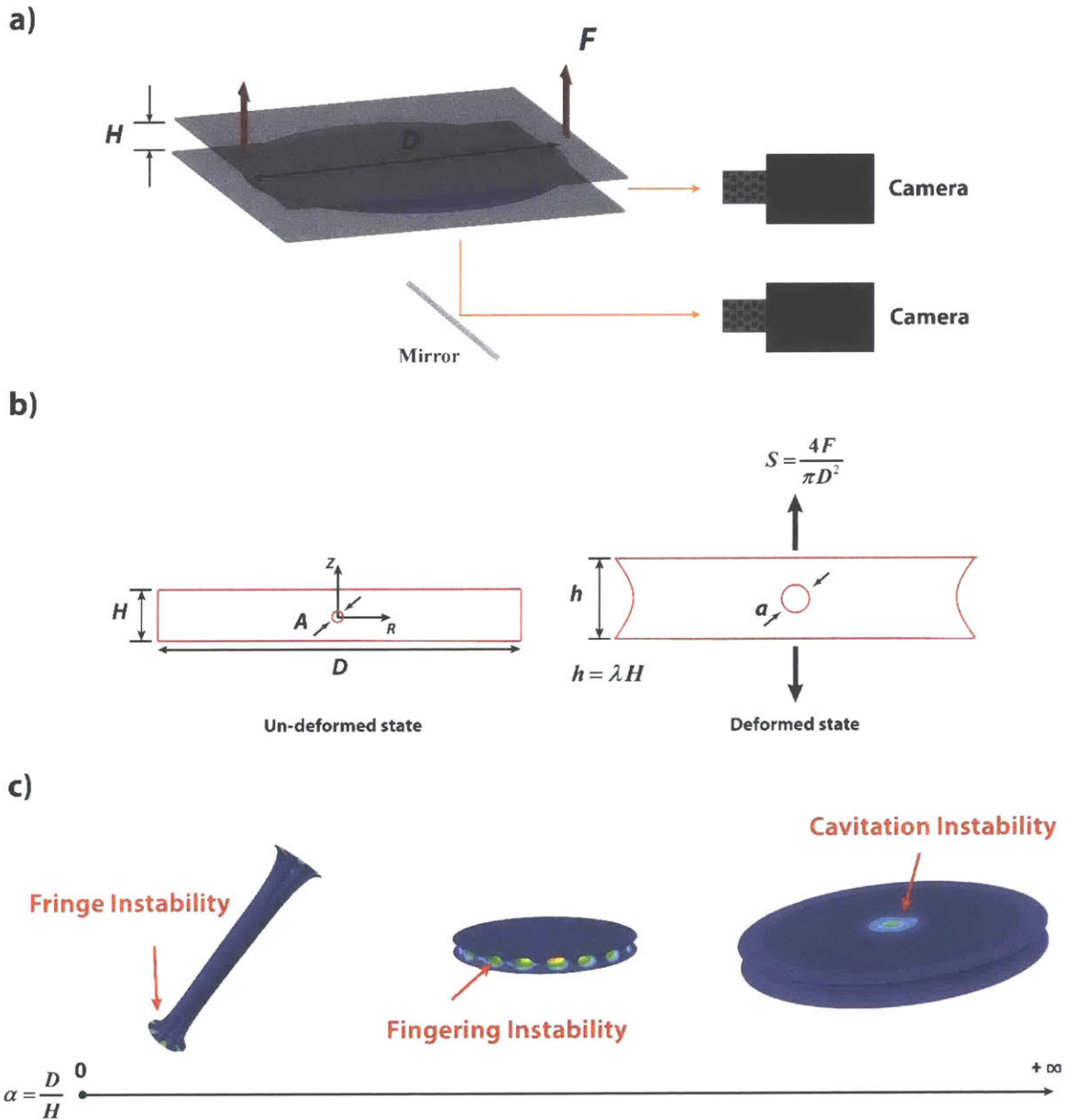


Figure 7-1: Schematics on deformation and instabilities in confined elastic layers under tension. (a) Experimental setup. (b) The cross-section of the constrained elastic layer in un-deformed and deformed state. (c) Illustration of fringe instability, fingering instability and cavitation instability, corresponding to small, moderate and large aspect ratio $\alpha = D/H$, respectively.

The plan of the paper is as follow. Section 7-2 defines the physical and dimensionless parameters used in this work. In Section 7-3, we discuss the experimental and simulation methods. In Section 7-4, we qualitatively discuss various modes of instabilities in elastic layers under tension. In Section 7-5, we first derive the deformation field in constrained elastic layer under tension, and then identify the critical point for the onset of each mode of instability using perturbation theory. In Section 7-6, we discuss the formation and evolution of each mode of instability through combined experimental and simulation results. We particularly discuss the relations between the applied stress and stretch in elastic layers under tension. In Section 7-7, we construct a phase diagram to predict the occurrence of any mode of instability in elastic layers. In Section 7-8, we discuss the coexistence and interactions of cavitation instability and fingering instability in one elastic layer under tension.

7.2 Physical and dimensionless parameters

As illustrated on Fig. 7-1b, we focus on elastic layers of cylindrical shape with height H and diameter D at the un-deformed (reference) state in this work. The material of the elastic layer is taken to be neo-Hookean with shear modulus μ and surface energy γ . Cavities with maximum diameter A may exist in the layer as defects. A ratio between surface energy and shear modulus of the material, γ/μ , gives the elastocapillary length, which characterizes the effect of the surface tension on the mechanical behaviors of the material. In the current study, we set the elastocapillary length γ/μ to be much smaller than the macroscopic dimensions of the sample (i.e. H and D), but on the same order or larger than the bulk defect size A . Through dimensional argument, we can obtain the following two dimensionless parameters:

$$\alpha = \frac{D}{H}, \quad \beta = \frac{\gamma}{\mu A}, \quad (7.1)$$

which affect the mechanical behavior of the elastic layer. The elastic layer is bonded on two rigid plates without delamination during its deformation and instabilities. A tensile force F is applied on the rigid plates, which deforms the elastic layer to the current height h . We define the applied nominal stress S and the applied stretch λ on the elastic layer as (see Fig. 7-1)

$$S = \frac{4F}{\pi D^2}, \quad \lambda = \frac{h}{H}. \quad (7.2)$$

When the applied nominal stress or stretch reaches a critical value S_c or λ_c , a mode of instability sets in the elastic layer.

Geometrically, the cylindrical elastic layer in the un-deformed state occupies a region $0 \leq R \leq D/2$, $0 \leq \Theta < 2\pi$ and $-H/2 \leq Z \leq H/2$. For convenience, we define the normalized location at the reference configuration $\bar{R} = \frac{R}{D/2}$ and $\bar{Z} = \frac{Z}{H/2}$ with $\bar{R} \in [0,1]$ and $\bar{Z} \in [-1,1]$.

7.3 Experimental and simulation methods

7.3.1 Sample preparation

We chose polyacrylamide hydrogel (PAAm) as a model hyper-elastic solid with negligible hysteresis and low rate sensitivity (51, 68, 118, 231). To make a PAAm hydrogel sample, a precursor solution was prepared by mixing acrylamide (Sigma, A8887), alginate (Sigma, A2033), N,Nmethylenebisacrylamide (Sigma, 146072) as the crosslinker for polyacrylamide and 102 μL 0.2 M ammonium persulphate (Sigma, 248614) as an initiator for polyacrylamide (118, 145). After degassing the precursor solution in a vacuum chamber, we added 8.2 μL N,N,N',N'-tetramethylethylenediamine (Sigma, T7024-50M) into the total precursor solution of 10 ml as the crosslinking accelerator for acrylamide. We tuned the shear modulus μ of the sample as 1.1 kPa, 2.2 kPa, 3.0 kPa, 3.6 kPa, 11 kPa and 14 kPa by controlling both the concentration of polymer and crosslink density (see detailed material constituents in Fig. 7-2). By adopting the measured surface

tension $\gamma = 0.07 \text{ J/m}^2$ for PAAm hydrogel (229), we can set the elastocapillary length γ / μ for gel A, gel B, gel C, gel D, gel E and gel F as $65 \mu\text{m}$, $32 \mu\text{m}$, $23 \mu\text{m}$, $19 \mu\text{m}$, $6.5 \mu\text{m}$ and $5 \mu\text{m}$ respectively. To control the maximum defect size within the sample, we degassed the precursor solution first and mixed a controlled volume amount of nitrogen gas of $100 \mu\text{l}$ in one syringe with 10 ml total precursor solution in another syringe for 10 times. The maximum defect size within the sample *A* is around $1 \mu\text{m}$ for the material with various constituents.

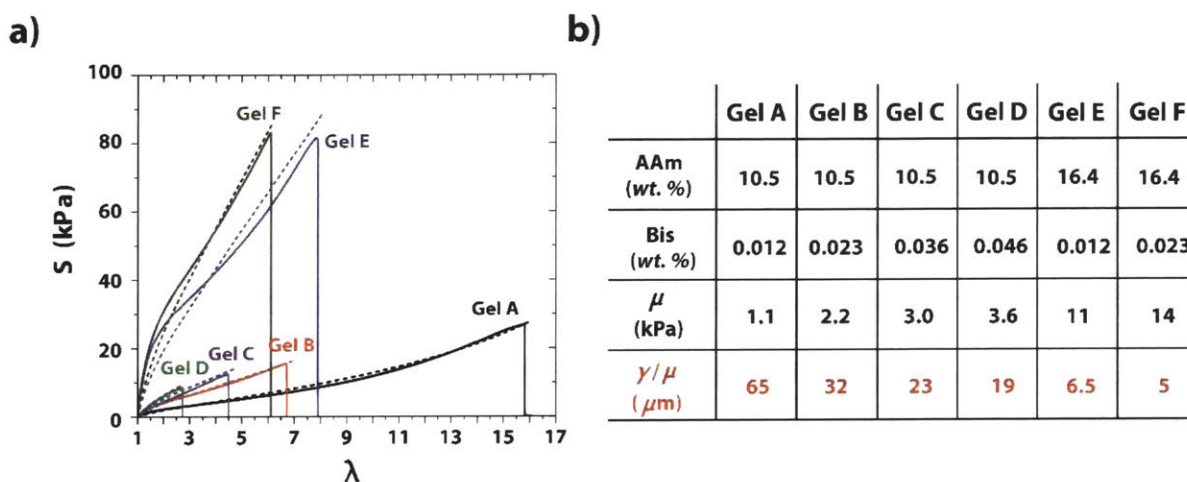


Figure 7-2: Materials for the constrained elastic layers. (a) Measured nominal stress-stretch curves for the samples with various constituents. Solid line represents the experimental data; dashed line represents the fitted neo-Hookean model. (b) Weight ratio of polyacrylamide (AAM) and N,N'-methylenebisacrylamide (Bis), shear modulus μ and elastocapillary length γ / μ for each material.

7.3.2 Mechanical testing

The experimental setup used in the current study is illustrated schematically in Fig. 7-1a. A layer of a soft yet stretchable hydrogel was robustly bonded onto two thick and transparent glass substrates (42). The diameter of the hydrogel layer D was varied from 6 mm to 140 mm and the thickness H from 1.5 mm to 6 mm , so that the aspect ratio of the elastic layer α was selected in a wide range from 1 to 50. During a typical test, the bottom glass substrate of the sample was fixed, and the top glass substrate was pulled upward at a controlled loading rate of 0.016 s^{-1} without

causing any lateral displacement, using a universal material test machine (2 kN load cell for samples with diameter $D > 12$ mm and 20 N load cell for samples with diameter $D < 12$ mm; Zwick / Roell Z2.5). Both the applied force and the loading displacement was measured by the load cell and the deformation of the layer's free surfaces was recorded by cameras viewing from both side view and top view. To suppress the interfacial detachment, we used a functional silane, 3-(trimethoxysilyl) propyl methacrylate (TMSPMA), to modify the surfaces of transparent glass and then covalently crosslinked the long chain polymer network of polyacrylamide (PAAm) to the silanes on the modified surfaces of glass substrates (42). All the mechanical tests in this paper were performed in the air and measured in an "as-prepared" state.

7.3.3 Finite-element simulation

In addition to a set of systematic experimental studies, we performed corresponding numerical simulations to capture the deformation and instability of an elastic layer with the finite element method using ABAQUS/Explicit. To focus on a pure elastic behavior at relative short time scale, we modeled the hydrogel as a neo-Hookean material and suppressed the water diffusion in the hydrogel in the current study. We set K / μ as large as we can, and in this case is 2000, to capture the incompressibility of the material. The type of element was taken as C3D8R and the mesh size was taken as small as $\sim 1/10$ of the smallest feature dimension for all samples to ensure the accuracy of the simulation. Additionally, a mass scaling technique was used to obtain results within a reasonable computation time. All numerical models have the same dimensions and loading setup as the experimental specimens.

7.4 Modes of instabilities

Figure 7-1c schematically illustrates the qualitative differences among fringe, fingering and cavitation instabilities. If the elastic layer's radius is comparable with or lower than its

thickness (e.g., $\alpha < 4$), the free surfaces of the fringe portions of the layer gradually undulate into a periodic pattern under a critical applied stretch, giving the fringe instability (51). If the layer's aspect ratio is moderately high (e.g., $6 < \alpha < 20$), the deformed meniscus maintains a parabolic shape, until a spatially periodic pattern of air fingers invade the meniscus at a critical applied stretch (93, 94). If the layer's aspect ratio is extremely high (e.g., $\alpha > 30$) or the dimensionless elastocapillary number β is relatively low, a cavity nucleates and grows within the bulk sample prior to the formation of the undulating patterns on the exposed lateral surfaces.

While both fringe and fingering instabilities feature the undulation of the elastic layer's meniscus, they initiate at the fringe and middle portions of the meniscus, respectively. Therefore, the highest amplitude of the undulation for fringe and fingering, right after their initiation, is expected to appear at the fringe and middle portions of the meniscus, respectively (i.e. we take the vertical location that gives the highest undulation amplitude \bar{Z}_0 as the location where the undulations initiate in simulation). In Fig. 7-3, a and b, we give the simulation results for fringe ($\alpha = 2$) and fingering ($\alpha = 12$) instabilities in elastic layers with different aspect ratios. We further quantify the undulation amplitude A_m for fringe ($\alpha = 2$) and fingering ($\alpha = 12$) instabilities as a function of the normalized vertical location \bar{Z} (see Fig. 7-3c). Evidently, the highest amplitude of the undulation for fringe and fingering indeed appears at the fringe ($\bar{Z} = 0.81$) and middle ($\bar{Z} = 0$) portions of the meniscus, respectively. In Fig. 7-3d, we further plot the vertical location that gives the highest undulation amplitude \bar{Z}_0 as a function of the elastic layer's aspect ratio α , which shows that critical transition aspect ratio from fringe to fingering instability as $\alpha_{\text{fringe-fingering}} = 5$.

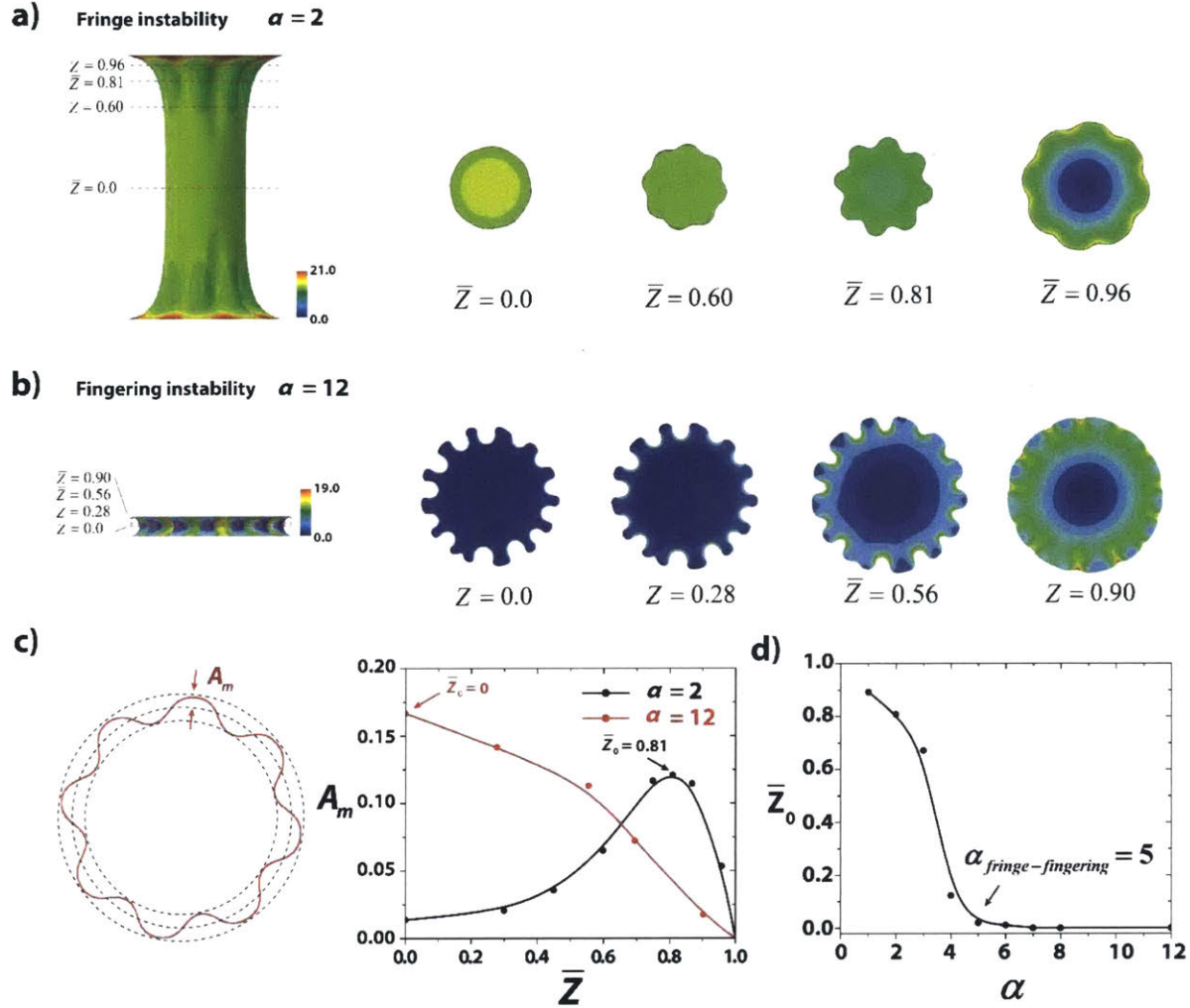


Figure 7-3: Morphology difference between fringe instability and fingering instability. (a) Undulation contours at the different planes right after the onset of fringe instability for the sample with $\alpha = 2$. Maximum amplitude occurs at $\bar{Z} = \pm 0.81$. (b) Undulation contours at the different planes right after the onset of fingering instability for the sample with $\alpha = 12$. Maximum amplitude occurs at $\bar{Z} = 0$. (c) The normalized amplitude of undulation contours versus \bar{Z} right after the onset of instabilities for the sample with $\alpha = 2$ and $\alpha = 12$. (d) The \bar{Z}_0 for the maximum amplitude of the undulation contours versus aspect ratios.

7.5 Theoretical analysis

In this part, we will develop a theory to understand i). the large deformation and stress fields in the constrained elastic layer under tension and ii). the critical points for the onset of fringe, fingering and cavitation instabilities. We first solve the equations of an incompressible neo-

Hookean layer under tension and obtain the meniscus shapes, the applied stress-stretch relations, and the hydrostatic pressure versus stretch in the elastic layer. Thereafter, we perform the linear perturbation analysis to predict the critical stretch λ_c and the critical stress S_c for the onset of both fringe instability and fingering instability.

7.5.1 Large deformation and stress fields in constrained elastic layers under tension

Geometrically, the elastic layer in the undeformed state occupies a region $0 \leq R \leq D/2$, $0 \leq \Theta < 2\pi$ and $-H/2 \leq Z \leq H/2$. A material particle in the layer is labeled by its coordinate (R, Θ, Z) in the un-deformed state with $\{\mathbf{e}_R, \mathbf{e}_\Theta, \mathbf{e}_Z\}$ as the basis in cylindrical coordinate (see Fig. 7-1b). In the deformed state, the material particle moves to a place of coordinates (r, θ, z) , which are functions of (R, Θ, Z) . Since the elastic layer deforms axisymmetrically prior to instability, the displacement in Θ direction $u_\Theta = 0$ and the displacement in radius direction u_R and that in axial direction u_Z are independent of Θ . Here, we make a single assumption on the deformation of the layer, that is: *any horizontal plane in the layer at the un-deformed state remains planar upon deformation* (51, 219, 232). Based on the axisymmetric deformation, horizontal-plane assumption and incompressibility of the material, we can specify the displacement field in the elastic layer as

$$u_R(\bar{R}, \bar{Z}) = \bar{R}u_1(\bar{Z}), \quad (7.3)$$

$$u_Z(\bar{Z}) = u_2(\bar{Z}), \quad (7.4)$$

with $\bar{R} = \frac{R}{D/2}$, $\bar{Z} = \frac{Z}{H/2}$. The linear dependence of u_R on \bar{R} is directly from the horizontal plane assumption with the incompressibility. Using the displacement field in Eq. (7.3) and Eq. (7.4), we can express the deformation gradient in the layer as:

$$\mathbf{F} = \begin{bmatrix} \lambda_{rR} & 0 & \gamma_{rZ} \\ 0 & \lambda_{\theta\theta} & 0 \\ 0 & 0 & \lambda_{zZ} \end{bmatrix}, \quad (7.5a)$$

with

$$\lambda_{rR} = 1 + \frac{1}{D/2} u_1, \quad (7.5b)$$

$$\lambda_{\theta\theta} = 1 + \frac{1}{D/2} u_1, \quad (7.5c)$$

$$\lambda_{zZ} = 1 + \frac{1}{H/2} u'_2, \quad (7.5d)$$

$$\gamma_{rZ} = \frac{1}{H/2} \bar{R} u'_1, \quad (7.5e)$$

with the prime for differentiating respect to \bar{Z} , or explicitly, $u'_1 = \frac{du_1}{d\bar{Z}}$ and $u'_2 = \frac{du_2}{d\bar{Z}}$. The

incompressibility of the elastic layer also enforces the conservation of volume, which reads as:

$$\det(\mathbf{F}) = \lambda_{rR} \lambda_{\theta\theta} \lambda_{zZ} = 1. \quad (7.6)$$

The elastic layer is taken as an incompressible neo-Hookean solid with strain energy density function $\psi = \frac{\mu}{2} [\text{tr}(\mathbf{F}^T \mathbf{F}) - 3]$. Therefore, the nominal stress tensor \mathbf{S} is expressed through $\mathbf{S} = \mu \mathbf{F} - p^* \mathbf{F}^{-T}$ and the Cauchy stress tensor is expressed through $\boldsymbol{\sigma} = \mathbf{S} \mathbf{F}^T$, namely:

$$\mathbf{S} / \mu = \begin{pmatrix} \lambda_{rR} - \bar{p} / \lambda_{rR} & 0 & \gamma_{rZ} \\ 0 & \lambda_{\theta\theta} - \bar{p} / \lambda_{\theta\theta} & 0 \\ \lambda_{\theta\theta} \gamma_{rZ} \bar{p} & 0 & \lambda_{zZ} - \bar{p} / \lambda_{zZ} \end{pmatrix}, \quad (7.7a)$$

$$\boldsymbol{\sigma} / \mu = \begin{pmatrix} \lambda_{rR}^2 - \bar{p} + \gamma_{rZ}^2 & 0 & \gamma_{rZ} \lambda_{zZ} \\ 0 & \lambda_{\theta\theta}^2 - \bar{p} & 0 \\ \gamma_{rZ} \lambda_{zZ} & 0 & \lambda_{zZ}^2 - \bar{p} \end{pmatrix}, \quad (7.7b)$$

where p^* is the Lagrange multiplier to enforce the incompressibility and $\bar{p} = p^* / \mu$ is the corresponding dimensionless form. The equilibrium equations read $\text{Div } \mathbf{S} = \mathbf{0}$. Since the equilibrium equation along the hoop direction will be satisfied automatically, then the remaining equilibrium equations along radius direction and axial direction are

$$-\frac{1}{\lambda_{rR}} \frac{\partial \bar{p}}{\partial \bar{R}} + \alpha \frac{\partial \gamma_{rZ}}{\partial \bar{Z}} = 0, \quad (7.8)$$

$$\lambda_{rR} \frac{\partial (\gamma_{rZ} \bar{p})}{\partial \bar{R}} + \frac{\lambda_{rR} \gamma_{rZ} \bar{p}}{\bar{R}} + \alpha \frac{\partial (\lambda_{zZ} - \bar{p} / \lambda_{zZ})}{\partial \bar{Z}} = 0, \quad (7.9)$$

with $\alpha = D/H$. Since the highest order of \bar{R} in γ_{rZ} is linear and in order to satisfy Eq. (7.8), \bar{p} should be a function of \bar{R}^2 . With this observation, we can solve both Eq. (7.8) and Eq. (7.9) analytically (See Appendix. A2 for more details). By imposing the boundary conditions: $du_1 / d\bar{Z} |_{\bar{Z}=0} = 0$, $u_1(\bar{Z} = \pm 1) = 0$ and $u_2(\bar{Z} = 0) = 0$, the specific functions $u_1(\bar{Z})$ and $u_2(\bar{Z})$ can be identified by solving Eq. (7.8) and Eq. (7.9)

$$u_1(\bar{Z}) = \frac{D}{2} \left[\frac{\cosh(\kappa \bar{Z})}{\cosh(\kappa)} - 1 \right], \quad (7.10a)$$

$$u_2(\bar{Z}) = \frac{H}{2} \left[\frac{\sinh(2\kappa)}{2\kappa} \frac{\tanh(\kappa \bar{Z})}{\tanh(\kappa)} - \bar{Z} \right], \quad (7.10b)$$

where κ is an internal loading parameter which is correlated with the applied stretch through

$$\lambda = \frac{\sinh(2\kappa)}{2\kappa}. \quad (7.10c)$$

With the calculated functions of $u_1(\bar{Z})$ and $u_2(\bar{Z})$, we further plot the meniscus shape at various stretches for the sample with $\alpha = 4$ and $\alpha = 8$ shown in Fig. 7-4. Our analytical results match well with the numerical results from 2D asymmetrical finite-element model. At small

stretches (e.g. $\lambda = 1.5$ for $\alpha = 4$), the meniscus shape is parabolic (93); while as stretch becomes large (e.g. $\lambda = 2.5$ for $\alpha = 4$), the meniscus shape deviates from the parabolic profile severely and the middle portion of the sample is almost uniformly deformed as discussed in previous report (51).

With the specified functions of $u_1(\bar{Z})$ and $u_2(\bar{Z})$, we can further calculate the dimensionless Lagrange multiplier \bar{p} in the form of (see details in Appendix. A2):

$$\bar{p}(\bar{R}, \bar{Z}) = q_0(\bar{Z}) + (\bar{R}^2 - 1)q_1(\bar{Z}), \quad (7.11a)$$

with

$$q_0(\bar{Z}) = \frac{\cosh^2(\kappa\bar{Z})}{2 \cosh^2 \kappa} \kappa^2 \alpha^2 + \frac{\cosh^4 \kappa}{2 \cosh^4(\kappa\bar{Z})} + C_3, \quad (7.11b)$$

$$q_1(\bar{Z}) = \frac{\cosh^2(\kappa\bar{Z})}{2 \cosh^2 \kappa} \kappa^2 \alpha^2, \quad (7.11c)$$

where C_3 is to be determined by a boundary condition.

Owing to the assumption that any horizontal plane in the layer at the un-deformed state remains planar upon deformation, it's impossible to satisfy the traction free boundary conditions for the whole exposed surfaces (i.e. at any height of the sample). Here, since we specifically focus on the case when the instabilities initiates at exact the middle plane or closer to the middle plane, we enforce the boundary condition at $\bar{Z} = 0$, namely the traction $\mathbf{t}_r = \mathbf{S} \cdot \mathbf{e}_r$ shall be zero at $\bar{R} = 1$ and $\bar{Z} = 0$, where $\{\mathbf{e}_r, \mathbf{e}_\theta, \mathbf{e}_z\}$ is the basis in cylindrical coordinate. Since $S_{\theta r} = S_{zr} = 0$ owing to the symmetric condition at the middle plane, the only boundary condition needs to be satisfied is $S_{rr} = \mu(\lambda_{rr} - \bar{p} / \lambda_{rr}) = 0$ at the middle plane. Therefore, constant C_3 can be identified as:

$$C_3 = \frac{1}{\cosh^2 \kappa} \left(1 - \frac{1}{2} \kappa^2 \alpha^2 \right) - \frac{1}{2} \cosh^4 \kappa, \quad (7.12)$$

and full expression of dimensionless Lagrange multiplier reads as

$$\bar{p} = \frac{1}{2} \left(\frac{\cosh^4 \kappa}{\cosh^4(\kappa \bar{Z})} - \cosh^4 \kappa \right) + \frac{\kappa^2 \alpha^2}{2} \left(\bar{R}^2 \frac{\cosh^2(\kappa \bar{Z})}{\cosh^2 \kappa} - \frac{1}{\cosh^2 \kappa} \right) + \frac{1}{\cosh^2 \kappa}. \quad (7.13)$$

We further calculate the averaged nominal stress applied on the layer S through

$$S = \frac{4}{H\pi D^2} \cdot \frac{dW}{d\lambda}, \quad (7.14)$$

where W is the total elastic energy of the layer which can be calculated by integrating ψ over the

volume of the layer: $W = 2 \int_0^{\frac{H}{2}} \int_0^{\frac{D}{2}} 2\pi R \psi(R, Z) dR dZ$. After algebraic simplification, the applied

nominal stress S can be expressed as (see details in Appendix. A2):

$$S / \mu = S_0(\kappa) + \alpha^2 S_1(\kappa), \quad (7.15)$$

where both S_0 and S_1 are functions of a single variable with respect to the loading parameter κ

(see detailed expressions in Appendix. A2). As shown in Fig. A2-1, S_0 monotonically increases

with the applied stretch, while S_1 is non-monotonic with a peak point at $\kappa = 0.89$ (i.e. $\lambda = 1.62$).

When α is very small, S_0 is dominated, and there is no peak displayed in the stress-stretch curve.

With the increase of aspect ratio α , the second term $\alpha^2 S_1$ will gradually become dominated and

a peak stress will display in the overall applied stress-stretch curve which is associated with the

global necking mode (51). The overall S / μ curves for various α are shown in Fig. 7-4c. In Fig.

A2-2a, we further show that the initial slope of our curves agrees with the result from the

calculations based on small deformation (218, 219, 233).

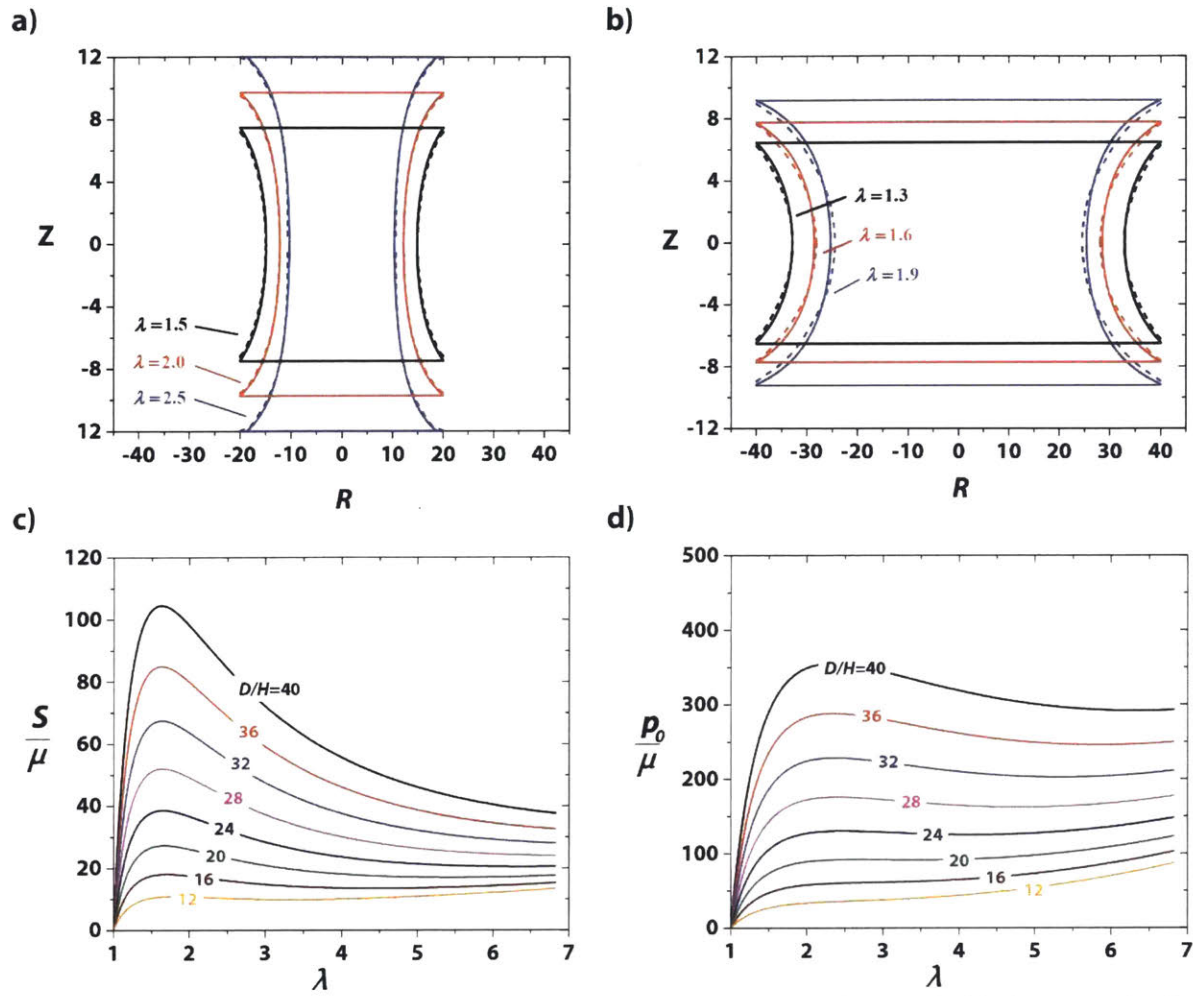


Figure 7-4: Theoretical and simulation results on the deformation and stress fields in constrained neo-Hookean layers under tension. (a) Comparison between theory and simulation of the meniscus profiles for the sample with aspect ratio of $\alpha = 4$ at the stretch of $\lambda = 1.5$, $\lambda = 2.0$ and $\lambda = 2.5$. Solid line represents the theoretical results; dashed line represents the simulation results. (b) Comparison between theory and simulation of the meniscus profiles for the sample with aspect ratio of $\alpha = 8$ at the stretch of $\lambda = 1.3$, $\lambda = 1.6$ and $\lambda = 1.9$. Solid line represents the theoretical results; dashed line represents the simulation results. (c) Theoretically calculated applied nominal stress versus stretch for the samples with various aspect ratios. (d) Theoretically calculated hydrostatic pressure at the center of the samples versus stretch for the sample with various aspect ratios.

Next, we derive the hydrostatic pressure at the center of the sample, which is given by

$$p_0 = p(\bar{Z} = 0, \bar{R} = 0) = \frac{1}{3} \text{tr}(\boldsymbol{\sigma})|_{\bar{Z}=0, \bar{R}=0} \text{ where } \boldsymbol{\sigma} = \mathbf{S}\mathbf{F}^T \text{ is the Cauchy stress tensor. From Eq. (7b),}$$

the expression of the hydrostatic pressure can be expressed as:

$$p_0 / \mu = \frac{\lambda_{rR}^2 + \lambda_{\theta\theta}^2 + \lambda_{zZ}^2 + \gamma_{rZ}^2}{3} - \bar{p}. \quad (7.16)$$

Inserting $\lambda_{rR}(\bar{Z} = 0) = \lambda_{\theta\theta}(\bar{Z} = 0) = \frac{1}{\cosh \kappa}$, $\lambda_{zZ}(\bar{Z} = 0) = \cosh^2 \kappa$, $\gamma_{rZ}(\bar{R} = 0, \bar{Z} = 0) = 0$ and

$$\bar{p}(\bar{R} = 0, \bar{Z} = 0) = \frac{1}{\cosh^2 \kappa} - \frac{\kappa^2 \alpha^2}{2 \cosh^2 \kappa}, \text{ one can write the hydrostatic pressure at the center of the}$$

sample as

$$p_0 / \mu = \frac{\cosh^4(\kappa)}{3} - \frac{1}{3 \cosh^2(\kappa)} + \frac{\kappa^2 \alpha^2}{2 \cosh^2(\kappa)} \quad (7.17)$$

The p_0 / μ vs λ curves for elastic layers with various aspect ratios α are shown in Fig. 7-4d. To

validate our results, we calculate $\frac{1}{\mu} \frac{dp_0}{d\lambda}|_{\lambda=1}$ and compare it with the reported small-strain solutions

(219), which shows good agreement (see Fig. A2-2b).

As a summary of this part, we have developed an analytical model to account for the large deformation of a constrained incompressible neo-Hookean layer under tension. The model gives analytic results on the deformation (Eq. (7.10), Fig. 7-4, a and b), the applied nominal stress (Eq. (7.15), Fig. 7-4c), and the hydrostatic pressure at the center of the layer (Eq. (7.17), Fig. 7-4d) as functions of the applied stretch on the layer. Our analytical model is validated by the results from numerical simulations and reported small-deformation solutions.

7.5.2 Onset of fringe and fingering instabilities

In this section, we will use the perturbation analysis to calculate the critical points for the onset of fringe and fingering instabilities. We introduce a trial form for the solutions consisting of the rotational invariant part at base state solved in Section 7.5.1 and an infinitesimal oscillatory part.

The fields of deformation and Lagrange multiplier with first order perturbation read as:

$$\mathbf{x} = (\mathbf{x})^0 + \varepsilon \tilde{\mathbf{x}}, \quad (7.18)$$

$$\bar{p} = (\bar{p})^0 + \varepsilon \tilde{p}, \quad (7.19)$$

where ε is a dimensionless small parameter, $\tilde{\mathbf{x}}$ and \tilde{p} are perturbed fields, $(\mathbf{x})^0$ and $(\bar{p})^0$ are the rotational invariant fields at base state, which is solved in Section 7.5.1 in the cylindrical basis $\{\mathbf{e}_R, \mathbf{e}_\Theta, \mathbf{e}_Z\}$ as:

$$(\mathbf{x})^0 = \frac{D\bar{R}}{2} \left[\frac{\cosh(\kappa\bar{Z})}{\cosh(\kappa)} - 1 \right] \mathbf{e}_R + \frac{H}{2} \left[\frac{\sinh(2\kappa)}{2\kappa} \frac{\tanh(\kappa\bar{Z})}{\tanh(\kappa)} - \bar{Z} \right] \mathbf{e}_Z, \quad (7.20)$$

$$(\bar{p})^0 = \frac{1}{2} \left[\frac{\cosh^4 \kappa}{\cosh^4(\kappa\bar{Z})} - \cosh^4 \kappa \right] + \frac{\kappa^2 \alpha^2}{2} \left[\bar{R}^2 \frac{\cosh^2(\kappa\bar{Z})}{\cosh^2 \kappa} - \frac{1}{\cosh^2 \kappa} \right] + \frac{1}{\cosh^2 \kappa}. \quad (7.21)$$

We assume the perturbed displacement field and the perturbed Lagrange multiplier follow the forms,

$$\tilde{\mathbf{x}} = A_1(R)u_1(Z) \cos(\omega\Theta) \mathbf{e}_R + A_2(R)u_1(Z) \sin(\omega\Theta) \mathbf{e}_\Theta + A_3(R)u_2(Z) \sin(\omega\Theta) \mathbf{e}_Z, \quad (7.22)$$

$$\tilde{p} = A_4(Z, R) \cos(\omega\Theta), \quad (7.23)$$

where A_i ($i = 1, 2, 3, 4$) are the amplitudes of perturbation. Therefore, the perturbed deformation gradient may write as $\mathbf{F} = (\mathbf{F})^0 + \varepsilon \text{Grad} \tilde{\mathbf{x}}$, where $(\mathbf{F})^0$ is the rotational invariant deformation

gradient at base state expressed in Eq. (7.5). By inserting the perturbed displacement field, the deformation gradient reads as:

$$\mathbf{F} = \begin{bmatrix} \lambda_{rR} + \varepsilon A_1' u_1 \cos(\omega\Theta) & -\varepsilon \frac{A_1\omega + A_2}{R} u_1 \sin(\omega\Theta) & \gamma_{rZ} + \varepsilon A_1 u_1' \cos(\omega\Theta) \\ \varepsilon A_2' u_1 \sin(\omega\Theta) & \lambda_{\theta\theta} + \varepsilon \frac{A_2\omega + A_1}{R} u_1 \cos(\omega\Theta) & \varepsilon A_2 u_1' \sin(\omega\Theta) \\ \varepsilon A_3' u_2 \cos(\omega\Theta) & -\varepsilon \frac{A_3\omega}{R} u_2 \sin(\omega\Theta) & \lambda_{zZ} + \varepsilon A_3 u_2' \cos(\omega\Theta) \end{bmatrix}. \quad (7.24)$$

Here the prime represents for differentiating respects to R or Z , i.e. $A_1' = \frac{dA_1}{dR}$, $A_2' = \frac{dA_2}{dR}$,

$A_3' = \frac{dA_3}{dR}$, $u_1' = \frac{du_1}{dZ}$ and $u_2' = \frac{du_2}{dZ}$. The incompressibility of the elastic layer is enforced by

$\det \mathbf{F} = 1$, which implies (expand to the first order of ε , see details in Appendix A2):

$$\lambda_{zZ} A_1' u_1 + \lambda_{zZ} \frac{A_2\omega + A_1}{R} u_1 - \gamma_{rZ} A_3' u_2 + \lambda_{rR} A_3 u_2' = 0. \quad (7.25)$$

The perturbation in deformation gradient will further induce a perturbation in nominal stress which reads as $\mathbf{S} / \mu = (\mathbf{S})^0 / \mu + \varepsilon \tilde{\mathbf{S}}$. Here, $\tilde{\mathbf{S}}$ is the perturbed normalized nominal stress, and each component of which is expressed as:

$$\tilde{S}_{rR} = \left[A_1' u_1 - (\bar{p})^0 (\gamma_{rZ} A_3' u_2 - \lambda_{zZ} A_1' u_1) - \frac{A_4}{\lambda_{rR}} \right] \cos(\omega\Theta), \quad (7.26a)$$

$$\tilde{S}_{r\theta} = \left[-\frac{A_1\omega + A_2}{R} u_1 + (\bar{p})^0 \lambda_{zZ} A_2' u_1 \right] \sin(\omega\Theta), \quad (7.26b)$$

$$\tilde{S}_{rZ} = \left[A_1 u_1' + (\bar{p})^0 \lambda_{rR} A_3' u_2 \right] \cos(\omega\Theta), \quad (7.26c)$$

$$\tilde{S}_{\theta R} = \left[A_2' u_1 - (\bar{p})^0 \lambda_{zZ} \frac{A_1\omega + A_2}{R} u_1 + (\bar{p})^0 \gamma_{rZ} \frac{A_3\omega}{R} u_2 \right] \sin(\omega\Theta), \quad (7.26d)$$

$$\tilde{\mathbf{S}}_{\Theta\Theta} = \left[\lambda_{rR}^2 \gamma_{rZ} A_3' u_2 - \lambda_{rR}^3 A_3 u_2' - A_1' u_1 - (\bar{p})^0 (\lambda_{zZ} A_1' u_1 - \gamma_{rZ} A_3' u_2 + \lambda_{rR} A_3 u_2') - \frac{A_4}{\lambda_{rR}} \right] \cos(\omega\Theta), \quad (7.26e)$$

$$\tilde{\mathbf{S}}_{\Theta Z} = \left[A_2 u_1' - (\bar{p})^0 \lambda_{rR} \frac{A_3 \omega}{R} u_2 \right] \sin(\omega\Theta), \quad (7.26f)$$

$$\tilde{\mathbf{S}}_{zR} = \left[A_3' u_2 + \lambda_{rR} \gamma_{rZ} A_4 + (\bar{p})^0 \gamma_{rZ} (\lambda_{rR}^2 \gamma_{rZ} A_3' u_2 - \lambda_{rR}^3 A_3 u_2' - A_1' u_1) + (\bar{p})^0 \lambda_{rR} A_1 u_1' \right] \cos(\omega\Theta), \quad (7.26g)$$

$$\tilde{\mathbf{S}}_{z\Theta} = \left[-\frac{A_3 \omega}{R} u_2 - (\bar{p})^0 \gamma_{rZ} A_2' u_1 + (\bar{p})^0 \lambda_{rR} A_2 u_1' \right] \sin(\omega\Theta), \quad (7.26h)$$

$$\tilde{\mathbf{S}}_{zZ} = \left[A_3 u_2' - \lambda_{rR}^2 A_4 - (\bar{p})^0 \lambda_{rR} u_1 \left(A_1' + \frac{A_2 \omega + A_1}{R} \right) \right] \cos(\omega\Theta), \quad (7.26i)$$

A balance of the forces exerted on an element of the perturbed material further leads to three equations of equilibrium $\text{Div } \tilde{\mathbf{S}} = 0$. These equations are only required to satisfy in $\bar{Z} = \bar{Z}_0$ with \bar{Z}_0 is the vertical location where the undulations initiates. The four unknown A_i ($i = 1, 2, 3, 4$) can be fully specified by these three equations and the incompressibility condition in Eq. (7.25) with boundary conditions. The boundary conditions are still the traction $\mathbf{t}_R = \mathbf{S} \cdot \mathbf{e}_R$ be zero at $\bar{R} = 1$ (For cases when $\bar{Z}_0 \neq 0$, this is an approximation). Since the rotational invariant stress at base state already satisfies the boundary conditions, then we have $\tilde{\mathbf{S}} \cdot \mathbf{e}_R = 0$ at $\bar{R} = 1$. Also we are looking for the solution which decays as $\bar{R} \rightarrow 0$ (See details in Appendix. A2).

By simplifying the four equations through eliminating A_2 and A_4 , we can finally obtain two governing equations in the dimensionless form with respect to A_1 and A_3 (for more details, see Appendix. A2). We can solve these equations by numerically or even analytically with infinite series. However, to obtain the physical insight, we choose to make some approximations to simplify the equations. We notice the difference between fingering and fringe instabilities:

fingering instability is an instability mode with $A_3 = 0$ (see Fig. A2-3a) while the fringe instability is an instability mode with generally $A_3 \neq 0$ (see Fig. A2-3b). Physically, the zero amplitude along Z direction for fingering instability is a consequence of symmetry. For fringe instability, we argue that if α is slightly smaller than the theoretical transition aspect ratio $\alpha_{\text{fringe-fingering}}$ between fingering instability and fringe instability, $A_3 \ll A_1$ and $A_3 \ll A_2$, or explicitly $A_3 \approx 0$. By adopting this approximation, the only governing ODE to be solved is with respect to the amplitude along radius direction A_1 in the dimensionless form, reading as (see details in Appendix. A2 For dimensionless form, the prime is for differentiating respect to \bar{R}):

$$\begin{aligned} \bar{R}^4 A_1^{(4)} + 6\bar{R}^3 A_1^{(3)} + (5 - 2\omega^2) \bar{R}^2 A_1'' - (2\omega^2 + 1) \bar{R} A_1' + (\omega^2 - 1)^2 A_1 \\ - A_h^2 \bar{R}^2 \left[\bar{R}^2 A_1'' + 3\bar{R} A_1' - (\omega^2 - 1) A_1 \right] = 0, \end{aligned} \quad (7.27)$$

with $A_h = \sqrt{\frac{\kappa^2 \alpha^2}{1 - \lambda_{rR}}}$. Next we impose the boundary conditions on this governing ODE. The

boundary condition of $\tilde{S}_{zR} = 0$ automatically satisfies with the condition that $A_3 \ll A_1$ and $A_3 \ll A_2$.

The remaining two boundary conditions in the dimensionless form read as:

$$A_1^{(3)}(1) + 4A_1''(1) + \left[1 - 2\omega^2 - \zeta\omega^2 - A_h^2 \right] A_1'(1) + \left[\omega^2 - 1 + \omega^2 \kappa^2 \alpha^2 - A_h^2 \right] A_1(1) = 0, \quad (7.28a)$$

$$A_1''(1) + (2 - \zeta) A_1'(1) + \zeta (\omega^2 - 1) A_1(1) = 0, \quad (7.28b)$$

with

$$\zeta(\bar{Z}_0) = \frac{1}{2} \kappa^2 \alpha^2 + \frac{1}{2} \lambda_{rR}^{-6} + C_3 \lambda_{rR}^{-2}, \quad (7.28c)$$

$$C_3 = \frac{1}{\cos^2 \kappa} \left[1 - \frac{1}{2} \kappa^2 \alpha^2 \right] - \frac{1}{2} \cos^4 \kappa. \quad (7.28d)$$

There are four characteristic roots for Eq. (7.27): two of them are decay solutions (decreases as $\bar{R} \rightarrow 0$) and the other two are non-decay (diverges as $\bar{R} \rightarrow 0$). The two non-decay solutions vanish. After going through the algebra, the general solution of A_1 can be written as (see details in Appendix. A2):

$$A_1 = c_1 \bar{R}^{\omega-1} + c_2 \frac{1}{I_\omega(A_h)} I_\omega(A_h \bar{R}) \bar{R}^{-1}, \quad (7.29)$$

where $I_\omega(\bullet)$ is the modified Bessel function of the first kind, c_1 and c_2 are arbitrary pre-factors (see details in Appendix. A2). Insert this solution into the two boundary conditions in Eq. (7.28a) and Eq. (7.28b), The existence of the non-trivial solution depends on whether the following equation has solution or not:

$$\begin{aligned} & \left(l^2 \omega^3 A_h + l A_h^3 - l^2 \omega A_h \right) \frac{I_{\omega-1}(A_h)}{I_\omega(A_h)} - \left(2l \omega^2 A_h^2 + 2l^2 \omega^4 - 2l^2 \omega^2 + A_h^4 \right) \\ & + \left(2l \omega^2 + \omega A_h^2 - l \omega A_h \frac{I_{\omega-1}(A_h)}{I_\omega(A_h)} \right) \kappa^2 \alpha^2 = 0, \end{aligned} \quad (7.30)$$

where $l = 1 + \zeta$.

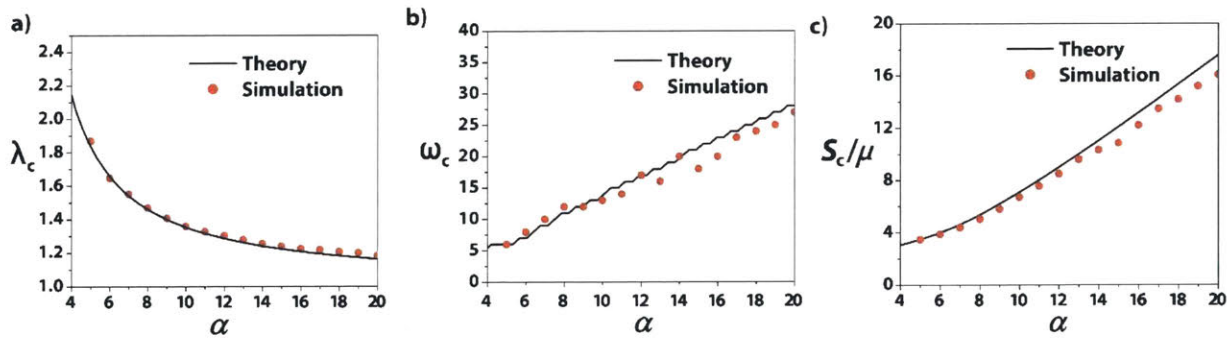


Figure 7-5: Theoretical and simulation results on the critical points of fingering instability and fringe instability for the sample with aspect ratios $\alpha > 4$. a) Comparison of the critical stretch λ_c for the onset of instabilities between theory and simulation. b) Comparison of the critical mode number ω_c between theory and simulation. a) Comparison of the critical applied stress S_c between theory and simulation.

By minimizing κ through ω at each plane \bar{Z} , we can have the critical stretch λ_c , the critical number of undulations ω_c and the vertical location of the plane where the undulations initiate \bar{Z}_0 . As shown in Fig. 7-5, a and b, our theory predicts quite well for both λ_c and ω_c at the onset of instabilities in the range $\alpha > 4$, comparing with the simulation results. With the deformation field we derived in Section 7.5.1, we further predict the critical applied nominal stress S_c for the onset of instabilities shown in Fig. 7-5c. Our theory with incompressible assumption is slightly higher than the simulation results with negligible compressibility (in simulation, bulk modulus is set 2000 times the shear modulus, i.e. $K/\mu=2000$), which is reasonable.

Moreover, to theoretically identify the critical geometrical aspect ratio between fringe instability and fingering instability $\alpha_{fringe-fingering}$, we compare the critical stretch for the case with initial location of undulations at $\bar{Z}_0 = 0$ and $\bar{Z}_0 \neq 0$. If the critical stretch for the case $\bar{Z}_0 = 0$ is the smallest, then fingering instability will be triggered first. On the other hand, if the critical stretch for the case $\bar{Z}_0 = 0$ is not the smallest, fringe instability will be triggered first and fingering instability will be suppressed. Fig. 7-6a presents the critical stretch for both cases with $\bar{Z}_0 = 0$ and $\bar{Z}_0 = 0.2$ calculated from Eq. (30) as an example. As show in Fig. 7-6a, when α is below a critical value, fringe instability will be more favorable than fingering instability. In order to identify the boundary between these two instabilities, we plot the location of the initiation of the instabilities for layers with various aspect ratios α . In the current work, we focus on the case with very small \bar{Z}_0 (i.e. $\bar{Z}_0 \leq 0.3$). As we can see in Fig. 7-6b, when $\alpha > 4.9$, the initiation of the instability occurs at the middle plane, which is the case of fingering instability. In contrast, when

$\alpha < 4.9$, the lower critical stretch is identified at $\bar{Z}_0 \neq 0$, which is corresponding to fringe instability. Therefore, the theoretically calculated critical transition between fingering instability and fringe instability is identified as 4.9, which agrees with the simulation results (i.e. $\alpha_{fringe-fingering} = 5$) discussed in Section 7-4.

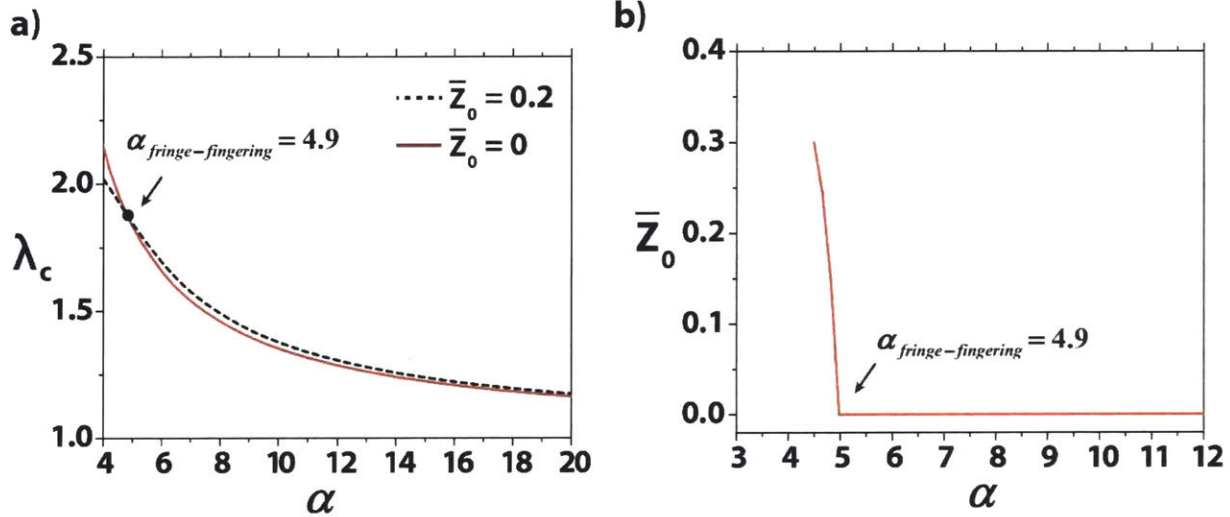


Figure 7-6: Theoretical results on the transition between fringe and fingering instability. (a) Critical stretch for the sample with the locations for the initiation of undulations at $\bar{Z}_0 = 0$ and $\bar{Z}_0 = 0.2$. (b) The location of the initiation of the instabilities \bar{Z}_0 for the sample with different aspect ratios.

7.6 Onset of cavitation instability

Cavitation is the another mode of mechanical instability emerging in elastic layers under tension, as the hydrostatic pressure in the layer reaches a critical value (101, 234). Theoretical explanation of the nucleation and growth of a cavity within a bulk material has been intensively studied, which was either considered as a process of creation of a new surface representing fracture (235) or regarded as an elastic instability of a pre-existing cavity undergoing hydrostatic pressure (211, 236, 237). Here, we take the emergence of cavity as an elastic instability and adopt the bifurcation

theory (236) to calculate the critical hydrostatic traction on the pre-existing cavity for the onset of cavitation instability in an incompressible Neo-Hookean solid (211).

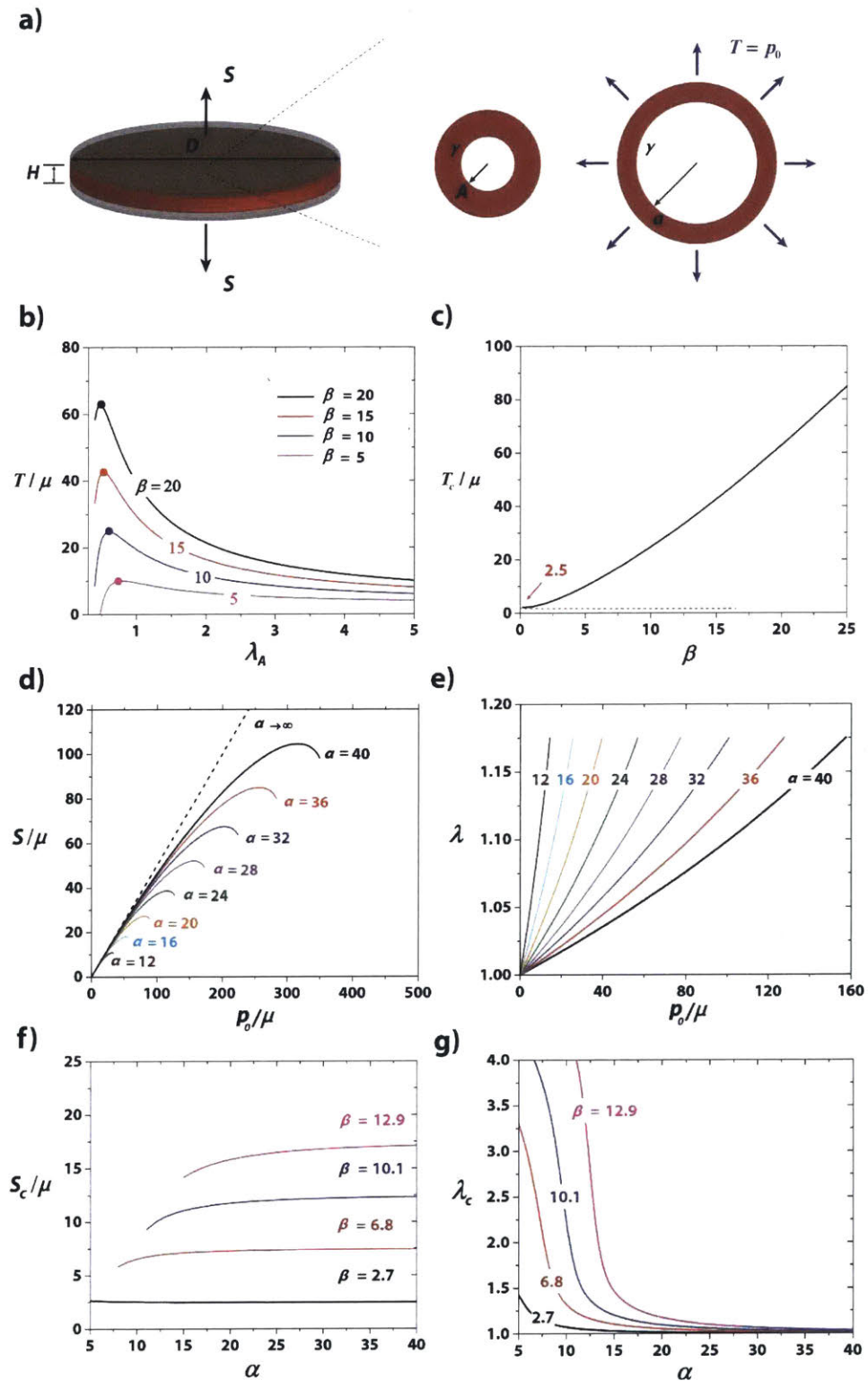


Figure 7-7: Theoretical results on the critical points for cavitation instability. (a) Schematic of the growth of pre-existing cavity within a cylindrical sample. (b) Applied hydrostatic traction T/μ on the spherical shell versus the expansion ratio λ_A of pre-existing cavity for the material with various β . (c) Critical hydrostatic traction T_c/μ for the material with various β . (d) Theoretically calculated applied nominal stress S/μ versus hydrostatic pressure p_0/μ at the center of the sample. Dash line denotes the solution from theory with small strain assumption when $\alpha \rightarrow \infty$. (e) Theoretically calculated stretch λ versus hydrostatic pressure p_0/μ at the center of the sample. (f) Critical applied nominal stress S_c/μ for cavitation instability in samples with various α and β . (g) Critical applied nominal stretch λ_c/μ for cavitation instability in samples with various α and β .

For a cavity under uniform hydrostatic traction T , by analyzing the force balance on the spherical shell surrounding the cavity with outer surface of $B \gg A$ (see Fig. 7-7a), the relation between the applied hydrostatic traction T and the expansion of the cavity can be expressed as (211):

$$\frac{T}{\mu} = \frac{2\beta}{\lambda_A} - \frac{2}{\lambda_A} - \frac{1}{2\lambda_A^4} + \frac{2}{\lambda_R} + \frac{1}{2\lambda_R^4}, \quad (7.31)$$

Where $\lambda_A = a/A$, $\beta = \gamma/(\mu A)$ and $\lambda_R = (1 - f^3 + f^3 \lambda_A^3)^{1/3}$ with $f = B/A$ comes from the constraints of volume conservation. In this study, f is set as 1000, which is sufficient large to ensure that the result is independent of B (as $B \gg A$). From this expression, we can see that the expansion of a cavity highly depends on the dimensionless elastocapillary number β (91, 101, 238). For example, if $\beta < 1$, the critical hydrostatic traction T_c approaches to 2.5μ and the cavity grows gradually with the increase of the hydrostatic traction T , which is the common case for rubbers. However, if $\beta \gg 1$, the applied hydrostatic traction T first increases dramatically with a negligible expansion of the cavity up to a maximum critical value shown in Fig. 7-7b, and thereafter the cavity bifurcates to a stable state suddenly with a large expansion ratio (211, 236).

The maximum hydrostatic traction T_c determines the critical point for the onset of cavitation instability. As shown in Fig. 7-7c, the effect of surface tension can enhance the critical hydrostatic traction T_c by multiple times, which is common for soft hydrogels with relative high dimensionless capillary number β (91).

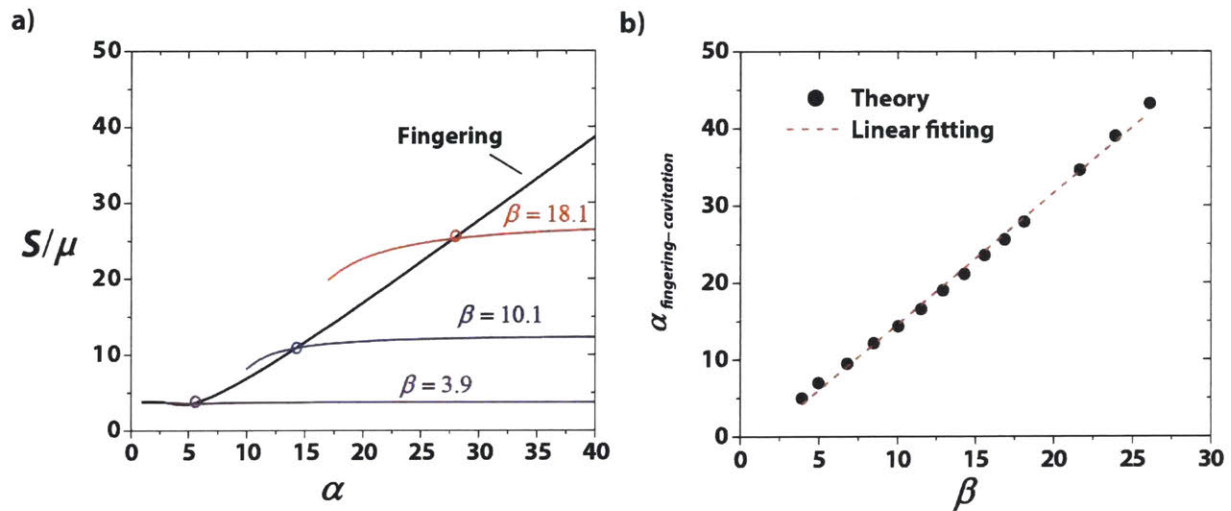


Figure 7-8: Theoretical results on the transition between fingering instability and cavitation instability. a) Critical applied nominal stress for fingering stability and cavitation instability with various dimensionless capillary number β . b) Theoretical calculation of the critical transition aspect ratio $\alpha_{\text{fingering-cavitation}}$. Dashed line represents the linear fitting curve from the theoretical calculation.

When a cylindrical layer is under tension as illustrated in Fig. 7-7a, the pre-existing cavity within the layer can be approximated in the state of uniform hydrostatic stress if the layer's aspect ratio is relative large (e.g. $\alpha > 5$) (102, 230). Specifically focusing on the center of the layer with the highest chance of emergence of cavitation, when the hydrostatic pressure p_0 reaches the critical hydrostatic traction T_c shown in Fig. 7-7c, cavitation instability sets in the layer. To identify the critical applied stress S_c or the applied stretch λ_c for the onset of cavitation, we recall Eq. (7.15) and Eq. (7.17) derived in Section 7.5.1 and calculate the correlation between the applied nominal stress S or the applied nominal stretch λ and the hydrostatic pressure at the center of

the sample p_0 for various aspect ratios α in Fig. 7-7, d and e. In the limiting case of $\alpha \rightarrow \infty$, our theory is reduced to $S = \frac{p_0}{2}$, which is consistent with the reported results (100). We summarize the calculated critical stress S_c and the critical stretch λ_c for the layers with various aspect ratio α and dimensionless capillary number β shown in Fig. 7-7, f and g. The critical nominal stress S_c for the onset of cavitation instability weakly dependent on layers' aspect ratio α while the critical stretch λ_c decreases dramatically as the increase of layers' aspect ratio α . For a layer with relatively small aspect ratios (e.g. $\alpha < 5$), there will be no cavitation emerging owing to the non-symmetric stress state (95, 102) and therefore only fringe instability sets in with the increase of the applied load.

To further theoretically calculate the critical transition aspect ratio from fingering to cavitation $\alpha_{\text{fingering-cavitation}}$, we plot the critical applied stress for both fingering instability and cavitation instability with various dimensionless capillary number β (see Fig. 7-8a). The intersections of both curves identify the critical transition aspect ratio from fingering to cavitation $\alpha_{\text{fingering-cavitation}}$ for the samples with various β . As shown in Fig. 7-8b, the correlation between $\alpha_{\text{fingering-cavitation}}$ and β can be fitted simply by a linear relation:

$$\alpha_{\text{fingering-cavitation}} = 1.7\beta - 2.5, \alpha > 5. \quad (7.32)$$

7.7 Evolution of instabilities

In Section 7.5, we use linear perturbation analysis to calculate the critical points for the onset of fringe instability and fingering instability. In this Section, we further use simulation and experiment to discuss the evolution of fringe and fingering instabilities after their onsets and their corresponding applied stress-stretch relations (S vs. λ).

7.7.1 Monotonic vs. non-monotonic stress-stretch relations

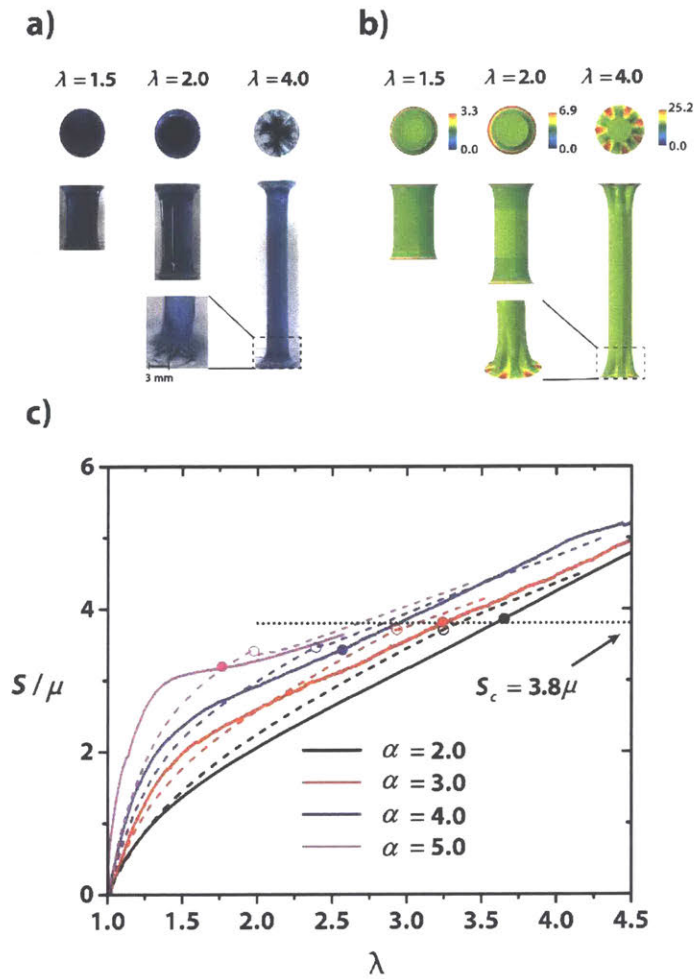


Figure 7-9: Experimental and simulation results on fringe instability. a) Experimental observation and b) corresponding simulations for the formation of fringe instability for the sample with $\alpha = 2$. c) Applied nominal stress versus stretch curves from experiments (solid lines) and simulations (dashed line) for the sample with $\alpha = 2, 3, 4$, and 5 .

For the samples with small aspect ratios (e.g. $\alpha = 2$), the middle portion of the layer elongates uniformly and the constrained fringe portions deform non-uniformly into a V shape, prior to instability. Since the middle portion of the layer is almost uniformly elongated under high applied stretches (e.g. $\lambda = 1.5, 2$), the driving force for the formation of any instability in the middle portion of the layer in the sample, is limited. Instead, as the soft elastic layer is further stretched to

a critical point (i.e. $\lambda_c = 3.6$ in experiment and $\lambda_c = 3.2$ in simulation), the exposed surface of the fringe portions becomes unstable – beginning to undulate periodically. The applied stress-stretch curves corresponding to fringe instability (e.g. $\alpha = 2, 3, 4, 5$) are all shown to be monotonic from both experiment and simulation in Fig. 7-9c, indicating that fringe instability is a local instability mode. The critical applied nominal stress for the onset of fringe instability with various aspect ratios is equal to 3.8 times shear modulus of the layer (see Fig. 7-9c and Fig. 7-11), which is consistent with the layers with rectangular shape (51). With the increase of aspect ratio of the layer ($\alpha > 5$), fingering instability initiates at the middle plane of the layer. As shown from the experimental and simulation results in Fig. 7-10a, the layer with aspect ratio $\alpha = 12$ deforms as the meniscus shape at the exposed surface at the stretch of $\lambda = 1.1$. As the stretch reaches $\lambda_c = 1.3$, undulation forms at the exposed surface and the amplitude of the fingers increases gradually with the further increase of the applied load. Different from fringe instability, the applied nominal stress-stretch curves are shown to be non-monotonic (see Fig. 7-10b and Fig. 7-10d). In addition, the critical applied stress increases with the increase of aspect ratio α shown in Fig. 7-11.

7.7.2 Type I fingering vs. Type II fingering

While the applied stress-stretch relations in samples subjected to fingering instability are non-monotonic, the peak stress (S_p) can exactly correspond to or slightly fall behind the critical point (S_c) for the onset of fingering instability. As shown in Fig. 7-10, a and b, for the sample with moderate aspect ratio $\alpha = 12$, the onset of fingering instability is exactly corresponding to the peak stress, which indicates this type of fingering instability is a global instability mode. In contrast, for the sample with large aspect ratio (e.g. $\alpha = 32$ in Fig. 7-10, c and d), the emergence of fingering instability corresponds to an inflection point in the applied nominal stress-stretch curve and the stress keeps increasing until the layer reaches the peak stress, manifesting that this type of fingering

instability is a local instability mode. To distinguish the two types of fingering instability, we term the instability as *Type I fingering instability* if the onset of the undulations corresponds to the maximum applied nominal stress; and term the instability as *Type II fingering instability* if the onset of the undulations deviates from the maximum applied nominal stress (Fig. 7-11, a and b). We further performed cyclic loading for both layers and found that the stress-stretch curves at first loading and subsequent loading are consistent with each other, which manifests that both types of fingering instability are reversible and elastic response (see in Fig. 7-10, b and d). To further visualize the evolution of the two types of fingering instabilities, we performed the corresponding numerical simulation in Abaqus/Explicit. Fig. 7-10a shows the formation of Type I fingering instability in the layer with $\alpha = 12$ and Fig. 7-10c shows the formation of Type II fingering instability in the layer with $\alpha = 32$. Different from Type I fingering instability, after the initiation of fingering undulations at the lateral surfaces, the applied nominal stress keeps increasing.

To further identify the transition between type I fingering instability and type II fingering instability, we measured both the critical applied nominal stress S_c for the onset of instability and the peak stress S_p from experimental and simulation results. As summarized in Fig. 7-11, for the samples with moderate aspect ratios (e.g. $5 < \alpha < 20$), the critical stress for the onset of instability exactly corresponds to the peak stress (i.e. $S_c = S_p$); while for the samples with large aspect ratios (e.g. $\alpha > 20$), the critical stress for the onset of instability is slightly lower than the peak stress (i.e. $S_c < S_p$). Here, we identify the critical transition aspect ratio between two types of fingering instability as $\alpha_{\text{TypeI-TypeII}} = 20$ from the numerical simulation.

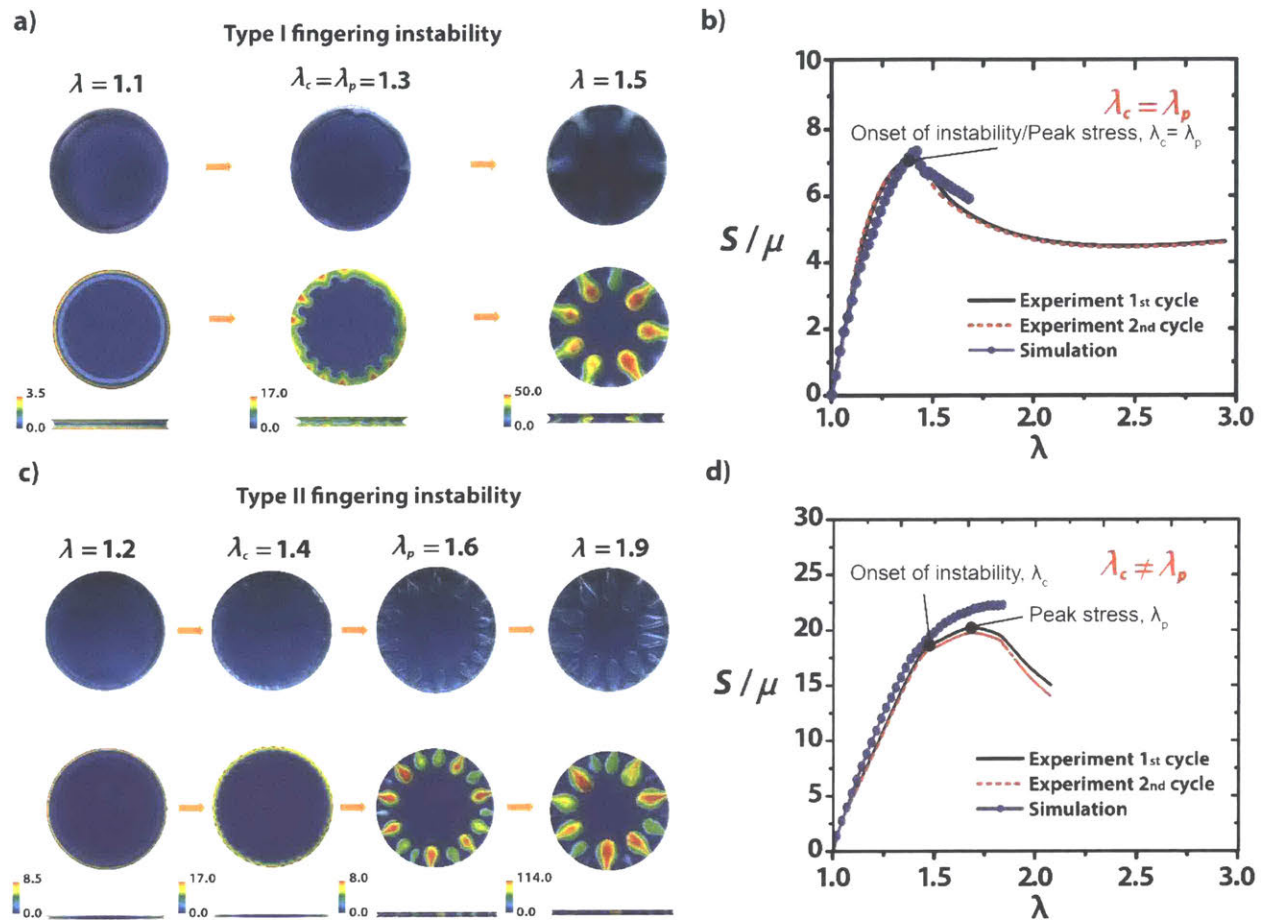


Figure 7-10: Experimental and simulation results on fingering instability. (a) Experimental observation and corresponding simulations for the formation of Type I fingering instability for the sample with $\alpha = 12$. (b) Applied nominal stress versus stretch curves from experiments and simulations for the sample with $\alpha = 12$. (c) Experimental observation and corresponding simulations for the formation of Type II fingering instability for the sample with $\alpha = 32$. (d) Applied nominal stress versus stretch curves from experiments and simulations for the sample with $\alpha = 32$. Here, the bulk modulus in simulation is set as $K = 200\mu$ to match well with the experimental results, which means the sample we used is not ideally incompressible.

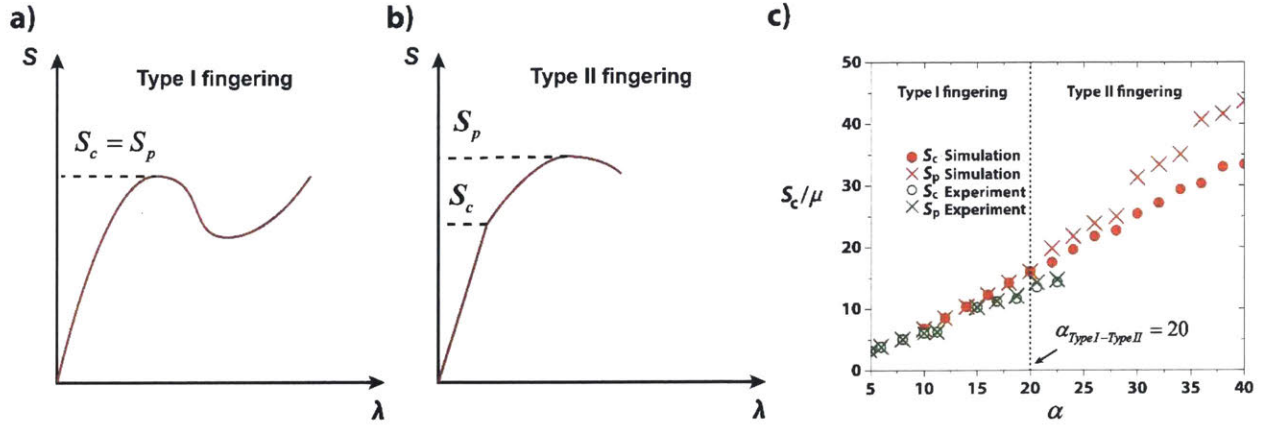


Figure 7-11: (a) Schematic illustration of the stress versus stretch curve for type I fingering instability occurring in the layer with small α . (b) Schematic illustration of the stress versus curve for type II fingering instability occurring in the layer with large α . (c) Experimental and simulation results on the critical stress S_c and the peak stress S_p to identify the transition between Type I fingering instability and Type II fingering instability. When $\alpha > 20$, the critical stress for the onset of fingering instability deviates from the maximum peak stress, where Type II fingering instability sets in.

7.8 A phase diagram for instabilities

As the applied stretch or stress on the constrained elastic layer reaches a critical value, a mode of mechanical instability sets in the layer. While the selection of fringe or fingering instability is governed by the geometry of the elastic layer via $\alpha = D/H$, the cavitation instability is also affected by material properties and defects of the elastic layer via $\beta = \gamma / \mu A$. Therefore, we can predict the occurrence of any mode of instability using a phase diagram with two control parameters: $\alpha = D/H$ and $\beta = \gamma / \mu A$.

In Section 7.4 and Section 7.5.2, we have illustrated the transition from fringe instability to fingering instability as $\alpha_{fringe-fingering} = 5$ from simulation and $\alpha_{fringe-fingering} = 4.9$ from theory. In Section 7.5.3, we identify the transition from fingering instability to cavitation instability as $\alpha_{fingering-cavitation} = 1.7\beta - 2.5$ for the samples with aspect ratios $\alpha > 5$. In Section 7.6, we identify the

transition aspect ratio from Type I fingering instability to Type II as $\alpha_{TypeI-TypeII} = 20$ from numerical calculation.

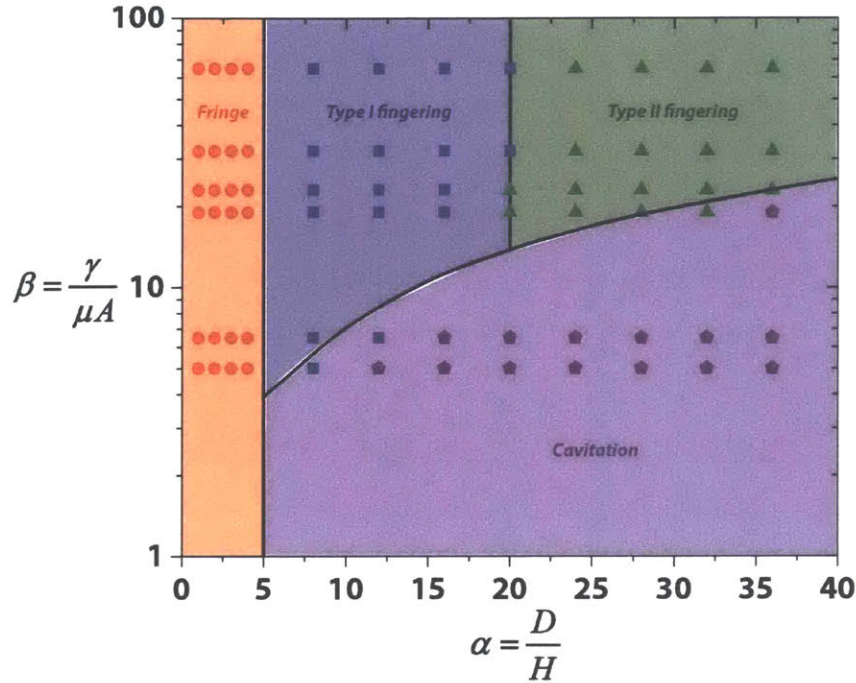


Figure 7-12: Phase diagram for the initial occurrence mode of mechanical instabilities. The lines are from theory and simulation, and the dots are from experiments. Red circular dots denote the occurrence of fringe instability, blue square dots denote the occurrence of Type I fingering instability, green triangular dots denote the occurrence of Type II fingering instability and purple pentagon dots denote the occurrence of cavitation instability.

With the identified $\alpha_{fringe-fingering}$, $\alpha_{fingering-cavitation}$ and $\alpha_{TypeI-TypeII}$, we construct the phase diagram in the plot of aspect ratio α and dimensionless capillary number β shown in Fig. 7-12. The solid lines in Fig. 7-12 are from theory and simulations. To illustrate the phase diagram, we qualitatively discuss three representative cases for the initial occurrence mode of the samples with wide range of β . For the sample with small dimensionless capillary number β (e.g. $\beta = 3.9$ in Fig. 7.8a and Fig. 7.12), fringe instability emerges at the exposed free surfaces of the sample with small aspect ratio (i.e. $\alpha < 5$). As the increase of α , cavitation instability within the sample

forms prior to the formation of fingering instability. Both Type I and Type II fingering instabilities are suppressed in this case, which is commonly observed for rubber-like samples. If β is moderate large (e.g. $\beta = 10.1$ in Fig. 7-8a and Fig. 7-12), the sample exhibits fringe instability if aspect ratio is small (e.g. $\alpha < 5$), Type I fingering instability if aspect ratio is moderate large (i.e. $5 < \alpha < 14$), and cavitation instability within the sample if aspect ratio is extremely large (i.e. $\alpha > 14$). In this case, Type II fingering instability is suppressed. If β is sufficient high (e.g. $\beta = 18.1$ in Fig. 7-8a and Fig. 7-12), all modes of mechanical instabilities including fringe instability, Type I fingering instability, Type II fingering instability and cavitation instability can be observed across a wide range of aspect ratios α .

The phase diagram is also validated by experiments. We chose materials with six constituents with controlled critical defect size of $A = 1\mu\text{m}$, surface tension $\gamma = 0.07\text{N/m}$ while varying the shear modulus μ (see details in Fig. 7-2). For each constituent, samples were measured across wide range of aspect ratios to investigate the initial mode of mechanical instabilities. The experimental data matches relatively well compared with the theoretical predication of the phase diagram in Fig. 7-12.

7.9 Coexistence and interactions of instabilities

From our experiments and simulations, we find that cavitation instability can coexist with fingering instability and their interactions can affect each other. We will discuss two scenarios on coexistence and interactions of cavitation and fingering instabilities: cavitation instability occurs prior to the formation of fingering instability; fingering instability forms prior to the nucleation of cavitation instability.

As shown in Fig. 7-13a, we show the evolution of a sample under tension from top view with aspect ratio of $\alpha = 20$ and dimensionless capillary number of $\beta \approx 7$ ($\gamma \approx 0.07\text{N/m}^2$,

$\mu \approx 10$ kPa and $A \approx 1$ μm). At small deformation, the applied nominal stress increases linearly with uniform shrinkage of the sample (see Fig. 7-13b). When the applied nominal stress reaches ~ 60 kPa, a cavity nucleates suddenly in the sample and more and more cavities nucleates within the sample with the further increase of load. When the applied nominal stress reaches the maximum stress ~ 105 kPa, the exposed meniscus becomes unstable and form periodic undulated patterns, demonstrating the coexistence of cavitation instability within the sample and fingering instability at the exposed meniscus. As the sample is further loaded, the growth of fingering tends to suppress the growth of cavitation within the sample. The coexistence of cavitation instability and fingering instability can be interpreted as follows. As shown in Fig. 7-13c, since the critical applied nominal stress for the onset of cavitation instability is smaller than that of the initiation of fingering instability, the onset of cavitation instability occurs first, corresponding to a negligible kink in the applied nominal stress-stretch curve (shown in Fig. 7-13b). The further increase of the applied load can serve as an additional driving force to initiate the fingering instability at the exposed lateral surface.

Likewise, we demonstrate another example with the sample of aspect ratio $\alpha = 28$ and dimensionless number of $\beta \approx 35$ ($\gamma \approx 0.07$ N/m², $\mu \approx 2$ kPa and $A \approx 1$ μm), in which fingering instability forms first at the exposed surface and a cavity nucleates within the sample thereafter. As shown in Fig. 7-13, d and e, when the applied nominal stress reaches ~ 40 kPa, the exposed meniscus undulated, showing fingering instability. Thereafter, the amplitude of the fingers increases gradually and a cavity nucleates within the sample when the applied nominal stress reaches ~ 43 kPa. As the further increase of the applied load, both fingers at the exposed surfaces and the cavity within the sample grow by size gradually. As theoretical interpretation shown in Fig. 7-13f, the critical applied nominal stress for the onset of fingering instability is smaller than

that of the initiation of cavitation instability, fingering instability forms first. Since the fingering instability in this sample ($\alpha = 24$) is Type II fingering instability, the applied nominal stress keeps increasing and gives a further driving force for the initiation of the cavitation instability.

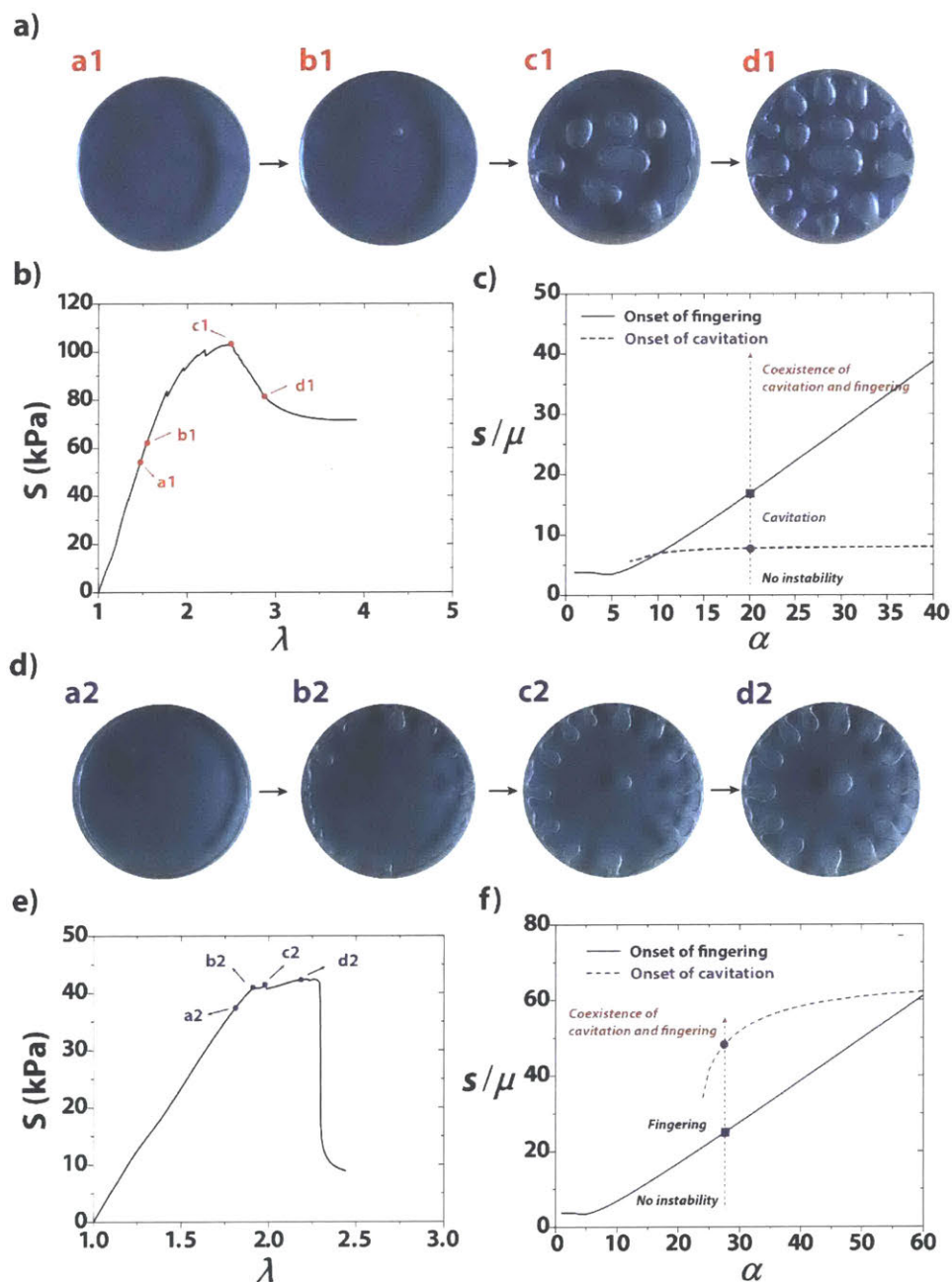


Figure 7-13: Coexistence of cavitation instability and fingering instability. a), b) and c) A cavity forms suddenly within the sample, and then the applied nominal stress keeps increasing up to the maximum point which corresponds to the initiation of fingering instability at the exposed surface. The sample has an aspect

ratio $\alpha = 20$ (i.e. $D = 40\text{mm}$ and $H = 2\text{mm}$) and dimensionless number of $\beta \approx 7$ ($\gamma \approx 0.07 \text{ N/m}^2$, $\mu \approx 10 \text{ kPa}$ and $A \approx 1 \mu\text{m}$). d), e) and f) Type II fingering forms first at the exposed surface and a cavity forms suddenly within the sample with the further increase of the applied nominal stress, which exhibits the coexistence of Type II fingering instability and cavitation instability. The sample has an aspect ratio $\alpha = 28$ (i.e. $D = 56\text{mm}$ and $H = 2\text{mm}$) and dimensionless number of $\beta \approx 35$ ($\gamma \approx 0.07 \text{ N/m}^2$, $\mu \approx 2 \text{ kPa}$ and $A \approx 1 \mu\text{m}$). The stretch rate of both experiments are 0.016 s^{-1} .

7.10 Concluding remarks

In this paper, we perform a systematic study on the formation, transition, interaction and coexistence of mechanical instabilities in confined elastic layers under tension through combined experimental, simulation and theoretical analysis. A phase diagram is constructed to quantitatively predict the occurrence of any mode of instability. The main conclusions are summarized as follows:

- Both fringe instability and fingering instability feature the undulation at the exposed surface. The main differences between the two instabilities are twofold. First, fringe instability initiates at the fringe portion while fingering instability forms at exact the middle plane of the layer; the stress-stretch response of the sample with fringe instability is monotonic while that of the sample with fingering instability is non-monotonic. There exists a critical transition aspect ratio between fringe and cavitation, which we identify as $\alpha_{\text{fringe-fingering}} = 5$ from simulation and $\alpha_{\text{fringe-fingering}} = 4.9$ from theory.
- For fingering instability, the point of the peak stress can exactly correspond to or slightly fall behind the critical point for the onset of fingering instability, which is corresponding to Type I fingering instability and Type II fingering instability, respectively. We identify

the critical transition aspect ratio between Type I fingering and Type II fingering as

$$\alpha_{\text{TypeI-TypeII}} = 20 \text{ from simulation.}$$

- The initial occurrence mode of instability can be tuned by two dimensionless numbers: aspect ratio α and dimensionless capillary number β . For a material with controlled capillary number β , there exists a critical transition aspect ratio between fingering instability and cavitation instability, can be approximately identified as $\alpha_{\text{fingering-cavitation}} = 1.7\beta - 2.5$.

- The cavitation instability can coexist with fingering instability and interact with each other.

The systematic study on various mechanical instabilities in this paper can serve as a foundation on predicting the mechanical responses in confined elastic layers and thereafter facilitate to enhance the mechanical performance and prevent failures or ruptures. In addition to the significance in mechanical design, the tunable mode of mechanical instability can have the potential to tune the functional responses such as light transmission, electrical conductivity and acoustic transmission through mechanical stimuli.

Chapter 8

Conclusions and future outlook

8.1 Summary of contributions

How to design hydrogels that can possess a set of tissue-like combinational properties in one material system remains an open challenge in the field of soft materials. This thesis focuses on the design of three mechanical properties of synthetic hydrogels. We perform scaling analysis of fracture energies in tough hydrogels and develop a coupled cohesive zone and Mullins effect model for prediction. The principle for the design of tough hydrogels is to build dissipation into stretchy network. We propose a method to design resilient yet tough hydrogels by pre-deforming tough hydrogel via delayed dissipation. Furthermore, we show that fatigue thresholds of hydrogels can be highly enhanced by the introduction of crystalline domains and aligned nanofibrils.

Surface instabilities in hydrogels (e.g., wrinkles, creases, and folds) have been intensively studied. However, three-dimensional instabilities of hydrogels are rarely reported due to the difficulty in experiment. In this dissertation, we use the technique of tough hydrogel bonding to perfectly anchor hydrogel layers on rigid glass substrates, which allows systematic studies on various modes of instabilities forming in 3D hydrogel layers. We discover a new mode of instability, i.e, fringe instability, which forms at the exposed surface of fringe portion. We also provide a phase diagram that can predict the initial occurrence modes of elastic instabilities in confined hydrogel layers.

In addition to the design of hydrogel properties and study of mechanical instabilities, we also demonstrate a few applications of hydrogels including hydrogel wound dressing (145), stretchable hydrogel electronics (145), and ingestible hydrogel device (175).

8.2 Outlook for future work

This thesis lays the fundamental understanding in terms of designing tissue-like properties in hydrogels. Beyond the study reported in the thesis, directions such as advanced manufacture, multi-scale simulations, understanding pathologies, and exploring new applications in human body are challenging yet rewarding as the next stage of research.

Specifically, the general idea for the design of tissue-like hydrogels highlights the importance of design soft materials via engineering nanoscale structures as natural tissues do. 3D printing is regarded as a mature additive manufacture technique for creating three-dimensional structures. The highest resolution for 3D printing robust hydrogels can be as high as 30 μm (239), which is still much larger than the dimension of building block in natural tissues (i.e., ~ 10 nm). Electrospinning can be an alternative way to engineer structures down to the scale of nano meter. Combining 3D printing and electrospinning could be the potential route to achieve tissue-like hydrogels through multi-scale fabrications.

The understanding of physics and mechanics in tissue-like hydrogels also requires multi-scale simulation techniques. Previous work mostly focus on the study on rigid biomaterials including bone, silk, and nacre. Multi-scale simulations of tissue-like hydrogels can provide new insights on how defects and topology of polymer chains influence bulk properties of hydrogels.

Furthermore, the methodology for understanding mechanics in tissue-like hydrogels may further evoke the routes for understanding failure, deformation, and fatigue-induced fracture in

biological tissues, therefore potentially giving hints on pathologies in certain diseases (e.g., aortic dissection, aging of tissues, and chronic foreign body response due to medical implants).

Appendix A1: Detailed Derivation of the Theory in Chapter 6

Problem setting. Consider a semi-infinite incompressible elastic strip with a rectangular cross-section as illustrated on Fig. 6-1. A material particle in the layer is labeled by its coordinates (X, Y, Z) in the undeformed state. The undeformed width of the specimen is W and its height H such that the strip occupies the region

$$-W/2 < X < W/2, \quad -\infty < Y < \infty, \quad -H/2 < Z < H/2. \quad (\text{A1.1})$$

The top and bottom surfaces of the strip (at $Z = \pm H/2$) are perfectly adhered to rigid plates while the sides (at $X = \pm W/2$) are traction free. As the rigid plates are drawn away from each other, the specimen is stretched to the new deformed thickness h , while the free surfaces retreat to form a meniscus shape to comply with the incompressibility constraint. We denote the spatial coordinate system in the deformed configuration by (x, y, z) and by limiting the analysis to plane-strain deformation patterns we have $y = Y$. Therefore, in the deformed state, the specimen occupies the range

$$-\frac{W}{2} \lambda_x \leq x \leq \frac{W}{2} \lambda_x, \quad -\infty < y < \infty, \quad -h/2 \leq z \leq h/2. \quad (\text{A1.2})$$

where $\lambda_x(Z)$ represents the in-plane stretch of the layer in the X -direction and as such is the normalized meniscus shape which we attempt to find in the present analysis. Here we have anticipated the fact that λ_x is independent of X , a fact that is established below.

Horizontal planes remain planes. The only additional assumption made about the deformation field of the specimen under tensile deformation, is that any horizontal plane in the unloaded state, remains planar and horizontal upon deformation. This assumption was employed in previous studies (219) and, intuitively, is motivated by the fact that both the midplane and the constrained

planes necessarily remain planar. Our numerical simulations indicate that this is a good approximation and is not compromised even as the extension progresses and, in fact, the opposite tendency is observed. Note that in compression this assumption holds only in the small strains regime and thus the present study, in pursuit of the large strains response, is limited to tension.

Constitutive response. In the present study we employ the neo-Hookean constitutive model which can be written in terms of the elastic strain energy density per unit volume of undeformed material, in the form

$$\Psi = \frac{\mu}{2} (\text{tr}(\mathbf{F}\mathbf{F}^T) - 3), \quad (\text{A1.3})$$

where μ is the shear modulus and \mathbf{F} is the deformation gradient which, for incompressible materials must obey the constraint

$$\det \mathbf{F} = 1. \quad (\text{A1.4})$$

Formulation. Since planes of constant Z are taken to remain planar upon deformation, the vertical coordinate z of any material point depends only on its initial vertical location Z while the in-plane coordinate x may depend on both X and Z . Hence we write the location of a material particle in the deformed configuration in the most general form as

$$x = g(X, Z), \quad y = Y, \quad z = f(Z). \quad (\text{A1.5})$$

Considering perfect adhesion of the specimens to the plates with no rigid motion, we write the boundary conditions

$$f(0) = 0, \quad f(\pm H/2) = \pm h/2, \quad g(0, Z) = 0, \quad g(X, \pm H/2) = X. \quad (\text{A1.6})$$

The deformation gradient \mathbf{F} and the stretch λ_x can now be written in the form

$$F = \begin{bmatrix} \frac{\partial g}{\partial X} & 0 & \frac{\partial g}{\partial Z} \\ 0 & 1 & 0 \\ 0 & 0 & f' \end{bmatrix}, \lambda_x = \frac{\partial g}{\partial X}, \quad (\text{A1.7})$$

where the prime denotes differentiation with respect to Z . The incompressibility condition in (A1.4) yields the differential equation

$$\frac{\partial g}{\partial X} = \frac{1}{f'} = \lambda_x. \quad (\text{A1.8})$$

Since f is a function of Z alone, it now follows that so is the stretch λ_x . By integrating the above equation and using the boundary condition (A1.6)³ we arrive at the relation

$$g(X, Z) = X \lambda_x. \quad (\text{A1.9})$$

We now insert the relations for g and f in terms of the meniscus shape λ_x back into (A1.7)¹ to write

$$F = \begin{bmatrix} \lambda_x & 0 & X \lambda'_x \\ 0 & 1 & 0 \\ 0 & 0 & 1/\lambda_x \end{bmatrix}. \quad (\text{A1.10})$$

Hence, for the class of deformations at hand, the problem reduces to finding a single unknown function $\lambda_x(Z)$ with the remaining boundary conditions translated to the form

$$\lambda_x(\pm H/2) = 1, \lambda'_x(0) = 0, \lambda = \int_0^{H/2} \frac{2}{\lambda_x H} dZ \quad (\text{A1.11})$$

where the second condition is due to symmetry and the specimen stretch is $\lambda = h/H$.

Since the boundary conditions on the traction-free side-surfaces cannot be identically satisfied, we seek a deformation field that minimizes the elastic energy in the system within the class of deformations being considered. The total elastic energy stored in the system is obtained

by integrating the energy density (A1.3) over the cross-section of the specimen, which upon inserting the deformation gradient in (A1.10), can be written as

$$E = 2\mu \int_0^{H/2} \int_0^{W/2} \left(2 - \lambda_x^2 - \lambda_x^{-2} - X^2 (\lambda'_x)^2 \right) dXdZ, \quad (\text{A.12})$$

where we have taken advantage of symmetry. This can be simplified by integration over X :

$$E = \mu W \int_0^{H/2} \left(2 - \lambda_x^2 - \lambda_x^{-2} - \frac{1}{3} \left(\frac{W}{2} \right)^2 (\lambda'_x)^2 \right) dZ - \frac{\mu WC}{6} \left(\int_0^{H/2} \frac{dZ}{\lambda_x} - \frac{h}{2} \right), \quad (\text{A.13})$$

where the second term incorporates the displacement constraint (A1.11)³ with the Lagrange multiplier C .

To find a function λ_x which minimizes the total energy, we begin by calculating the first variation of the elastic energy E

$$\delta E = 2\mu W \int_0^{H/2} \left(\left(\lambda_x^{-3} + \frac{C}{6} \lambda_x^{-2} - \lambda_x \right) \delta \lambda_x - \frac{1}{3} \left(\frac{W}{2} \right)^2 \lambda'_x \delta \lambda'_x \right) dZ, \quad (\text{A.14})$$

This can be further simplified via integration by parts to write

$$\delta E = 2\mu W \int_0^{H/2} \left(\lambda_x^{-3} + \frac{C}{6} \lambda_x^{-2} - \lambda_x + \frac{1}{3} \left(\frac{W}{2} \right)^2 \lambda_x'' \right) \delta \lambda_x dZ - \frac{2\mu W}{3} \left(\frac{W}{2} \right)^2 \left[\lambda'_x \delta \lambda_x \right]_0^{H/2}, \quad (\text{A.15})$$

where, since λ_x is prescribed at $Z = \pm H/2$, we require its variation to vanish there. Moreover the slope λ'_x vanishes at $Z = 0$ according to (A1.11). Therefore the last term in the above relation cancels out and the vanishing of the first variation, $\delta E = 0$, requires

$$\left(\frac{W}{2} \right)^2 \lambda_x'' = 3\lambda_x - \frac{C}{2} \lambda_x^{-2} - 3\lambda_x^{-3}, \quad (\text{A.16})$$

This can be integrated after replacing $\lambda_x'' = \frac{\partial \lambda'_x}{\partial \lambda_x} \lambda'_x$, to arrive at a separable equation which by integration reads

$$\frac{W}{2} \lambda'_x = \left(3\lambda_x^2 + C\lambda_x^{-1} + 3\lambda_x^{-2} + D \right)^{1/2}, \quad (\text{A1.17})$$

where D is an integration constant. Here, in taking the square root, we have chosen the physically relevant branch with positive slope in the midplane. It is instructive to notice from (A1.16) with $\lambda_x = 1$ that the coefficient C is proportional to the curvature of the meniscus shape near the constrained surfaces.

Numerical solution of the above nonlinear differential equation can be obtained by straight forward integration as conducted in the present study via the Runge-Kutta Merson method. To account for all three boundary conditions (A1.11), a shooting method is applied in which the value of C is guessed to iteratively arrive at the required stretch ($\lambda = h/H$). Specifically for the first order equation (A1.17), it is convenient to apply the symmetry boundary condition by defining the in-plane stretch in the midplane by

$$\lambda_x(Z=0) = \lambda_{x0}, \quad (\text{A1.18})$$

and thus via (A1.11)² it is possible to eliminate D from (17) to write

$$\frac{W}{2} \lambda'_x = \left[3(\lambda_x^2 - \lambda_{x0}^2) + C(\lambda_x^{-1} - \lambda_{x0}^{-1}) + 3(\lambda_x^{-2} - \lambda_{x0}^{-2}) \right]^{1/2}. \quad (\text{A1.19})$$

A shooting method can then be applied to relate the midplane stretch λ_{x0} to the specimen stretch h/H .

The applied stress. After carrying out the analysis of the previous section, we can insert the deformation field characterized by the single function $\lambda_x(Z)$ back into the energy integral in (A1.12). This allows us to express the stored elastic energy (per unit length) as a function of the specimen's deformed thickness $E = E(h)$. The increment of work (per unit length) invested by

the nominal averaged nominal stress S acting on the plates is $WS\delta h$ and this must equal the increment in energy δE :

$$\delta E = WS\delta h, \quad (\text{A1.20})$$

Therefore we may write

$$S = \frac{1}{W} \frac{dE}{dh} = \frac{1}{WH} \frac{dE}{d\lambda}, \quad (\text{A1.21})$$

and hence we arrive at the stress-stretch relationship $S = S(\lambda)$.

Appendix A2: Detailed Derivation of the Theory in Chapter 7

A2.1 Large Deformation Field in Cylindrical Layer under Tension

We set the center of the sample as the origin point of the coordinate. We assume that the separable form is applicable to the displacement along radius direction. Therefore, the displacement field can be approximated as a 2D field, namely

$$u_r(\bar{R}, \bar{Z}) = \bar{R}u_1(\bar{Z}), \quad (\text{A2.1})$$

$$u_z(\bar{Z}) = u_2(\bar{Z}), \quad (\text{A2.2})$$

with $\bar{R} = \frac{R}{D/2}$, $\bar{Z} = \frac{Z}{H/2}$. Applying the displacement fields, we can further express the

deformation gradient of the layer through $\mathbf{F} = \nabla \mathbf{u} + \mathbf{1}$ as:

$$\mathbf{F} = \begin{bmatrix} \lambda_{rR} & 0 & \gamma_{rZ} \\ 0 & \lambda_{\theta\theta} & 0 \\ 0 & 0 & \lambda_{zZ} \end{bmatrix}, \quad (\text{A2.3})$$

with $\lambda_{rR} = 1 + \frac{1}{D/2}u_1$, $\lambda_{\theta\theta} = 1 + \frac{1}{D/2}u_1$, $\lambda_{zZ} = 1 + \frac{1}{H/2} \frac{du_2}{d\bar{Z}}$ and $\gamma_{rZ} = \frac{\bar{R}}{H/2} \frac{du_1}{d\bar{Z}}$. The

incompressibility of the elastic layer enforces the conservation of volume, which reads as:

$$\lambda_{rR}\lambda_{\theta\theta}\lambda_{zZ} = 1. \quad (\text{A2.4})$$

We further take the elastic layer as an incompressible neo-Hookean material with strain energy density function $\psi = \frac{\mu}{2} [\text{tr}(\mathbf{F}^T \mathbf{F}) - 3]$. Therefore, the nominal stress tensor \mathbf{S} is expressed through $\mathbf{S} = \mu \mathbf{F} - p^* \mathbf{F}^{-T}$ and the Cauchy stress tensor is expressed through $\boldsymbol{\sigma} = \mathbf{S} \mathbf{F}^T$, namely:

$$\mathbf{S} / \mu = \begin{pmatrix} \lambda_{rR} - \bar{p} / \lambda_{rR} & 0 & \gamma_{rZ} \\ 0 & \lambda_{\theta\theta} - \bar{p} / \lambda_{\theta\theta} & 0 \\ \lambda_{\theta\theta} \gamma_{rZ} \bar{p} & 0 & \lambda_{zZ} - \bar{p} / \lambda_{zZ} \end{pmatrix}, \quad (\text{A2.5a})$$

$$\boldsymbol{\sigma} / \mu = \begin{pmatrix} \lambda_{rR}^2 - \bar{p} + \gamma_{rZ}^2 & 0 & \gamma_{rZ} \lambda_{zZ} \\ 0 & \lambda_{\theta\theta}^2 - \bar{p} & 0 \\ \gamma_{rZ} \lambda_{zZ} & 0 & \lambda_{zZ}^2 - \bar{p} \end{pmatrix}, \quad (\text{A2.5b})$$

where p^* is the Lagrange Multiplier to enforce the incompressibility and $\bar{p} = p^* / \mu$ is the corresponding dimensionless form. The equilibrium equation reads $\text{Div } \mathbf{S} = \mathbf{0}$. Since the equilibrium equation along hoop direction will be satisfied automatically, then the equations along radius direction and axial direction are

$$-\frac{1}{\lambda_{rR}} \frac{\partial \bar{p}}{\partial \bar{R}} + \alpha \frac{\partial \gamma_{rZ}}{\partial \bar{Z}} = 0, \quad (\text{A2.6})$$

$$\lambda_{rR} \frac{\partial (\gamma_{rZ} \bar{p})}{\partial \bar{R}} + \frac{\lambda_{rR} \gamma_{rZ} \bar{p}}{\bar{R}} + \alpha \frac{\partial (\lambda_{zZ} - \bar{p} / \lambda_{zZ})}{\partial \bar{Z}} = 0, \quad (\text{A2.7})$$

with $\alpha = D / H$. Since the highest order of \bar{R} in γ_{rZ} is first order and in order to satisfy the equilibrium equation Eq. (A2.6), \bar{p} is a function of \bar{R}^2 and should be in the form as:

$$\bar{p}(\bar{R}, \bar{Z}) = q_0(\bar{Z}) + (\bar{R}^2 - 1)q_1(\bar{Z}). \quad (\text{A2.8})$$

By inserting Eq. (A2.8) into Eq. (A2.6) and using the relation of λ_{rR} and γ_{rZ} in Eq. (A3), we can attain an ODE with respect to \bar{Z} , reading as:

$$\alpha^2 \lambda_{rR}'' = \frac{2q_1}{\lambda_{rR}}. \quad (\text{A2.9})$$

By inserting Eq. (A2.8) into Eq. (A2.7) and using the incompressibility constraint Eq. (A4), we can attain another ODE:

$$\lambda_{rR} (2\lambda_{rR}' q_1 - \lambda_{rR} q_1') \bar{R}^2 + [\lambda_{zZ}' - \lambda_{rR}^2 (q_0' - q_1')] = 0. \quad (\text{A2.10})$$

In order to satisfy Eq. (A2.10) for all the value of $\bar{R} \in [0, 1]$, we can further attain the following two ODEs:

$$2q_1 \lambda_{rR}' = \lambda_{rR} q_1', \quad (\text{A2.11})$$

$$\lambda_{zZ}' = \lambda_{rR}^2 (q_0' - q_1'). \quad (\text{A2.12})$$

The combination of Eq. (A9) and Eq. (A11) results in one governing equation with respect to λ_{rR} , reading as:

$$\lambda_{rR}'' = \pm \kappa^2 \lambda_{rR}, \quad (\text{A2.13})$$

with $q_1 = \pm \frac{1}{2} \kappa^2 \alpha^2 \lambda_{rR}^2$, which is corresponding to two cases:

a) For case $\lambda_{rR}'' = -\kappa^2 \lambda_{rR}$, the general solution of Eq. (A13) is $\lambda_{rR} = C_1 \cos(\kappa \bar{Z}) + C_2 \sin(\kappa \bar{Z})$

where C_1 and C_2 are two constants to be determined by boundary conditions. By imposing

the boundary conditions: $du_1 / d\bar{Z} |_{\bar{Z}=0} = 0$, $u_1(\bar{Z} = \pm 1) = 0$, the specific function $u_1(\bar{Z})$ can be

identified as:

$$u_1(\bar{Z}) = \frac{D}{2} \left(\frac{\cos(\kappa \bar{Z})}{\cos(\kappa)} - 1 \right). \quad (\text{A2.14a})$$

Further combining the condition of volume conservation in Eq. (A2.4) and boundary condition of $u_2(\bar{Z} = 0) = 0$, the specific function $u_2(\bar{Z})$ can be calculated through

$$u_2 = \frac{H}{2} \int_0^{\bar{Z}} \left(\frac{\cos^2 \kappa}{\cos^2(\kappa \xi)} - 1 \right) d\xi, \text{ namely,}$$

$$u_2(\bar{Z}) = \frac{H}{2} \left(\frac{\sin(2\kappa)}{2\kappa} \frac{\tan(\kappa \bar{Z})}{\tan(\kappa)} - \bar{Z} \right). \quad (\text{A2.15a})$$

The deformation field in constrained elastic layer under tension can be fully specified by functions $u_1(\bar{Z})$ and $u_2(\bar{Z})$, expressed in Eq. (A2.14a) and Eq. (A2.15a), where κ is an internal loading parameter which is correlated with the applied stretch by $\lambda = \frac{u_2(\bar{Z} = 1)}{H/2} + 1$,

namely, $\lambda = \frac{\sin(2\kappa)}{2\kappa}$. For any $\kappa \in [0, \pi/2)$, we have $0 < \lambda \leq 1$ for this case, which is

corresponding to compression.

- b) For case $\lambda_{rR}'' = \kappa^2 \lambda_{rR}$, the general solution of Eq. (A2.13) is $\lambda_{rR} = C_1 \cosh(\kappa \bar{Z}) + C_2 \sinh(\kappa \bar{Z})$, where C_1 and C_2 are two constants to be determined by boundary conditions. By imposing the boundary conditions: $du_1/d\bar{Z}|_{\bar{Z}=0} = 0$, $u_1(\bar{Z} = \pm 1) = 0$, the specific function $u_1(\bar{Z})$ can be identified as:

$$u_1(\bar{Z}) = \frac{D}{2} \left(\frac{\cosh(\kappa \bar{Z})}{\cosh(\kappa)} - 1 \right). \quad (\text{A2.14b})$$

Further combining the condition of volume conservation in Eq. (A2.4) and boundary condition of $u_2(\bar{Z} = 0) = 0$, the specific function $u_2(\bar{Z})$ can be calculated through

$$u_2 = \frac{H}{2} \int_0^{\bar{Z}} \left(\frac{\cosh^2 \kappa}{\cosh^2(\kappa \xi)} - 1 \right) d\xi, \text{ namely,}$$

$$u_2(\bar{Z}) = \frac{H}{2} \left(\frac{\sinh(2\kappa)}{2\kappa} \frac{\tanh(\kappa\bar{Z})}{\tanh(\kappa)} - \bar{Z} \right). \quad (\text{A2.15b})$$

The deformation field in constrained elastic layer under tension can be fully specified by functions $u_1(\bar{Z})$ and $u_2(\bar{Z})$, expressed in Eq. (A2.14b) and Eq. (A2.15b), where κ is an

internal loading parameter which is correlated with the applied stretch by $\lambda = \frac{u_2(\bar{Z}=1)}{H/2} + 1$,

namely, $\lambda = \frac{\sinh(2\kappa)}{2\kappa}$. For any $\kappa \geq 0$, we have $\lambda \geq 1$ for this case, which is corresponding to

tension.

Since we are mainly interested in the tension case in this paper, we proceed using the conclusions in case (b).

To identify the dimensionless scalar pressure \bar{p} , we further attain the expression of $q_0(\bar{Z})$ from the integration of Eq. (A2.12), reading as:

$$q_0 = \frac{\alpha^2}{2} \kappa^2 \lambda_{rR}^2 + \frac{1}{2\lambda_{rR}^4} + C_3, \quad (\text{A2.16})$$

with C_3 being a constant determined by the boundary condition of free traction at $\bar{Z} = \bar{Z}_0$.

Owing to the assumption that any horizontal plane in the layer at the un-deformed state remains planar upon deformation, it's impossible to satisfy the traction free boundary conditions at all \bar{Z} .

Here, we enforce the boundary condition at $\bar{Z} = 0$, namely the traction $\mathbf{t}_R = \mathbf{S} \cdot \mathbf{e}_R$, shall be zero

at $\bar{R} = 1$. The Θ component of the traction is zero automatically and Z components of traction

also be zero owing to the symmetric condition of $\gamma_{rZ} = 0$ at the middle plane, and the R

component reads $\mu(\lambda_{rR} - \bar{p} / \lambda_{rR})$. Therefore, constant C_3 can be identified as

$\frac{1}{\cosh^2 \kappa} \left(1 - \frac{1}{2} \kappa^2 \alpha^2\right) - \frac{1}{2} \cosh^4 \kappa$ and the dimensionless scalar pressure reads as

$$\bar{p} = \frac{1}{2} \left(\frac{\cosh^4 \kappa}{\cosh^4(\kappa \bar{Z})} - \cosh^4 \kappa \right) + \frac{\alpha^2 \kappa^2}{2} \left(\frac{\bar{R}^2 \cosh^2(\kappa \bar{Z})}{\cosh^2 \kappa} - \frac{1}{\cosh^2 \kappa} \right) + \frac{1}{\cosh^2 \kappa}. \quad (\text{A2.17})$$

We further define the averaged nominal stress applied on the layer S as the applied force

divided by the un-deformed horizontal cross-section area $\frac{\pi}{4} D^2$, which can be calculated as

$$S = \frac{4}{H \pi D^2} \cdot \frac{dW}{d\lambda} = \frac{d\tilde{W}}{d\lambda}, \quad (\text{A2.18})$$

where W is the total elastic energy of the layer which can be calculated by integrating ψ over

the volume of the layer: $W = 2 \int_0^{\frac{H}{2}} \int_0^{\frac{D}{2}} 2\pi R \psi(R, Z) dR dZ$. Let

$\tilde{W} = \frac{4}{H \pi D^2} W = \int_0^1 \int_0^1 2\bar{R} \psi(\bar{R}, \bar{Z}) d\bar{R} d\bar{Z}$, by inserting the free energy $\psi = \frac{\mu}{2} [\text{tr}(\mathbf{FF}^T) - 3]$, we

can attain:

$$\tilde{W} = \frac{\mu}{2} \cdot \int_0^1 \int_0^1 2\bar{R} (\lambda_{rR}^2 + \lambda_{\theta\theta}^2 + \lambda_{zZ}^2 + \gamma_{rz}^2 - 3) d\bar{R} d\bar{Z}, \quad (\text{A2.19})$$

with $\lambda_{rR} = \lambda_{\theta\theta} = \frac{\cosh(\kappa \bar{Z})}{\cosh \kappa}$, $\lambda_{zZ} = \frac{\cosh^2 \kappa}{\cosh^2(\kappa \bar{Z})}$ and $\gamma_{rz} = \frac{\alpha \kappa}{\cosh \kappa} \sinh(\kappa \bar{Z}) \bar{R}$. By integral \tilde{W} over

\bar{R} , \tilde{W} can be reduced as:

$$\tilde{W} = \frac{\mu}{2} \cdot \int_0^1 \left[2 \frac{\cosh^2(\kappa \bar{Z})}{\cosh^2 \kappa} + \frac{\cosh^4 \kappa}{\cosh^4(\kappa \bar{Z})} + \frac{1}{2} \frac{\kappa^2 \alpha^2}{\cosh^2 \kappa} \sinh^2(\kappa \bar{Z}) - 3 \right] d\bar{Z}. \quad (\text{A2.20})$$

By integral \tilde{W} over \bar{Z} , \tilde{W} can be reduced as a function with respect to a single variable κ :

$$\tilde{W} = \frac{\mu}{2} \cdot \left[\frac{\sinh \kappa \cosh \kappa + \kappa}{\kappa \cosh^2 \kappa} + \frac{\sinh \kappa \cosh \kappa}{3\kappa} + \frac{2 \sinh \kappa \cosh^3 \kappa}{3\kappa} + \alpha^2 \frac{\kappa \sinh \kappa \cosh \kappa - \kappa^2}{4 \cosh^2 \kappa} - 3 \right]. \quad (\text{A2.21})$$

Combination of the Eq. (A2.18), Eq. (A2.21) and $\lambda = \frac{\sinh(2\kappa)}{2\kappa}$ gives rise to the expression of the applied nominal stress as:

$$S / \mu = S_0 + \alpha^2 S_1, \quad (\text{A2.22})$$

where both S_0 and S_1 are functions with respect to a single variable of loading parameter κ as:

$$S_0 = (6\kappa^2 \sinh \kappa + 3 \cosh^2 \kappa \sinh \kappa + \cosh^4 \kappa \sinh \kappa + 2 \cosh^6 \kappa \sinh \kappa - 3\kappa \cosh \kappa + \kappa \cosh^3 \kappa + 4\kappa \cosh^5 \kappa - 8\kappa \cosh^7 \kappa) / [6 \cosh^4 \kappa \sinh \kappa - 6\kappa \cosh^3 \kappa \cosh(2\kappa)], \quad (\text{A2.23})$$

$$S_1 = (\kappa^3 \cosh \kappa - 2\kappa^4 \sinh \kappa - \kappa^2 \cosh^2 \kappa \sinh \kappa) / [8 \cosh^4 \kappa \sinh \kappa - 8\kappa \cosh^3 \kappa \cosh(2\kappa)]. \quad (\text{A2.24})$$

As shown in Fig. A2-1, S_0 monotonically increases with the applied stretch while S_1 is non-monotonic with a peak point at $\kappa = 0.89$ (i.e. $\lambda = 1.62$).

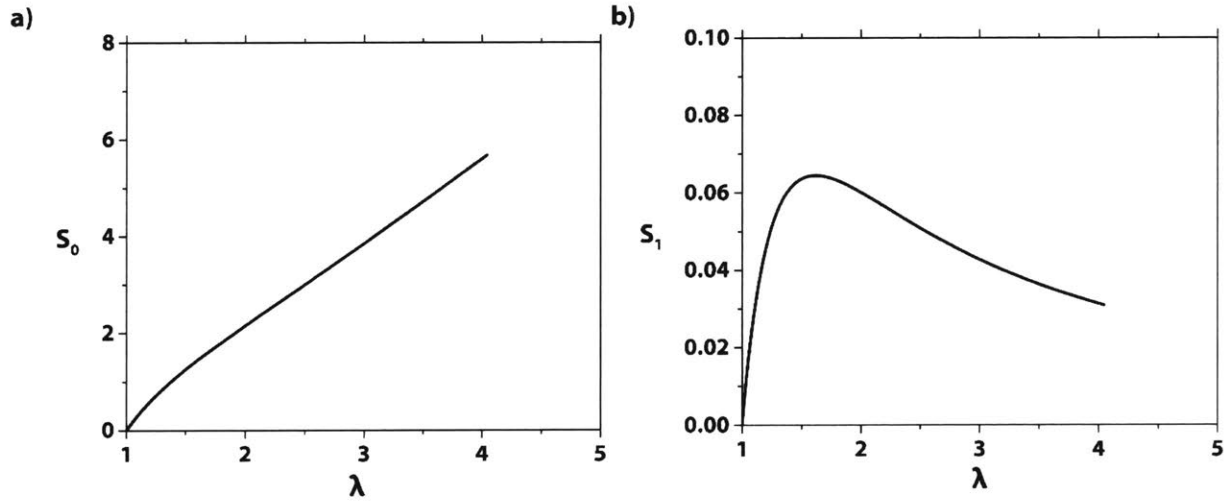


Figure A2-1. The theoretically calculated stress contains two parts: one is monotonic S_0 in (a) and the other is non-monotonic S_1 in (b).

In addition to the applied stretch λ and the applied nominal stress S we derived, the

hydrostatic pressure at the center of the sample can be calculated through $p_0 = \frac{1}{3} \text{tr}(\boldsymbol{\sigma})|_{\bar{z}=0, \bar{R}=0}$

with $\boldsymbol{\sigma} = \mathbf{S}\mathbf{F}^T$ being Cauchy stress tensor. Based on Eq. (A2.5b), the hydrostatic pressure reads as:

$$p_0 / \mu = \frac{\lambda_{rR}^2 + \lambda_{\theta\theta}^2 + \lambda_{zZ}^2 + \gamma_{rZ}^2}{3} - \bar{p}. \quad (\text{A2.25})$$

Inserting $\lambda_{rR}(\bar{Z} = 0) = \lambda_{\theta\theta}(\bar{Z} = 0) = \frac{1}{\cosh \kappa}$, $\lambda_{zZ}(\bar{Z} = 0) = \cosh^2 \kappa$, $\gamma_{rZ}(\bar{R} = 0, \bar{Z} = 0) = 0$ and

$\bar{p}(\bar{R} = 0, \bar{Z} = 0) = \frac{1}{\cosh^2 \kappa} - \frac{\kappa^2 \alpha^2}{2 \cosh^2 \kappa}$, one can write the hydrostatic pressure at the center of the

sample as

$$p_0 / \mu = \frac{\cosh^4(\kappa)}{3} - \frac{1}{3 \cosh^2(\kappa)} + \frac{\kappa^2 \alpha^2}{2 \cosh^2(\kappa)}. \quad (\text{A2.26})$$

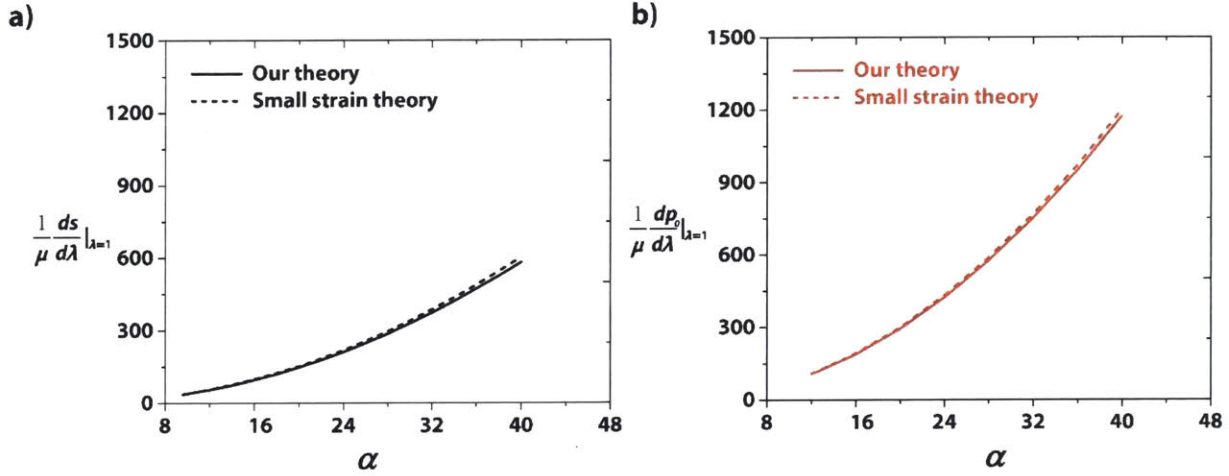


Figure A2-2. (a) Comparison of $\frac{1}{\mu} \frac{ds}{d\lambda} \Big|_{\lambda=1}$ between our result and previous result with the assumption of small deformation. (b) Comparison of $\frac{1}{\mu} \frac{dp_0}{d\lambda} \Big|_{\lambda=1}$ between our result and existing result with the assumption of small deformation.

A2.2 Detailed derivation of the onset of instabilities via linear perturbation analysis

To identify the onset of fingering instability and estimating the boundary between fingering and fringe instability, we applied an infinitesimal oscillatory part to the rotational invariant part at base state solved in Section 7.6.1. The perturbed deformation fields read as:

$$\mathbf{x} = (\mathbf{x})^0 + \varepsilon \tilde{\mathbf{x}}, \quad (\text{A2.27})$$

$$\bar{p} = (\bar{p})^0 + \varepsilon \tilde{p}, \quad (\text{A2.28})$$

where the rotational invariant part is solved in Appendix. A1, reading as:

$$(\mathbf{x})^0 = \frac{D\bar{R}}{2} \left(\frac{\cosh(\kappa\bar{Z})}{\cosh(\kappa)} - 1 \right) \mathbf{e}_R + \frac{H}{2} \left(\frac{\sinh(2\kappa) \tanh(\kappa\bar{Z})}{2\kappa \tanh(\kappa)} - \bar{Z} \right) \mathbf{e}_Z, \quad (\text{A2.29})$$

$$(\bar{p})^0 = \frac{1}{2} \left(\frac{\cosh^4 \kappa}{\cosh^4(\kappa\bar{Z})} - \cosh^4 \kappa \right) + \frac{\kappa^2 \alpha^2}{2} \left(\bar{R}^2 \frac{\cosh^2(\kappa\bar{Z})}{\cosh^2 \kappa} - \frac{1}{\cosh^2 \kappa} \right) + \frac{1}{\cosh^2 \kappa}. \quad (\text{A2.30})$$

Both the perturbed displacement field and the perturbed Lagrange multiplier read as

$$\tilde{\mathbf{x}} = A_1(R)u_1(Z) \cos(\omega\Theta) \mathbf{e}_R + A_2(R)u_1(Z) \sin(\omega\Theta) \mathbf{e}_\Theta + A_3(R)u_2(Z) \sin(\omega\Theta) \mathbf{e}_Z, \quad (\text{A2.31})$$

$$\tilde{p} = A_4(Z, R) \cos(\omega\Theta), \quad (\text{A2.32})$$

where A_i ($i = 1, 2, 3, 4$) are the amplitudes of perturbation. Therefore, the full deformation gradient may write as $\mathbf{F} = (\mathbf{F})^0 + \varepsilon \text{Grad} \tilde{\mathbf{x}}$, where $(\mathbf{F})^0$ is the rotational invariant deformation gradient at base state expressed in Eq. (A3). By inserting the displacement field, the deformation gradient reads as:

$$\mathbf{F} = \begin{bmatrix} \lambda_{rR} + \varepsilon A_1' u_1 \cos(\omega\Theta) & -\varepsilon \frac{A_1 \omega + A_2}{R} u_1 \sin(\omega\Theta) & \gamma_{rZ} + \varepsilon A_1 u_1' \cos(\omega\Theta) \\ \varepsilon A_2' u_1 \sin(\omega\Theta) & \lambda_{\Theta\Theta} + \varepsilon \frac{A_2 \omega + A_1}{R} u_1 \cos(\omega\Theta) & \varepsilon A_2 u_1' \sin(\omega\Theta) \\ \varepsilon A_3' u_2 \cos(\omega\Theta) & -\varepsilon \frac{A_3 \omega}{R} u_2 \sin(\omega\Theta) & \lambda_{zZ} + \varepsilon A_3 u_2' \cos(\omega\Theta) \end{bmatrix}. \quad (\text{A2.33})$$

Here the prime is for differentiating to R and Z . The incompressibility of the elastic layer is enforced by $\det \mathbf{F} = 1$, implying till first order of ε :

$$\lambda_{rR} \lambda_{\Theta\Theta} \lambda_{zZ} + \varepsilon \left(\lambda_{\Theta\Theta} \lambda_{zZ} A_1' u_1 + \lambda_{rR} \lambda_{zZ} \frac{A_2 \omega + A_1}{R} u_1 - \lambda_{\Theta\Theta} \gamma_{rZ} A_3' u_2 + \lambda_{rR} \lambda_{\Theta\Theta} A_3 u_2' \right) \cos(\omega\Theta) = 1. \quad (\text{A2.34})$$

By further using the conclusion from the case without perturbation we have $\lambda_{rR}\lambda_{\theta\Theta}\lambda_{zZ} = 1$ and

$\lambda_{rR} = \lambda_{\theta\Theta}$, Eq. (A34) can be further reduced as:

$$\lambda_{zZ}A_1'u_1 + \lambda_{zZ}\frac{A_2\omega + A_1}{R}u_1 - \gamma_{rZ}A_3'u_2 + \lambda_{rR}A_3u_2' = 0. \quad (\text{A2.35})$$

The perturbation in deformation gradient will further induce a perturbation in nominal stress

which results in the nominal stress reading as $\mathbf{S} / \mu = (\mathbf{S})^0 / \mu + \varepsilon\tilde{\mathbf{S}}$. The rotational invariant

nominal stress $(\mathbf{S})^0 / \mu = (\mathbf{F})^0 - (\bar{p})^0 (\mathbf{F})^{0-T}$ at base state is shown in Eq. (A5a). The total stress

can be calculated by inserting Eq. (A31) through $\mathbf{S} / \mu = \mathbf{F} - \bar{p}\mathbf{F}^{-T}$. Therefore, the perturbed

stress can be calculated as:

$$\tilde{\mathbf{S}} = \text{Grad}\tilde{\mathbf{x}} + \frac{1}{\varepsilon} \left[(\bar{p})^0 (\mathbf{F})^{0-T} - \bar{p}\mathbf{F}^{-T} \right]. \quad (\text{A2.36})$$

Or alternatively, $\tilde{\mathbf{S}} = \text{Grad}\tilde{\mathbf{x}} + (\bar{p})^0 (\mathbf{F})^{0-T} (\text{Grad}\tilde{\mathbf{x}})^{-T} (\mathbf{F})^{0-T} - \tilde{p}(\mathbf{F})^{0-T}$. By inserting Eq. (A2.3),

Eq. (A2.33), Eq. (A2.35) and Eq. (A2.36), each component of the perturbed nominal stress reads

as:

$$\tilde{S}_{rR} = \left[A_1'u_1 - (\bar{p})^0 (\gamma_{rZ}A_3'u_2 - \lambda_{zZ}A_1'u_1) - \frac{A_4}{\lambda_{rR}} \right] \cos(\omega\Theta), \quad (\text{A2.37a})$$

$$\tilde{S}_{r\Theta} = \left[-\frac{A_1\omega + A_2}{R}u_1 + (\bar{p})^0 \lambda_{zZ}A_2'u_1 \right] \sin(\omega\Theta), \quad (\text{A2.37b})$$

$$\tilde{S}_{rZ} = \left[A_1u_1' + (\bar{p})^0 \lambda_{rR}A_3'u_2 \right] \cos(\omega\Theta), \quad (\text{A2.37c})$$

$$\tilde{S}_{\theta R} = \left[A_2'u_1 - (\bar{p})^0 \lambda_{zZ}\frac{A_1\omega + A_2}{R}u_1 + (\bar{p})^0 \gamma_{rZ}\frac{A_3\omega}{R}u_2 \right] \sin(\omega\Theta), \quad (\text{A2.37d})$$

$$\tilde{S}_{\theta\Theta} = \left[\lambda_{rR}^2 \gamma_{rZ}A_3'u_2 - \lambda_{rR}^3 A_3u_2' - A_1'u_1 - (\bar{p})^0 (\lambda_{zZ}A_1'u_1 - \gamma_{rZ}A_3'u_2 + \lambda_{rR}A_3u_2') - \frac{A_4}{\lambda_{rR}} \right] \cos(\omega\Theta), \quad (\text{A2.37e})$$

$$\tilde{S}_{\theta z} = \left[A_2 u_1' - (\bar{p})^0 \lambda_{rR} \frac{A_3 \omega}{R} u_2 \right] \sin(\omega \Theta), \quad (\text{A2.37f})$$

$$\tilde{S}_{zR} = \left[A_3' u_2 + \lambda_{rR} \gamma_{rZ} A_4 + (\bar{p})^0 \gamma_{rZ} (\lambda_{rR}^2 \gamma_{rZ} A_3' u_2 - \lambda_{rR}^3 A_3 u_2' - A_1' u_1) + (\bar{p})^0 \lambda_{rR} A_1 u_1' \right] \cos(\omega \Theta), \quad (\text{A2.37g})$$

$$\tilde{S}_{z\Theta} = \left[-\frac{A_3 \omega}{R} u_2 - (\bar{p})^0 \gamma_{rZ} A_2' u_1 + (\bar{p})^0 \lambda_{rR} A_2 u_1' \right] \sin(\omega \Theta), \quad (\text{A2.37h})$$

$$\tilde{S}_{zZ} = \left[A_3 u_2' - \lambda_{rR}^2 A_4 - (\bar{p})^0 \lambda_{rR} u_1 \left(A_1' + \frac{A_2 \omega + A_1}{R} \right) \right] \cos(\omega \Theta). \quad (\text{A2.37i})$$

A balance of the forces exerted on an element of the perturbed elastomer further leads to three equations of equilibrium through $\text{Div } \tilde{\mathbf{S}} = \mathbf{0}$. The three equilibrium equations read:

$$\begin{aligned} & \left\{ A_1'' u_1 + \left[\partial_R (\bar{p})^0 \right] (\lambda_{zZ} A_1' u_1 - \gamma_{rZ} A_3' u_2) + (\bar{p})^0 \left[\lambda_{zZ} A'' u_1 - (\partial_R \gamma_{rZ}) A_3' u_2 - \gamma_{rZ} A_3'' u_2 \right] - (\partial_R A_4) / \lambda_{rR} \right\} \\ & + \frac{\omega}{R} \left[-\frac{A_1 \omega + A_2}{R} u_1 + (\bar{p})^0 \lambda_{zZ} A_2' u_1 \right] + A_1 u_1'' + (\partial_Z (\bar{p})^0) \lambda_{rR} A_3' u_2 + (\bar{p})^0 \lambda_{rR}' A_3' u_2 + (\bar{p})^0 \lambda_{rR} A_3' u_2' \\ & + \frac{1}{R} \left[2 A_1' u_1 + \lambda_{rR}^3 A_3 u_2' - \lambda_{rR}^2 \gamma_{rZ} A_3' u_2 + (\bar{p})^0 (2 \lambda_{zZ} A_1' u_1 - 2 \gamma_{rZ} A_3' u_2 + \lambda_{rR} A_3 u_2') \right] = 0, \quad (\text{A2.38}) \end{aligned}$$

$$\begin{aligned} & A_2'' u_1 - \left[\partial_R (\bar{p})^0 \right] \lambda_{zZ} \frac{A_1 \omega + A_2}{R} u_1 - (\bar{p})^0 \lambda_{zZ} \left(\frac{A_1 \omega + A_2}{R} \right)' u_1 + \partial_R (\bar{p})^0 \gamma_{rZ} \frac{A_3 \omega}{R} u_2 + (\bar{p})^0 \partial_R \gamma_{rZ} \frac{A_3 \omega}{R} u_2 \\ & + (\bar{p})^0 \gamma_{rZ} \left(\frac{A_3 \omega}{R} \right)' u_2 - \frac{\omega}{R} \left[\lambda_{rR}^2 \gamma_{rZ} A_3' u_2 - \lambda_{rR}^3 A_3 u_2' - A_1' u_1 - (\bar{p})^0 (\lambda_{zZ} A_1' u_1 - \gamma_{rZ} A_3' u_2 + \lambda_{rR} A_3 u_2') - \frac{A_4}{\lambda_{rR}} \right] \\ & - \left[\partial_Z (\bar{p})^0 \right] \lambda_{rR} \frac{A_3 \omega}{R} u_2 - (\bar{p})^0 \lambda_{rR}' \frac{A_3 \omega}{R} u_2 - (\bar{p})^0 \lambda_{rR} \frac{A_3 \omega}{R} u_2' + A_2 u_1'' \\ & + \frac{1}{R} \left[A_2' u_1 - (\bar{p})^0 \lambda_{zZ} \frac{A_1 \omega + A_2}{R} u_1 + (\bar{p})^0 \gamma_{rZ} \frac{A_3 \omega}{R} u_2 - \frac{A_1 \omega + A_2}{R} u_1 + (\bar{p})^0 \lambda_{zZ} A_2' u_1 \right] = 0, \quad (\text{A2.39}) \end{aligned}$$

$$\begin{aligned}
& A_3''u_2 + \lambda_R (\partial_R \gamma_{rZ}) A_4 + \lambda_{rR} \gamma_{rZ} (\partial_R A_4) + \left[\partial_R (\bar{p})^0 \right] \left(\lambda_{rR}^2 \gamma_{rZ}^2 A_3' u_2 - \lambda_{rR}^3 \gamma_{rZ} A_3 u_2' - \gamma_{rZ} A_1' u_1 \right) \\
& + (\bar{p})^0 \left[2 \lambda_{rR}^2 \gamma_{rZ} (\partial_R \gamma_{rZ}) A_3' u_2 + \lambda_{rR}^2 \gamma_{rZ}^2 A_3'' u_2 - \lambda_{rR}^3 (\partial_R \gamma_{rZ}) A_3 u_2' - \lambda_{rR}^3 \gamma_{rZ} A_3 u_2' - (\partial_R \gamma_{rZ}) A_1' u_1 - \gamma_{rZ} A_1'' u_1 \right] \\
& + \left[\partial_R (\bar{p})^0 \right] \lambda_{rR} A_1 u_1' + (\bar{p})^0 \lambda_{rR} A_1' u_1 + \frac{\omega}{R} \left[-\frac{A_3 \omega}{R} u_2 - (\bar{p})^0 \gamma_{rZ} A_2' u_1 + (\bar{p})^0 \lambda_{rR} A_2 u_1' \right] \\
& + \frac{1}{R} \left[A_3' u_2 + \lambda_{rR} \gamma_{rZ} A_4 + (\bar{p})^0 \gamma_{rZ} \left(\lambda_{rR}^2 \gamma_{rZ} A_3' u_2 - \lambda_{rR}^3 A_3 u_2' - A_1' u_1 \right) + (\bar{p})^0 \lambda_{rR} A_1 u_1' \right] + A_3 u_2'' - 2 \lambda_{rR} \lambda_{rR}' A_4 \\
& - \lambda_{rR}^2 (\partial_Z A_4) - (\bar{p})^0 \lambda_{rR}' \left(A_1' + \frac{A_2 \omega + A_1}{R} \right) u_1 - (\bar{p})^0 \lambda_{rR} \left(A_1' + \frac{A_2 \omega + A_1}{R} \right) u_1' = 0, \tag{A2.40}
\end{aligned}$$

with $\lambda_{rR} = 1 + \frac{2}{D} u_1$, $\lambda_{\theta\theta} = 1 + \frac{2}{D} u_1$ and $\gamma_{rZ} = \frac{2\bar{R}}{H} \frac{du_1}{dZ}$, we can attain $\gamma_{rZ} = \lambda_{rR}' R = \lambda_{\theta\theta}' R$. Taking

differentiation of the incompressibility condition in Eq. (A2.35), we can further attain:

$$\lambda_{zZ} A_1'' u_1 + \lambda_{zZ} \left(\frac{A_2 \omega + A_1}{R} \right)' u_1 - \lambda_{rR} A_3' u_2 - \gamma_{rZ} A_3'' u_2 + \lambda_{rR} A_3' u_2' = 0, \tag{A2.41}$$

By imposing Eq. (A2.35) and Eq. (A2.41), all terms with $(\bar{p})^0$ in the three equilibrium equations will vanish. Thus, the three equilibrium equations can be simplified as:

$$\begin{aligned}
& \left\{ A_1'' u_1 + \left[\partial_R (\bar{p})^0 \right] \left(\lambda_{zZ} A_1' u_1 - \gamma_{rZ} A_1' u_2 \right) \right\} - \frac{\omega^2 - 1}{R^2} A_1 u_1 + A_1 u_1'' + \left[\partial_Z (\bar{p})^0 \right] \lambda_{rR} A_3' u_2 \\
& + \frac{1}{R} \left(3 A_1' u_1 + 2 \lambda_{rR}^3 A_3 u_2' - 2 \lambda_{rR}^2 \gamma_{rZ} A_3' u_2 \right) = (\partial_R A_4) / \lambda_{rR}, \tag{A2.42}
\end{aligned}$$

$$\begin{aligned}
& \left\{ A_2'' u_1 - \left[\partial_R (\bar{p})^0 \right] \lambda_{zZ} \frac{A_1 \omega + A_2}{R} u_1 + \left[\partial_R (\bar{p})^0 \right] \gamma_{rZ} \frac{A_3 \omega}{R} u_2 \right\} - \frac{\omega}{R} \left[\lambda_{rR}^2 \gamma_{rZ} A_3' u_2 - \lambda_{rR}^3 A_3 u_2' - A_1' u_1 - \frac{A_4}{\lambda_{rR}} \right] \\
& - \left[\partial_Z (\bar{p})^0 \right] \lambda_{rR} \frac{A_3 \omega}{R} u_2 + A_2 u_1'' + \frac{1}{R} \left[A_2' u_1 - \frac{A_1 \omega + A_2}{R} u_1 \right] = 0, \tag{A2.43}
\end{aligned}$$

$$\begin{aligned}
& A_3'' u_2 + \lambda_{rR} \gamma_{rZ} (\partial_R A_4) + \left[\partial_R (\bar{p})^0 \right] \left(\lambda_{rR}^2 \gamma_{rZ}^2 A_3' u_2 - \lambda_{rR}^3 \gamma_{rZ} A_3 u_2' - \gamma_{rZ} A_1' u_1 + \lambda_{rR} A_1 u_1' \right) + \frac{\omega}{R} \left(-\frac{A_3 \omega}{R} u_2 \right) \\
& + \frac{A_3' u_2}{R} + \left[A_3 u_2'' - \lambda_{rR}^2 (\partial_Z A_4) - \partial_Z (\bar{p})^0 \lambda_{rR} \left(\lambda_{rR}^2 \gamma_{rZ} A_3' u_2 - \lambda_{rR}^3 A_3 u_2' \right) \right] = 0. \tag{A2.44}
\end{aligned}$$

Noting that all the three equilibrium equations are only required to be satisfied at $\bar{Z} = \bar{Z}_0$, where the instability initiates. For the other cross sections where $\bar{Z} \neq \bar{Z}_0$, the force balance can be satisfied automatically with $\varepsilon = 0$.

For the case when fingering instability initiates, the location of the undulation is at the center plane of the sample (i.e. $\bar{Z}_0 = 0$). Consequently, all the terms associated with λ'_{rR} , u_1' and u_2'' vanish due to the symmetric condition (e.g. $\gamma_{rZ} = 0$, $\partial_Z (\bar{p})^0_{\bar{Z}=\bar{Z}_0} = 0$). The first and third equilibrium equations can be further simplified as:

$$\left\{ A_1'' u_1 + \left[\partial_R (\bar{p})^0 \right] \lambda_{zZ} A_1' u_1 \right\} - \frac{\omega^2 - 1}{R^2} A_1 u_1 + A_1 u_1'' + \frac{1}{R} \left(3 A_1' u_1 + 2 \lambda_{rR}^3 A_3 u_2' \right) = (\partial_R A_4) / \lambda_{rR}, \tag{A2.45}$$

$$A_3'' u_2 - \frac{A_3 \omega^2}{R^2} u_2 + \frac{A_3' u_2}{R} = \lambda_{rR}^2 \partial_Z A_4. \tag{A2.46}$$

For the second equilibrium equation Eq. (A2.43), it can be further rearranged as:

$$\begin{aligned}
& -\frac{\lambda_{rR}}{\omega} \left\{ R A_2'' u_1 - \left[\partial_R (\bar{p})^0 \right] \lambda_{zZ} (A_1 \omega + A_2) u_1 + \left[\partial_R (\bar{p})^0 \right] \gamma_{rZ} A_3 \omega u_2 \right\} + \left[\lambda_{rR}^3 \gamma_{rZ} A_3' u_2 - \lambda_{rR}^4 A_3 u_2' - \lambda_{rR} A_1' u_1 \right] \\
& + \left[\partial_Z (\bar{p})^0 \right] \lambda_{rR}^2 A_3 u_2 - \frac{R \lambda_{rR}}{\omega} A_2 u_1'' - \frac{\lambda_{rR}}{\omega} \left[A_2' u_1 - \frac{A_1 \omega + A_2}{R} u_1 \right] = A_4. \tag{A2.47}
\end{aligned}$$

By taking differentiation of Eq. (A2.47) with respect to R and neglecting any terms associated with λ'_{rR} , we will attain:

$$-\frac{\lambda_{rR}}{\omega} \left\{ A_2'' u_1 + R A_2^{(3)} u_1 - \left[\partial_R^2 (\bar{p})^0 \right] \lambda_{zZ} (A_1 \omega + A_2) u_1 - \left[\partial_R (\bar{p})^0 \right] \lambda_{zZ} (A_1' \omega + A_2') u_1 \right\} - \lambda_{rR}^4 A_3' u_2' - \lambda_{rR} A_1'' u_1$$

$$-\frac{\lambda_{rR}}{\omega} A_2 u_1'' - \frac{R \lambda_{rR}}{\omega} A_2' u_1'' - \frac{\lambda_{rR}}{\omega} \left[A_2'' u_1 - \frac{A_1' \omega + A_2'}{R} u_1 + \frac{A_1 \omega + A_2}{R^2} u_1 \right] = \partial_R A_4. \quad (\text{A2.48})$$

By taking differentiation of Eq. (A2.47) with respect to Z and neglecting any terms associated with λ'_{rR} , we will attain:

$$\lambda_{rR}^3 \lambda_{rR}'' R A_3' u_2 + \left[\partial_Z^2 \bar{p}_0 \right] \lambda_{rR}^2 A_3 u_2 = \partial_Z A_4. \quad (\text{A2.49})$$

The combination of Eq. (A2.46) and Eq. (A2.49) results in the second order ODE with respect to A_3 , namely

$$\lambda_{rR}^3 \lambda_{rR}'' R A_3' u_2 + \left[\partial_Z^2 \bar{p}_0 \right] \lambda_{rR}^2 A_3 u_2 = \lambda_{zZ} A_3'' u_2 + \frac{\lambda_{zZ}}{R} A_3' u_2 - \lambda_{zZ} \frac{\omega^2}{R^2} A_3 u_2. \quad (\text{A2.50})$$

This equation contains two solutions: one is decay solution and the other diverges as $\bar{R} \rightarrow 0$. By applying the boundary condition that $A_3'(1) = 0$, then the solution for A_3 shall be zero. However, for fringe instability, if α is slightly smaller than the theoretical transition aspect ratio $\alpha_{\text{fringe-fingering}}$ between fingering instability and fringe instability, $A_3 \ll A_1$ and $A_3 \ll A_2$, therefore we approximate $A_3 = 0$.

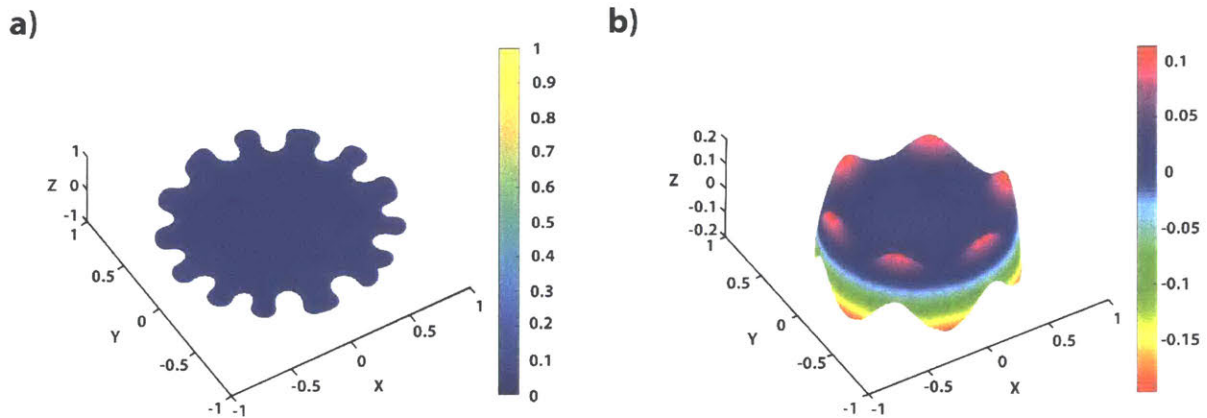


Figure A2-3. a) Undulation contour from simulation at the locus $\bar{Z}_0 = 0$ right after fingering instability for the sample with $\alpha = 8$. b) Undulation contour from simulation at the locus $\bar{Z}_0 = 0.81$ right after fringe instability for the sample with $\alpha = 4$.

By vanishing the term associated with A_3 , Eq. (A2.45) and Eq. (A2.48) can be further simplified as:

$$A_1''u_1 + \left[\partial_R (\bar{p})^0 \right] \lambda_{zz} A_1' u_1 - \frac{\omega^2 - 1}{R^2} A_1 u_1 + A_1 u_1'' + \frac{3A_1' u_1}{R} = \frac{\partial_R A_4}{\lambda_{rR}}, \quad (\text{A2.51})$$

$$-\frac{1}{\omega} \left\{ A_2'' u_1 + R A_2^{(3)} u_1 - \left[\partial_R^2 (\bar{p})^0 \right] \lambda_{zz} (A_1 \omega + A_2) u_1 - \left[\partial_R (\bar{p})^0 \right] \lambda_{zz} (A_1' \omega + A_2') u_1 \right\} - A_1'' u_1 - \frac{1}{\omega} A_2 u_1'' - \frac{R}{\omega} A_2' u_1'' - \frac{1}{\omega} \left[A_2'' u_1 - \frac{A_1' \omega + A_2'}{R} u_1 + \frac{A_1 \omega + A_2}{R^2} u_1 \right] = \frac{\partial_R A_4}{\lambda_{rR}}. \quad (\text{A2.52})$$

Recalling the condition of incompressibility in Eq. (A2.35) and neglecting the terms associated with λ_{rR}' and A_3 , we can attain a set of differential equations as follow:

$$A_2 \omega = -(R A_1' + A_1), \quad (\text{A2.53a})$$

$$A_2' \omega = -(2A_1' + R A_1''), \quad (\text{A2.53b})$$

$$A_2'' \omega = -(3A_1'' + R A_1^{(3)}), \quad (\text{A2.53c})$$

$$A_2^{(3)} \omega = -(4A_1^{(3)} + R A_1^{(4)}). \quad (\text{A2.53d})$$

The combination of Eq. (A2.51), Eq. (A2.52) and Eq. (A2.53) results in the fourth order ODE with respect to A_1 , namely,

$$R^4 A_1^{(4)} + 6R^3 A_1^{(3)} + \left\{ 5 - \left[\partial_R (\bar{p})^0 \right] \lambda_{zz} R + R^2 u_1'' / u_1 - 2\omega^2 \right\} R^2 A_1'' - \left\{ \left[\partial_R^2 (\bar{p})^0 \right] \lambda_{zz} R^2 + 2 \left[\partial_R (\bar{p})^0 \right] R \lambda_{zz} + 1 - 3R^2 u_1'' / u_1 + 2\omega^2 \right\} R A_1' - \left\{ R^2 \left[\partial_R^2 (\bar{p})^0 \right] \lambda_{zz} - 1 - R^2 u_1'' / u_1 - \omega^2 (\omega^2 - 2) + R^2 \omega^2 u_1'' / u_1 - R^2 \left[\partial_R^2 (\bar{p})^0 \right] \lambda_{zz} \omega^2 \right\} A_1 = 0, \quad (\text{A2.54})$$

The corresponding dimensionless form reads as:

$$\begin{aligned}
& \bar{R}^4 A_1^{(4)} + 6\bar{R}^3 A_1^{(3)} + \left\{ 5 - \left[\partial_{\bar{R}} (\bar{p})^0 \right] \lambda_{zZ} \bar{R} + \bar{R}^2 (\alpha^2 u_1'' / u_1) - 2\omega^2 \right\} \bar{R}^2 A_1'' \\
& - \left\{ \left[\partial_{\bar{R}}^2 (\bar{p})^0 \right] \lambda_{zZ} \bar{R}^2 + 2 \left[\partial_{\bar{R}} (\bar{p})^0 \right] \bar{R} \lambda_{zZ} + 1 - 3\bar{R}^2 (\alpha^2 u_1'' / u_1) + 2\omega^2 \right\} \bar{R} A_1' \\
& - \left\{ \bar{R}^2 \left[\partial_{\bar{R}}^2 (\bar{p})^0 \right] \lambda_{zZ} - 1 - \omega^4 + 2\omega^2 + \bar{R}^2 (\omega^2 - 1) (\alpha^2 u_1'' / u_1) - \bar{R}^2 \left[\partial_{\bar{R}}^2 (\bar{p})^0 \right] \lambda_{zZ} \omega^2 \right\} A_1 = 0, \quad (\text{A2.55})
\end{aligned}$$

It should be noted that the differentiations in Eq. (A2.55) is respecting to \bar{R} or \bar{Z} . From Eq. (A2.14) and Eq. (A2.17) in the theory of deformation field, we attain the following relations:

$$\left[\partial_{\bar{R}} (\bar{p})^0 \right] \lambda_{zZ} = \bar{R} \kappa^2 \alpha^2, \quad \left[\partial_{\bar{R}}^2 (\bar{p})^0 \right] \lambda_{zZ} = \kappa^2 \alpha^2 \text{ and } \alpha^2 u_1'' / u_1 = -\kappa^2 \alpha^2 \frac{\lambda_{rR}}{1 - \lambda_{rR}}. \text{ Therefore, Eq. (A2.55)}$$

can be further simplified as:

$$\begin{aligned}
& \bar{R}^4 A_1^{(4)} + 6\bar{R}^3 A_1^{(3)} + (5 - 2\omega^2) \bar{R}^2 A_1'' - (2\omega^2 + 1) \bar{R} A_1' + (\omega^2 - 1)^2 A_1 \\
& - A_h^2 \bar{R}^2 \left[\bar{R}^2 A_1'' + 3\bar{R} A_1' - (\omega^2 - 1) A_1 \right] = 0, \quad (\text{A2.56})
\end{aligned}$$

with $A_h = \sqrt{\frac{\kappa^2 \alpha^2}{1 - \lambda_{rR}}}$. By setting the boundary conditions of traction free at $\bar{R}=1$, namely $\tilde{S}_{rR} = 0$,

$\tilde{S}_{\theta R} = 0$ and $\tilde{S}_{zR} = 0$. We can attain the boundary conditions of Eq. (A2.56) which needs to

satisfy as:

$$A_1' u_1 - (\bar{p})^0 (\gamma_{rZ} A_3' u_2 - \lambda_{zZ} A_1' u_1) - \frac{A_4}{\lambda_{rR}} = 0, \quad (\text{A2.57})$$

$$A_2' u_1 - (\bar{p})^0 \lambda_{zZ} \frac{A_1 \omega + A_2}{R} u_1 + (\bar{p})^0 \gamma_{rZ} \frac{A_3 \omega}{R} u_2 = 0, \quad (\text{A2.58})$$

$$A_3' u_2 + \lambda_{rR} \gamma_{rZ} A_4 + (\bar{p})^0 \gamma_{rZ} (\lambda_{rR}^2 \gamma_{rZ} A_3' u_2 - \lambda_{rR}^3 A_3 u_2' - A_1' u_1) + (\bar{p})^0 \lambda_{rR} A_1 u_1' = 0. \quad (\text{A2.59})$$

The combination of Eq. (A2.47) and Eq. (A2.57) results in the following equation in the dimensionless form as:

$$A_1^{(3)}(1) + 4A_1''(1) + [1 - 2\omega^2 - \zeta\omega^2 - A_h^2]A_1'(1) + [\omega^2 - 1 + \omega^2\kappa^2\alpha^2 - A_h^2]A_1(1) = 0, \quad (\text{A2.60})$$

$$\text{with } \zeta(\bar{Z}_0) = \frac{1}{2}\kappa^2\alpha^2 + \frac{1}{2}\lambda_{rR}^{-6} + C_3\lambda_{rR}^{-2}, \quad C_3 = \frac{1}{\cos^2\kappa} \left[1 - \frac{1}{2}\kappa^2\alpha^2 \right] - \frac{1}{2}\cos^4\kappa.$$

The combination of Eq. (A2.53a) and Eq. (A2.58) results in the following equation in the dimensionless form as:

$$A_1''(1) + (2 - \zeta)A_1'(1) + \zeta(\omega^2 - 1)A_1(1) = 0. \quad (\text{A2.61})$$

The third boundary condition in Eq. (A2.59) automatically satisfies since $A_3 \approx 0$.

In summary, the ODE for A_1 in the dimensionless form is expressed in Eq. (A2.56) with two boundary conditions in Eq. (A2.60) and Eq. (A2.61). To solve the forth ODE, we observe that this ODE can be separated into following two parts, both of which are in the Euler-Cauchy type:

$$\bar{R}^4 A_1^{(4)} + 6\bar{R}^3 A_1^{(3)} + (5 - 2\omega^2)\bar{R}^2 A_1'' - (2\omega^2 + 1)\bar{R}A_1' + (\omega^2 - 1)^2 A_1, \quad (\text{A2.62})$$

$$\bar{R}^2 A_1^{(2)} + 3\bar{R}A_1' - (\omega^2 - 1)A_1. \quad (\text{A2.63})$$

If both of them goes to zero together, then the system can be solved. The corresponding characteristic functions of Eq. (A2.62) and Eq. (A2.63) are $f_1(\lambda)$ and $f_2(\lambda)$ respectively with λ is the characteristic solutions:

$$\begin{aligned} f_1(\lambda) = & \lambda(\lambda-1)(\lambda-2)(\lambda-3) + 6\lambda(\lambda-1)(\lambda-2) \\ & + (5 - 2\omega^2)\lambda(\lambda-1) - (2\omega^2 + 1)\lambda + (\omega^2 - 1)^2, \end{aligned} \quad (\text{A2.64})$$

$$f_2(\lambda) = \lambda(\lambda-1) + 3\lambda - (\omega^2 - 1). \quad (\text{A2.65})$$

Owing to $f_1(-\omega-1) = f_1(-\omega+1) = f_1(\omega-1) = f_1(\omega+1) = 0$ and $f_2(-\omega-1) = f_2(\omega-1) = 0$,

we know that both $-\omega-1$ and $\omega-1$ are roots of both characteristic functions. Thus, we can

attain the general solution of A_1 , reading as:

$$A_1(\bar{R}) = c_1 \bar{R}^{\omega-1} + c_2 g_2(\bar{R}) \bar{R}^{\omega+1} + c_3 \bar{R}^{-\omega-1} + c_4 g_4(\bar{R}) \bar{R}^{-\omega+1}, \quad (\text{A2.66})$$

where $h_1(\bar{R}) = \bar{R}^{\omega-1}$, $h_2(\bar{R}) = g_2(\bar{R}) \bar{R}^{\omega+1}$, $h_3(\bar{R}) = \bar{R}^{-\omega-1}$ and $h_4(\bar{R}) = g_4(\bar{R}) \bar{R}^{-\omega+1}$ are four

characteristic functions, and c_1 , c_2 , c_3 and c_4 are arbitrary pre-factors. Since we are interested in

the decay solutions, and h_3 and h_4 diverges as $\bar{R} \rightarrow 0$, thus $c_3 = c_4 = 0$.

Since c_1 and c_2 are arbitrary constants, then we can have the decay solutions in the form

with $g_2 = \sum_{i=0}^{\infty} \alpha_i \bar{R}^i$ and $\alpha_0 = 1$, which indicates $h_2 = \sum_{i=0}^{\infty} \alpha_i \bar{R}^{i+\omega+1}$. Insert these back to the ODE, we

can attain $\alpha_1 = 0$ and all odd terms are zero, and

$$\alpha_{i+2} f_1(i+\omega+3) - A_h^2 \alpha_i f_2(i+\omega+1) = 0; \quad i \geq 0. \quad (\text{A2.67})$$

This further indicates:

$$\alpha_{2n} = A_h^{2n} \prod_{i=0}^{n-1} \frac{f_2(2i+\omega+1)}{f_1(2i+\omega+3)} = A_h^{2n} \prod_{i=0}^{n-1} \left[\frac{1}{4(i+2)(\omega+i+2)} \right] = \left(\frac{1}{2} A_h \right)^{2n} \frac{(\omega+1)!}{(n+1)!(n+\omega+1)!}. \quad (\text{A2.68})$$

Consequently, the decay solution reads as:

$$h_2 = (\omega+1)! \left(\frac{2}{A_h} \right)^{\omega+1} \sum_{n=0}^{\infty} \left(\frac{1}{2} A_h \bar{R} \right)^{2n+\omega+1} \frac{1}{(n+1)!(n+\omega+1)!}, \quad (\text{A2.69})$$

which can be further reduced to:

$$h_2 = (\omega+1)! \left(\frac{2}{A_h} \right)^{\omega+1} \left[I_{\omega} (A_h \bar{R}) - \frac{1}{\omega!} \left(\frac{A_h \bar{R}}{2} \right)^{\omega} \right] \left(\frac{2}{A_h \bar{R}} \right), \quad (\text{A2.70})$$

with $I_\omega(\bullet)$ is the modified Bessel function of the first kind. For simplicity, we set $h_1 = \bar{R}^{\omega-1}$ and

$h_2 = \frac{1}{I_\omega(A_h)} I_\omega(A_h \bar{R}) \bar{R}^{-1}$, leading to the solution of A_1 :

$$A_1 = c_1 \bar{R}^{\omega-1} + c_2 \frac{1}{I_\omega(A_h)} I_\omega(A_h \bar{R}) \bar{R}^{-1}, \quad (\text{A2.71})$$

Non-trivial solution requires c_1 and c_2 cannot be zero simultaneously. Recalling the boundary condition in Eq. (A2.60) and Eq. (A2.61) and by combining these two with Eq. (A2.68), we can further attain

$$\frac{c_1}{c_2} = \frac{lA_h \frac{I_{\omega-1}(A_h)}{I_\omega(A_h)} - (A_h^2 + l\omega^2 + l\omega)}{l\omega(\omega-1)}, \quad (\text{A2.72})$$

$$\frac{c_1}{c_2} = \frac{l\omega^2 A_h \frac{I_{\omega-1}(A_h)}{I_\omega(A_h)} - [l\omega^3 + l\omega^2 + \omega^2 \kappa^2 \alpha^2]}{\omega^2 \kappa^2 \alpha^2 - \omega A_h^2 - l\omega^3 + l\omega^2}, \quad (\text{A2.73})$$

with $l = 1 + \zeta$. The existence of non-trivial solution requires Eq. (A2.72) and Eq. (A2.73) be satisfied simultaneously. After simplifying it, we have,

$$\begin{aligned} & (l^2 \omega^3 A_h + lA_h^3 - l^2 \omega A_h) \frac{I_{\omega-1}(A_h)}{I_\omega(A_h)} - (2l\omega^2 A_h^2 + 2l^2 \omega^4 - 2l^2 \omega^2 + A_h^4) \\ & + \left(2l\omega^2 + \omega A_h^2 - l\omega A_h \frac{I_{\omega-1}(A_h)}{I_\omega(A_h)} \right) \kappa^2 \alpha^2 = 0. \end{aligned} \quad (\text{A2.74})$$

Eq. (A2.74) gives the critical stretch for each mode of instability. The minimum critical stretch of a critical mode of instability ω_c results in the critical stretch λ_c of the sample with aspect ratio α . We solved Eq. (A2.74) numerically. The critical stretch λ_c , the critical number of

instability ω_c and the critical stress S_c for the sample with different aspect ratios of α are summarized in Fig. 7-5.

Bibliography

1. T. McCormack, J. M. Mansour, Reduction in tensile strength of cartilage precedes surface damage under repeated compressive loading in vitro. *J. Biomech.* **31**, 55-61 (1997).
2. R. Tavichakorntrakool, V. Prasongwattana, P. Sriboonlue, A. Puapairoj, C. Wongkham, T. Wiangsimma, W. Khunkitti, S. Triamjangarun, M. Tanratanaujitt, A. Chamsuwan, K⁺, Na⁺, Mg²⁺, Ca²⁺, and water contents in human skeletal muscle: correlations among these monovalent and divalent cations and their alterations in K⁺-depleted subjects. *Transl. Res.* **150**, 357-366 (2007).
3. J. M. Lee, D. W. Courtman, D. R. Boughner, The glutaraldehyde - stabilized porcine aortic valve xenograft. I. Tensile viscoelastic properties of the fresh leaflet material. *J. Biomed. Mater. Res.* **18**, 61-77 (1984).
4. J. M. Lee, D. R. Boughner, D. W. Courtman, The glutaraldehyde - stabilized porcine aortic valve xenograft. II. Effect of fixation with or without pressure on the tensile viscoelastic properties of the leaflet material. *J. Biomed. Mater. Res.* **18**, 79-98 (1984).
5. W. Qiu, Y. Huang, W. Teng, C. M. Cohn, J. Cappello, X. Wu, Complete recombinant silk-elastinlike protein-based tissue scaffold. *Biomacromolecules* **11**, 3219-3227 (2010).
6. J. Cui, M. A. Lackey, A. E. Madkour, E. M. Saffer, D. M. Griffin, S. R. Bhatia, A. J. Crosby, G. N. Tew, Synthetically simple, highly resilient hydrogels. *Biomacromolecules* **13**, 584-588 (2012).
7. V. C. Mow, M. H. Holmes, W. M. Lai, Fluid transport and mechanical properties of articular cartilage: a review. *J. Biomech.* **17**, 377-394 (1984).
8. K. Athanasiou, M. Rosenwasser, J. Buckwalter, T. Malinin, V. C. Mow, Interspecies comparisons of in situ intrinsic mechanical properties of distal femoral cartilage. *J. Orthop. Res.* **9**, 330-340 (1991).
9. J. T. Kaplan, C. P. Neu, H. Drissi, N. C. Emery, D. M. Pierce, Cyclic loading of human articular cartilage: the transition from compaction to fatigue. *J. Mech. Behav. Biomed. Mater.* **65**, 734-742 (2017).
10. A. K. Williamson, A. C. Chen, K. Masuda, E. J. M. Thonar, R. L. Sah, Tensile mechanical properties of bovine articular cartilage: variations with growth and relationships to collagen network components. *J. Orthop. Res.* **21**, 872-880 (2003).

11. S.-Y. Woo, W. Akeson, G. Jemcott, Measurements of nonhomogeneous, directional mechanical properties of articular cartilage in tension. *J. Biomech.* **9**, 785-791 (1976).
12. M. V. Chin-Purcell, J. L. Lewis, Fracture of articular cartilage. *J. Biomech. Eng.* **118**, 545-556 (1996).
13. S. Park, C. Hung, G. Ateshian, Mechanical response of bovine articular cartilage under dynamic unconfined compression loading at physiological stress levels. *Osteoarthr. Cartil.* **12**, 65-73 (2004).
14. C. N. Maganaris, J. P. Paul, Tensile properties of the in vivo human gastrocnemius tendon. *J. Biomech.* **35**, 1639-1646 (2002).
15. R. E. Shadwick, Elastic energy storage in tendons: mechanical differences related to function and age. *J. Appl. Physiol.* **68**, 1033-1040 (1990).
16. C. N. Maganaris, Tensile properties of in vivo human tendinous tissue. *J. Biomech.* **35**, 1019-1027 (2002).
17. A. Race, A. A. Amis, The mechanical properties of the two bundles of the human posterior cruciate ligament. *J. Biomech.* **27**, 13-24 (1994).
18. R. B. Martin, D. B. Burr, N. A. Sharkey, D. P. Fyhrie, *Skeletal tissue mechanics*. (Springer, 1998), vol. 190.
19. N. Broom, The stress/strain and fatigue behaviour of glutaraldehyde preserved heart-valve tissue. *J. Biomech.* **10**, 707-724 (1977).
20. F. Javid, N. Shahmansouri, M. Amabili, R. Mongrain, D. Pasini, J. Angeles, in *ASME 2013 Summer Bioengineering Conference*. (American Society of Mechanical Engineers, 2013), pp. V01AT04A024-V001AT004A024.
21. D. C. Iliopoulos, E. P. Kritharis, A. T. Giagini, S. A. Papadodima, D. P. Sokolis, Ascending thoracic aortic aneurysms are associated with compositional remodeling and vessel stiffening but not weakening in age-matched subjects. *J. Thorac. Cardiovasc. Surg.* **137**, 101-109 (2009).
22. D. Taylor, N. O'Mara, E. Ryan, M. Takaza, C. Simms, The fracture toughness of soft tissues. *J. Mech. Behav. Biomed. Mater.* **6**, 139-147 (2012).
23. G. Sommer, T. C. Gasser, P. Regitnig, M. Auer, G. A. Holzapfel, Dissection properties of the human aortic media: an experimental study. *J. Biomech. Eng.* **130**, 021007 (2008).

24. V. Kovanen, H. Suominen, E. Heikkinen, Mechanical properties of fast and slow skeletal muscle with special reference to collagen and endurance training. *J. Biomech.* **17**, 725-735 (1984).
25. P. Fratzl, in *Collagen*. (Springer, 2008), pp. 1-13.
26. P. Kumar, M. Oka, J. Toguchida, M. Kobayashi, E. Uchida, T. Nakamura, K. Tanaka, Role of uppermost superficial surface layer of articular cartilage in the lubrication mechanism of joints. *J. Anat.* **199**, 241-250 (2001).
27. A. Maroudas, P. Bullough, S. Swanson, M. Freeman, The permeability of articular cartilage. *J. Bone Joint. Surg.* **50**, 166-177 (1968).
28. G. M. Genin, S. Thomopoulos, The tendon-to-bone attachment: Unification through disarray. *Nat. Mater.* **16**, 607-608 (2017).
29. L. Rossetti, L. A. Kuntz, E. Kunold, J. Schock, K. W. Muller, H. Grabmayr, J. Stolberg-Stolberg, F. Pfeiffer, S. A. Sieber, R. Burgkart, A. R. Bausch, The microstructure and micromechanics of the tendon-bone insertion. *Nat. Mater.* **16**, 664-670 (2017).
30. H. J. Gao, B. H. Ji, I. L. Jager, E. Arzt, P. Fratzl, Materials become insensitive to flaws at nanoscale: Lessons from nature. *Proc. Natl. Acad. Sci. U. S. A.* **100**, 5597-5600 (2003).
31. W. M. Han, S.-J. Heo, T. P. Driscoll, J. F. Delucca, C. M. McLeod, L. J. Smith, R. L. Duncan, R. L. Mauck, D. M. Elliott, Microstructural heterogeneity directs micromechanics and mechanobiology in native and engineered fibrocartilage. *Nat. Mater.* **15**, 477 (2016).
32. G. E. Fantner, T. Hassenkam, J. H. Kindt, J. C. Weaver, H. Birkedal, L. Pechenik, J. A. Cutroni, G. A. Cidade, G. D. Stucky, D. E. Morse, Sacrificial bonds and hidden length dissipate energy as mineralized fibrils separate during bone fracture. *Nat. Mater.* **4**, 612 (2005).
33. A. K. Nair, A. Gautieri, S.-W. Chang, M. J. Buehler, Molecular mechanics of mineralized collagen fibrils in bone. *Nat. Commun.* **4**, 1724 (2013).
34. K. Y. Lee, D. J. Mooney, Hydrogels for tissue engineering. *Chem. Rev.* **101**, 1869-1880 (2001).
35. T. R. Hoare, D. S. Kohane, Hydrogels in drug delivery: Progress and challenges. *Polymer* **49**, 1993-2007 (2008).

36. L. Jones, M. Senchyna, M.-A. Glasier, J. Schickler, I. Forbes, D. Louie, C. May, Lysozyme and lipid deposition on silicone hydrogel contact lens materials. *Eye Contact Lens* **29**, S75-S79 (2003).
37. L. H. Christensen, V. B. Breiting, A. Aasted, A. Jørgensen, I. Kebuladze, Long-term effects of polyacrylamide hydrogel on human breast tissue. *Plast. Reconstr. Surg.* **111**, 1883-1890 (2003).
38. A. Richter, G. Paschew, S. Klatt, J. Lienig, K.-F. Arndt, H.-J. Adler, Review on hydrogel-based pH sensors and microsensors. *Sensors* **8**, 561-581 (2008).
39. J. H. Holtz, S. A. Asher, Polymerized colloidal crystal hydrogel films as intelligent chemical sensing materials. *Nature* **389**, 829 (1997).
40. L. Dong, H. Jiang, Autonomous microfluidics with stimuli-responsive hydrogels. *Soft Matter* **3**, 1223-1230 (2007).
41. J. P. Gong, Why are double network hydrogels so tough? *Soft Matter* **6**, 2583-2590 (2010).
42. H. Yuk, T. Zhang, S. Lin, G. A. Parada, X. Zhao, Tough bonding of hydrogels to diverse non-porous surfaces. *Nat. Mater.* **15**, 190 (2016).
43. J. P. Gong, Y. Katsuyama, T. Kurokawa, Y. Osada, Double - network hydrogels with extremely high mechanical strength. *Adv. Mater.* **15**, 1155-1158 (2003).
44. J.-Y. Sun, X. Zhao, W. R. Illeperuma, O. Chaudhuri, K. H. Oh, D. J. Mooney, J. J. Vlassak, Z. Suo, Highly stretchable and tough hydrogels. *Nature* **489**, 133-136 (2012).
45. I. C. Liao, F. T. Moutos, B. T. Estes, X. Zhao, F. Guilak, Composite three - dimensional woven scaffolds with interpenetrating network hydrogels to create functional synthetic articular cartilage. *Adv. Funct. Mater.* **23**, 5833-5839 (2013).
46. X. Zhao, Multi-scale multi-mechanism design of tough hydrogels: building dissipation into stretchy networks. *Soft Matter* **10**, 672-687 (2014).
47. N. A. Peppas, S. R. Stauffer, Reinforced uncrosslinked poly (vinyl alcohol) gels produced by cyclic freezing-thawing processes: a short review. *J. Control. Release* **16**, 305-310 (1991).
48. A. Miserez, P. A. Guerette, Phase transition-induced elasticity of α -helical bioelastomeric fibres and networks. *Chem. Soc. Rev.* **42**, 1973-1995 (2013).
49. S. Lin, J. Liu, X. Liu, X. Zhao, Muscle-like fatigue-resistant hydrogels by mechanical training. *Proc. Natl. Acad. Sci. U. S. A.* **116**, 10244-10249 (2019).

50. S. Lin, C. Cao, Q. Wang, M. Gonzalez, J. E. Dolbow, X. Zhao, Design of stiff, tough and stretchy hydrogel composites via nanoscale hybrid crosslinking and macroscale fiber reinforcement. *Soft Matter* **10**, 7519-7527 (2014).
51. S. Lin, T. Cohen, T. Zhang, H. Yuk, R. Abeyaratne, X. Zhao, Fringe instability in constrained soft elastic layers. *Soft Matter* **12**, 8899-8906 (2016).
52. S. Lin, Y. Mao, R. Radovitzky, X. Zhao, Instabilities in confined elastic layers under tension: Fringe, fingering and cavitation. *J. Mech. Phys. Solids* **106**, 229-256 (2017).
53. Y. Mao, L. Anand, Fracture of elastomeric materials by crosslink failure. *J. Appl. Mech.* **85**, 081008 (2018).
54. Y.-R. Luo, *Comprehensive handbook of chemical bond energies*. (CRC press, 2007).
55. J. Tang, J. Li, J. J. Vlassak, Z. Suo, Fatigue fracture of hydrogels. *Extreme Mech. Lett.* **10**, 24-31 (2017).
56. Y. Akagi, H. Sakurai, J. P. Gong, U.-i. Chung, T. Sakai, Fracture energy of polymer gels with controlled network structures. *J. Chem. Phys.* **139**, 144905 (2013).
57. C. Yang, T. Yin, Z. Suo, Polyacrylamide hydrogels. I. Network imperfection. *J. Mech. Phys. Solids*, (2019).
58. Y. Mao, B. Talamini, L. Anand, Rupture of polymers by chain scission. *Extreme Mech. Lett.* **13**, 17-24 (2017).
59. B. Talamini, Y. Mao, L. Anand, Progressive damage and rupture in polymers. *J. Mech. Phys. Solids* **111**, 434-457 (2018).
60. T. Zhang, S. Lin, H. Yuk, X. Zhao, Predicting fracture energies and crack-tip fields of soft tough materials. *Extreme Mech. Lett.* **4**, 1-8 (2015).
61. Y. Qi, J. Caillard, R. Long, Fracture toughness of soft materials with rate-independent hysteresis. *J. Mech. Phys. Solids* **118**, 341-364 (2018).
62. T. L. Sun, T. Kurokawa, S. Kuroda, A. B. Ihsan, T. Akasaki, K. Sato, M. A. Haque, T. Nakajima, J. P. Gong, Physical hydrogels composed of polyampholytes demonstrate high toughness and viscoelasticity. *Nat. Mater.* **12**, 932 (2013).
63. X. Wang, W. Hong, Delayed fracture in gels. *Soft Matter* **8**, 8171-8178 (2012).
64. Y. Mao, L. Anand, A theory for fracture of polymeric gels. *J. Mech. Phys. Solids* **115**, 30-53 (2018).

65. J. Diani, B. Fayolle, P. Gilormini, A review on the Mullins effect. *Eur. Polym. J.* **45**, 601-612 (2009).
66. R. Dargazany, M. Itskov, A network evolution model for the anisotropic Mullins effect in carbon black filled rubbers. *Int. J. Solids Struct.* **46**, 2967-2977 (2009).
67. T. Lu, J. Wang, R. Yang, T. Wang, A constitutive model for soft materials incorporating viscoelasticity and Mullins effect. *J. Appl. Mech.* **84**, 021010 (2017).
68. Y. Mao, S. Lin, X. Zhao, L. Anand, A large deformation viscoelastic model for double-network hydrogels. *J. Mech. Phys. Solids* **100**, 103-130 (2017).
69. L. Mullins, N. Tobin, Theoretical model for the elastic behavior of filler-reinforced vulcanized rubbers. *Rubber Chem. Technol.* **30**, 555-571 (1957).
70. R. Long, K. Mayumi, C. Creton, T. Narita, C.-Y. Hui, Time dependent behavior of a dual cross-link self-healing gel: Theory and experiments. *Macromolecules* **47**, 7243-7250 (2014).
71. S. C. Grindy, R. Learsch, D. Mozhdehi, J. Cheng, D. G. Barrett, Z. Guan, P. B. Messersmith, N. Holten-Andersen, Control of hierarchical polymer mechanics with bioinspired metal-coordination dynamics. *Nat. Mater.* **14**, 1210-1216 (2015).
72. D. E. Fullenkamp, L. He, D. G. Barrett, W. R. Burghardt, P. B. Messersmith, Mussel-inspired histidine-based transient network metal coordination hydrogels. *Macromolecules* **46**, 1167-1174 (2013).
73. C. Shao, H. Chang, M. Wang, F. Xu, J. Yang, High-Strength, Tough, and Self-Healing Nanocomposite Physical Hydrogels Based on the Synergistic Effects of Dynamic Hydrogen Bond and Dual Coordination Bonds. *ACS Appl. Mater. Interfaces* **9**, 28305-28318 (2017).
74. M. Nakahata, Y. Takashima, A. Harada, Highly Flexible, Tough, and Self-Healing Supramolecular Polymeric Materials Using Host - Guest Interaction. *Macromol. Rapid Commun.* **37**, 86-92 (2016).
75. N. Bouklas, C. M. Landis, R. Huang, Effect of solvent diffusion on crack-tip fields and driving force for fracture of hydrogels. *J. Appl. Mech.* **82**, 081007 (2015).
76. A. Lucantonio, G. Noselli, X. Trepas, A. DeSimone, M. Arroyo, Hydraulic fracture and toughening of a brittle layer bonded to a hydrogel. *Phys. Rev. Lett.* **115**, 188105 (2015).
77. C. Yang, Z. Suo, Hydrogel ionotronics. *Nat. Rev. Mater.* **3**, 125 (2018).

78. R. Bai, Q. Yang, J. Tang, X. P. Morelle, J. Vlassak, Z. Suo, Fatigue fracture of tough hydrogels. *Extreme Mech. Lett.* **15**, 91-96 (2017).
79. R. Bai, J. Yang, X. P. Morelle, C. Yang, Z. Suo, Fatigue fracture of self-recovery hydrogels. *ACS Macro Lett.* **7**, 312-317 (2018).
80. W. Zhang, X. Liu, J. Wang, J. Tang, J. Hu, T. Lu, Z. Suo, Fatigue of double-network hydrogels. *Eng. Fract. Mech.* **187**, 74-93 (2018).
81. T. Tallinen, J. Y. Chung, F. Rousseau, N. Girard, J. Lefèvre, L. Mahadevan, On the growth and form of cortical convolutions. *Nat. Phys.* **12**, 588 (2016).
82. J. Genzer, J. Groenewold, Soft matter with hard skin: From skin wrinkles to templating and material characterization. *Soft Matter* **2**, 310-323 (2006).
83. Q. Wang, X. Zhao, Phase diagrams of instabilities in compressed film-substrate systems. *J. Appl. Mech.* **81**, 051004 (2014).
84. K. R. Shull, C. Creton, Deformation behavior of thin, compliant layers under tensile loading conditions. *J. Polym. Sci. B* **42**, 4023-4043 (2004).
85. M. B. Amar, P. Ciarletta, Swelling instability of surface-attached gels as a model of soft tissue growth under geometric constraints. *J. Mech. Phys. Solids* **58**, 935-954 (2010).
86. A. Goriely, M. B. Amar, Differential growth and instability in elastic shells. *Phys. Rev. Lett.* **94**, 198103 (2005).
87. W. Hong, X. Zhao, Z. Suo, Formation of creases on the surfaces of elastomers and gels. *Appl. Phys. Lett.* **95**, 111901 (2009).
88. B. Li, Y.-P. Cao, X.-Q. Feng, H. Gao, Mechanics of morphological instabilities and surface wrinkling in soft materials: a review. *Soft Matter* **8**, 5728-5745 (2012).
89. L. Jin, Mechanical Instabilities of Soft Materials: Creases, Wrinkles, Folds, and Ridges. Harvard thesis (2014).
90. C. Cao, H. F. Chan, J. Zang, K. W. Leong, X. Zhao, Harnessing localized ridges for high-aspect-ratio hierarchical patterns with dynamic tunability and multifunctionality. *Adv. Mater.* **26**, 1763-1770 (2014).
91. J. A. Zimberlin, N. Sanabria-DeLong, G. N. Tew, A. J. Crosby, Cavitation rheology for soft materials. *Soft Matter* **3**, 763-767 (2007).
92. A. Ghatak, M. K. Chaudhury, Adhesion-induced instability patterns in thin confined elastic film. *Langmuir* **19**, 2621-2631 (2003).

93. J. S. Biggins, B. Saintyves, Z. Wei, E. Bouchaud, L. Mahadevan, Digital instability of a confined elastic meniscus. *Proc. Natl. Acad. Sci. U. S. A.* **110**, 12545-12548 (2013).
94. K. R. Shull, C. M. Flanigan, A. J. Crosby, Fingering instabilities of confined elastic layers in tension. *Phys. Rev. Lett.* **84**, 3057 (2000).
95. A. Gent, P. Lindley, in *Proc. Royal Soc. A.* (The Royal Society, 1959), vol. 249, pp. 195-205.
96. J. Chung, K. Kim, M. Chaudhury, J. Sarkar, A. Sharma, Confinement-induced instability and adhesive failure between dissimilar thin elastic films. *Eur. Phys. J. E* **20**, 47-53 (2006).
97. M. K. Chaudhury, A. Chakrabarti, A. Ghatak, Adhesion-induced instabilities and pattern formation in thin films of elastomers and gels. *Eur. Phys. J. E* **38**, 1-26 (2015).
98. A. Chakrabarti, M. K. Chaudhury, Direct measurement of the surface tension of a soft elastic hydrogel: Exploration of elastocapillary instability in adhesion. *Langmuir* **29**, 6926-6935 (2013).
99. J. Y. Chung, M. K. Chaudhury, Soft and hard adhesion. *J. Adhes.* **81**, 1119-1145 (2005).
100. C. Fond, Cavitation criterion for rubber materials: A review of void-growth models. *J. Polym. Sci. B* **39**, 2081-2096 (2001).
101. J. M. Ball, Discontinuous equilibrium solutions and cavitation in nonlinear elasticity. *Philos. Trans. Royal Soc. A* **306**, 557-611 (1982).
102. H. Hang-Sheng, R. Abeyaratne, Cavitation in elastic and elastic-plastic solids. *J. Mech. Phys. Solids* **40**, 571-592 (1992).
103. O. Lopez-Pamies, M. I. Idiart, T. Nakamura, Cavitation in elastomeric solids: I—A defect-growth theory. *J. Mech. Phys. Solids* **59**, 1464-1487 (2011).
104. J. T. Overvelde, D. M. Dykstra, R. de Rooij, J. Weaver, K. Bertoldi, Tensile Instability in a Thick Elastic Body. *Phys. Rev. Lett.* **117**, 094301 (2016).
105. P. Calvert, Hydrogels for soft machines. *Adv. Mater.* **21**, 743-756 (2009).
106. C. Creton, M. Ciccotti, Fracture and adhesion of soft materials: a review. *Rep. Prog. Phys.* **79**, 046601 (2016).
107. A. J. Crosby, K. R. Shull, H. Lakrout, C. Creton, Deformation and failure modes of adhesively bonded elastic layers. *J. Appl. Phys.* **88**, 2956-2966 (2000).
108. P. Fratzl, Biomimetic materials research: what can we really learn from nature's structural materials? *J. Royal Soc. Interface* **4**, 637-642 (2007).

109. J. Wang, L. Lin, Q. Cheng, L. Jiang, A Strong Bio-Inspired Layered PNIPAM-Clay Nanocomposite Hydrogel. *Angew. Chem. Int. Ed.* **51**, 4676-4680 (2012).
110. J. Li, Z. Suo, J. J. Vlassak, Stiff, strong, and tough hydrogels with good chemical stability. *J. Mater. Chem. B* **2**, 6708-6713 (2014).
111. Q. He, Z. Wang, Y. Yan, J. Zheng, S. Cai, Polymer nanofiber reinforced double network gel composite: Strong, tough and transparent. *Extreme Mech. Lett.* **9**, 165-170 (2016).
112. A. E. Brown, R. I. Litvinov, D. E. Discher, P. K. Purohit, J. W. Weisel, Multiscale mechanics of fibrin polymer: gel stretching with protein unfolding and loss of water. *Science* **325**, 741-744 (2009).
113. K. Ito, Novel cross-linking concept of polymer network: synthesis, structure, and properties of slide-ring gels with freely movable junctions. *Polym. J.* **39**, 489 (2007).
114. T. Sakai, T. Matsunaga, Y. Yamamoto, C. Ito, R. Yoshida, S. Suzuki, N. Sasaki, M. Shibayama, U.-i. Chung, Design and fabrication of a high-strength hydrogel with ideally homogeneous network structure from tetrahedron-like macromonomers. *Macromolecules* **41**, 5379-5384 (2008).
115. G. Lake, A. Thomas, The strength of highly elastic materials. *Proc. Royal Soc. A* **300**, 108-119 (1967).
116. H. R. Brown, A model of the fracture of double network gels. *Macromolecules* **40**, 3815-3818 (2007).
117. R. E. Webber, C. Creton, H. R. Brown, J. P. Gong, Large strain hysteresis and Mullins effect of tough double-network hydrogels. *Macromolecules* **40**, 2919-2927 (2007).
118. S. Lin, Y. Zhou, X. Zhao, Designing extremely resilient and tough hydrogels via delayed dissipation. *Extreme Mech. Lett.* **1**, 70-75 (2014).
119. R. Rivlin, A. G. Thomas, Rupture of rubber. I. Characteristic energy for tearing. *J. Polym. Sci.* **10**, 291-318 (1953).
120. D. Moreira, L. Nunes, Comparison of simple and pure shear for an incompressible isotropic hyperelastic material under large deformation. *Polym. Test* **32**, 240-248 (2013).
121. R. Long, C.-Y. Hui, Crack tip fields in soft elastic solids subjected to large quasi-static deformation—a review. *Extreme Mech. Lett.* **4**, 131-155 (2015).
122. C. Chen, Z. Wang, Z. Suo, Flaw sensitivity of highly stretchable materials. *Extreme Mech. Lett.* **10**, 50-57 (2017).

123. C.-Y. Hui, S. Bennison, J. Londono, Crack blunting and the strength of soft elastic solids. *Proc. Royal Soc. A* **459**, 1489-1516 (2003).
124. T. Baumberger, C. Caroli, D. Martina, Solvent control of crack dynamics in a reversible hydrogel. *Nat. Mater.* **5**, 552 (2006).
125. T. Nguyen, S. Govindjee, Numerical study of geometric constraint and cohesive parameters in steady-state viscoelastic crack growth. *Int. J. Fract.* **141**, 255-268 (2006).
126. R. Ogden, D. Roxburgh, A pseudo-elastic model for the Mullins effect in filled rubber. *Proc. Royal Soc. A* **455**, 2861-2877 (1999).
127. R. Ogden, G. Saccomandi, I. Sgura, Fitting hyperelastic models to experimental data. *Comput. Mech.* **34**, 484-502 (2004).
128. B. P. Pereira, P. W. Lucas, T. SweeHin, Ranking the fracture toughness of thin mammalian soft tissues using the scissors cutting test. *J. Biomech.* **30**, 91-94 (1997).
129. M. S. Sacks, W. D. Merryman, D. E. Schmidt, On the biomechanics of heart valve function. *J. Biomech.* **42**, 1804-1824 (2009).
130. J. Li, W. R. K. I. Illeperuma, Z. Suo, J. J. Vlassak, Hybrid hydrogels with extremely high stiffness and toughness. *ACS Macro Lett.* **3**, 520-523 (2014).
131. C. He, Z. Zheng, D. Zhao, J. Liu, J. Ouyang, H. Wang, Tough and super-resilient hydrogels synthesized by using peroxidized polymer chains as polyfunctional initiating and cross-linking centers. *Soft Matter* **9**, 2837-2844 (2013).
132. J. Liu, C. Chen, C. He, L. Zhao, X. Yang, H. Wang, Synthesis of Graphene Peroxide and Its Application in Fabricating Super Extensible and Highly Resilient Nanocomposite Hydrogels. *Acs Nano* **6**, 8194-8202 (2012).
133. M. Zhu, Y. Liu, B. Sun, W. Zhang, X. Liu, H. Yu, Y. Zhang, D. Kuckling, H.-J. P. Adler, A novel highly resilient nanocomposite hydrogel with low hysteresis and ultrahigh elongation. *Macromol. Rapid Commun.* **27**, 1023-1028 (2006).
134. H. Kamata, Y. Akagi, Y. Kayasuga-Kariya, U.-i. Chung, T. Sakai, "Nonswellable" Hydrogel Without Mechanical Hysteresis. *Science* **343**, 873-875 (2014).
135. I. Vesely, The role of elastin in aortic valve mechanics. *J. Biomech.* **31**, 115-123 (1997).
136. G. A. Holzapfel, *Nonlinear solid mechanics*. (Wiley Chichester, 2000), vol. 24.
137. M. C. Boyce, E. M. Arruda, Constitutive models of rubber elasticity: A review. *Rubber Chem. Technol.* **73**, 504-523 (2000).

138. H. Tsukeshiba, M. Huang, Y. H. Na, T. Kurokawa, R. Kuwabara, Y. Tanaka, H. Furukawa, Y. Osada, J. P. Gong, Effect of polymer entanglement on the toughening of double network hydrogels. *J. Phys. Chem. B* **109**, 16304-16309 (2005).
139. H. A. Bruck, S. R. McNeill, M. A. Sutton, W. H. Peters, Digital image correlation using Newton-Raphson method of partial differential correction. *Exp. Mech.* **29**, 261-267 (1989).
140. W. H. Peters, W. F. Ranson, DIGITAL IMAGING TECHNIQUES IN EXPERIMENTAL STRESS-ANALYSIS. *Opt. Eng.* **21**, 427-431 (1982).
141. A. Tinker, K. P. Jones, *Blends of natural rubber: novel techniques for blending with speciality polymers*. (Springer, 1998).
142. E. Ducrot, Y. Chen, M. Bulters, R. P. Sijbesma, C. Creton, Toughening Elastomers with Sacrificial Bonds and Watching Them Break. *Science* **344**, 186-189 (2014).
143. J. Li, D. J. Mooney, Designing hydrogels for controlled drug delivery. *Nat. Rev. Mater.* **1**, 16071 (2016).
144. L. Casares, R. Vincent, D. Zalvidea, N. Campillo, D. Navajas, M. Arroyo, X. Trepát, Hydraulic fracture during epithelial stretching. *Nat. Mater.* **14**, 343 (2015).
145. S. Lin, H. Yuk, T. Zhang, G. A. Parada, H. Koo, C. Yu, X. Zhao, Stretchable hydrogel electronics and devices. *Adv. Mater.* **28**, 4497-4505 (2016).
146. X. Liu, T.-C. Tang, E. Tham, H. Yuk, S. Lin, T. K. Lu, X. Zhao, Stretchable living materials and devices with hydrogel–elastomer hybrids hosting programmed cells. *Proc. Natl. Acad. Sci. U. S. A.* **114**, 2200-2205 (2017).
147. H. Yuk, S. Lin, C. Ma, M. Takaffoli, N. X. Fang, X. Zhao, Hydraulic hydrogel actuators and robots optically and sonically camouflaged in water. *Nat. Commun.* **8**, 14230 (2017).
148. H. Yuk, T. Zhang, G. A. Parada, X. Liu, X. Zhao, Skin-inspired hydrogel-elastomer hybrids with robust interfaces and functional microstructures. *Nat. Commun.* **7**, 12028 (2016).
149. Q. Liu, G. Nian, C. Yang, S. Qu, Z. Suo, Bonding dissimilar polymer networks in various manufacturing processes. *Nat. Commun.* **9**, 846 (2018).
150. D. Wirthl, R. Pichler, M. Drack, G. Kettlguber, R. Moser, R. Gerstmayr, F. Hartmann, E. Bradt, R. Kaltseis, C. M. Siket, Instant tough bonding of hydrogels for soft machines and electronics. *Sci. Adv.* **3**, e1700053 (2017).

151. Q. Chen, L. Zhu, C. Zhao, Q. Wang, J. Zheng, A robust, one-pot synthesis of highly mechanical and recoverable double network hydrogels using thermoreversible sol-gel polysaccharide. *Adv. Mater.* **25**, 4171-4176 (2013).
152. C. Creton, 50th anniversary perspective: networks and gels: soft but dynamic and tough. *Macromolecules* **50**, 8297-8316 (2017).
153. R. Berisio, L. Vitagliano, L. Mazzarella, A. Zagari, Crystal structure of the collagen triple helix model [(Pro - Pro - Gly) 10] 3. *Protein Sci.* **11**, 262-270 (2002).
154. A. J. Kinloch, *Fracture behaviour of polymers*. (Springer Science & Business Media, 2013).
155. A. Gent, P. Lindley, A. Thomas, Cut growth and fatigue of rubbers. I. The relationship between cut growth and fatigue. *J. Polym. Sci.* **8**, 455-466 (1964).
156. G. Lake, P. Lindley, Cut growth and fatigue of rubbers. II. Experiments on a noncrystallizing rubber. *J. Polym. Sci.* **8**, 707-721 (1964).
157. N. A. Peppas, E. W. Merrill, Differential scanning calorimetry of crystallized PVA hydrogels. *J. Appl. Polym. Sci.* **20**, 1457-1465 (1976).
158. C. M. Hassan, N. A. Peppas, Structure and morphology of freeze/thawed PVA hydrogels. *Macromolecules* **33**, 2472-2479 (2000).
159. J. Y. Chang, D. Godovsky, M. Han, C. Hassan, J. Kim, B. Lee, Y. Lee, N. Peppas, R. Quirk, T. Yoo, *Biopolymers: PVA Hydrogels Anionic Polymerisation Nanocomposites*. (Springer Science & Business Media, 2000), vol. 153.
160. K. C. Figueiredo, T. L. Alves, C. P. Borges, Poly (vinyl alcohol) films crosslinked by glutaraldehyde under mild conditions. *J. Appl. Polym. Sci.* **111**, 3074-3080 (2009).
161. R. Zhang, Q. Zhang, Y. Ji, F. Su, L. Meng, Z. Qi, Y. Lin, X. Li, X. Chen, F. Lv, Stretch-induced complexation reaction between poly (vinyl alcohol) and iodine: an in situ synchrotron radiation small-and wide-angle X-ray scattering study. *Soft Matter* **14**, 2535-2546 (2018).
162. R. Ricciardi, F. Auriemma, C. De Rosa, F. Lauprêtre, X-ray diffraction analysis of poly (vinyl alcohol) hydrogels, obtained by freezing and thawing techniques. *Macromolecules* **37**, 1921-1927 (2004).
163. A. Patterson, The Scherrer formula for X-ray particle size determination. *Phys. Rev.* **56**, 978 (1939).

164. E. Otsuka, S. Komiya, S. Sasaki, J. Xing, Y. Bando, Y. Hirashima, M. Sugiyama, A. Suzuki, Effects of preparation temperature on swelling and mechanical properties of PVA cast gels. *Soft Matter* **8**, 8129-8136 (2012).
165. S. M. Liff, N. Kumar, G. H. McKinley, High-performance elastomeric nanocomposites via solvent-exchange processing. *Nat. Mater.* **6**, 76 (2007).
166. M. Vatankhah-Varnosfaderani, A. N. Keith, Y. Cong, H. Liang, M. Rosenthal, M. Sztucki, C. Clair, S. Magonov, D. A. Ivanov, A. V. Dobrynin, Chameleon-like elastomers with molecularly encoded strain-adaptive stiffening and coloration. *Science* **359**, 1509-1513 (2018).
167. A. R. Gillies, R. L. Lieber, Structure and function of the skeletal muscle extracellular matrix. *Muscle Nerve* **44**, 318-331 (2011).
168. M. I. Baker, S. P. Walsh, Z. Schwartz, B. D. Boyan, A review of polyvinyl alcohol and its uses in cartilage and orthopedic applications. *J. Biomed. Mater. Res. B* **100**, 1451-1457 (2012).
169. S. Zhao, P. Tseng, J. Grasman, Y. Wang, W. Li, B. Napier, B. Yavuz, Y. Chen, L. Howell, J. Rincon, Programmable Hydrogel Ionic Circuits for Biologically Matched Electronic Interfaces. *Adv. Mat.* **30**, 1800598 (2018).
170. Y. Liu, J. Liu, S. Chen, T. Lei, Y. Kim, S. Niu, H. Wang, X. Wang, A. M. Foudeh, J. B.-H. Tok, Soft and elastic hydrogel-based microelectronics for localized low-voltage neuromodulation. *Nat. Biomed. Eng.* **3**, 58 (2019).
171. B. Lu, H. Yuk, S. Lin, N. Jian, K. Qu, J. Xu, X. Zhao, Pure PEDOT: PSS hydrogels. *Nat. Commun.* **10**, 1043 (2019).
172. H. Yuk, B. Lu, X. Zhao, Hydrogel bioelectronics. *Chem. Soc. Rev.*, (2019).
173. J. Guo, X. Liu, N. Jiang, A. K. Yetisen, H. Yuk, C. Yang, A. Khademhosseini, X. Zhao, S. H. Yun, Highly stretchable, strain sensing hydrogel optical fibers. *Adv. Mater.* **28**, 10244-10249 (2016).
174. M. Choi, M. Humar, S. Kim, S. H. Yun, Step - index optical fiber made of biocompatible hydrogels. *Adv. Mater.* **27**, 4081-4086 (2015).
175. X. Liu, C. Steiger, S. Lin, G. A. Parada, J. Liu, H. F. Chan, H. Yuk, N. V. Phan, J. Collins, S. Tamang, Ingestible hydrogel device. *Nat. Commun.* **10**, (2019).

176. G. A. Parada, H. Yuk, X. Liu, A. J. Hsieh, X. Zhao, Impermeable robust hydrogels via hybrid lamination. *Adv. Healthc. Mater.* **6**, 1700520 (2017).
177. R. Takahashi, K. Shimano, H. Okazaki, T. Kurokawa, T. Nakajima, T. Nonoyama, D. R. King, J. P. Gong, Tough Particle - Based Double Network Hydrogels for Functional Solid Surface Coatings. *Adv. Mater. Interfaces* **5**, 1801018 (2018).
178. Y. Yu, H. Yuk, G. A. Parada, Y. Wu, X. Liu, C. S. Nabzdyk, K. Youcef-Toumi, J. Zang, X. Zhao, Multifunctional “Hydrogel Skins” on Diverse Polymers with Arbitrary Shapes. *Adv. Mater.* **31**, 1807101 (2018).
179. Y. Kim, H. Yuk, R. Zhao, S. A. Chester, X. Zhao, Printing ferromagnetic domains for untethered fast-transforming soft materials. *Nature* **558**, 274 (2018).
180. S. Y. Chin, Y. C. Poh, A.-C. Kohler, J. T. Compton, L. L. Hsu, K. M. Lau, S. Kim, B. W. Lee, F. Y. Lee, S. K. Sia, Additive manufacturing of hydrogel-based materials for next-generation implantable medical devices. *Sci. Robot.* **2**, eaah6451 (2017).
181. P. H. Kouwer, M. Koepf, V. A. Le Sage, M. Jaspers, A. M. van Buul, Z. H. Eksteen-Akeroyd, T. Woltinge, E. Schwartz, H. J. Kitto, R. Hoogenboom, Responsive biomimetic networks from polyisocyanopeptide hydrogels. *Nature* **493**, 651 (2013).
182. M. Jaspers, M. Dennison, M. F. Mabeoone, F. C. MacKintosh, A. E. Rowan, P. H. Kouwer, Ultra-responsive soft matter from strain-stiffening hydrogels. *Nat. Commun.* **5**, 5808 (2014).
183. M. Vatankhah-Varnosfaderani, W. F. Daniel, M. H. Everhart, A. A. Pandya, H. Liang, K. Matyjaszewski, A. V. Dobrynin, S. S. Sheiko, Mimicking biological stress-strain behaviour with synthetic elastomers. *Nature* **549**, 497 (2017).
184. S. Lin, X. Liu, J. Liu, H. Yuk, H.-C. Loh, G. A. Parada, C. Settens, J. Song, A. Masic, G. H. McKinley, Anti-fatigue-fracture hydrogels. *Sci. Adv.* **5**, eaau8528 (2019).
185. Y. Huang, D. R. King, T. L. Sun, T. Nonoyama, T. Kurokawa, T. Nakajima, J. P. Gong, Energy - dissipative matrices enable synergistic toughening in fiber reinforced soft composites. *Adv. Funct. Mater.* **27**, 1605350 (2017).
186. C. M. Hassan, N. A. Peppas, in *Biopolymers· PVA Hydrogels, Anionic Polymerisation Nanocomposites*. (Springer, 2000), pp. 37-65.

187. J. L. Holloway, A. M. Lowman, G. R. Palmese, The role of crystallization and phase separation in the formation of physically cross-linked PVA hydrogels. *Soft Matter* **9**, 826-833 (2013).
188. N. A. Peppas, Turbidimetric studies of aqueous poly (vinyl alcohol) solutions. *Macromol. Chem. Phys.* **176**, 3433-3440 (1975).
189. P. J. Willcox, D. W. Howie Jr, K. Schmidt - Rohr, D. A. Hoagland, S. P. Gido, S. Pudjijanto, L. W. Kleiner, S. Venkatraman, Microstructure of poly (vinyl alcohol) hydrogels produced by freeze/thaw cycling. *J. Polym. Sci. B* **37**, 3438-3454 (1999).
190. B. J. Schoenfeld, The mechanisms of muscle hypertrophy and their application to resistance training. *J. Strength Cond. Res.* **24**, 2857-2872 (2010).
191. S. Toki, T. Fujimaki, M. Okuyama, Strain-induced crystallization of natural rubber as detected real-time by wide-angle X-ray diffraction technique. *Polymer* **41**, 5423-5429 (2000).
192. T. Matsuda, R. Kawakami, R. Namba, T. Nakajima, J. P. Gong, Mechanoresponsive self-growing hydrogels inspired by muscle training. *Science* **363**, 504-508 (2019).
193. W. Yang, V. R. Sherman, B. Gludovatz, E. Schaible, P. Stewart, R. O. Ritchie, M. A. Meyers, On the tear resistance of skin. *Nat. Commun.* **6**, 6649 (2015).
194. F. Fergg, F. Keil, H. Quader, Investigations of the microscopic structure of poly (vinyl alcohol) hydrogels by confocal laser scanning microscopy. *Colloid Polym. Sci.* **279**, 61-67 (2001).
195. H. Sehaqui, N. Ezekiel Mushi, S. Morimune, M. Salajkova, T. Nishino, L. A. J. A. a. m. Berglund, Cellulose nanofiber orientation in nanopaper and nanocomposites by cold drawing. *ACS Appl. Mater. Interfaces* **4**, 1043-1049 (2012).
196. T. Fukumori, T. Nakaoki, High strength poly (vinyl alcohol) films obtained by drying and then stretching freeze/thaw cycled gel. *J. Appl. Polym. Sci.* **132**, 41318 (2015).
197. M. T. I. Mredha, Y. Z. Guo, T. Nonoyama, T. Nakajima, T. Kurokawa, J. P. Gong, A Facile Method to Fabricate Anisotropic Hydrogels with Perfectly Aligned Hierarchical Fibrous Structures. *Adv. Mater.* **30**, 1704937 (2018).
198. Q. Zhang, R. Zhang, L. Meng, Y. Ji, F. Su, Y. Lin, X. Li, X. Chen, F. Lv, L. Li, Stretch-induced structural evolution of poly (vinyl alcohol) film in water at different temperatures:

- An in-situ synchrotron radiation small-and wide-angle X-ray scattering study. *Polymer* **142**, 233-243 (2018).
199. R. Bai, J. Yang, Z. Suo, Fatigue of hydrogels. *Eur. J. Mech. A Solids* **74**, 337-370 (2019).
 200. K. Haraguchi, T. Takehisa, Nanocomposite hydrogels: a unique organic-inorganic network structure with extraordinary mechanical, optical, and swelling/de-swelling properties. *Adv. Mater.* **14**, 1120-1124 (2002).
 201. W. Kong, C. Wang, C. Jia, Y. Kuang, G. Pastel, C. Chen, G. Chen, S. He, H. Huang, J. Zhang, Muscle-Inspired Highly Anisotropic, Strong, Ion - Conductive Hydrogels. *Adv. Mater.* **30**, 1801934 (2018).
 202. S. R. Stauffer, N. A. Peppast, Poly (vinyl alcohol) hydrogels prepared by freezing-thawing cyclic processing. *Polymer* **33**, 3932-3936 (1992).
 203. R. Bai, J. Yang, X. P. Morelle, Z. Suo, Flaw-Insensitive Hydrogels under Static and Cyclic Loads. *Macromol. Rapid Commun.* **2019**, 1800883 (2019).
 204. Z. Wang, C. Xiang, X. Yao, P. Le Floch, J. Mendez, Z. Suo, Stretchable materials of high toughness and low hysteresis. *Proc. Natl. Acad. Sci. U. S. A.* **116**, 5967-5972 (2019).
 205. S. Ling, D. L. Kaplan, M. J. Buehler, Nanofibrils in nature and materials engineering. *Nat. Rev. Mater.* **3**, 18016 (2018).
 206. K. W. Desmond, N. A. Zacchia, J. H. Waite, M. T. Valentine, Dynamics of mussel plaque detachment. *Soft Matter* **11**, 6832-6839 (2015).
 207. N. V. Gohad, N. Aldred, C. M. Hartshorn, Y. J. Lee, M. T. Cicerone, B. Orihuela, A. S. Clare, D. Rittschof, A. S. Mount, Synergistic roles for lipids and proteins in the permanent adhesive of barnacle larvae. *Nat. Commun.* **5**, (2014).
 208. Y. Sun, S. Guo, G. C. Walker, C. J. Kavanagh, G. W. Swain, Surface elastic modulus of barnacle adhesive and release characteristics from silicone surfaces. *Biofouling* **20**, 279-289 (2004).
 209. E. Vaccaro, J. H. Waite, Yield and post-yield behavior of mussel byssal thread: a self-healing biomolecular material. *Biomacromolecules* **2**, 906-911 (2001).
 210. A. Kinloch, Interfacial fracture mechanical aspects of adhesive bonded joints—a review. *J. Adhes.*, (1979).

211. J. Dollhofer, A. Chiche, V. Muralidharan, C. Creton, C. Hui, Surface energy effects for cavity growth and nucleation in an incompressible neo-Hookean material—modeling and experiment. *Int. J. Solids Struct.* **41**, 6111-6127 (2004).
212. J. Zhu, T. Li, S. Cai, Z. Suo, Snap-through expansion of a gas bubble in an elastomer. *J. Adhes.* **87**, 466-481 (2011).
213. P. G. Saffman, G. Taylor, in *Proceedings of the Royal Society of London A: Mathematical, Physical and Engineering Sciences*. (The Royal Society, 1958), vol. 245, pp. 312-329.
214. G. M. Homsy, Viscous fingering in porous media. *Annu. Rev. Fluid Mech.* **19**, 271-311 (1987).
215. G. H. McKinley, T. Sridhar, Filament-stretching rheometry of complex fluids. *Annu. Rev. Fluid Mech.* **34**, 375-415 (2002).
216. I. Bischofberger, R. Ramachandran, S. R. Nagel, Fingering versus stability in the limit of zero interfacial tension. *Nat. Commun.* **5**, (2014).
217. C. Zhong, T. Gurry, A. A. Cheng, J. Downey, Z. Deng, C. M. Stultz, T. K. Lu, Strong underwater adhesives made by self-assembling multi-protein nanofibres. *Nat. Nanotechnol.* **9**, 858-866 (2014).
218. A. Gent, P. Lindley, The compression of bonded rubber blocks. *Proc. Inst. Mech. Eng.* **173**, 111-122 (1959).
219. W. W. Klingbeil, R. T. Shield, Large-deformation analyses of bonded elastic mounts. *Z. Angew. Math. Phys.* **17**, 281-305 (1966).
220. J. H. Waite, N. H. Andersen, S. Jewhurst, C. Sun, Mussel adhesion: finding the tricks worth mimicking. *J. Adhes.* **81**, 297-317 (2005).
221. M. Benjamin, H. Toumi, J. Ralphs, G. Bydder, T. Best, S. Milz, Where tendons and ligaments meet bone: attachment sites ('entheses') in relation to exercise and/or mechanical load. *J. Anat.* **208**, 471-490 (2006).
222. K. R. Shull, Contact mechanics and the adhesion of soft solids. *Mater. Sci. Eng. R Rep.* **36**, 1-45 (2002).
223. C. Cha, E. Antoniadou, M. Lee, J. H. Jeong, W. W. Ahmed, T. A. Saif, S. A. Boppart, H. Kong, Tailoring hydrogel adhesion to polydimethylsiloxane substrates using polysaccharide glue. *Angew. Chem. Int. Ed.* **52**, 6949-6952 (2013).

224. S. Rose, A. PrevotEAU, P. Elzière, D. Hourdet, A. Marcellan, L. Leibler, Nanoparticle solutions as adhesives for gels and biological tissues. *Nature* **505**, 382-385 (2014).
225. E. Palleau, D. Morales, M. D. Dickey, O. D. Velev, Reversible patterning and actuation of hydrogels by electrically assisted ionoprinting. *Nature Commun.* **4**, (2013).
226. Y. S. Kim, M. Liu, Y. Ishida, Y. Ebina, M. Osada, T. Sasaki, T. Hikima, M. Takata, T. Aida, Thermoresponsive actuation enabled by permittivity switching in an electrostatically anisotropic hydrogel. *Nat. Mater.* **14**, 1002-1007 (2015).
227. C. Keplinger, J.-Y. Sun, C. C. Foo, P. Rothmund, G. M. Whitesides, Z. Suo, Stretchable, transparent, ionic conductors. *Science* **341**, 984-987 (2013).
228. J. U. Lind, T. A. Busbee, A. D. Valentine, F. S. Pasqualini, H. Yuan, M. Yadid, S.-J. Park, A. Kotikian, A. P. Nesmith, P. H. Campbell, Instrumented cardiac microphysiological devices via multimaterial three-dimensional printing. *Nat. Mater.* **16**, 303-308 (2017).
229. S. Kundu, A. J. Crosby, Cavitation and fracture behavior of polyacrylamide hydrogels. *Soft Matter* **5**, 3963-3968 (2009).
230. R. Stringfellow, R. Abeyaratne, Cavitation in an elastomer: comparison of theory with experiment. *Mater. Sci. Eng. A* **112**, 127-131 (1989).
231. C. H. Yang, M. X. Wang, H. Haider, J. H. Yang, J.-Y. Sun, Y. M. Chen, J. Zhou, Z. Suo, Strengthening alginate/polyacrylamide hydrogels using various multivalent cations. *ACS Appl. Mater. Interfaces* **5**, 10418-10422 (2013).
232. M. Shariff, An analysis of non-linear deformation of bonded rubber mounts. *Proc. Inst. Mech. Eng. C* **203**, 113-119 (1989).
233. G. Tupholme, M. Gover, Axial loading of bonded rubber blocks. *J. Appl. Mech.*, (2002).
234. A. Gent, Cavitation in rubber: a cautionary tale. *Rubber Chem. Technol.* **63**, 49-53 (1990).
235. R. Long, C.-Y. Hui, Effects of triaxiality on the growth of crack-like cavities in soft incompressible elastic solids. *Soft Matter* **6**, 1238-1245 (2010).
236. S. Biwa, Cavitation in finite elasticity with surface energy effects. *Int. J. Nonlin. Mech.* **41**, 1084-1094 (2006).
237. V. Lefèvre, K. Ravi-Chandar, O. Lopez-Pamies, Cavitation in rubber: an elastic instability or a fracture phenomenon? *International Journal of Fracture* **192**, 1-23 (2015).
238. J. A. Zimmerman, A. J. Crosby, Water cavitation of hydrogels. *J. Polym. Sci. B* **48**, 1423-1427 (2010).

239. X. Liu, H. Yuk, S. Lin, G. A. Parada, T. C. Tang, E. Tham, C. de la Fuente-Nunez, T. K. Lu, X. Zhao, 3D printing of living responsive materials and devices. *Adv. Mater.* **30**, 1704821 (2018).